POLITECNICO
MILANO 1863

School of Civil, Environmental and Land Management Engineering

M.Sc. in Civil Engineering for Risk Mitigation

EXPERIMENTAL AND NUMERICAL ANALYSIS OF CHANNEL AGGRADATION IN SUPERCRITICAL CONDITION

Supervisor: Dr. Alessio Radice

Co-supervisor: Hasan Eslami

Master of Science Thesis by:

Keivan Tavakoli (942211)

Ehsan Zadehali (941263)

Reihaneh Zarrabi (942147)

Academic Year 2021-2022

ACKNOWLEDGMENTS

We would like to thank everyone who supported us in completing this master thesis.

Special thanks to our supervisor, Professor Alessio Radice, and Hassan Eslami as co-supervisor, for their time, support, and guidance throughout this journey.

We are also grateful to all staff and professors of the Politecnico di Milano for showing us the way during this master’s degree program.

Finally, we would like to express our deepest appreciation to our friends and families for supporting and encouraging us during these years, also dear Pardis and Elham for all their helps.

Table of Contents

List Of Figures

List Of Tables

Appendix Contents

Experiment AE06

Experiment AE07

Experiment AE08

Experiment AE10

Experiment AE11

Experiment AE13

Experiment AE07

ABSTRACT (ENGLISH)

Dangerous natural events such as floods are probable to cause substantial disasters with a devastating effect on the quality of human life. The flood as a dynamic phenomenon (both in space and time) can be even more threatening when it carries a significant volume of sediment which can change the riverbed elevation through deposition and erosion incidents. Indeed, while the degradation phenomenon causes damage to structures located in the riverbed, the aggradation phenomenon can raise the level of the riverbed and thus reduce the river's ability to carry sediments. This reduction is able to be developed into growth in flood risk.

The current study aims to deepen the knowledge of channel aggradation phenomena in supercritical flow by coupling both experimental and numerical approaches. The first approach is better for observing and interpreting processes, whereas the second approach is more commonly utilized in hazard assessments.

The experimental campaign related to supercritical flow, performed at the Mountain Hydraulics Lab of the Politecnico di Milano (Lecco campus), includes 14 experiments with different boundary conditions, regarding various water and sediment inflow discharges. Moreover, the aggradation phenomenon in the studied channel is formed by choosing the value of sediment inflow discharge larger than the sediment transport capacity of the channel.

Due to the dynamic nature of the campaign, different parts of the channel are observed and recorded by cameras. Then the taken videos during the experiment are processed by image processing methods provided in MATLAB code to measure the sediment feeding rate, the water and bed profiles, and the sediment transport capacity of the channel as the primary data. Furthermore, the Froude number Frs and propagation celerity of the aggradation phenomena are evaluated to have a better view of the deposition phenomenon.

It should be mentioned that in supercritical flow, aggradation happens in a dispersive way since it deals with higher flow velocities. Therefore, it gets difficult and almost impossible to detect any aggradation front. In the present research, two different methods are employed to measure the value of celerity, and then a comparison is made between them.

Also, in this thesis, numerical models developed by BASEMENT software, provided by ETH Zurich, are adapted to relate the experimental campaign to theoretical concepts of hydro-morphology. Indeed, this numerical model, calibrated by considering Manning’s coefficient n and Bedload factor α to have better consistency with experimental outcomes, can be used as a predictive tool for infeasible physical situations.

Keywords: Aggradation, overLoading ratio Lr, supercritical flow, celerity of propagation, local celerity, eigenvalues λ, experimental model, numerical model, dimension analysis.

SOMMARIO (ITALIANO)

È probabile che eventi naturali pericolosi come le inondazioni causino disastri sostanziali con effetti devastanti sulla qualità della vita umana. L'alluvione come fenomeno dinamico (sia nello spazio che nel tempo) può essere ancora più minaccioso quando trasporta un volume significativo di sedimenti che possono modificare l'elevazione del letto del fiume a causa di depositi ed erosioni. Infatti, mentre il fenomeno del degrado provoca danni alle strutture poste nell'alveo del fiume, il fenomeno dell'aggressione può innalzare il livello dell'alveo e quindi ridurre la capacità del fiume di trasportare sedimenti. Questa riduzione può trasformarsi in una crescita del rischio di alluvione.

Lo studio corrente mira ad approfondire la conoscenza dei fenomeni di aggregazione di canale nel flusso supercritico accoppiando approcci sperimentali e numerici. Il primo approccio è migliore per osservare e interpretare i processi, mentre il secondo approccio è più comunemente utilizzato nelle valutazioni dei rischi.

La campagna sperimentale relativa al flusso supercritico, eseguita presso il Laboratorio di Idraulica della Montagna del Politecnico di Milano (sede di Lecco), prevede 14 esperimenti con diverse condizioni al contorno, riguardanti vari scarichi di acqua e sedimenti. Inoltre, il fenomeno di aggregazione nel canale studiato si forma scegliendo un valore di portata di sedimento in entrata maggiore della capacità di trasporto dei sedimenti del canale.

A causa della natura dinamica della campagna, diverse parti del canale vengono osservate e registrate dalle telecamere. Quindi i video registrati durante l'esperimento sono trattati dai metodi di elaborazione delle immagini forniti nel codice MATLAB per misurare la velocità di alimentazione dei sedimenti, i profili dell'acqua e dell'alveo e la capacità di trasporto dei sedimenti del canale come dati primari. Inoltre, si valutano i numeri di Froude e la velocità di propagazione dei fenomeni di aggregazione per avere una visione migliore del fenomeno di deposizione.

Va menzionato che nel flusso supercritico, l'aggradazione avviene in modo dispersivo poiché si occupa di velocità di flusso più elevate. Pertanto, diventa difficile e quasi impossibile rilevare qualsiasi fronte di aggregazione. Nella presente ricerca, vengono utilizzati due diversi metodi per misurare il valore della celerità, quindi viene effettuato un confronto tra di loro.

Inoltre, in questa tesi, i modelli numerici sviluppati dal software BASEMENT, fornito dall'ETH di Zurigo, sono adattati per mettere in relazione la campagna sperimentale con concetti teorici di idromorfologia. In effetti, questo modello numerico, calibrato tenendo conto il coefficiente di Manning e il fattore di carico utile per avere una migliore coerenza con i risultati sperimentali, può essere utilizzato come strumento predittivo per situazioni fisiche irrealizzabili.

Parole chiave: Aggradazione, rapporto di sovraccarico, flusso supercritico, celerità di propagazione, celerità locale, autovalori, modello sperimentale, modello numerico, analisi dimensionale.

ABSTRACT (PERSIAN)

وقوع بلایای طبیعی همواره باعث خسارات جبران ناپذیری به انسان ها و محیط اطراف آن ها شده است. بررسی علل وقوع سیل به عنوان یکی از شایع ترین خطرات موجود و شناسایی عوامل موثر بر آن، امکان مدیریت این پدیده را فراهم می کند. انتقال رسوب در ایجاد سیل همواره نقش پررنگی را ایفا کرده است. در هنگام وقوع بارندگی به علت کاهش ظرفیت بستر رودخانه تو سط رسوبات انتقالی احتمال وقوع سیل در دبی های پایین تر وجود داشته و لذا اهمیت بررسی پدیده انتقال رسوب در مدیریت سیلاب را دوچندان خواهد کرد. تعیین بازه زمانی در کاهش ظرفیت بستر رودخانه یا به بیان دیگر سرعت رسوبگذاری در بستر رودخانه همواره در تخمین زمان وقوع سیل کمک کننده می باشد .لازم به ذکر است به علت زیاد بودن شیب سطح زمین در مناطق کوهستانی نوع جریان موجود در این نواحی هنگام وقوع سیل اکثرا از نوع جریان فوق بحرانی است. در این نوع جریان پشته رسوبی قابل تشخیص نیست، لذا انجام مطالعات بیشتر در زمینه شناسایی روند انتشار رسوبات ضروری خواهد بود.

تحقیق موجود در راستای بررسی بیشتر پارامترهای موثر بر پدیده انتقال رسوب، انتشار آن و پدیده رسوب گذاری در جریان فوق بحرانی صورت گرفته و در این راستا از روش های آزمایشگاهی و عددی استفاده شده است. مدل های عددی کالیبره شده بر مبنای مدل های آزمایشگاهی به عنوان ابزاری برای پیش بینی در مدل سازی وقایعی مانند سیل کمک می کنند.

مطالعات موجود در ازمایشگاه هیدرولیک دانشگاه پلی تکنیک میلان (واحد لکو) انجام گرفته و تکمیل کننده آزمایشات صورت گرفته قبل در زمینه جریان فوق بحرانی می باشد. لازم به ذکر است، هر آزمایش شرایط هیدرولیکی مانند دبی مخصوص، و مقدار رسوب تزریق شده خود را دارا می باشد. با توجه به ثابت بودن فیزیک کانال و خصوصیات ذرات رسوب در طول آزمایش، دبی آب ورودی و درصد رسوب تزریقی به عنوان دو پارامتر تعیین کننده شناخته می شوند. بررسی تغییرات پارامترهای دیگر بر مبنای این دو پارامتر اصلی همواره از اهمیت بسیار زیادی برخوردار است، زیرا پدیده رسوبگذاری بر مبنای این دو پارامتر تعیین می شود.در این آزمایش با کمک گرفتن از روش پردازش تصویر، ویدویوهای ضبط شده از روند ازمایش انالیز شده و خروجی های لازم جهت بررسی داده های مختلف از جمله برداشت پروفیل های طولی آب و رسوب، تعیین دبی رسوب ورودی و مقدار ظرفیت اولیه انتقال رسوب صورت می گیرد. لازم به ذکر است که گرفتن خروجی قابل اعتماد با هزینه محاسباتی کمتر یکی از دستاورهای مهم این پروژه بوده ودر در راستای تحقق آن تغییراتی در زمینه تغییر کد و تجهیزات آزمایشگاهی صورت گرفته است.

آزمایشات انجام شده برای مطالعه روند رسوب گذاری در کانال، با نرم افزار BASEMENT به صورت عددی شبیه سازی می شود. با هدف پیدا کردن هماهنگی مناسب بین مدل عددی و مدل آزمایشگاهی، عملیات کالیبریشن نسبت به پارامتر های ضریب زبری (مانینگ) و ضریب مرتبط به محاسبه ی ظرفیت انتقال ذرات کانال انجام می شود.

کلید واژه:سیل، رسوبگذاری، سرعت انتقال رسوب، پشته رسوبی، جریان فوق بحرانی، پدیده انتقال رسوب، مدل عددی

Chapter 1:

INTRODUCTION

1.1 Context

As a consequence of the population boost, urbanization caused an increase in the interaction between constructed and natural areas. These urban extensions are sometimes formed in hazardous areas that increase hydrological risk, such as floods.

The flood phenomenon mostly happens due to two main factors: the rise of water discharge and the increase of the riverbed elevation due to the deposition of sediments called the aggradation of the riverbed. Combining these two factors can result in flooding occurrence in lower water discharge than the calculated one without any deformation in the riverbed. It happened due to the river’s capacity decline as an effect of reduction in the riverbed slope due to the aggradation. On the other hand, lowering the riverbed surface level due to erosional processes is called degradation. Degradation can negatively influence the structures near a river, leading to their collapse.

The sediment transport capacity influences the process of aggradation and degradation as a prominent phenomenon. This phenomenon, based on different slopes, shapes a riverbed in response to an interaction between the sediment yield and the transport capacity of the flow.

In 2013, the feasibility and positive outcome of incorporating sediment transport modeling into the flood hazard evaluation were assessed concerning the case of the Mallero River in northern Italy by Radice (Radice, et al., 2013). According to this research, sediment transport processes cannot be ignored to obtain reliable water level predictions and appropriate timescales even within a single event. Furthermore, in this research, it is mentioned that the flood event in Sondrio in 1987 did not occur because of the peak water discharge occurrence but due to the maximum aggradation height. Therefore, considering the velocity of sediment front or celerity along the riverbed is fundamental in hydro-morphological evolution studies. It should be mentioned that based on the physical properties of rivers, they may possess two types of flow, supercritical and subcritical. Since the slope could be high in the mountain, the flow is mainly supercritical and can carry coarse sediment. In this type of flow, sediment front rush because of high flow velocity, and it is dispersive; thus, measuring celerity value could be quite beneficial.

This research follows the campaign carried out at the Politecnico di Milano (Unigarro Villota, 2017), (Zanchi, 2018), (Zucchi, 2018), (Heydari, 2020) and, (Eslami et al.,2021) where sediment aggradation was studied in subcritical and supercritical flow. In this research, the knowledge of the hydro-morphologic evolution of a river reach, considering the aggradation phenomena in supercritical flow, is studied. An experimental series of laboratory tests are carried out. The temporal and spatial evolutions of the bed and water profiles are obtained from each experiment. Then a comparison between the numerical and experimental results is carried out to calibrate and validate the numerical model, observing how the two models (physical and numerical) react to the imposed boundary conditions and discussing the advantages and limitations of each approach.

1.2 Sediment transport Phenomena: main parameters

The general term “sediment transport” involves an environmental process that occurs at a wide range of spatial and temporal scales. This phenomenon depends on the flow conditions and sediment characteristics. Flow conditions can be affected by water flow, roughness, and cross-section geometry. And features of an individual sediment particle, which y or indirectly shows the particle's history, are mentioned below.

1.2.1 Sediment particles

Geometric and material properties can characterize sediment particles:

- Geometric properties
    1) Size: The size of a geometrical solid with a regular shape can be simply illustrated, and there is no difficulty in its measurement. However, for all irregularly shaped particles like a sediment particle, to give only its size is not enough unless the measuring method and the definition of the size must also be fully explained. The terminology used to define the size of particles starts from a boulder and descends to clay particles. Naturally, more than one method of measuring the size is needed. For particles larger than cobbles, three axial lengths are taken as the representative dimensions, and a mean value is then be obtained. For particle sizes ranging between cobbles and fine sand, sieving is the most convenient method of measuring size. Results obtained from sieving show that the particle size is between two sieve mesh openings, D_1 and D_2. It gives a range for the size $D_2 < D < D_1$, rather than an absolute value. The mean size can be expressed as the algebraic average $\frac{(D_1+D_2)}{2}$, the geometric average $\sqrt{D_1 D_2}$ or more generally $D_t = \frac{(D_1+D_2+D_3)}{3}$. Sometimes, the diameter of a sphere of equal volume is used, and it is called the nominal diameter.
    2) Shape and roundness: Shape and roundness are two different properties of sediment particles. The shape factor describes the geometric form of the particle as a whole. By measuring maximum, medium, and minimum diameters of a sediment particle and using the below Table 1-1, the shape factor of a particle can be calculated.

    Table 1-1 Shape factor formula

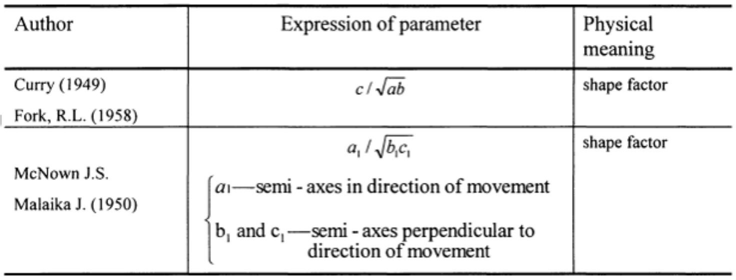

Author	Expression of parameter	Physical meaning
Curry (1949) Fork, R.L. (1958)	$c / \sqrt{ab}$	shape factor
McNown J.S. Malaika J. (1950)	$a_1 / \sqrt{b_1 c_1}$ a_1—semi - axes in direction of movement b_1 and c_1—semi - axes perpendicular to direction of movement	shape factor

The Roundness is a parameter that is used to indicate the sharpness of edges of an irregular sediment particle, and it is defined by Wadell as follows:

$$Roundness = \frac{\sum_{i=1}^{n} \left(\frac{r_i}{R}\right)}{n}$$

Equation 1-1

Where, r_i shows the radius of curvature of particle corners, R is the radius of the most enormous, surrounded sphere, and n is the number of particle corners measured.

- Material properties (density)

The particle density describes the mass of a unit volume of sediment solids. The below equation shows the relationship between the particle density ρ_s and the specific particle weight γ_s.

$$\rho_s = \frac{m_s}{V_s} = \frac{\gamma_s}{g} \qquad \text{Equation 1-2}$$

Where, m_s is the mass of the solid, V_s is the solid volume and γ_s shows the unit weight of the solid.

1.2.2 Pattern of sediment motion

Sediment particles in motion can be classified according to their patterns of movement as contact load, saltation load, suspended load, and laminated load. In Figure 1-1, the differences of all types are cleared.

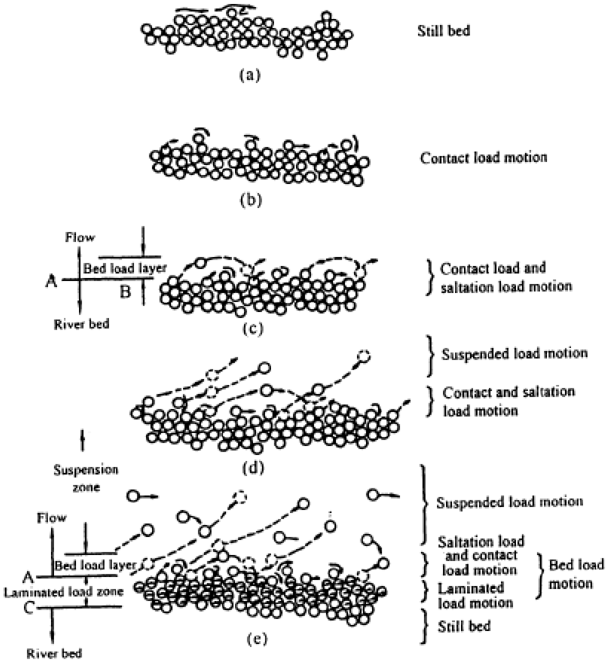

Figure 1-1 Pattern of sediment motion

- Bedload: Among all the loads mentioned above, contact load, saltation load, and laminated load belong to the category of bedload. Increasing the flow velocity can directly affect the sediment motion in a riverbed. There is no sediment motion when the flow velocity is low, and all particles are immobile. As the velocity increases to a threshold value, some particles vibrate because of the fluctuating velocity of the turbulent flow but do not move from their original positions. In this case, the force acting on a particle is high enough to move the particle at some instants. Still, the particle cannot move from its position immediately because of its inertia and the short duration of the force. Therefore, the particles slide, roll and bounce in the flow direction. This phenomenon is related to heavy particles. (Big granulometry particles like sands, gravels, and stones)

- Suspended load: High-velocity flows are turbulent, with different sizes of eddies. If a particle jumps off the bed into one of these eddies, it may be dragged a long distance away from the bed. The eddy must be significantly larger than the particle to transport it, and its upward velocity component must be greater than the particle's fall velocity. If an eddy is about the same size as a particle, the latter is liable to fall out of the eddy; hence, the eddy would no longer affect the particle’s movement. On the contrary, if an eddy is much greater than a particle, the eddy may carry the particle for a long time. The transport of suspended particles is mainly the effect of large-scale eddies. A significant deduction from the impact of large-scale eddies in bringing sediment particles into suspension is as follows: the eddies generated in the zone close to the bed are small because the boundary constrained them; thus, they cannot cause the suspension of particles. Only at a certain distance from the boundary are the eddies big enough to carry particles. Therefore, bed particles must go through the saltation process before becoming a suspended load.

1.2.3 The threshold of the motion

Sediment motion was extensively studied in the literature regarding critical velocity and critical shear stress (Buffington and Montgomery, 1999). The critical velocity method correlates sediment initiation to an average flow velocity by a resistance law, whereas the critical shear stress method correlates the initiation to a bed shear stress. In the context of this research, the following review is limited to the shear stress method, which is fundamental in developing the Shields diagram. First, the concept of the critical shear stress τ_c was introduced by Du Boys (Du Boys, 1879), who expressed unit volumetric bedload transport rate q_b (Hager, 2005):

$$q_b \propto \tau_0(\tau_0 - \tau_c)$$ Equation 1-3

Where, τ_0 is shear stress applied on bed sediment and $\tau_0 - \tau_c$ is called the excess shear stress. The Equation 1-3 states that sediment starts to move only if $\tau_0 \geq \tau_c$. The excess shear stress, $\tau_0 - \tau_c$, has been used in many bedload transport formulas (Chien and Wan, 1999). Therefore, the determination of the critical shear stress τ_c is necessary for predicting sediment transport.
A particle currently in stable condition on the bed’s surface will start to move due to the fluid flow when the bed shear stress τ applied by flow overpasses the critical shear stress τ_c. Therefore, the incipient movement happens when:

$$\tau_0 = \tau_c$$ Equation 1-4

Typically, the dimensionless numbers are used to represent this criterion:

$$\tau^* = \tau_c^*$$ Equation 1-5

Where τ^* and τ_c^* are dimensionless shear stress and dimensionless critical shear stress, respectively. The dimensionless shear stress τ^* is known as Shields stress and is given by:

$$\tau^* = \frac{\tau}{(\rho_s - \rho)gd}$$ Equation 1-6

Where, ρ_s represents the solid density, ρ represents the fluid density, g is the gravitational acceleration, and d is the sediment diameter.

These equations are used for granular sediment, and they do not work for clays and muds because these sediments do not match the geometric simplification in equations. Also, these equations do not consider the electrostatic force found in the clay sediments. The equations are designed for riverine sediment transport carried along with the fluid flow like streams, canals, or other open channels.

1.2.3.1 Critical shear stress

The drag force applies to the particles on the bed, and it causes initiating sediment motion. Sediment motion will start whenever the drag force exceeds the resistance force (Chaudhry, 2007). The drag force F_D and the submerged weight F_G are obtained by:

$$F_D = \frac{1}{2}\pi\left(\frac{d}{2}\right)^2 \rho C_D {u_f}^2 \qquad \text{Equation 1-7}$$

$$F_G = \frac{4}{3}\pi\left(\frac{d}{2}\right)^3 \rho R g \qquad \text{Equation 1-8}$$

Where, ρ represents the fluid density, g is the gravitational acceleration, d shows the sediment diameter, $\bar{u}$ denotes the fluid velocity at the grain level, and R is the submerged specific gravity of the sediment particle which is equal to**:**

$$R = (\rho_s - \rho)/\rho \qquad \text{Equation 1-9}$$

C_D shows the drag coefficient that is related to the Reynolds number:

$$R_e = \frac{u_f \times d}{\nu} \qquad \text{Equation 1-10}$$

Where ν is the kinematic viscosity, it can be calculated by the dynamic viscosity μ divided by the fluid density ρ.

$$\nu = \frac{\mu}{\rho} \qquad \text{Equation 1-11}$$

The frictional resistance F_R is given by:

$$F_R = \mu_c F_G \qquad \text{Equation 1-12}$$

Where μ_c denotes the frictional coefficient.

By establishing the following conditions, the sediment is on the motion threshold.

$$F_D = F_R \qquad \text{Equation 1-13}$$

$$\frac{{u_f}^2}{R\,g\,d} = \frac{4}{3}\frac{\mu_c}{C_D} \qquad \text{Equation 1-14}$$

In the situation of the hydraulically rough, turbulent flow, the logarithmic profile or the law of the wall can be written as:

$$\frac{\bar{u}}{u_*} = \frac{1}{\kappa}\, ln\left(\frac{z}{K_s}\right) + 8.5 \qquad \text{Equation 1-15}$$

Where $\bar{u}$ is Reynolds-averaged streamwise velocity, u_* is the shear velocity that is defined as ($u_* = \sqrt{\tau_b/\rho}$), κ is von Kármán constant that is equal to 0.41, K_s is the roughness height ($K_s = n_k d$ that n_k is dimensionless), and z is the height from the bed.

Consider an exposed grain that the distance of its centroid from the mean level of the bed equals $z = n_e d$ that n_e is a dimensionless number. For the exposed grain shown in Figure 1-1, the Equation 1-15 is written as below:

$$\frac{\bar{u}}{u_*} = \frac{1}{\kappa} ln\left(\frac{n_e}{n_k}\right) + 8.5$$ *Equation 1-16*

By mixing the Equation 1-14 and Equation 1-16, it can be shown that:

$$\frac{u_*^2}{R\ g\ d} = \tau_c^* = \frac{4\ \mu_c}{3\ C_D}\left[\kappa\ ln\left(\frac{n_e}{n_k}\right) + 8.5\right]^{-2}$$ *Equation 1-17*

The term τ_c^* in Equation 1-17 is introduced as the critical Shields stress. Suppose the particle on the bed surface has to start motion because of the fluid flow; the non-dimensional bed shear stress (Shield stress τ^*) must surpass the critical Shields stress (τ_c^*).

1.2.3.2 Shields diagram

Shields (Shields, 1936) worked on the incipient motion of granular sediment in the fluvial stream and bedload transportation. He ran many experiments and drew their results in a graph known as a Shields diagram. This diagram illustrates the relationship between the non-dimensional critical shear stress τ_c^* and the shear Reynolds number ($R_e^* = u_* d/\nu$) (Chaudhry, 2007). Figure 1-2 shows the Shields diagram. The relationship between τ_c^* and R_e^* was determined experimentally (Dey, 2014).

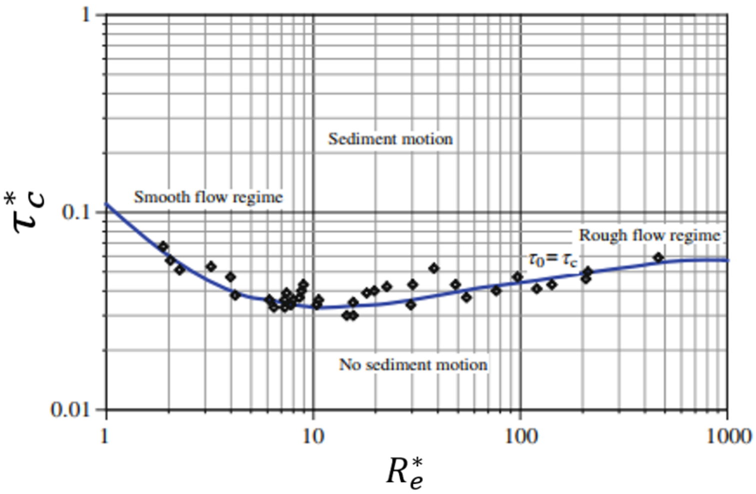

Figure 1-2 Shields diagram depicts critical Shields number ($\boldsymbol{\tau_c^*}$) as a function of shear Reynolds number ($\boldsymbol{R_e^*}$) (Dey 2014)

According to the graph, the zone above the curve corresponds to the motion conditions for a specific sediment size, and the area below the curve represents no sediment motion. This figure illustrates three distinguished flow regions:

1) hydraulically smooth flow ($R_e^* \leq 2$)
2) hydraulically rough flow ($R_e^* \geq 500$)
3) hydraulically transitional flow ($2 < R_e^* < 500$)

The original Shields graph has no information for a smooth flow regime ($R_e^* \leq 2$). The linear relationship of the $\tau_c^*(R_e^*)$ curve is an extrapolation (Dey , 2014).

1.2.3.3 Prediction of bedload transport

In the 19th century, the French scientist Du Boys advanced a theory for bedload motion based on shear stress. Then, many scientists have studied the phenomenon, and they have proposed several relations for bedload transport. These formulas are based on different modes of motion and employ different parameters, including shear stress, flow velocity, and power. These formulas can be classified into the following groups according to the approaches used:

1) Empirical formulas provided based on amounts of experimental data, like the Meyer-Peter Formula.
2) Semi-theoretical formulas are obtained based on physical concepts and mechanical analysis, such as the Bagnold Formula.
3) Probability theory-based formulas are approached through a combination of probability theory and mechanics, for instance, the one represented by the Einstein Bed Load Function.

Some of the formulas are represented in Table 1-2:

Table 1-2 Formulation for bedload transport (Chanson 2004)

Reference	Formulation	Range	Remarks
Boys (1879)	$q_s = \lambda\tau_0(\tau_0 - (\tau_0)_c)$ $\boldsymbol{\lambda} = \frac{\mathbf{0.54}}{(\boldsymbol{\rho_s}-\boldsymbol{\rho})\mathbf{g}}$ Schoklitsch (1914) $\lambda \sim d_s^{-3/4}$ Sraub (1935)	$0.125 < \mathrm{d_s} < 4\ \mathrm{mm}$	$\boldsymbol{\lambda}$ was called the characteristic sediment coefficient Laboratory experiments with uniform grains of various kinds of sand and porcelain Based upon laboratory data
Schoklitsch (1930)	$q_s = \lambda'(\sin\theta)^k(q - q_c)$ $q_c = 1.944 \times 10^{-2} d_s (\sin\theta)^{-4/3}$	$0.305 < \mathrm{d_s} < 7.02\ \mathrm{mm}$	Based upon laboratory experiments
Shields (1936)	$\frac{q_s}{q} = 10\frac{\sin\theta}{s}\frac{\tau_0 - (\tau_0)_c}{\rho g(S-1)d_s}$	$1.06 < \mathrm{S} < 4.25$ $1.56 < \mathrm{d_s} < 2.47\ \mathrm{mm}$	
Einstein (1942)	$\frac{\mathrm{q_s}}{\sqrt{(\mathrm{S}-1)\mathrm{gd_s}}} = 2.15\exp\left(-0.391\frac{\rho(\mathrm{S}-1)\mathrm{gd_s}}{\tau_0}\right)$	$\frac{\mathrm{q_s}}{\sqrt{(\mathrm{S}-1)\mathrm{gd_s}}} < 0.4$ $1.25 < \mathrm{S} < 4.25$ $0.315 < \mathrm{d_s} < 28.6\ \mathrm{mm}$	Laboratory experiments. Weak sediment transport formula for sand mixtures. Note*:* $\mathrm{d_s} \approx \mathrm{d_{35}}$ to $\mathrm{d_{45}}$
Meyer- Peter (1949,1951)	$\frac{\dot{m}^{2/3}\sin\theta}{d_s} - 9.57(\rho g(S-1))^{10/9} = 0.462(S-1)\frac{(\rho g(\dot{m}_s)^2)^{2/3}}{d_s}$ $\frac{\mathrm{q_s}}{\sqrt{(\mathrm{S}-1)\mathrm{gd_s}^3}} = \left(\frac{4\tau_0}{\rho(\mathrm{S}-1)\mathrm{gd_s}} - 0.188\right)^{3/2}$	$1.25 < \mathrm{S} < 4.2$	Laboratory experiments. Uniform grain size distribution**.** Laboratory experiments. Particle mixtures. Note: $\mathrm{d_s} \approx \mathrm{d_{50}}$

Einstein (1950)	Design chart $\frac{q_s}{\sqrt{(S-1)g{d_s}^3}} = f\left(\frac{\rho(S-1)gd_s}{\tau_0}\right)$	$\frac{q_s}{\sqrt{(S-1)g{d_s}^3}} < 10$ $1.25 < S < 4.25$ $0.315 < d_s < 28.6\ \mathrm{mm}$	Laboratory experiments. For sand mixtures. Note: $d_s \approx d_{35}\ to\ d_{45}$
Schoklitsch (1950)	$\dot{m}_s = 2500\ (\sin\theta)^{3/2}(q - q_c)$ $q_c = 0.26(S-1)^{5/3}\ d_{40}^{3/2}\ (\sin\theta)^{-7/6}$		Based upon laboratory experiments and field measurements (Danube and Aare rivers).
Nielsen (1992)	$\frac{q_s}{\sqrt{(S-1)g{d_s}^3}} = \left(\frac{12\tau_0}{\rho(S-1)gd_s} - 0.05\right)\sqrt{\frac{\tau_0}{\rho(S-1)gd_s}}$	$1.25 < S < 4.22$ $0.69 < d_s < 28.7\ \mathrm{mm}$	Re-analysis of laboratory data
Bagnold (1973)	$\emptyset = \theta(\sqrt{\theta} - \sqrt{\theta_c})\frac{1}{k}(5.75\log\left[30.2\ \frac{mD}{K_s}\right] - \frac{w}{u_*})$		
Ackers-White	$Y = 0.025\left(\frac{M}{0.17} - 1\right)^{1.5}$ $M = \frac{U}{\sqrt{g\frac{\gamma_s - \gamma}{\gamma}D}}\ \frac{1}{\sqrt{32}\frac{10h}{D}}$ $Y = \frac{\gamma S_{wb} h}{\gamma_s D}$		Re-analysis of laboratory data
Note: $\dot{m}$ = mass water flow rate per unit width; $\dot{m}_s$ = mass sediment flow rate per unit width; q = volumetric water discharge; q_s = volumetric sediment discharge per unit width; $(\tau_0)_c$ = critical bed shear for initiation of bed load; S_{wb}=average concentration of sediment load in weight per unit volume.			

Figure 1-3 shows the comparison of the Meyer-Peter, Einstein, Bagnold, and Yalin formulas. The Meyer-Peter formula follows the experimental data better than does the Einstein bed load function for low intensities of bedload motion, but the opposite is true for moderate intensities. The Bagnold formula gives a larger transport rate than the measured data in this range. The main differences among the formulas arise for the higher intensities of bedload motion.

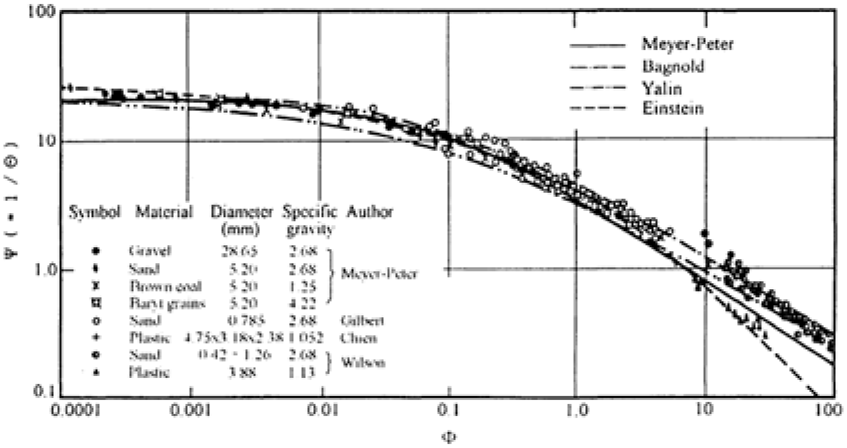

Figure 1-3 Comparison of the formulas of Meyer-Peter, Einstein, Bagnold, and Yalin

Where, φ is the dimension expressing sediment size, ψ is a parameter of flow related to sediment movement, and θ is a parameter of flow intensity.

1.3 Analytical model for morphological evolution

Some parameters like the particles' properties, the sediment transport capacity, the inflow sediment discharge, and the inflow water discharge can influence the morphological evolution of a mobile river's bed (Exner, 1925). The global bed material conservation equation known as the Exner equation is acquired by adding up the masses of all sediment material layers between the bed surface and a reference level (fixed bed). The Exner equation is used for sediment mass conservation in a stream; It presents the mass conservation between sediment in the channel bed and transported sediment. In the case of the rectangular channel, erodible bed, homogenous material, and by neglecting the suspended load, the conservation of mass for sediment is presented as below:

$$(1-\mathrm{p})\frac{\partial \mathrm{z_b}}{\partial \mathrm{t}}+\frac{\partial \mathrm{q_s}}{\partial \mathrm{x}}=0$$ *Equation 1-18*

Where, p is the porosity of the sediment material, z_b is the bed elevation, $q_s = Q_s/B$ represents the unit sediment discharge, and B shows the channel width.

The Exner equation represents the mass conservation law for the sediment particles.

There is degradation when $\frac{\partial q_s}{\partial x} > 0$, $\frac{\partial Z_b}{\partial t} < 0$

There is aggradation when $\frac{\partial q_s}{\partial x} < 0$, $\frac{\partial Z_b}{\partial t} > 0$

Besides the Exner equation, to express the one-dimensional morphological evolution of the riverbed, two Saint-Venant equations are also used, which represent the mass balance and momentum conservation for water:

$$\frac{\partial h}{\partial t}+\frac{\partial q}{\partial x}=0$$ *Equation 1-19*

$$\frac{\partial q}{\partial t}+\frac{\partial}{\partial x}\left(\frac{q^2}{h}\right)+gh\frac{\partial h}{\partial x}=gh(S_0-S_f)$$ *Equation 1-20*

Where $q = u \times h$ is unit flow discharge, h shows the water depth, u is the depth-averaged velocity, and S_0, S_f are bottom and friction slope, respectively.

To simulate the aggradation and degradation of particles on the bed river, one can assume that Equation 1-19 and Equation 1-20 are valid in the presence of the sediment. If the bottom slope expresses as $S_0 = -\partial z_b / \partial x$, the Equation 1-20 can be rewritten as below:

$$\frac{\partial q}{\partial t} + \frac{\partial}{\partial x}\left(\frac{q^2}{h}\right) + gh\left(\frac{\partial h}{\partial x} + \frac{\partial z_b}{\partial x}\right) = -ghS_f \quad \text{Equation 1-21}$$

The governing equations consist of three Equation 1-18, Equation 1-19, and Equation 1-20, with five unknowns $(h, q, z_b, q_s, and\ S_f)$; then two additional relations are needed to calculate q_s and S_f in order to use the system. The friction slope (S_f) can be calculated by the Manning formula:

$$S_f = \frac{n^2 \times U^2}{R_H^{4/3}} \quad \text{Equation 1-22}$$

Where, n is the Manning's coefficient, R_H shows the hydraulic radius, and U is the local velocity of the flow.

The sediment discharge q_s is estimated from general formulae like Meyer-Peter and Müller (1948) as below:

$$q_s(q,h) = 8\sqrt{g(s-1)d_{50}^3}\left(\frac{n^2 q^2}{(s-1)d_{50}h^{7/3}} - 0.047\right)^{3/2} \quad \text{Equation 1-23}$$

Where, n is the Manning's coefficient, $s = \rho_s/\rho_w$ shows the relative sediment density, and d_{50} denotes the median grain diameter.

In conclusion, Equation 1-18, Equation 1-19, and Equation 1-21 represented a PDE system that demonstrates the bed and water level evolutions in a one-dimensional case and uses only the bedload for sediment motion.

$$\begin{cases} \dfrac{\partial \mathrm{h}}{\partial \mathrm{t}} + \dfrac{\partial \mathrm{q}}{\partial \mathrm{x}} = 0 \\ \dfrac{\partial \mathrm{q}}{\partial \mathrm{t}} + \dfrac{\partial}{\partial \mathrm{x}}\left(\dfrac{\mathrm{q}^2}{\mathrm{h}}\right) + \mathrm{gh}\left(\dfrac{\partial \mathrm{h}}{\partial \mathrm{x}} + \dfrac{\partial \mathrm{z_b}}{\partial \mathrm{x}}\right) = -\mathrm{ghS_f} \\ (1-\mathrm{p})\dfrac{\partial \mathrm{z_b}}{\partial \mathrm{t}} + \dfrac{\partial \mathrm{q_s}}{\partial \mathrm{x}} = 0 \end{cases} \quad \text{Equation 1-24}$$

The system was solved by Goutière and his colleagues (Goutière, et al., 2008) in a novel, simple, but a relatively accurate approximation of the system's eigenvalues λ composed of Saint-Venant-Exner equations. The system of the equations can be rewritten in vector form as**:**

$$\frac{\partial U}{\partial t} + \frac{\partial F(U)}{\partial x} + H(U)\frac{\partial U}{\partial x} = S(U) \quad \text{Equation 1-25}$$

where:

$$\mathrm{U} = \begin{bmatrix} \mathrm{h} \\ \mathrm{q} \\ \mathrm{z_b} \end{bmatrix} \qquad \mathrm{F(U)} = \begin{bmatrix} \mathrm{q} \\ \dfrac{\mathrm{q}^2}{\mathrm{h}} + \mathrm{g}\dfrac{\mathrm{h}^2}{2} \\ \dfrac{\mathrm{q_s}}{(1-\mathrm{p})} \end{bmatrix} = \begin{bmatrix} \mathrm{q} \\ \sigma \\ \psi \end{bmatrix}$$

$$\mathrm{H(U)} = \begin{bmatrix} 0 & 0 & 0 \\ 0 & 0 & \mathrm{gh} \\ 0 & 0 & 0 \end{bmatrix} \qquad \mathrm{S(U)} = \begin{bmatrix} 0 \\ -\mathrm{ghS_f} \\ 0 \end{bmatrix}$$

Equation 1-25 can be formulated as below:

$$\begin{aligned} &\frac{\partial U}{\partial t} + \frac{\partial F(U)}{\partial x} + H(U)\frac{\partial U}{\partial x} \\ &= \frac{\partial U}{\partial t} + A(U)\frac{\partial U}{\partial x} + H(U)\frac{\partial U}{\partial x} \\ &= \frac{\partial U}{\partial t} + A'(U)\frac{\partial U}{\partial x} \\ &= S(U) \end{aligned} \qquad \text{Equation 1-26}$$

where $A(U) = \partial F(U)/\partial U$ is Jacobian matrix; and $A'(U) = A(U) + H(U)$ is a kind of pseudo-Jacobian, which is:

$$A'(U) = \frac{\partial F(U)}{\partial U} + H(U) = \begin{bmatrix} 0 & 1 & 0 \\ -\dfrac{q^2}{h^2} + gh & 2\dfrac{q}{h} & gh \\ \dfrac{1}{1-p}\dfrac{\partial q_s}{\partial h} & \dfrac{1}{1-p}\dfrac{\partial q_s}{\partial q} & 0 \end{bmatrix} \qquad \text{Equation 1-27}$$

1.3.1 Eigenvalue analysis and approximation

The characteristic polynomial related to matrix $A'(U)$ (Equation 1-27) can be written as follow:

$$|A' - \lambda I| = \lambda^3 + a_1\lambda^2 + a_2\lambda + a_3 = 0 \qquad \text{Equation 1-28}$$

With

$$\begin{aligned} a_1 &= -2\frac{q}{h} && (a) \\ a_2 &= \frac{q^2}{h^2} - gh - \frac{gh}{1-p}\frac{\partial q_s}{\partial q} && (b) \\ a_3 &= -\frac{gh}{1-p}\frac{\partial q_s}{\partial h} && (c) \end{aligned} \qquad \text{Equation 1-29}$$

Where $\partial q_s/\partial q$ and $\partial q_s/\partial h$ are calculated from Equation 1-23. The three eigenvalues $\lambda\ \lambda_{1,2,3}$ of the matrix A', which are related to the respective celerity dx/dt of the three characteristics are the roots of the polynomial of the Equation 1-28. The theoretical calculation of these roots is possible, but the analytical computation is so complicated that it is not used practically (Lyn, 1987) (Lyn and Altinakar, 2002) (Goutière et al., 2008).

A new approximation of analytical computation is derived by using the properties of cubic polynomial $\alpha x^3 + \beta x^2 + \gamma x + \delta = 0$ that its roots $x_1,\ x_2,\ and\ x_3$ are connected according to the below expressions:

$$\begin{aligned} &x_1 + x_2 + x_3 = -\frac{\beta}{\alpha} && (a) \\ &x_1x_2 + x_2x_3 + x_3x_1 = \frac{\gamma}{\alpha} && (b) \\ &x_1x_2x_3 = -\frac{\delta}{\alpha} && (c) \end{aligned} \qquad \text{Equation 1-30}$$

By applying the Equation 1-30 (a) to the characteristic polynomial Equation 1-28 and using the coefficients of Equation 1-29 (a), one can write the below equation:

$$\lambda_1 + \lambda_2 + \lambda_3 = -a_1 = 2\frac{q}{h} = 2u \qquad \text{Equation 1-31}$$

As the impact of sediments on the characteristic equations is assumed to be a slight perturbation, It can be assumed that the presence of sediments does not affect the largest eigenvalue (Lyn and Altinakar 2002) (Goutière et al., 2008).

$$\lambda_1 = \lambda_{H1} = u + c \qquad \text{Equation 1-32}$$

Where $c = \sqrt{gh}$ shows hydrodynamic wave celerity, and the subscript H uses for hydrodynamic value. By using the assumption of the Equation 1-32, the Equation 1-31 can be rewritten as:

$$\lambda_2 + \lambda_3 = (\lambda_1 + \lambda_2 + \lambda_3) - \lambda_1 = 2u - (u + c) = u - c \qquad \text{Equation 1-33}$$

Because λ_1 does not account for sediment effects; therefore, this effect is only applied to λ_2 and λ_3 in the form of symmetrical deviation from $\lambda_{H2} = u - c$.
The Equation 1-30 (c) can be rewritten by applying Equation 1-33:

$$\lambda_1\lambda_2\lambda_3 = \lambda_{H1}\lambda_2(\lambda_{H2} - \lambda_2) = (u + c)\lambda_2(u - c - \lambda_2) = -a_3 = \frac{gh}{1-p}\frac{\partial q_s}{\partial h} \qquad \text{Equation 1-34}$$

That creates a quadratic polynomial in λ_2, whose roots give λ_2 and hence also λ_3 in such a way that the three eigenvalues λ can be written in a non-dimensional form as follows:

$$\begin{aligned} &\frac{\lambda_1}{u} \cong \left(1 + \frac{1}{Fr}\right) && (a) \\ &\frac{\lambda_{2,3}}{u} \cong \frac{1}{2}\left[\left(1 - \frac{1}{Fr}\right) \mp \sqrt{\left(1 - \frac{1}{Fr}\right)^2 - \frac{4}{(Fr^2 + Fr)}\chi}\,\right] && (b) \end{aligned} \qquad \text{Equation 1-35}$$

Where $Fr = u/\sqrt{gh}$ is the Froude number Fr, and χ is the non-dimensional factor that is related to the sediment discharge and can be described as follow:

$$\chi = \frac{1}{(1-p)u}\frac{\partial q_s}{\partial h} \qquad \text{Equation 1-36}$$

The comparison among the non-dimensional eigenvalues λ acquired by the approximate analytical formula (Equation 1-35), the exact value is taken by a numerical eigenvalue solver, and the approximation proposed by Lyn and Altinakar (Lyn and Altinakar, 2002) is illustrated in Figure 1-4.

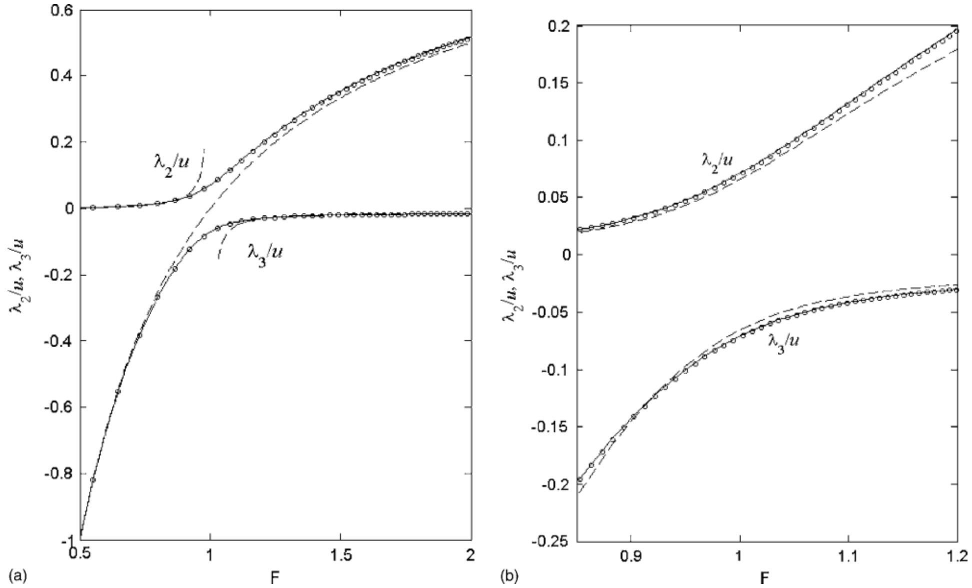

Figure 1-4 Comparison of exact and approximate eigenvalues λ: (a) in the region outside $Fr = 1$; (b) close to $Fr = 1$. Circles mark exact values, dashed lines are used for approximation by Lyn and Altinakar (Lyn and Altinakar, 2002), and continuous lines are used for the proposed approximation Equation 1-35 (Goutière et al., 2008)

To acquire a unique solution for the partial differential equations, it is necessary to impose the initial and boundary conditions. According to the obtained results for eigenvalues λ (Equation 1-35), two of them will be positive, while the remaining one is negative. To solve the system of Equation 1-24, two boundary conditions must be introduced upstream, and a boundary condition must be imposed downstream.

1.4 History of experimental studies

Studying the evolution of the unbalanced state in a fluvial system is quite complex, and therefore, numerous campaigns have analyzed this phenomenon over the years. Furthermore, it is beneficial to use calibration or the validation of analytical models to predict the evolution of the morphology of the river in real situations.

Soni (Soni et al., 1980) studied aggradation in the fluvial channel, integrating the experimental model with an analytical model where the sediment supply constant feeding rate is located along the river course. The initial bed elevation z_b, water level h along the channel, and the equilibrium bed slope S_0 changed due to the turbulence induced by the incoming sediment produce aggradation both upstream and downstream concerning the injection point.

In order to calibrate the analytical model, the experimental result was employed, especially in the calibration of a and b coefficients that are employed in the modeling of the sediment transport law equation ($Q_s = aU^b$) and also for aggradation coefficient K, found in the simplified differential equation for bed evolution ($\partial z/\partial t = K\ \partial^2 z/\partial x^2$ where z is the aggradation depth).

The channel-bed evolution under the condition of overloading followed by under-loading in terms of non-uniform sediment was analyzed by Yen (Yen, et al., 1992) experimentally. The response time is defined as the time needed to reach a new equilibrium state after a perturbation (in terms of sediment over or under-loading) of the equilibrated system in this paper. The non-uniform granulometry of the sediment causes the armoring phenomenon in the degradation process in these studies, demonstrating that a complete recovery ($R = 100$ %) is only feasible in the case of uniform sediment content.

Lee Bena (Lee Bena, et al., 1997) investigated how the waveform of bed material is changed by diffusion and interference at tributary junctions. They used field measurement and a simulation model to illustrate the interaction between the primary controls on large-scale process function over a long period. Model prediction suggested that sediment storage and transport waves with characteristic length and height scales are a fundamental characteristic of sediment transport systems in basins where portions of the sediment influx to the channel are nonuniform and unsteady.

Alves and Cardoso (Alves and Cardoso, 1999) conducted an experimental work consisting of six tests on aggradation phenomena concentrated on the rising Manning's coefficient n due to the dune's formation in the aggradation phase and on the celerity of the observed sediment front. The analytical findings are then established and compared to the experimental ones regarding aggradation height along the channel bed. For the solution of the linear parabolic model, the mathematical model used is the one proposed by Jain (Jain, 1981).

Miglio and his colleagues (Miglio, et al., 2009) derived their results from different morphological empirical simulations operated in a narrow semi-ovoid laboratory channel, handling aggradation and degradation scenarios. There were two types of material used in the experiments: sand and gravel.

These data are compared to their numerical simulations (DORA model) that employed the Ackers formula (1984), the Meyer-Peter and Müller formula (1948), and their calibrated sediment transport discharge empirical power-law formula. The calibration formula results illustrated an excellent correspondence concerning the measured sediment transport values for the equilibrium state. In the equation of Meyer-Peter and Müller and Ackers's formula tended to overestimate this amount in general.

Radice and Zanchi (Radice and Zanchi, 2018) used multicamera, multimethod measurements for hydro morphologic laboratory experiments. They measured all needed quantities by using image processing techniques. The system used five action cameras shooting different parameters and the flume with a rectangular cross-section, $5.2\ m$ longitude, $0.3\ m$ width, and $0.45\ m$ height. A $15 - cm$ layer of loose sediment was placed on the channel bottom. The sediment was made of Polyvinyl Chloride (PVC) cylindrical particles with size= $3.8\ mm$, geometric standard deviation of the grain size distribution= 1.04, and density= $1443\ kg/m^3$. The result showed that the automatic process dramatically reduced the time of collecting data. Even though the system used five cameras simultaneously, the issue of camera synchronization was not addressed.

Figure 1-5 Cameras for measurement of bed elevation (Radice et al. 2018)

Figure 1-6 Detected bed profile (Radice et al. 2018)

Propagation of aggrading sediment fronts in a laboratory flume was investigated by Radice and Villota (Radice and Villota, 2018). The series of tests were applied on the flume mentioned in the previous work, and the type of flow was subcritical. These aggradation tests had a constant feeding rate, and the particle size was the same during the experiment. The imaging method was used to measure the temporal and spatial evolutions of the sediment surface, and they also aimed to calculate the velocity of propagation of aggrading sediment fronts.

Their results highlighted that:

1. The front heights increased with increasing sediment supply, while the front celerity decreased.
2. The bed elevation gradually raised due to the appearance of a deposition front that migrated downstream as the process developed.
3. The bed profiles showed the presence of bed-forms superimposed to the deposition front.

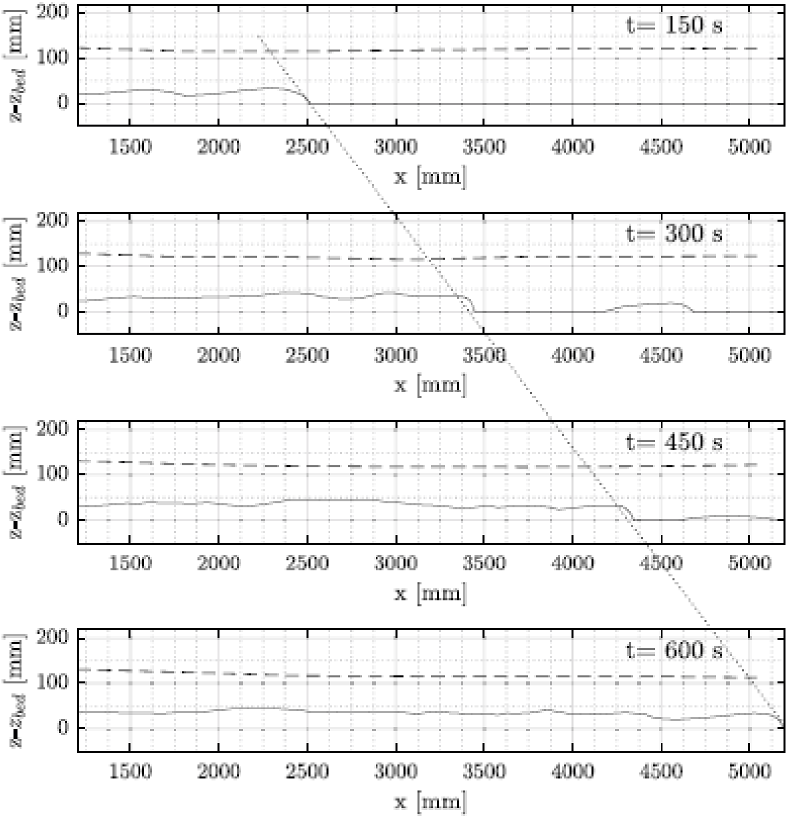

Figure 1-7 Spatial evolutions of bed in subcritical flow (Radice et al. 2018)

Zucchi (Zucchi, 2018) performed his master thesis at the Mountain Hydraulics Lab of the Politecnico di Milano, located in the Lecco campus. It aimed to deepen knowledge of aggradation phenomena caused by overloading through numerical and experimental approaches. The experiments were performed with different sediment discharges, which were higher than the channel's sediment transport capacity, resulting in aggradation in the studied channel. In this study, 17 aggradation experiments were conducted with various water and inflow sediment discharges. The numerical study was performed using the BASEMENT software, and the numerical results were calibrated according to the outcome of the experimental tests.

Heydari (Heydari, 2020) carried out his master thesis and conducted a series of experiments analysis in the overloading channel in the supercritical regime. He did the tests on the channel with an initial bed slope of 1.2 %. He used the Browline (1981) formula to estimate the threshold flow rate. The aggradation happened with the maximum height close to the inlet point and decreased along the channel, resulting in the minimum height in the downstream part. Also, he studied celerity propagation along the channel.

Eslami and his colleagues (Eslami et al., 2021) studied the bed aggradation process in an overloaded channel with a supercritical flow regime experimentally and numerically. For experimental data acquisition, various parts of the experimental system were monitored with different cameras. In this way, image processing methods were employed. BASEMENT was used for simulation in the numerical part, and by comparing the numerical and experimental work, the calibration process for two parameters, the Manning coefficient, and a Bedload factor α, was done.

1.5 objectives and contents

In this thesis, six AE experimental works (AE09 to AE14) are conducted to follow the previous works. Also, experiments three experiments (AE6, AE7, AE8) from the previous thesis (Eslami et al., 2021) have been done again according to the changes made in this thesis. Then by coupling experimental and numerical models, the bed aggradation process in an overloaded channel with a supercritical flow regime will then be analyzed by connecting experimental and numerical models. As a toolbox of MATLAB code, image processing is used for data acquisition. Some results such as sediment and water profiles will be gained at different times; then, the calibration process for two coefficients (Manning's coefficient n and a Bedload factor α) are proceeding. Furthermore, to decrease the computational cost of using MATLAB code and generate more accurate profiles, some code and experimental setup modifications and innovations are done; then, due to the importance of the celerity factor, this factor will be analyzed in supercritical flow regime, and some theoretical methods are used.

The present thesis involves four chapters:

- Chapter 1: General information of the work and the concept of the sediment transport phenomenon are introduced.
- Chapter 2: The description of the laboratory equipment used in the experiments, the methods for data acquisition, and a brief description of the experimental and numerical procedures are presented.
- Chapter 3: The results of morphologic experiments and the corresponding numerical simulation are presented.

- Chapter 4: The summary and conclusion of the study and some suggestions for future studies are presented.

Chapter 2:

EXPERIMENTAL SET-UP AND METHODS OF DATA ACQUISITION

2.1 Experimental setup

The experimental campaign is performed at the Mountain Hydraulics Laboratory of the Politecnico di Milano, Lecco campus. The experimental setup consists of various parts explained in this sub-chapter. A schematic figure of the experimental setup is shown in Figure 2-1.

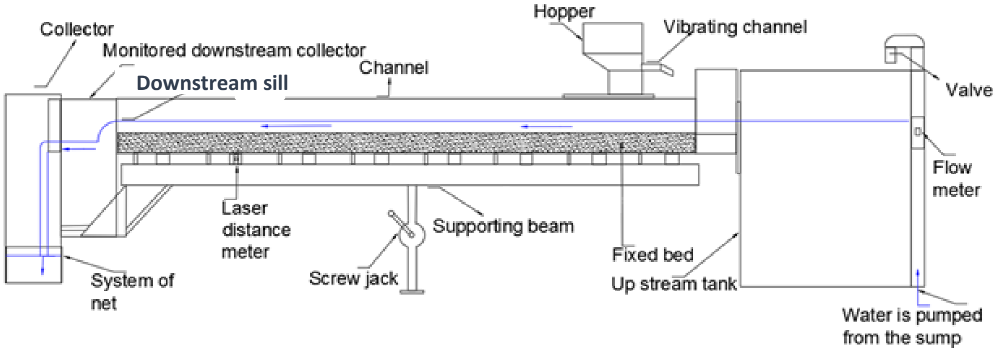

Figure 2-1 Schematic presentation of the experimental facility (Unigarro Villota 2017).

- **Experimental channel**

  The central part of the experimental setup is a $5.2-m$ long, $0.3-m$ wide, and $0.45-m$ deep flume with a rectangular cross-section and adjustable longitudinal slope S_0 (Figure 2-2). The flume has transparent Plexiglas walls, creating favorable conditions for observing hydro morphologic processes. Also, two different rulers (Figure 2-3) are fixed along the channel. Which are mainly used as an indicator for the elevation of the bed (15 cm) at the initial stage of the experiment and as a tool for validation. A $15-cm$ layer of polyvinyl chloride (PVC) particles (the properties of particles will be discussed in the following) is spread along the whole channel.

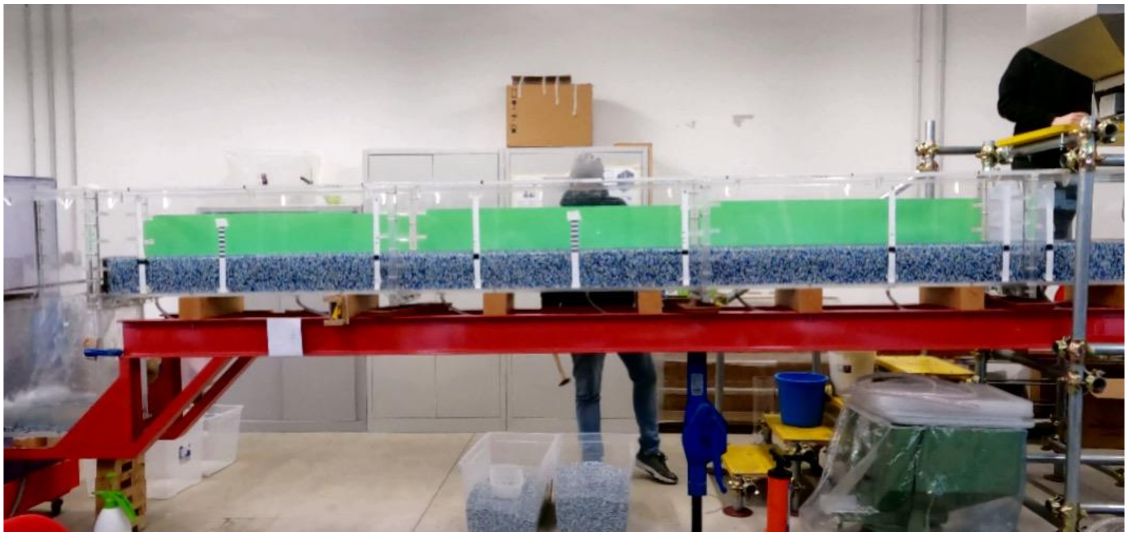

Figure 2-2 The experimental flume.

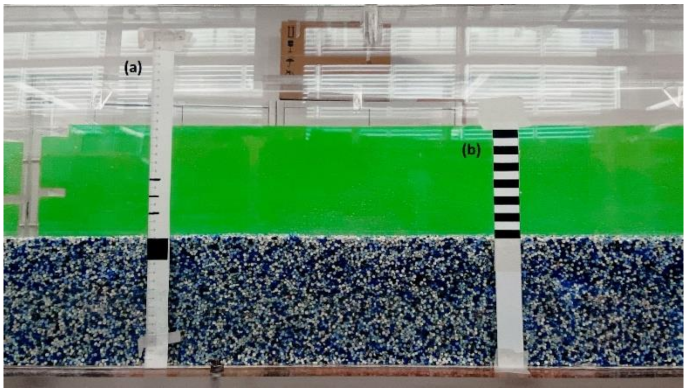

Figure 2-3 Installed rulers on the wall of the channel used as an indicator for the bed elevation (15 cm) at the initial stage of the experiment and as a tool for validation

The first $75\ cm$ of the flume is fixed by putting three plastic plates (Figure 2-4) to avoid the local scour resultant from the movement of the water flow and sediment fed by the sediment feeder. It should be mentioned that similar sediment particles are glued on the mentioned plastic plates to have a roughness similar to the other parts of the channel.

Figure 2-4 Plastic plates located in the first 75 cm of the channel

Channel's slope can be measured with a laser distance meter (Figure 2-5) fixed to the channel. It is used to read the distance between itself and the ground. This number can be transformed into a slope by utilizing a function (Figure 2-6).

Figure 2-5 Laser distance meter fixed to the channel

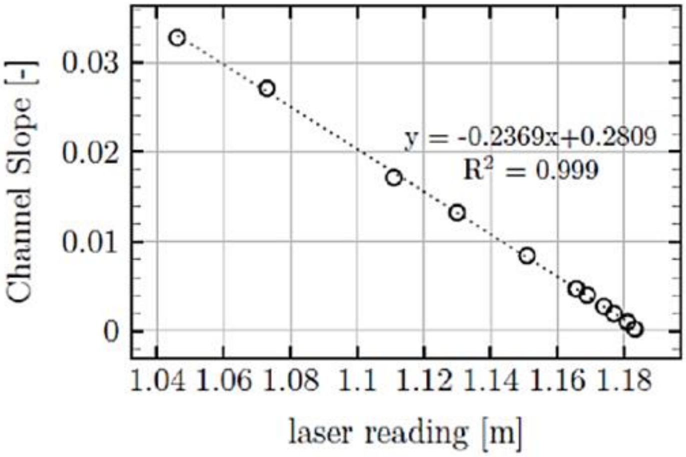

Figure 2-6 The relationship between the laser reading and the channel slope (Unigarro Villota, 2017)

- **Water feeding and re-circulation system**
  The water stored in an underground sump is pumped into the upstream tank (Figure 2-7) with a flow rate Q. When the water level inside the tank reaches the channel height, the water starts to flow into the channel.

Figure 2-7 Upstream water tank

There are two collectors located downstream. The sediments are blocked in a system of screens positioned in the second collector preventing particles from falling into the recirculating system and being transported into the underground sump (Figure 2-8).

Figure 2-8 Collectors in downstream

The flow rate of water upstream is regulated by operating a guillotine valve where a flowmeter measures the water discharge. This equipment uses the electromagnetic induction of Faraday's law (Figure 2-9).

Figure 2-9 Guillotine valve and flow meter

- **Sediment material**
  The sediment material used in this thesis is small and thick cylindrical-shaped PVC grains in different colors (18% black, 36% blue, 46% white, and a minimal amount of orange ones) (Figure 2-10).

Figure 2-10 Sediment particles made of PVC

The equivalent mean diameter (d_{50}) is $3.8\,mm$ with a standard deviation of the granulometric distribution of 1.04, the material density ρ_s is $1443\ kg/m^3$, and the porosity p is 0.45. The particle characteristics are derived by Unigarro (Unigarro Villota, 2017).

- **Sediment container (Hopper) and sediment feeder**
  Sediments enter the channel from a sediment feeder, a vibrating channel located in the channel upstream. Furthermore, a sediment container, hopper, is situated above the vibrating channel to ensure sediment availability during the experiment. (Figure 2-11) The sediment feeding rate can be controlled by setting the opening of a sluice gate between the hopper and the vibrating channel. (Figure 2-12)

Figure 2-11 Hopper and vibrating channel

Figure 2-12 Vibration level indicator

- **Cameras**
  Different numbers and types of cameras are used in this thesis to record various spatial and temporal changes in different parts of every single experiment. (See Table 2-1 and Table 2-2)

Table 2-1 The type and number of cameras used for each type of measurement for each experiment

EXPERIMENT	SEDIMENT INFLOW DISCHARGE	BED AND WATER PROFILES	SEDIMENT INSIDE THE COLLECTOR
AE06 TO AE08	1 GoPro hero 4	2 GoPro hero 7	1 GoPro hero 4
AE09	1 GoPro hero 4	2 GoPro hero 7	1 GoPro hero 4
AE10	1 GoPro hero 4	1 GoPro hero 7 (2K)	1 GoPro hero 4
AE11 AND AE12	1 GoPro hero 4	2 GoPro hero 7 + 1 GoPro hero 10	1 GoPro hero 4
AE13 AND AE14	1 GoPro hero 4	1 GoPro hero 10	1 GoPro hero 4

Table 2-2 Characteristics of each camera

CAMERA	FRAME RATE	RESOLUTION
GOPRO HERO 4	30 fps	1080*1920
GOPRO HERO 7	30 fps	2K and 1080*1920
GOPRO HERO 10	30 fps	5K

2.2 Calculation of sediment inflow discharge

This section presents the process of evaluating sediment inflow discharge using Particles Image Velocimetry (PIV) algorithm, MATLAB code mainly developed by Radice and his colleagues (Radice et al., 2006) and modified by Zanchi (Zanchi, 2018), and the transfer function.

2.2.1 Image processing: PIV (Particles Image Velocimetry) (Zanchi 2018)

Considering the sediment movement inside the vibrating channel over a small-time duration, the PIV is used to compute their mean velocity.

The mentioned camera in Table 2-1 with characteristics mentioned in Table 2-2 is located above the vibrating channel with an inclination to provide a video with a perpendicular view as input data for this algorithm. (Figure 2-13)

Figure 2-13 The camera used for recording the sediment movement along the vibrating channel

Angular distortion, which is the result of the short focal length of the lens of this camera model, can be detected in the recorded video. This distortion increases from the center to the video frame borders. Also, recorded videos may have rotation concerning the horizontal surface due to the inaccurate placement of the camera, which is unavoidable. These issues negatively affect the calculation of the correct average sediment velocity. Therefore, as the first step after recording the video, the corrections concerning the angular distortion and unavoidable rotation must be done. The Fisheye Removal algorithm provided by the camera manufacturer is used to correct image distortion. After implementing the mentioned corrections, the frames are extracted from the video. Then the extracted frames are changed from RGB scale to the grayscale to have a more manageable workspace by considering one color channel instead of three ones. (Figure 2-14)

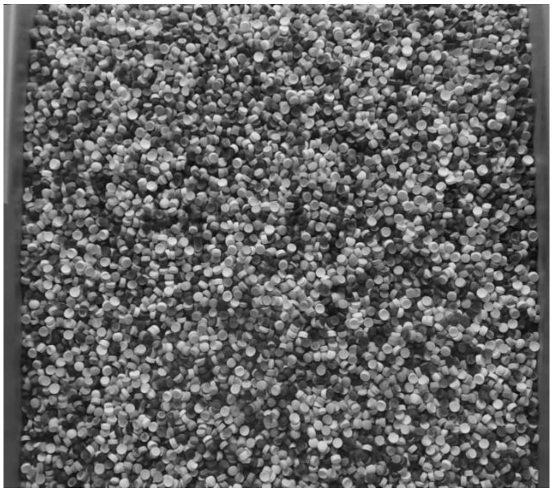

Figure 2-14 An extracted frame after the correction of the distortion, rotation, and color

The required materials for applying the PIV algorithm are ready at this step. This algorithm includes several iterations and, like any other algorithm, needs some parameters which should be defined as input values. These input values are addressed by explaining the code in the following. The main steps are:

1. **Selecting two subsequent photos (F_1 and F_2)**

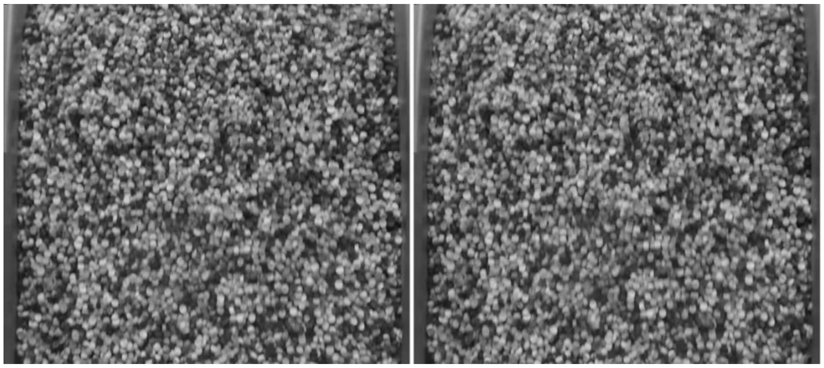

(a) (b)

Figure 2-15 (a) The first selected photo ($F1$). (b) The second selected photo ($F2$)

By considering $t_1 < t_2$, the first photo F_1 is captured at time t_1, and the second photo $F_2$is captured at time t_2. (Figure 2-15)

The selection of these photos is a function of two concepts: the jump, the distance between two pictures for successive iteration, and the step, the distance of two pictures in the current iteration. (Figure 2-16)

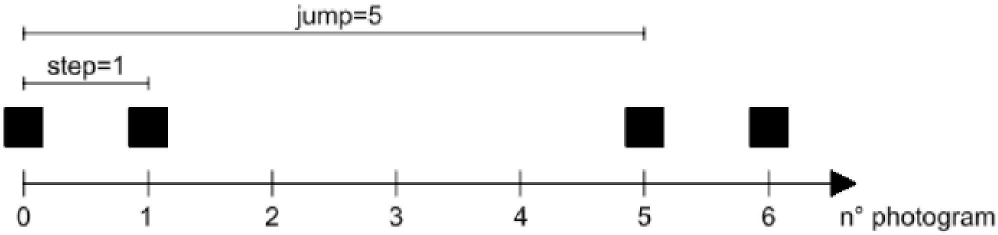

Figure 2-16 Graphical explanation of the jump and step parameters, where the values are selected as an example and equal to 5 and 1, respectively.

It should be mentioned that the value of jump in this thesis is considered as one to avoid the data loss while the value of the step is changing differently. (1, 2, 5, and 8)

2. **Defining a working area on F_1 and saving the pixels' intensity inside this area as a matrix A_1** (Figure 2-17)

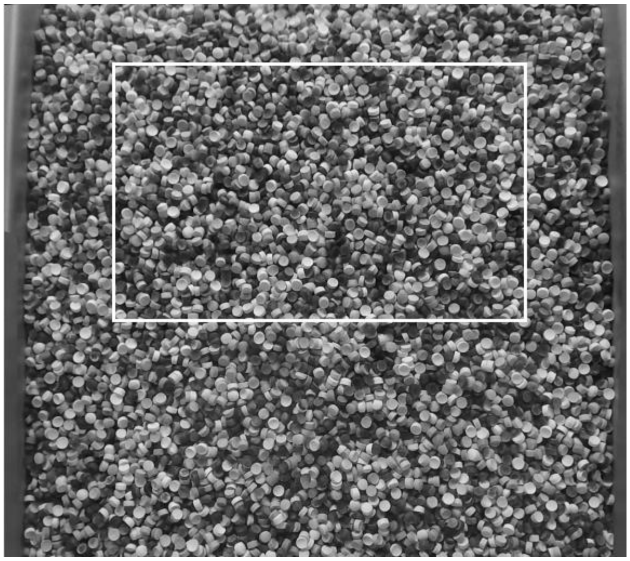

Figure 2-17 Selected working area specified with white rectangular

3. **Moving of working area, which is similar to that of F_1, pixel by pixel on F_2 and saving the pixels' intensity inside this area as a matrix A_1, then calculating parameter S from Equation 2-1.**

$$S = \frac{N_x \times N_y}{\sum_{i=1}^{N_x} \sum_{j=1}^{N_y} |A_1(i,j) - A_2(i,j)|} \qquad \text{Equation 2-1}$$

Where, N_x and N_x are the working area's dimensions in pixels along x and y directions.

It should be mentioned that F_1 displaces the working area's pixels in F_2 in two orthogonal directions of x and y because of the movements of the particles (Figure 2-18). The main direction of movement in this thesis is x-direction, so dx is critical. The maximum value of S can be interpreted as the most probable dx, and the working area can move through all the pixels, resulting in a high computational cost.

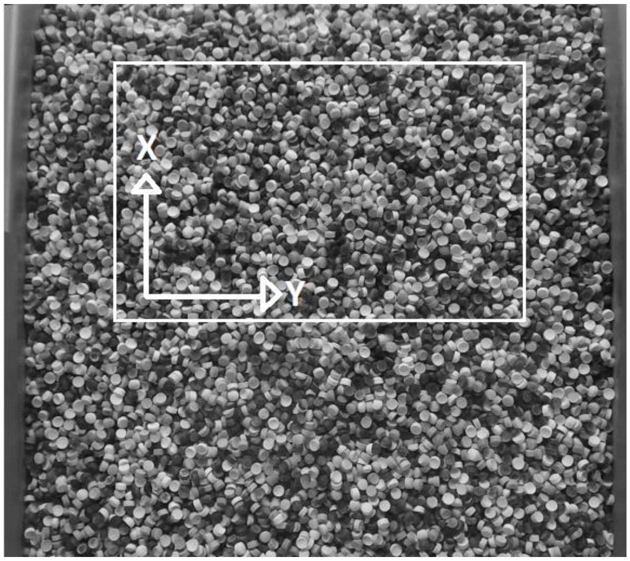

Figure 2-18 The direction of x and y in the working area

4. **Convert the obtained dx in pixel scale into a metric scale (cm) through a conversion factor**
   The conversion factor is calculated by dividing the width of the vibrating channel in pixel to the measured width in centimeters ($22\ cm$). (Figure 2-19)

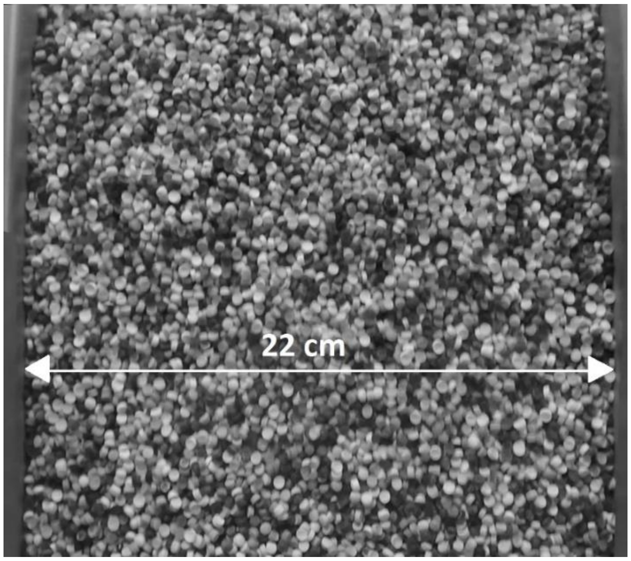

Figure 2-19 The width of the vibrating channel

5. **Define the limitation of U_{max} and V_{max}**
   The U_{max} and V_{max} as the maximum velocities in the x and y directions should be defined to limit the mentioned cost in step 3. In this thesis, the $U_{max} = 18\ cm/s$ and the$V_{max} = 0.5\ cm/s$ are chosen as the limits.

6. **Calculating the velocity in the x-direction (u) from Equation 2-2**

$$u = \frac{dx \times fps}{conv \times step}$$ Equation 2-2

Where, fps is the video frame rate, and $conv$ is the conversion factor.

7. **Obtaining the temporal evolution of the velocity by repeating all the mentioned steps for all the possible pairs of photos** (Figure 2-20)

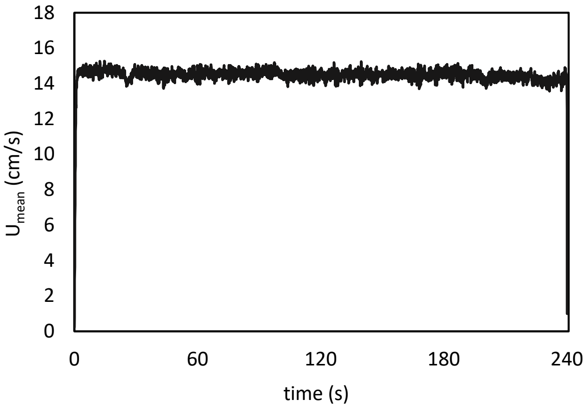

Figure 2-20 An example of the temporal evolution of the mean sediment velocity u_{mean} (AE14)

2.2.2 Calibration process

After obtaining the temporal evolution of the mean sediment velocity u_{mean}, a proper function based on experiment characteristics should be obtained for converting the mean sediment velocity u_{mean} into sediment inflow discharge Q_{sin}. These functions are obtained through a calibration process mentioned below in detail.

First, the elevation of an opening height is set ($1, 2, or\ 3\ cm$), and a vibration level is chosen. Then, the camera starts recording, and after that, the sediment feeder is turned on to pour sediments into a container located below it. After that, sediment's weight in the container is measured. This explained process is called a trial. Ten different trials have been done for each vibration level and opening height.

Afterward, the sediment inflow discharge for any trial is calculated by Equation 2-3.

$$Q_{sin} = \frac{W_s/\rho_s}{t}$$ Equation 2-3

Where W_s is sediment weight, ρ_s is sediment density, and t is the duration of the experiment.

The average Q_{sin} for each vibration level and opening height is calculated by an average of 10 trials.

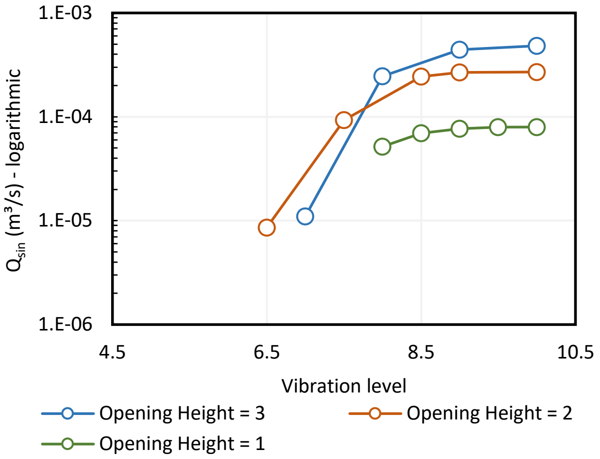

Figure 2-21 Curves show the effect of vibration level and opening height on Q_{sin} (Eslami et al., 2021)

After calculating Q_{sin} for all the trials, the PIV algorithm is implemented on the recorded video of each trial to find the average velocity of the vibrating channel u_{mean}. Then the estimated Q_{sin} and u_{mean} are mapped on a graph. And a second-degree polynomial of $y = ax^2 + bx + c$ fits the data considering the coefficient c is equal to zero since the inflow discharge must be equal to zero for sediment velocity of zero. (Figure 2-22) This second-degree polynomial is called the transfer function.

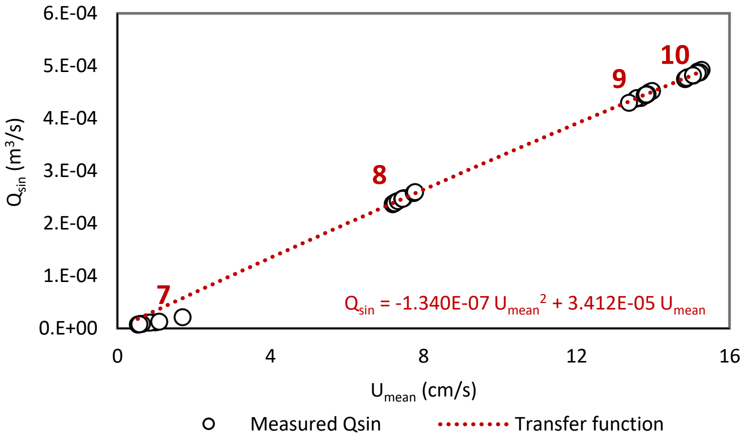

Figure 2-22 The transfer function for opening height 3 cm and its curve fit the black points done in the previous thesis. (Eslami et al., 2021)

In the previous experimental work related to this campaign (Eslami et al., 2021), the hopper calibration process and finding the transfer functions were done for three different opening heights ($1, 2, and\ 3\ cm$).

Considering Figure 2-21, it is illustrated that for opening heights of $1\ and\ 2\ cm$, the measured Q_{sin} are obtained correctly, resulting in appropriate transfer functions. In contrast, if one considers the drop in the trend of opening height $3\ cm$ for vibration levels before 7.5, it seems that the Q_{sin} is not estimated correctly, which leads to an incorrect transfer function. So, a calibration process for the opening height of $3\ cm$ has been done again in this thesis. This process consists of 70 trials, ten trials for seven different vibration levels (starting from 7 and ending to 10), and its results are provided below.

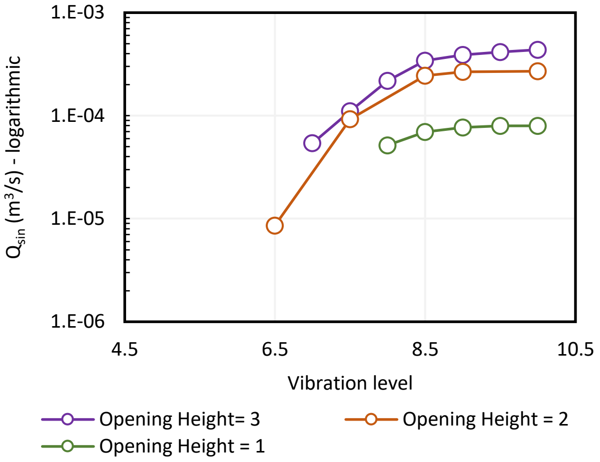

Figure 2-23 Curves show the effect of vibration level and opening height on Q_{sin}, Current thesis.

Comparing Figure 2-21 and Figure 2-23, it is shown that the trends of average Q_{sin} for opening height are $1\ and\ 2\ cm$ in both diagrams are similar, while that of opening height is $3\ cm$ is changed. For comparing the trends of opening height $3\ cm$ in detail, see Figure 2-24 below. It is illustrated that the trends are different for vibration levels less than 8, while after that, their trends are almost the same.

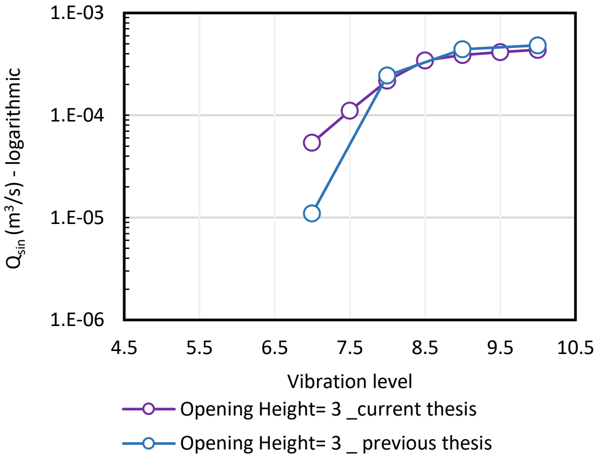

Figure 2-24 Comparison between the trends of average Q_{sin} measured by previous thesis (Eslami et al., 2021) and current thesis

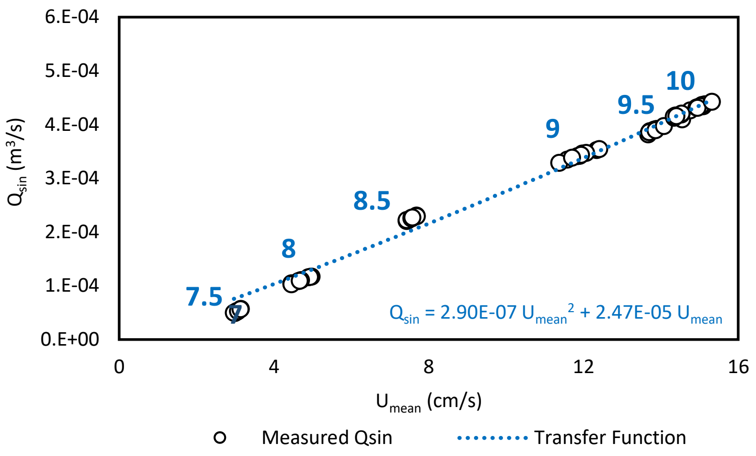

Figure 2-25 The transfer function for opening height 3 cm and its curve fitted to the blue points done in the current thesis.

Then the obtained transfer functions are used to calculate the temporal evolution of Q_{sin} (Figure 2-26) by considering the temporal evolution of u_{mean} (Figure 2-20).

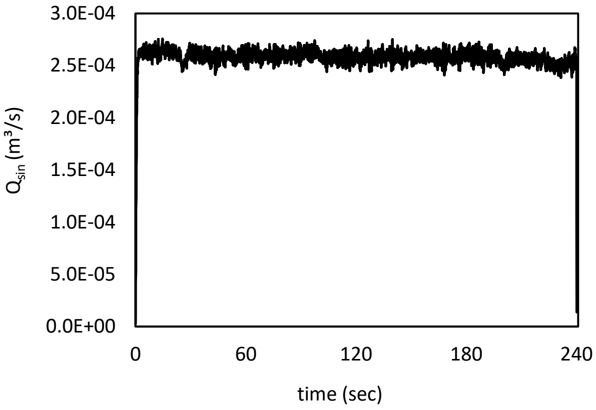

Figure 2-26 An example of temporal Evolution of sediment inflow discharge Q_{sin}. (AE14)

Figure 2-26 helps check whether the hopper is functioning steadily during a trial.

2.3 Measurement of the bed and water levels

2.3.1 Previous motion-based method (Eslami et al., 2021)

In previous work, the motion detection method was used to recognize bed and water levels by analyzing images taken by two cameras installed parallel to upstream and downstream of the flume. (Figure 2-27)

Figure 2-27 Cameras positioned in front of the channel

The process of motion detection will be defined below.

1. **Frame extraction**
   Extracting the first camera's video frames and converting them to grayscale.
2. **Distortion removal**
   Removing images' distortions by applying the radial transformation (Equation 2-4)

$$\frac{r}{1 + k \times r^2} \qquad \text{Equation 2-4}$$

   Where r is the radial distance concerning the center, and k is a calibration factor obtained with trial and error. The undistorted frame is shown in Figure 2-28.

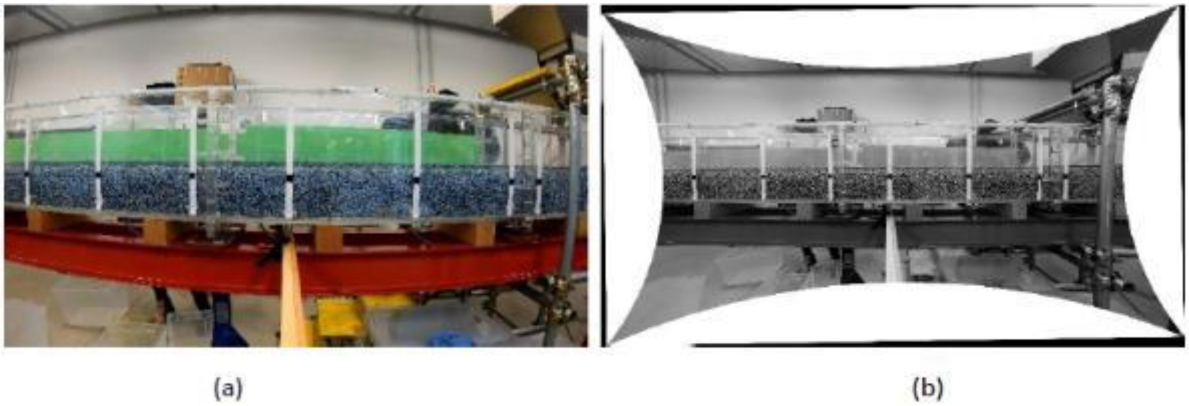

(a) (b)

Figure 2-28 (a) Frame extracted from the video (b) Extracted frame after the correction of the distortion

3. **Frame selection**
   Two subsequent photos (F_1 and F_2) needed to be chosen (Figure 2-29). Each selected photo is a frame of the channel through the experiment captured at a specific time. They are chosen as a function of jump and step parameters; jump and step are introduced

earlier in 2.2.1. Jump and step values equal $30\,frames\,(1\,sec)$ and one frame, respectively. Then the matrixes A_1 and A_2 are created, representing the pixels intensity of F_1 and F_2.

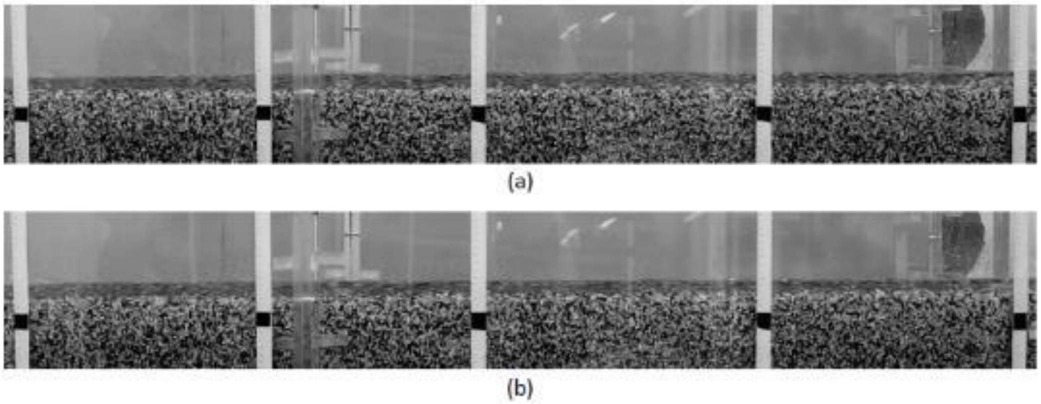
(a)

(b)

Figure 2-29 (a) The first selected photo (F_1). (b) The second selected photo (F_2)

4. **"Gaussian" Filter**
   A Gaussian filter is applied to the photos to remove the noises to avoid detecting them as motion.
5. **Subtraction**
   To continue, it is needed to determine the difference between two chosen subsequence images. The difference between the two images is represented by calculating the absolute value of the subtraction of matrices A_1 and A_2.
6. **Define threshold and binarization**
   A threshold is defined by trial and error. If the subtraction values obtained from the previous step are more significant than the specified threshold, it is detected as motion, and the pixel intensity is set to zero; otherwise, it is set to one. The result of this stage is a binary image, in which its black pixels $(pixel\ intensity = 0)$ represent the areas where a motion is detected, and the white pixels $(pixel\ intensity = 1)$ represent the areas where no motion is detected. (Figure 2-30)

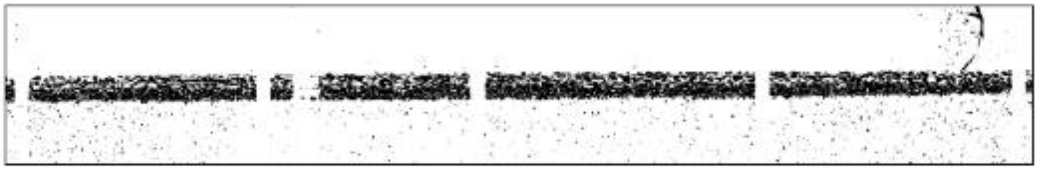

Figure 2-30 The processed photo shows the motion with black color $(threshold\ value =\ 0.04)$

7. **Signal production**
   The moving sediment layer and water are highlighted in black in the sketch below (Figure 2-31). The lowest side of this black area is the border between the stationary bed and the moving bed, so recognizing it can be so beneficial to spot the edge of the bed. In this way, a moving window with a specific dimension $(4 \times 10\,pixels)$ is selected, and it starts to move pixel by pixel from the top left corner to the down left corner, and then it shifts a

pixel to the right side, and again it starts moving from up to down. It should be mentioned that the size of the moving window is changeable.

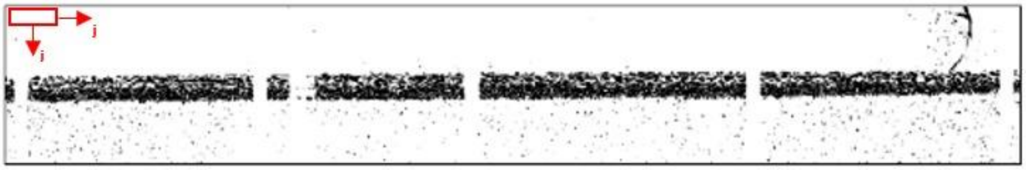

Figure 2-31 Schematic representation of the moving window from its initial position

The moving frame calculates the average value of the pixels' intensity $p(i)$, and based on this, the signal for each column is provided (column or cell). The signal presents the value of mean intensity for each row of the column (Figure 2-31). This figure shows that the black layer exists at the middle of two white layers so that the signal value can be different in each pixel. These changes are significant either entering the black layer or exiting from the black layer. It rises significantly by entering the black layer, and the signal value significantly drops by exiting from the black layer. As a result, there are two significant signal changes. The first (upper one) is related to the water surface, and the second belongs to the border between the moving layer and the stationary bed.

8. **"Findchangepts" function**

   A MATLAB function (Findchangepts) is used to detect the locations of changes. (Figure 2-32)

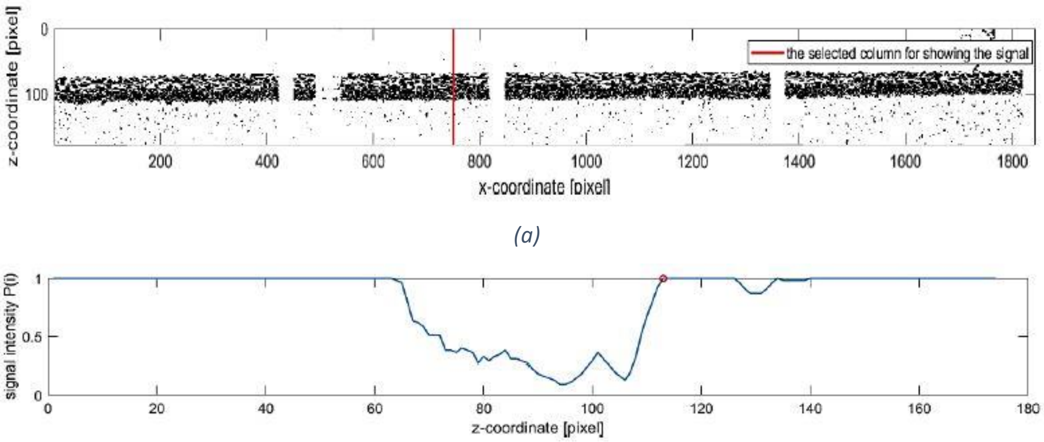

(a)

(b)

Figure 2-32 (a) The selected column is shown in red for showing its related signal. (b) The signal along the selected column with a red dot on it represents the location of the center of the moving window when the moving window leaves the black layer completely

Based on the previous steps, the sediment surface for each column is recognized, and by putting these points beside each other, the profile is provided. (Figure 2-33)

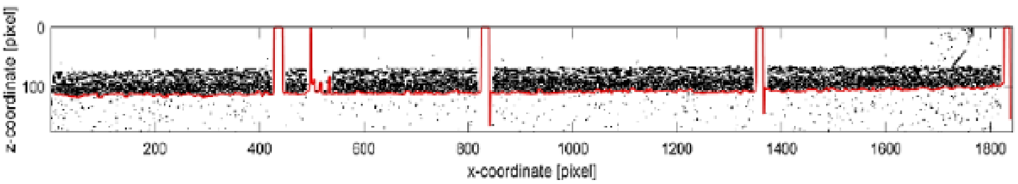

Figure 2-33 The produced bed profile is shown in red

9. “Filloutliers” function on motion intervals

In this step, the "Filloutliers" MATLAB function was used to deal with outlier data. In this way, the motion intervals were selected, and then the "Filloutliers" function was applied to selected intervals. (Figure 2-34)

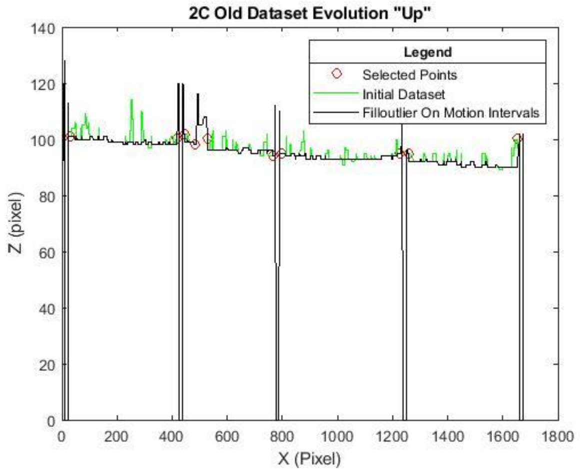

Figure 2-34 Apply “Filloutlier” function on selected motion intervals of water profile (“Up” camera _ AE11 _(2C_Old))

10. “Filloutlier” function on the entire profile

In this step, another "Filloutlier" function was used to deal with objects that obstruct the view of the cameras (location of the tapes). However, this time it applied to the entire dataset (even the selected motion intervals that the "Filloutlier" function had been used to them in the previous step). (Figure 2-35)

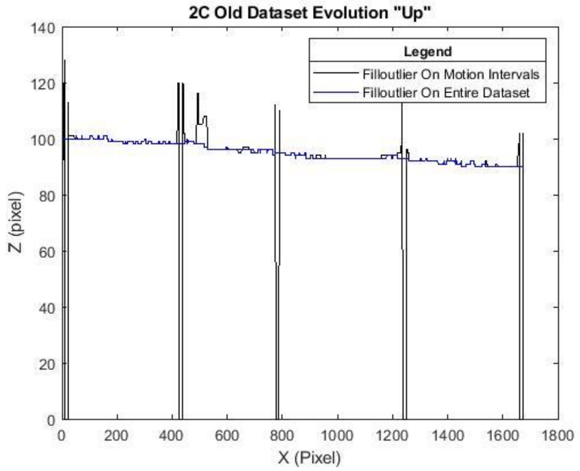

Figure 2-35 Apply “Filloutlier” function on entire dataset of water profile (“Up” camera _ AE11_(2C_Old))

11. **“Smoothdata” function (Moving-Average)**
    Moving average filter is smoothing data by replacing each data point with the average of the neighboring data points.

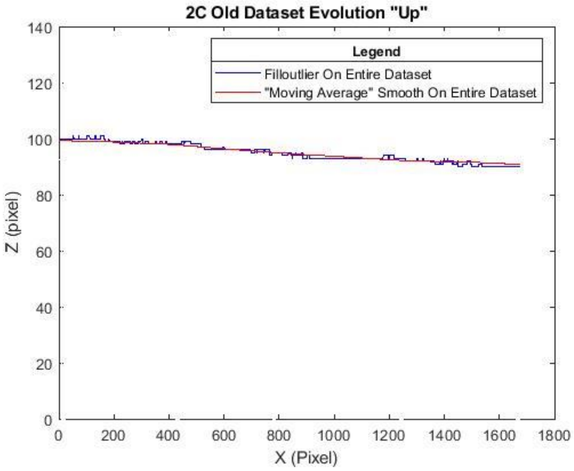

Figure 2-36 Apply “moving average” smoothing function on entire dataset of water profile (“Up” camera _ AE11_(2C_Old))

12. **Reference dataset**
    The coordinates should be referenced in x-direction concerning the origin located upstream (the x-coordinate increases moving from upstream to downstream) and in z-direction concerning the position of black tapes situated 15 cm above the bottom of the channel.
13. **Conversion**
    The coordinates of the profile data are in the pixel scale; they should be converted into a metric scale through a conversion factor.
14. **Repeat steps 1 to 13**
    After finding the profile for this instant, another pair of photos are chosen based on the jump and step parameters, and the code repeats all the steps mentioned above.

The above algorithm was for frames taken by the first camera, so all the above steps must be done for the second camera.

15. **Regrouping**
    The obtained profiles from each camera should be put together to create profiles for the entire channel. Therefore, the first profiles generated from each camera are selected and placed next to each other, resulting in a final profile representing the channel as a whole.

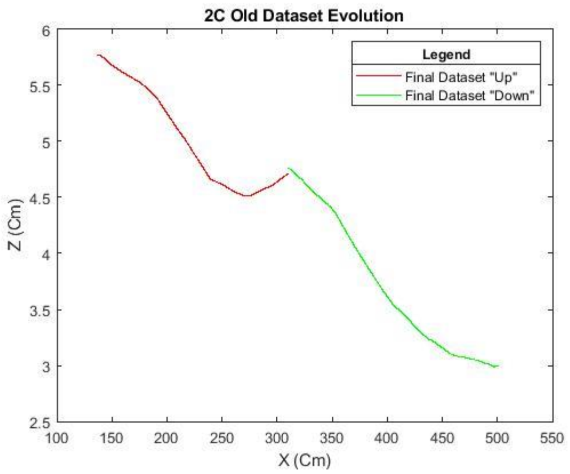

Figure 2-37 Putting generated profiles from each camera (Up and Down) next to each other (AE11_(2C_Old))

16. **Repeat step 15:**
    After generating the first profile related to the entire channel for the first instant, all possible pairs of corresponding profiles from each camera were chosen based on the jump parameter. The regrouping step was repeated for them.

Finally, it gives the profiles related to the entire channel for all selected times (every 1 sec).

2.3.2 Errors and solutions

Analyzing the pattern of the profiles obtained from previous experiments, the relevant codes and functions, and the laboratory setting to generate the profiles determined that some factors may contribute to errors. These factors are generally mentioned below.

1. Noises need to be reduced, resolved or prevented to improve the motion detection process and generation of the profiles.
2. Objects obstruct the view of cameras along the channel, causing data loss by making the sediment and water invisible in their locations and disturbing the dataset. These objects include strips mounted along the channel and other cameras in some experiments.
3. Distortions caused by the "Wide" mode of the camera's lens, which increases (distortion) with distance from the center of each image, make the results unreliable on the final generated profiles. These distortions significantly affect last generated profiles on upstream (upstream of the Up camera), downstream (downstream of the Down camera), and center (downstream of the Up camera and upstream of the Down camera) of them.
4. Discontinuity of the final profile and creation of a step in its center, which is due to the juxtaposition of two separate processed data sets

Some modifications and innovations are made to find practical solutions for addressing the mentioned errors, and then the results are compared with previous works.

These solutions are classified into three groups applied to the listed error factors to improve the final profiles.

a. Laboratory setup

b. Measuring devices
c. Code modifications

The table below (Table 2-3) shows their three classes' performed solutions and innovations for the mentioned error factors.

Table 2-3 Performed solutions and innovations for addressing the errors regarding the previous motion-based method (Eslami et al., 2021)

ERROR FACTORS	SOLUTIONS AND INNOVATIONS		
	a) Laboratory setup	**b) Measuring device**	**c) Code modification**
1. NOISES	• Install black, anti-reflective curtains		• Changing the smoothing method
2. OBJECTS THAT OBSTRUCT THE VIEW OF CAMERAS ALONG THE CHANNEL			• Changing the way that data is processed by code in the places where the objects are obstructing the view of the cameras • Changing the considered longitudinal interval for processing
3. DISTORTIONS		• Using linear mode instead of wide mode	• Changing the removal distortion method
4. DISCONTINUITY OF THE FINAL PROFILE AND CREATION OF A STEP IN ITS CENTER		• Using one camera instead of two cameras	• Changing the way that two datasets from two separate cameras are regrouped • Making the code compatible with one camera

2.3.2.1.1 Error caused by noises

Solutions and innovations related to upgrading the laboratory setup and code modification in the case of dealing with errors caused by data noises are discussed below.

- **Laboratory setup: Install black anti-reflective curtains**
  Checking the images and data from the previous experimental campaign highlights shadows and reflections observed due to the location of the channel in the laboratory and its glassy lateral body. These reflections are various for each experiment frame and significantly affect image processing by causing noises in data. Therefore, a black anti-reflective curtain (Figure 2-38) is installed on the laboratory windows (behind the cameras). The effects of this change can be recognized well. (Figure 2-39)

Figure 2-38 Black and anti-reflective curtain

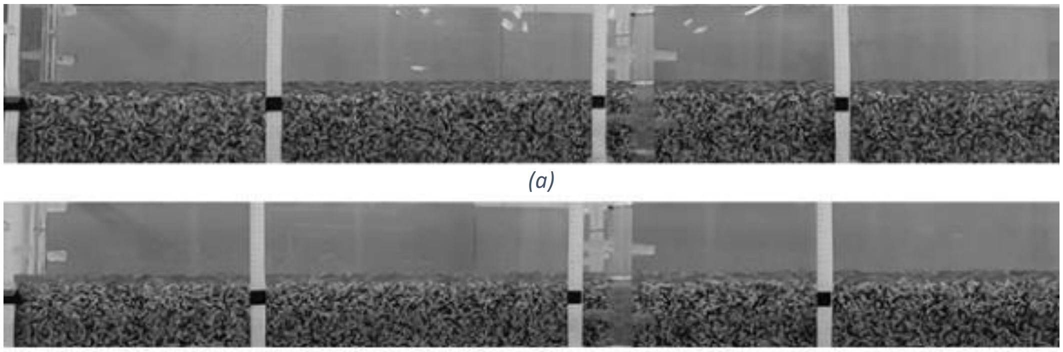

(a)

(b)

Figure 2-39 (a) The light reflection in AE09 (b) The light reflection in AE11

- **Code modification: Changing the smoothing method**

  The moving average filtering was used to smooth the data in the previous code. Moving average filter smooths data by replacing each data point with the average of the neighboring data points defined within the window determined heuristically. The window slides down the length of the vector, computing an average over the elements within each window.

  Checking of smoothing methods shows that the moving average smoothing method contributes to data loss. As a result, the trend of bed and water elevation changes in the experiments, especially in upstream, downstream, and the center of the profile.

  Due to laboratory conditions, the collected data of experiments have outliers in addition to noise. The robust Lowess method (rLowess) is a smoothing method that is particularly helpful when outliers are presented in the data in addition to noise which is almost similar to this thesis case and useful for data smoothing.

  The name “Lowess” is derived from the term “locally weighted scatter plot smooth,” as this method uses locally weighted linear regression to smooth data. The smoothing process is considered local because, like the moving average method, each smoothed value is determined by neighboring data points defined within the window. The process is weighted as a regression weight function is defined for the data points contained within the window, and it uses linear polynomial as a regression model.

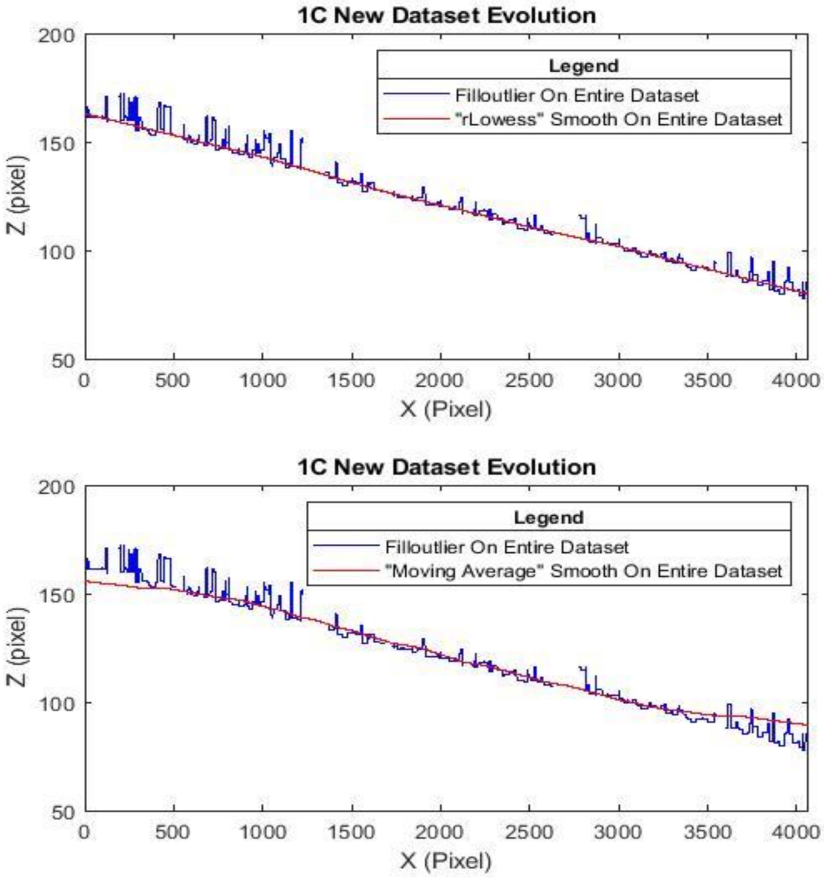

Figure 2-40 (a) "rLowess" smoothing method (b) "Moving average" smoothing method.

The local regression smoothing process follows these steps:

1. Compute the regression weights for each data point in the span. The weights are given by the tricube function shown below.

$$w_i = \left(1 - \left|\frac{x - x_i}{d(x)}\right|^3\right)^3 \qquad \text{Equation 2-5}$$

   Where x is the predictor value associated with the response value to be smoothed, x_i are the nearest neighbors of x as defined by the span, and $d(x)$ is the distance along the abscissa from x to the most distant predictor value within the span.

2. A weighted linear least-squares regression is performed. The regression uses the first-degree polynomial.
3. The weighted regression gives the smoothed value at the predictor value of interest.

In addition to the regression weight function, it uses a robust weight function, which makes the process resistant to outliers. If the data contains outliers, the smoothed values can become distorted and not reflect the behavior of the bulk of the neighboring data points to overcome this problem, a method using a robust procedure that is not influenced by a small fraction of outliers. The robust smoothing procedure follows these steps:

1. Compute the robust weights for each data point in the span. The bisquare function gives the weights:

   $$w_i = \begin{cases} \left(1 - (r_i/6MAD)^2\right)^2 & , |r_i| < 6MAD, \\ 0 & , |r_i| \geq 6MAD \end{cases} \qquad \text{Equation 2-6}$$

   Where r_i is the residual of the ith data point produced by the regression smoothing procedure, and MAD is the median absolute deviation of the residuals:

   $$MAD = median(|r|) \qquad \text{Equation 2-7}$$

   The median absolute deviation is a measure of how spread out the residuals are. If r_i is small compared to $6MAD$, then the robust weight is close to 1. If r_i is greater than $6MAD$, the robust weight is 0 and the associated data point is excluded from the smooth calculation.
2. Smooth the data again using the robust weights. The final smoothed value is calculated using both the local regression and robust weights.
3. Repeat the previous two steps.

2.3.2.1.2 Error caused by objects that obstruct the cameras’ view along the channel

Solutions and innovations related to code modification in the case of dealing with errors caused by objects that obstruct the view of cameras along the channel are discussed below.

- **Code modification: Changing the way that data is processed where the objects are obstructing the view of the cameras**

  In previous experiments to manage objects that obstruct the view of the cameras, such as tapes mounted on the channel, first, the visible intervals of the profile were selected, and the first outlier function was applied to them. Then, another outlier function was applied to the entire profile (Both on the location of visible parts and the location of view's obstruction objects). Applying the outlier functions in this way would be the reason for the unrealistic pattern of the profiles since the outlier functions are not applied homogeneously to all data. The unrealistic behavior has affected the sides of the photos (upstream, downstream, and center of the profile) and the view's obstructed intervals.

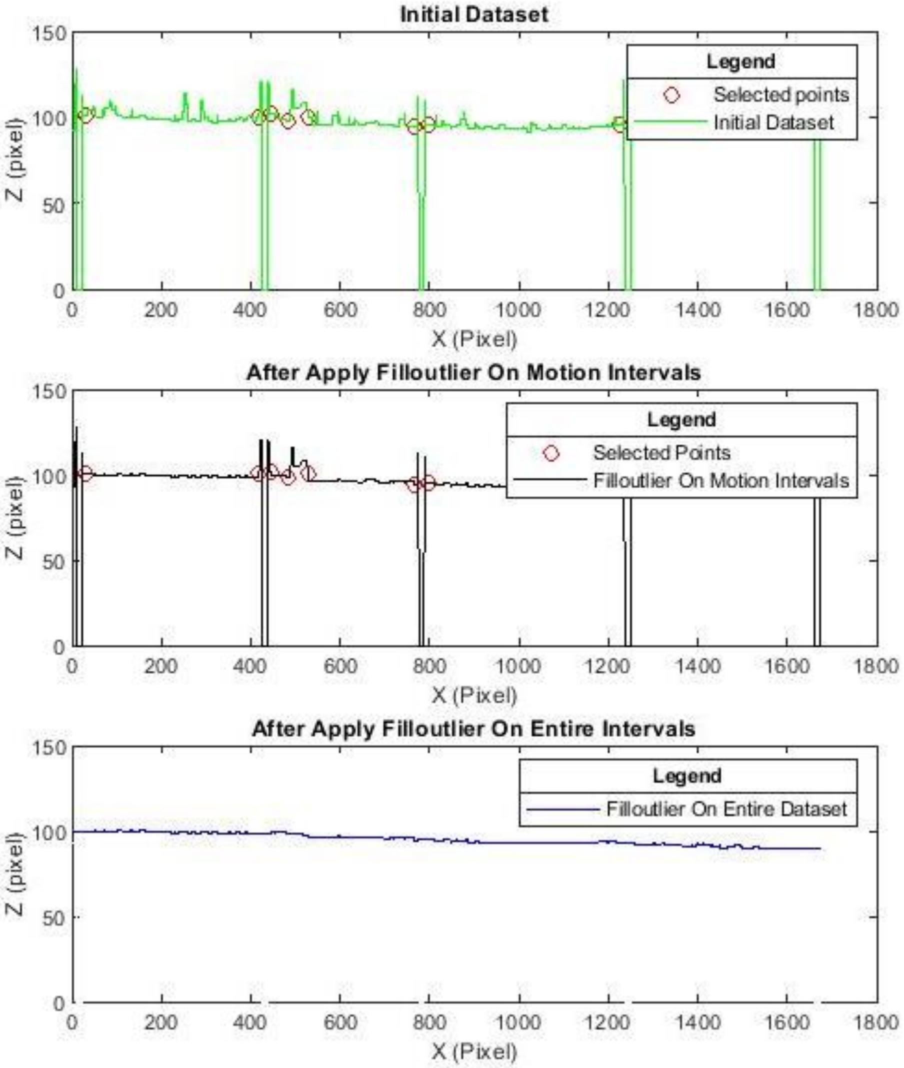

Figure 2-41The procedure of dealing with objects that obstruct the view of cameras in previous method

In the newly modified code, instead of selecting the motion interval manually and applying the outlier function on this interval and then on the entire profile, the interval that obstructed the view of the camera (the tape parts in this case) is selected with the same procedure as before, and it is deleted (Figure 2-42). This process also can lead to decreasing the computational cost.

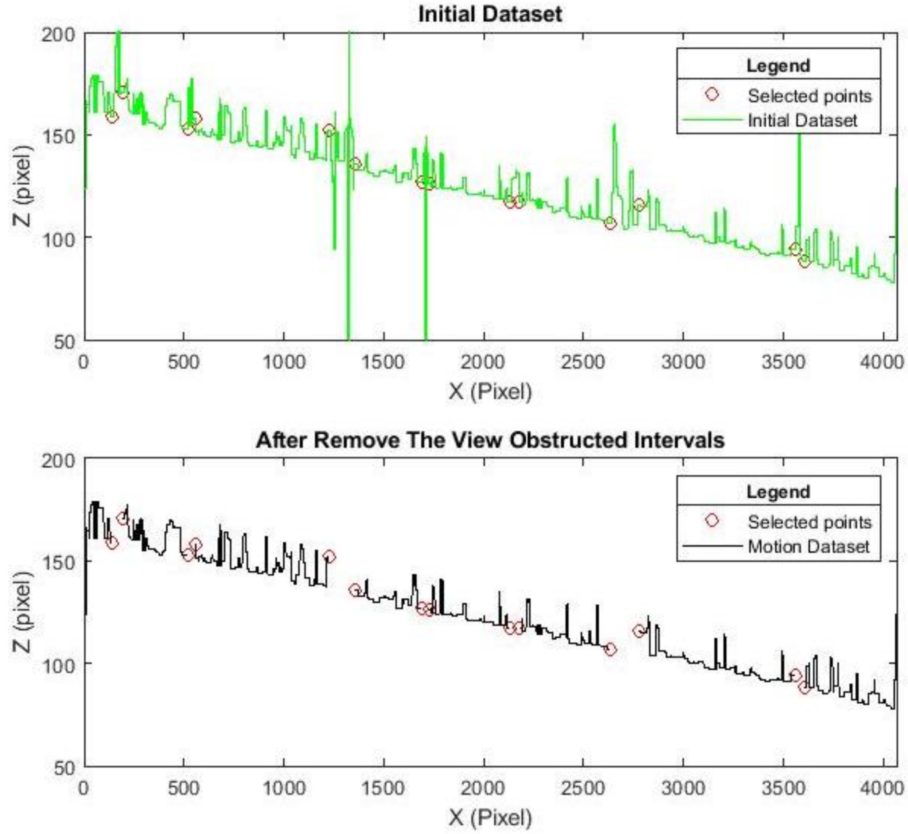

Figure 2-42 The procedure of dealing with objects that obstruct the view of cameras in new method (a) Initial dataset (b) dataset after deleting the wrong data

- **Code modification: Changing the considered longitudinal interval for processing**
  In addition to the lack of applying the outlier function homogeneously, the effect of choosing the longitudinal interval for the image processing and whether the view's obstructed part is at the start, or the end of the longitudinal interval contribute to profiles' unrealistic behavior. Thus, if a view's obstructed part is at the beginning or end of the longitudinal interval since it is the beginning or end of the longitudinal processing interval, there is no data on the other side. So, the motion detection will have more errors. In previous experiments, this has been the case with the upstream of the upstream's camera and the upstream of the downstream's camera (upstream and center of the profile). The no data parts that existed at the beginning and end were removed from the considered interval to prevent the presence of invisible parts at the beginning and end of the longitudinal interval. Indeed, the length of profiles are reduced from $384\ cm$ ($x_1 = 136.75\ cm,\ x_2 = 520.75\ cm$) to $378.5\ cm$ ($x_1 = 139.25\ cm,\ x_2 = 517.75\ cm$) due to this reason. So, there is no view obstructed part (no data part) at the beginning and the end of the considered interval but the motion.

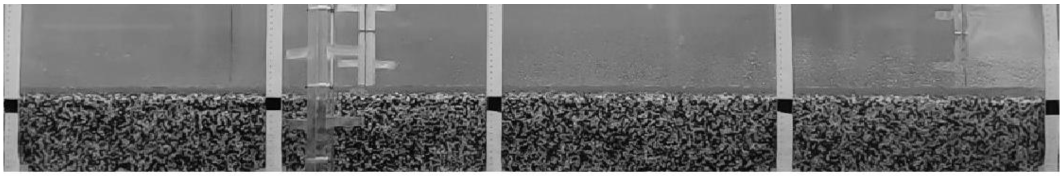

(a)

(b)

Figure 2-43 (a) Longitudinal interval with invisible parts at the beginning and end (b) Longitudinal interval with motion at the beginning and end

2.3.2.1.3 Error caused by distortions

Solutions and innovations related to measuring devices in the case of dealing with errors caused by distortions are discussed below:

- **Code modification: Changing the removal distortion method**
  The algorithm provided by GoPro Studio software is used to eliminate the distortion of wide images taken by GoPro cameras. In this way, due to the compatibility of the algorithm with the camera, more accurate results are obtained.
- **Measuring device: Using linear mode instead of wide mode**
  Due to the maximum use of the field of view, previous tests have been done using an extremely wide-angle lens. This lens allows the user to take photos and videos of more space, but the price that pays is distorted bulging fisheye images, where horizons and straight lines get curved.
  It is possible to correct the images in the post-process procedure. However, it is very time-consuming and sensitive to choose the best coefficients, so the computational cost will significantly increase, and there will always be the possibility of an error.
  It is decided to use a linear field of view lens to have more useful images. Linear lenses have a field of view that is correct for fisheye distortion, straightens the horizon and verticals, and narrows the perspective. This feature eliminates the need to post-process images to correct them and reduce the computational cost. (Figure 2-44)

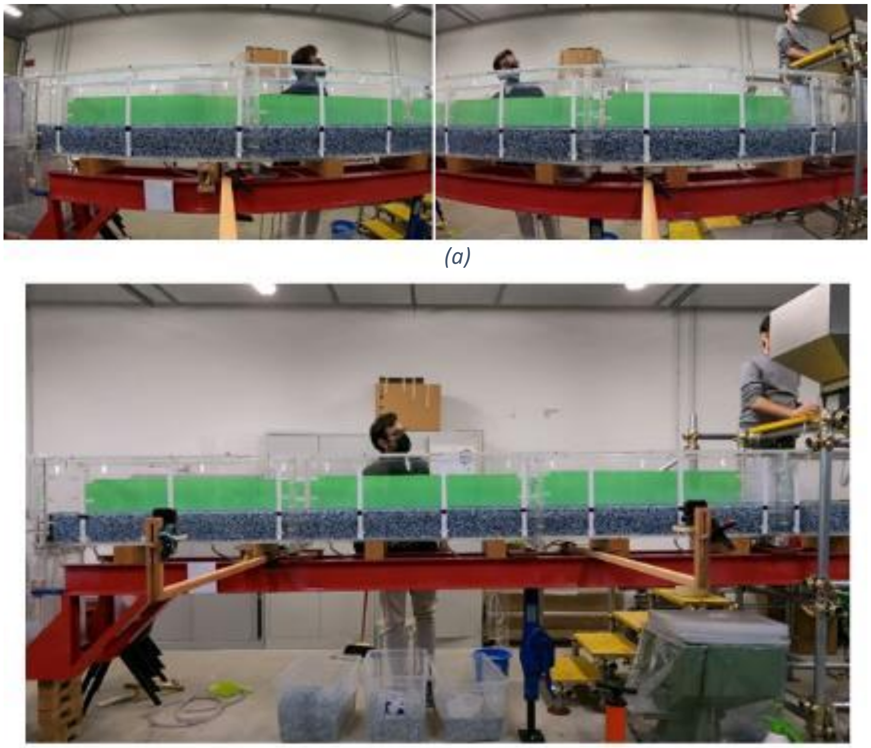

(a)

(b)

Figure 2-44 (a) Using wide mode (b) Using linear mode

2.3.2.1.4 Error caused by discontinuous profiles (step in the middle by using two cameras)

To handle these errors, some modifications are implemented as below.

- **Code modification: Changing the way that two datasets from two separate cameras are regrouped**

  In previous experiments, all processing steps were performed for each dataset from each camera separately. Then the two final profiles were placed next to each other in the "regrouping" step (Figure 2-37 and Figure 2-45). This method for regrouping the datasets is one of the crucial reasons for occurring a step in the center of the final profile where they are connected.

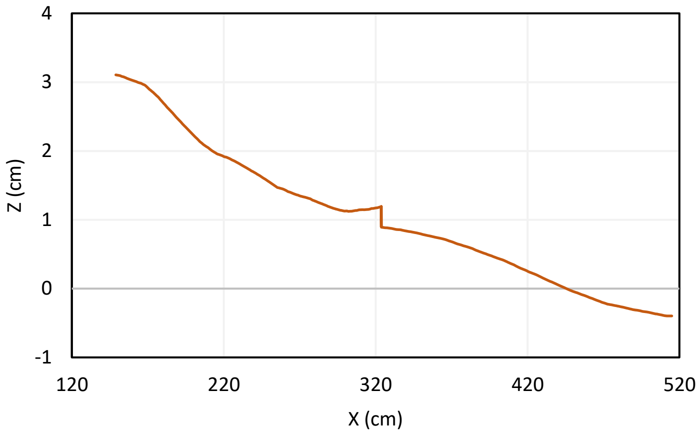

Figure 2-45 Final profile obtained from previous method and step in the middle of the profile where two profiles connected. (AE11 _ (2C_Old) _ t=120)

In the newly modified code, no function is initially applied to the new code's raw data extracted from each camera. The two raw datasets are referenced and placed next to each other by a gap in the location of the predetermined tape, thus forming a single dataset. Then all the required processes and profile finalization are applied homogeneously to a single dataset (Figure 2-46).

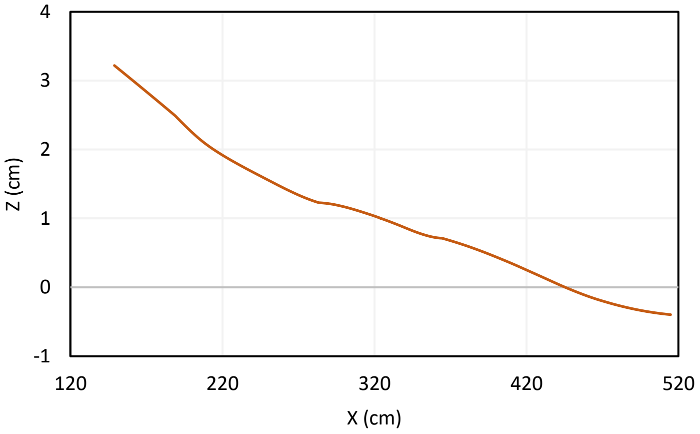

Figure 2-46 Final profile obtained from new method (AE11 _ (2C_New) _ t=120)

- **Measuring device: using one camera instead of two cameras**
  A combination of several errors that were mentioned earlier was caused a step to be seen in the middle of the final water and bed's profiles. The process of transition from the obtained profile of each camera to a final single profile for the whole channel cannot properly regroup and overlap the data that each of which was processed separately, and it will have errors. It results in a step in the middle and unrealistic behavior upstream and downstream of the final profile. This problem can be solved by correcting the mentioned errors, so the previous experiments conducted using two cameras were corrected (AE06, AE07, and AE08).

Due to what was observed from regrouping data problems for the new experiments, it was decided to use one camera instead of two. In addition to satisfying the required quality, using one camera solves the problem of regrouping the data obtained from two cameras which significantly reduces the processing time and the use of different codes.

- **Code modification: Making the code compatible with one camera**

  The code used for data processing must be modified to be consistent with the change done in the number of cameras in the new experiments (from two cameras to one camera) and address the mentioned errors.

2.3.3 Newly modified motion-based method

All experiments related to previous theses have been performed with two cameras or more, which requires a new modified motion-based method to correct the mentioned error factors in previous experiments. Moreover, some experiments in this thesis are performed with two cameras to compare with experiments in the previous thesis (Eslami et al.,2021) to validate the changes made in this thesis (for example, to validate using one camera instead of two cameras)

On the other hand, almost all the experiments of this thesis have been performed with one camera, which requires a new modified motion-based method to correct the mentioned error factors. So, in this thesis, it can be concluded that the data collected in different experiments are divided into two groups:

1) Performed by two cameras (2C_New): related to all of the previous thesis experiments and some of the current thesis experiments.
2) Performed by one camera (1C_New): related to the current thesis experiments

Since these two groups do not have the same analysis process, the new modified codes compatible with one camera and two cameras have been needed.

2.3.3.1 Newly modified motion-based method performed by two cameras (2C_N)

Part of the innovations and solutions mentioned to deal with errors related to the code and laboratory conditions can be applied to experiments performed with two cameras.

The main modifications made are related to the code. Below is how the newly modified code compatible with the two cameras works.

2.3.3.1.1 Procedure

1. **Distortion removal**

   The camera lenses must be in the wide mode to cover the needed length of the channel when two cameras are used. Then, it is necessary to remove the fisheye distortions caused by the "wide" mode of the camera lenses.

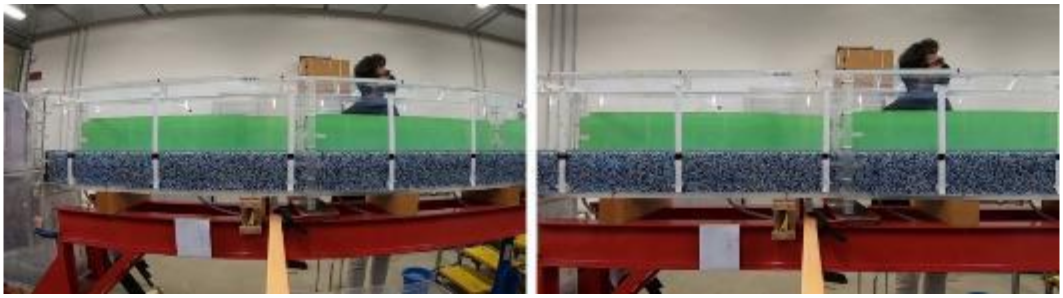

(a) (b)

Figure 2-47 (a) Before removing the fisheye distortion (b) After removing the fisheye distortion

2. **Frame extraction**
   The video frames are extracted from the first camera, and the images are converted to grayscale.
3. **Frame selection**
   It is needed to have two images in a row to detect the motion, so a step value equal to one frame is used to select two images in a row (F_n , F_{n+1}), and a jump value of $30\ frames\ (1\ second)$ is used to choose the rest of two subsequent images (F_{30i} , F_{30i+1}),.

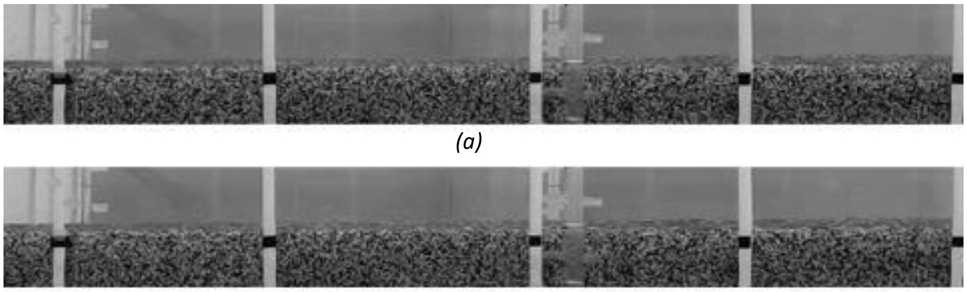

(a)

(b)

Figure 2-48 (a) Frame 1540 of AE11-2C-downstream camera (b) Frame 1541 of AE11-2C-downstream camera

4. **“Gaussian” Filter**
   A “Gaussian” filter is applied to the selected images to reduce noises and prevent them from being detected as motion.
5. **Subtraction**
   The pixels intensity of each selected image is saved as a matrix (A_{30i} , A_{30i+1}), and the absolute value of subtraction of two matrices is related to two chosen subsequent images in each jump ($|A_{30i} , A_{30i+1}|$) is calculated.
6. **Define threshold and binarization**
   Considering that in two images in a row, in places with no motion, no difference in pixels intensity (or by considering the noises, it is deficient) is expected. While in places with motion, a difference in pixel intensity is expected, so a threshold is required to discriminate between these two states, as mentioned below:

If ($|A_{30i}, A_{30i+1}|$) > threshold value → there is motion → black pixel → pixel intensity = 0
If ($|A_{30i}, A_{30i+1}|$) < threshold value → there is no motion → white pixel → pixel intensity = 1

As a result of this step, black and white images (binary matrix) are obtained that the black layer in the middle shows the motion related to water and sediment in the channel. The upper boundary of this layer indicates the water surface position, and the lower boundary of this layer indicates the channel stationary bed at the time of the image.

7. **Signal production**

   To find this motion layer's top and bottom boundary, a moving window with chosen dimensions (in this case, $4 \times 10\,pixels$) is defined.

   This window starts moving, pixel by pixel, from the top-left corner of the image to the bottom of the first column and calculates the average intensity of the pixels fitted inside. Then, the window shifts by a pixel to the right and moves downward again. As a result, a signal is produced for each column that shows the average intensity amount for each row of the column. This process continues until covering all of the columns.

8. **"Findchangepts" function**

   As mentioned before, the motion pixels are defined as zero-pixel intensity by a threshold, and it is expected that the average pixel intensity value in the motion layer be meager and close to zero, while the average pixel intensity value of stationary layers be higher and close to one. Therefore, the signal decreases as it enters from above to the motion layer, and it increases again as it exits from the motion layer in each column. The MATLAB function "Findchangepts" is used to detect the location of these two significant changes in the signal, and two points are obtained that represent the water surface and the stationary bed, respectively.

   After applying this function on all columns and putting the points obtained from it together, two profiles related to water and stationary bed were generated.

9. **Delete wrong data**

   Since it is impossible to detect the motion in places where objects obstruct the camera's view (such as tapes mounted on the channel's body), the generated profiles have a lot of errors in these places. The erroneous data recorded in these places were selected and were deleted.

10. **Reference dataset**

    Due to the rotation that may exist in the taken images by the camera, all data should be referenced considering a reference line. This reference line is generated by the points with the same height and marked on the channel.

11. **Conversion**

    Next, a conversion factor should be specified to convert all data from the pixel scale to the metric scale. The conversion factor is obtained by dividing the monitoring channel length in pixel unit to the monitoring channel length in centimeter unit.

12. **Repeat steps 1 to 11**

    After that, the following two images are selected according to the jump value ($30\ frames\ (1\ second)$), and all the previous steps are repeated for them.

    By iteration until the last two frames chosen concerning step and jump value, the data set of the water and bed profiles are obtained for every second.

After these steps, all the previous steps have to perform again for the second camera image. As a result, it obtains two different sets of data related to each camera's water and bed profiles for every second.

13. **Regroup**

    The two data sets are connected from a chosen tape of the channel, which is $2.5\ cm$ long. By putting the two data sets together and regrouping them, the $2.5\ cm$ gap between them is obtained, which is already considered in the coordinates of each data set (the coordinates of the second data set starting from $2.5\ cm$ after the end of the first data set coordinates). In the final coordinates of the channel, this gap becomes as same as other tape locations in each data set that were deleted in step 9.

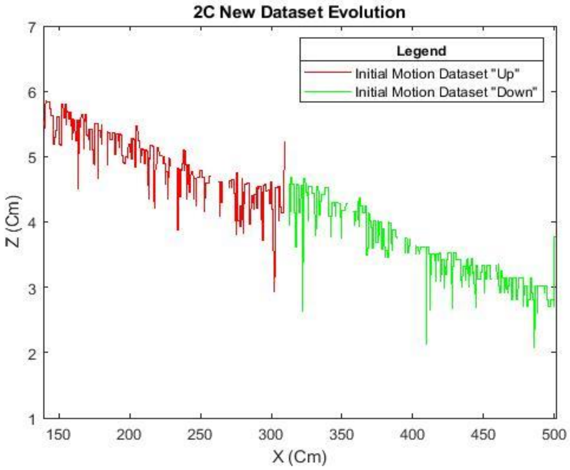

Figure 2-49 Obtained dataset after regrouping data

14. **"Filloutliers" function on the entire profile**

    The MATLAB function "Filloutliers" detects and replaces outlier data according to the "fill method" to deal with outlier data. The "fill method" used is "center," which replaces outlier data with the center value determined by the "Moving method." The "Move-median" moving method is defined for detecting local outliers according to a chosen window length. In this method, outliers are defined as elements more than three local scaled MAD from the local median over a window length. This method is also known as a Hampel filter. Also, a threshold is introduced, which defines outliers as points outside of the percentiles specified in the threshold. This threshold is a two-element row vector containing the lower and upper percentile thresholds.

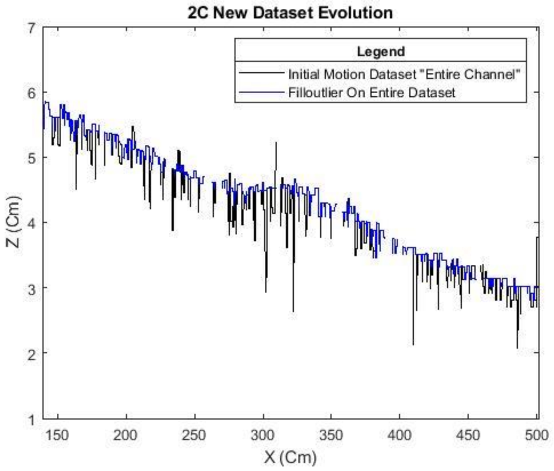

Figure 2-50 "Filloutlier" function on entire dataset of water profile (AE11_(2C_New))

15. "Smoothdata" function (rLowess)

The "Smoothdata" function is used to have a smoother profile and fill the blanks where the data is previously deleted after replacing the outlier data with the appropriate data. (See rLowess)

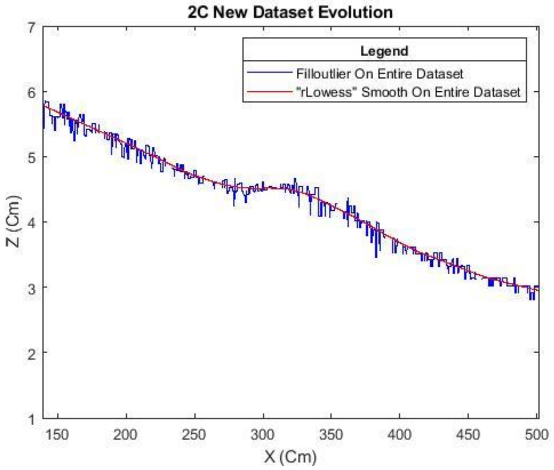

Figure 2-51 Apply "rLowess" smoothing function on entire dataset of water profile (AE11_(2C_New))

16. Repeat steps 13 to 15

After finding the water and bed profiles in the first two images, the following two images are selected according to the jump value ($30\ frames\ (1\ second)$), and all the steps are repeated for them.

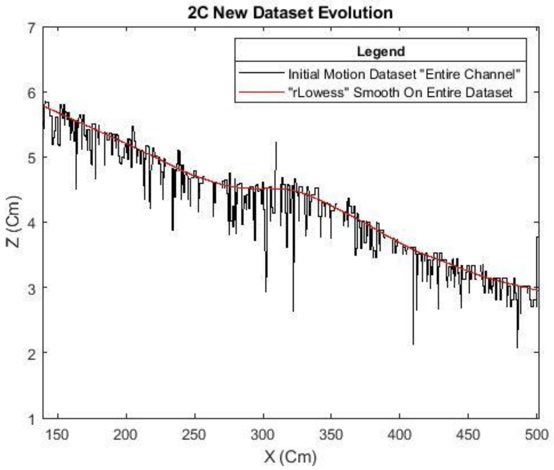

Figure 2-52 Generated profile from the initial dataset (AE11 _ (2C_New))

By iteration to the last frames concerning step and jump value, the water and bed profiles will be obtained for every second.

2.3.3.1.2 Comparison

To clarify the differences in modifications made in the experiments performed by two cameras, bed and water profiles which are resulted from two codes (new and old), are compared with each other below (Figure 2-53 and Figure 2-54). The results show a considerable gap between the profiles, particularly in the bed profile's upstream, downstream, and middle. Furthermore, it should be noted that water profiles have changed at different times but not significantly.

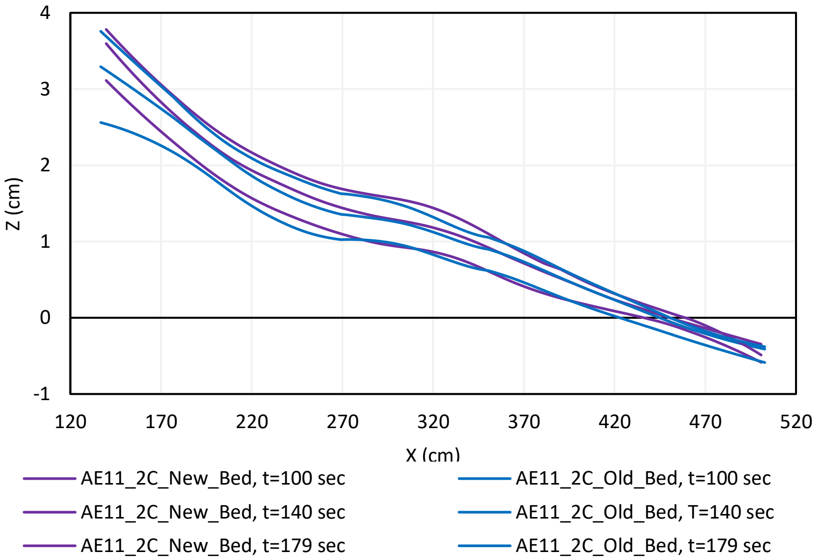

Figure 2-53 Comparison between bed elevation profiles obtained from old code and new code for two cameras

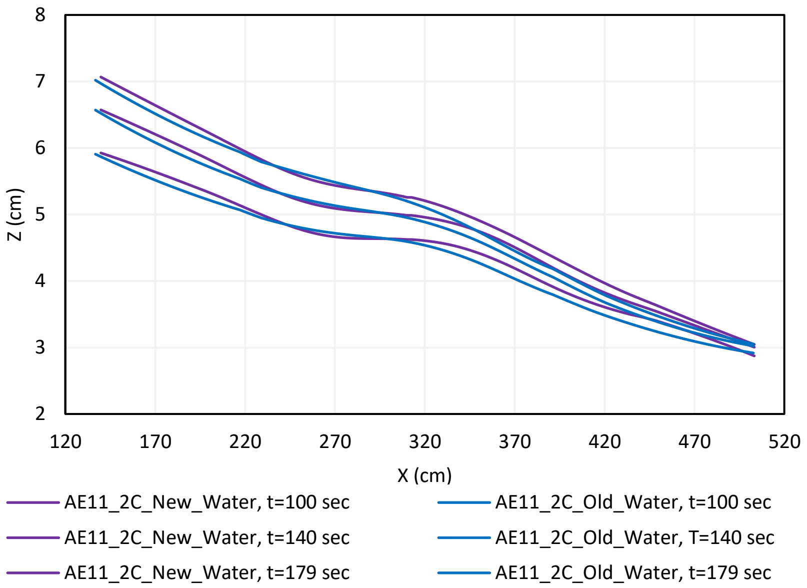

Figure 2-54 Comparison between water surface elevation profiles obtained from old code and new for two cameras

2.3.3.1.3 Advantages

The advantages of using the new code in two cameras can be divided into two general groups, which include:

- More accuracy in detecting and producing the required profiles.
- Reduction in computational cost and user dependency.

The following are some of the factors in various stages of the process that have led to mentioned benefits:

- Using the Removal Fisheye algorithm, provided by the manufacturer of used cameras and compatible with them, will result in less distorted images, so the produced profiles will be more accurate than before. Also, there is no need to calibrate the coefficients related to the undistorted algorithms by the user in different experiments.
- To deal with the objects that obstruct the cameras' view, wrong data intervals are selected to be deleted. While in the old code, the "Filloutlier" function was used to deal with the erroneous data of these locations. Using this function, the incorrect data of these locations will not get a good effect from the neighboring data. However, they will affect the adjacent data and ultimately reduce the accuracy of the final profile. Also, applying this function to the images of each camera has a higher computational cost than deleting them.
- In the old code, the moving average filter was used to smooth the data, while in the new code, the "rLowess" method is used to smooth the data, which is a more helpful method for processing the experimental data. (See 2.3.2.1.1- Smoothing method). Using this smoothing method gives more accurate profiles.
- In the old code, in addition to using the "Filloutlier" function to deal with places where objects were obstructing the camera's view, another "Filloutlier" function was used to

deal with outlier data by the Smooth Data function. All the relevant processes and finalization of each camera's images were done separately. The final processed data and profiles of each camera were put together to make the last profile, which was one of the main reasons for obtaining a step in the last profile in the previous thesis. Whereas in the new code, after deleting the data related to the places where the objects are obstructing the cameras' view, the data set taken from each camera is referenced and placed next to each other, forming a final data set and process and the required functions are applied homogeneously on the last dataset.

- This method makes the final profile more accurate, especially in important places such as the middle, upstream and downstream compared to the old code; also, it prevents the creation of the step in the profile. The stages for applying the functions and processes for finalizing the profile are applied to a single final data set, rather than being done separately on each camera dataset, resulting in lower computational costs.

2.3.3.2 Newly modified motion-based method performed by one camera (1C_N)

In contrast with two camera which able to address some of mentioned errors, all innovations and solutions mentioned to deal with errors can be applied to experiments performed by one camera.

2.3.3.2.1 Procedure

1. **Frame extraction**

   After extracting the video frames, the images are cropped and are converted to grayscale (Figure 2-55).

Figure 2-55 The extracted frame that converted to grayscale

2. **Frame selection:**

   Same as step 3 for 2C_N

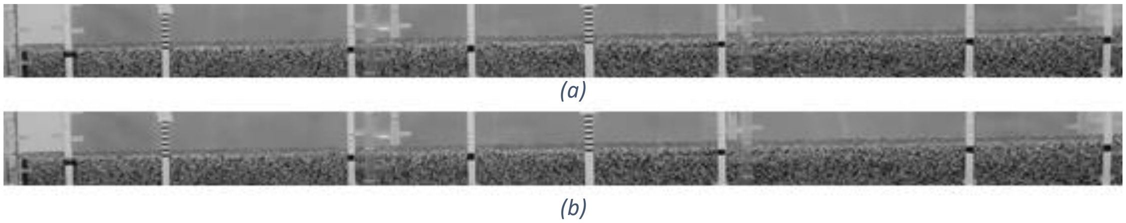

(a)

(b)

Figure 2-56 (a) Frame number 4511 of AE13 (b) Frame number 4512 of AE13

3. **“Gaussian” Filter:**

   Same as step 4 for 2C_N

4. **Subtraction:**

   Same as step 5 for 2C_N

5. **Define threshold and binarization:**

   Same as step 6 for 2C_N

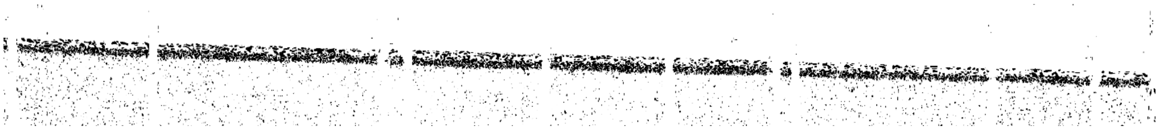

Figure 2-57 Binary image

6. **Signal production:**
   To find this motion layer's top and bottom boundary, a moving window with chosen dimensions (in this case, $5 \times 20\ pixels$) is defined. This window starts moving, pixel by pixel, from the top-left corner of the image to the bottom of the first column and calculates the average intensity of the pixels fitted inside. Then, the window shifts by a pixel to the right and moves downward again. As a result, a signal is produced for each column that shows the average intensity amount for each row of the column. This process continues until covering all of the columns.
7. **"Findchangepts" function:**
   Same as step 8 for 2C_N

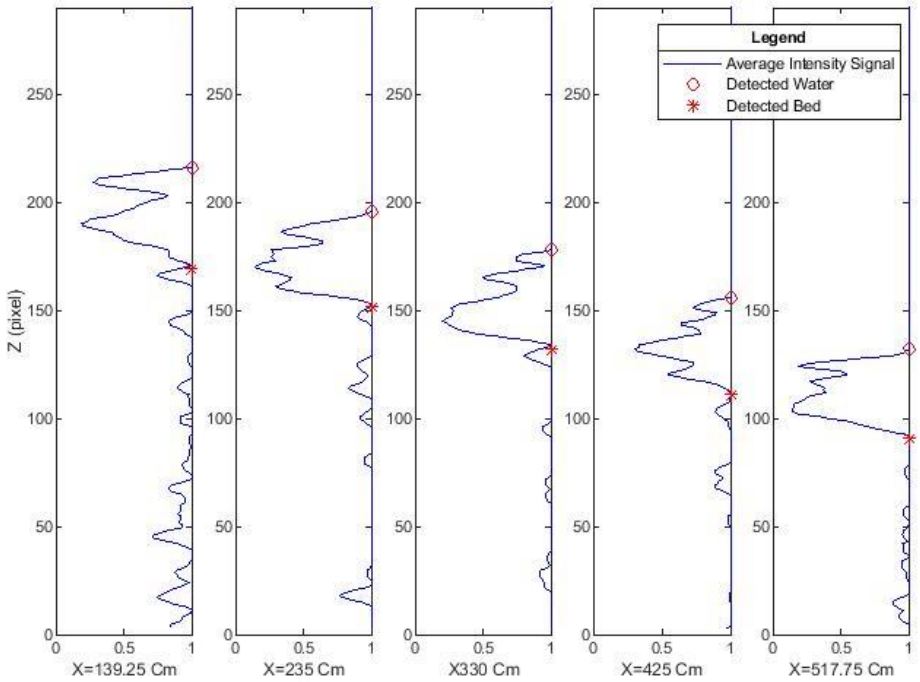

Figure 2-58 Produced intensity signals P(i) in different locations and position of detected bed and water level

8. **Delete incorrect data:**
   Same as step 9 for 2C_N

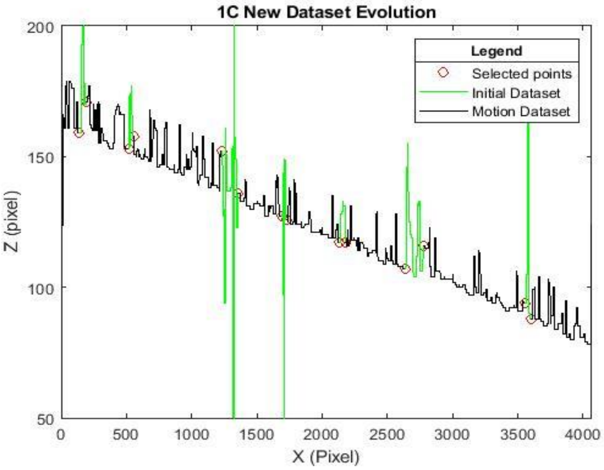

Figure 2-59 Initial motion data obtained after deleting the wrong data intervals of water profile (AE14 _ (1C_New))

9. "Filloutlier" function

Same as step 14 for 2C_N

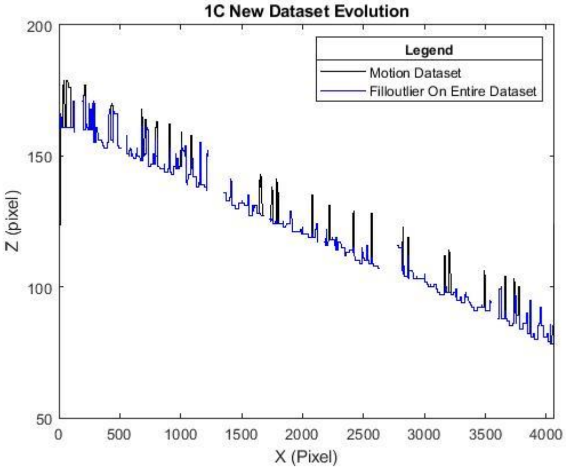

Figure 2-60 Apply "Filloutlier" function on entire dataset of water profile (AE14 _ (1C_New))

10. "Smoothdata" function (rLowess):

Same as step 15 for 2C_N

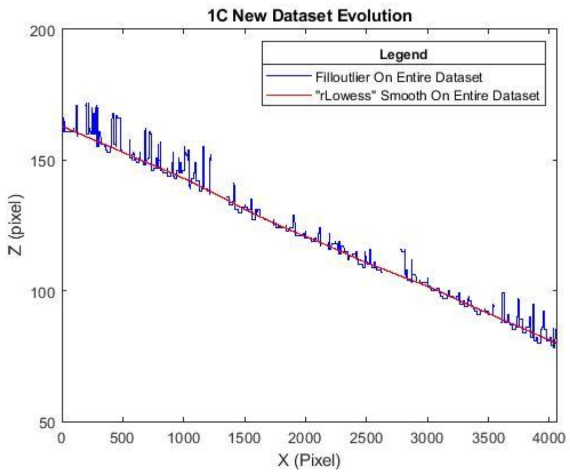

Figure 2-61 Apply "rLowess" smooth function on entire dataset of water profile (AE14 _ (1C_New))

11. Reference dataset:
Same as step 10 for 2C_N

12. Conversion:
Same as step 11 for 2C_N

13. Repeat steps 1 to 12:
After finding the water and bed profiles in the first two images, the following two images were selected according to the jump value ($30\ frames\ (1\ second)$), and all the steps were repeated for them.

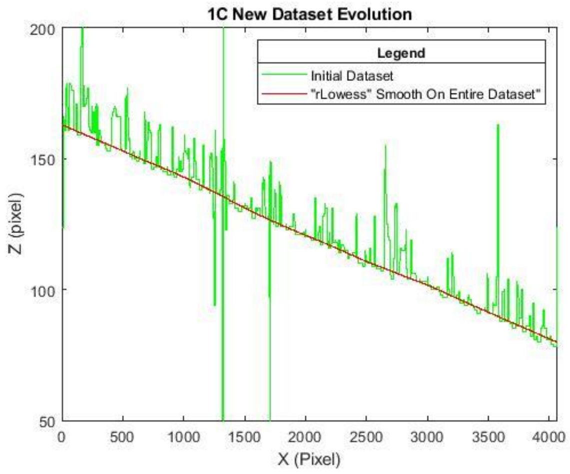

Figure 2-62 Generated profile from the initial dataset (AE14 _ (1C_New))

By iteration to the last frames concerning step and jump value, the water and bed profiles will be obtained for every second.

2.3.3.2.2 Comparison

Bed and water profiles resulting from one camera with two various code (new and old) are compared below (Figure 2-63 and Figure 2-64) to highlight the differences. The results show a large gap in upstream, downstream, and middle of sediment and water surface profile.

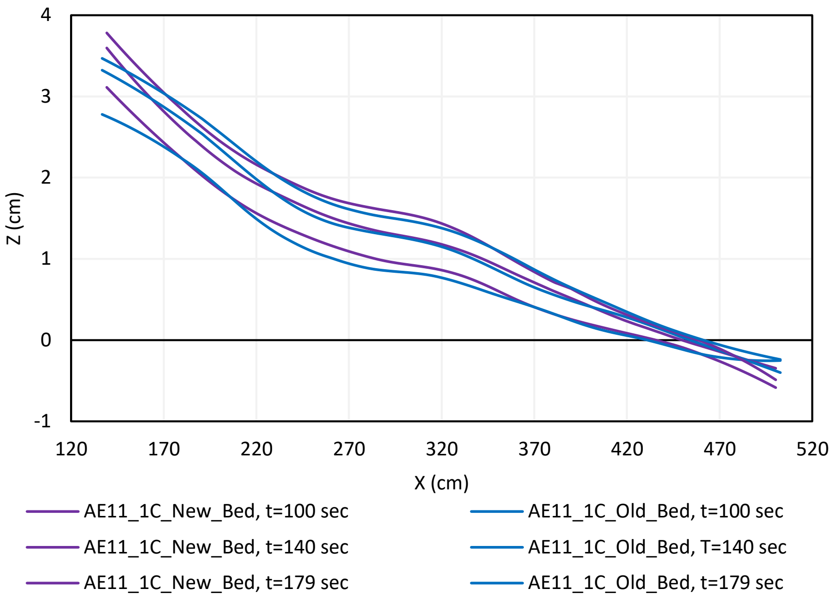

Figure 2-63 Comparison between bed elevation profiles obtained from old code and new code for one camera

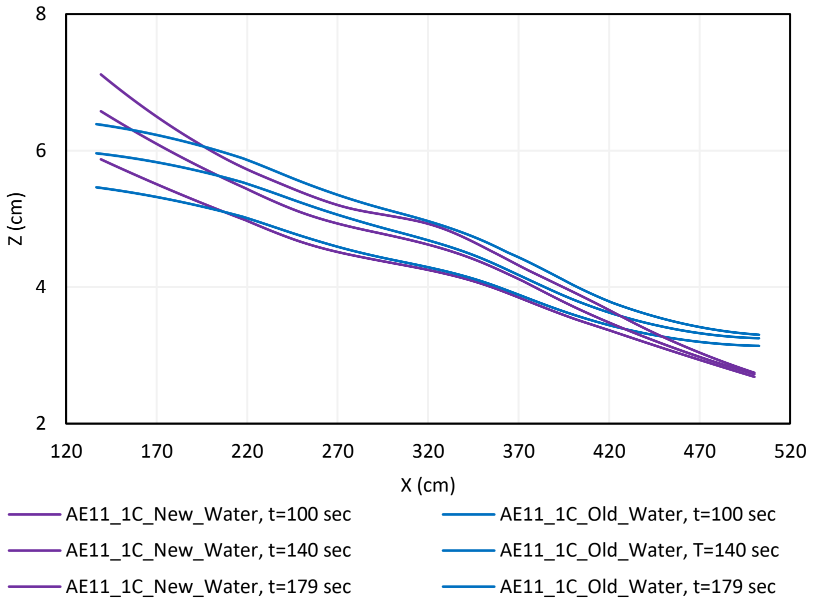

Figure 2-64 Comparison between bed elevation profiles obtained from old code and new code for one camera

2.3.3.2.3 Advantages

This method, in addition to the benefits listed in 2.3.3.1.3, also includes the following advantages:

- There is no need to undistort the images with one linear camera for the entire channel. This step was time-consuming, which was previously performed twice (separately for each camera) for the whole duration of the test and all the frames. The removal of this step significantly reduces the computational cost. Therefore, the distortion correction process steps of all frames for two separate cameras are removed.

- Motion detection is done for images of only one camera instead of two separate cameras, leading to more homogeneous results.
- There is a step where the user must manually select the appropriate longitudinal intervals. This step is done only once instead of for each camera using one camera.
- Finding the best coefficients and required windows needed for image processing, applying functions, and bed detection, are chosen and applied only once due to images related to one camera. While with two cameras, coefficients and windows must be selected and applied for each camera separately.
- With two cameras, after applying different functions and motion detection for a dataset of each camera, to have one final profile, there is a step, for bed and water separately, called "regroup data," which connects the output processed data from each camera.
- In the case of using one camera, since motion detection and applying functions are performed using one single dataset from one camera, this step, which was performed separately for water and bed, has been eliminated. Also, by deleting this step, the errors related to this step, which was one of the main reasons for creating a step at the junction of the two profiles, are eliminated.

2.3.4 Validation

Due to the code modification and other changes, profiles are adapted, as mentioned above, in some particular parts. The results are evaluated in two main ways to ensure that the new code and applied changes work correctly.

2.3.4.1 Recording the ruler level on the tapes by image

In this way, the height of the water is read and recorded from the photos. At different times and places, water elevation can be seen from the ruler stock to PVC glass (Figure 2.3). It should be mentioned that just the elevation of the water profile in a different place can be recognized in this method. Figure 2-65 shows the differences between water profiles found by image processing and reading points. It is clear that the new code and new modification have good compatibility with reading points.

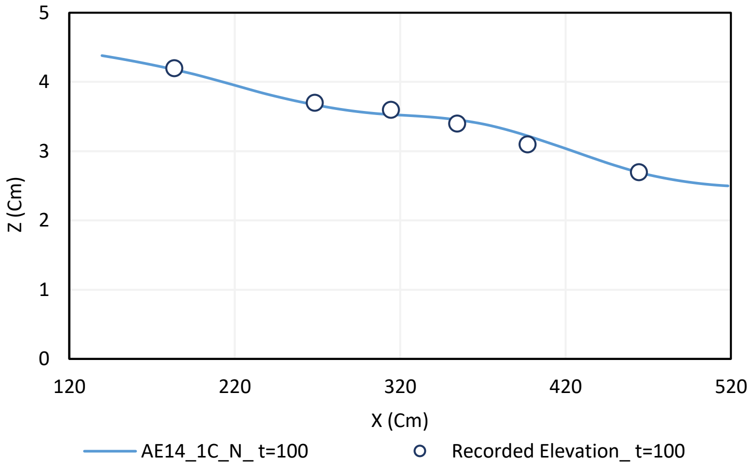

Figure 2-65 Validation by recorded water levels and generated profile (AE14_ t=100 sec)

Also, the mean square error values are calculated by Equation 2-8. Its results are provided in Table 2-4 Mean Square Error of generated water profiles and recorded water levels by images (AE14) to support the compatibility between generated water profiles and recorded water levels by images.

$$Mean\ square\ error = \frac{1}{N}\sum_{i=1}^{N}(Y_i - Y'_i)^2 \qquad \text{Equation 2-8}$$

Where, N is the total number of data, Y_i is the ith generated water profile, and Y'_i is the ith recorded water levels by images.

Table 2-4 Mean Square Error of generated water profiles and recorded water levels by images (AE14)

TIME	$t = 20\ sec$	$t = 60\ sec$	$t = 100\ sec$	$t = 140\ sec$	$t = 180\ sec$	$t = 240\ sec$
MEAN SQUARED ERROR (cm^2)	0.011	0.012	0.004	0.006	0.012	0.020

2.3.4.2 Recording the ruler level on the tapes by person

In the second way, the experiment AE12 is performed with three cameras (one camera and two cameras simultaneously) to evaluate the new method and code. Before starting the experiment, three rulers were installed at the flume's upstream, middle, and downstream. An attempt was made that three people simultaneously record the water and bed levels from each ruler to compare the recorded levels with new method results. It should be mentioned that this method may consist of a bit of error since every person may recognize different points as a bed and water. The results illustrate that the profiles are harmonized with these points, particularly at the first and end of the channel, either for sediment or water.

Figure 2-66 Read and record the bed and water level by a person (AE12_t=160 sec)

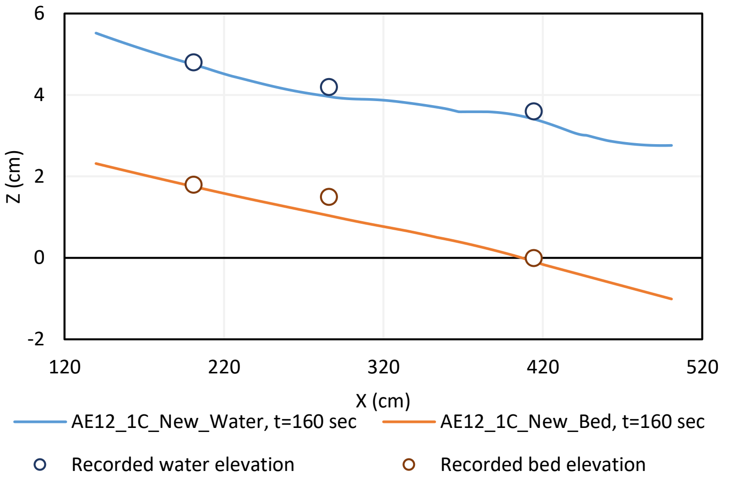

Figure 2-67 Validation by recorded water and bed levels by person and generated profiles (AE12 _t=160 sec)

Also, the mean square error, using Equation 2-8, shows the reasonable values for this validation (Table 2-5).

Table 2-5 Mean Square Error of generated bed and water Profiles and read levels by the person (AE12 _t=160 sec)

$T = 160\ sec$	BED	WATER
MEAN SQUARED ERROR (cm^2)	0.044	0.013

2.4 Calculation of initial sediment transport capacity

Sediment transport capacity can be defined as the maximum sediment passing through a specific river section. This parameter is a function of the flow properties, physical properties of the channel, and sediment material properties. Furthermore, this is vital to find this parameter since it can be employed to describe the aggradation and degradation process in the riverbed. Aggradation occurs when the sediment inflow discharge in a specific section exceeds its sediment transport capacity. In degradation, the process is happening inversely. Also, the equilibrium condition occurs when the sediment inflow discharge Q_{sin} is equal to the initial sediment transport capacity Q_{s0}. The Loading ratio Lr can be defined as the ratio between the sediment inflow discharge Q_{Sin} and the initial sediment transport capacity Q_{s0}.. (Equation 2-9)

$$Lr = \frac{Q_{Sin}}{Q_{S0}}$$ *Equation 2-9*

Where, Q_{S0} is the initial sediment transport capacity and Q_{Sin} is sediment inflow discharge. In this campaign, it is essential to mention that it is tried to find sediment transport capacity in initial times since the bed is not influenced by aggradation.

In this thesis, three different methods are used for finding the value of the initial sediment transport capacity Q_{S0}.

1. Meyer-peter and Müller formula (MPM formula)
2. Collector method
3. Continuity method

2.4.1 Meyer-Peter and Müller formula (MPM formula)

As discussed in 1.3, the Meyer-Peter formula is one of the most useful formulas for estimating sediment transport capacity. (Equation 2-10)

$$\Phi = 8(\tau^* - {\tau_c}^*)^{1.5}$$ Equation 2-10

Where, Φ is non-dimensional solid discharge per unit width, $\tau^*$is Shields parameter, and ${\tau_c}^*$ is critical Shields parameter and there are two methods to evaluate the value of the critical shields number. First, Using the Shields diagram directly as a function of the shear Reynolds number (Figure 1-2). Second, transforming Shields diagram as a function of the dimensionless grain diameter D^* (${\tau_c}^* = f(D^*)$).

There are various formulae to transform the Shields diagram and estimate ${\tau_c}^*$ as a function of D^*. In the presented work, two formulae are used to calculate ${\tau_c}^*$, the Brownlie (1981) formula, and the Van Rijn (1984) formula.

- **Brownlie approach to estimate the critical Shields parameter**
  In this approach, the following formula is used to calculate the critical Shields parameter, ${\tau_c}^*$:

$$\tau_c^* = 0.22{D^*}^{-1} + 0.06e^{-17.77{D^*}^{-1}}$$ Equation 2-11

$$D^* = d\left(\frac{(\rho_s - \rho)g}{\rho \nu^2}\right)^{1/3}$$ Equation 2-12

  Where, D^* is the dimensionless grain diameter, d is the diameter of the sediment material which in this work is equal to $0.0038\ m$, ρ_s is the material density which is equivalent to $1443\ kg/m^3$, ρ is the water density which is $1000\ kg/m^3$, ν is the water kinematic viscosity, equal to $1 \times 10^{-6}\ m^2/s$.

  By using the above values, the dimensionless grain diameter is equal to 62, and consequently, the critical Shields parameter is obtained equivalent to:

$$\tau_c^* = 0.0486$$

- **Van Rijn approach to estimate the critical Shields parameter**
  In this approach, different equations have been proposed to estimate the critical Shields parameter, depending on the value of the dimensionless grain diameter (Equation 2-13).

$$\begin{cases} \tau_c^* = 0.24{D^*}^{-1} & for \quad 1 \le D^* \le 4 \\ \tau_c^* = 0.14{D^*}^{-0.64} & for \quad 4 < D^* \le 10 \\ \tau_c^* = 0.04{D^*}^{-0.1} & for \quad 10 < D^* \le 20 \\ \tau_c^* = 0.013{D^*}^{0.29} & for \quad 20 < D^* \le 150 \\ \tau_c^* = 0.055 & for \quad D^* > 15 \end{cases}$$ Equation 2-13

where D^* is calculated using Equation 2-12, similarly to the previous method. Since in this work D^* was calculated to equal to 62, the following equation would be valid to estimate τ_c^*:

$$\tau_c^* = 0.013{D^*}^{0.29} \qquad \text{Equation 2-14}$$

Substituting $D^* = 62$ in this formula, the critical Shields parameter is obtained equal to:

$$\tau_c^* = 0.043$$

The other important parameter in the MPM formula is the Shields parameter, τ^*, which is computed using Equation 2-15 (presented in chapter 1.5.1):

$$\tau^* = \frac{\tau}{(\rho_s - \rho)gd} \qquad \text{Equation 2-15}$$

Where, τ is the bed shear stress and is calculated using Equation 2-16:

$$\tau = \rho g R_H S_f \qquad \text{Equation 2-16}$$

Where R_H shows the hydraulic radius and S_f represents the friction slope and can be calculated using Equation 2-17.

$$S_f = \frac{n^2 \times U^2}{R_H^{4/3}} \qquad \text{Equation 2-17}$$

In this formula, U is the velocity of the flow, and $n = 0.015\ s/m^{1/3}$ is the Manning's coefficient n, obtained experimentally by Unigarro (Unigarro Villota, 2017) with performing multiple tests in uniform flow.

Having the values of the critical Shields parameter and calculation of the Shields parameter, now the non-dimensional solid discharge (Φ can be calculated applying the MPM formula (Equation 2-10). By obtaining Φ, the initial sediment transport capacity of the channel (Q_{s0}) Can be computed using Equation 2-18.

$$Q_{s0,MPM} = Bq_{s0} \qquad \text{Equation 2-18}$$

Where, B is the width of the channel and equal to 0.3 m in this work and q_{s0} = sediment transport capacity per unit width, which is calculated as follows:

$$q_{s0} = \Phi\sqrt{g\left(\frac{\rho_s - \rho}{\rho}\right)d^3} \qquad \text{Equation 2-19}$$

2.4.2 Collector method

During experimental work and based on different parameters such as water discharge and sediment feeding ratio, a volume of sediment is transported through the channel. These numbers of sediments are trapped inside the collector installed downstream of the channel. The volume of sediments in the collector should be measured at different times to calculate the channel's initial sediment transport capacity. The collector manual method is used to calculate this volume of sediment trapped.

After extracting the frames, changing the color scale into grayscale, and removing the distortion, different points on the edge of the sediment are selected to extract their coordinates in pixel scale. These points should be chosen so that the polygon created by these points can almost represent the shape of sediments accumulated inside the collector. (Figure 2-68)

Figure 2-68 Polygon is provided to spot the volume of sediment

After extracting the coordinates of the points, the area of the polygon as mentioned above can be calculated through Equation 2-20.

$$A = \frac{(x_1 \times y_2 - x_2 \times y_1) + (x_2 \times y_3 - x_3 \times y_2) + \cdots + (x_n \times y_1 - x_1 \times y_n}{2} \qquad \text{Equation 2-20}$$

Where A is polygon's area, and x_n and y_n are the x-coordinate and y-coordinate of the point number n.

The obtained area is pixel scale, so it must be converted into a metric scale through a conversion factor. Now that the area of the sediments seen in the picture is available, one can find the apparent volume by multiplying this area into the width of the collector (0.3 m). After finding the cumulative volume in each step (every five seconds), this value will be changed to the sediment transport capacity $Q_{S,collector}$, calculated from t_0 to t (t can be different depending on trial's elongation) using Equation 2-21.

$$Q_{s,collector} = \frac{V(t)_{measured\_collector} \times (1-p)}{t}$$

Equation 2-21

The initial sediment transport capacity of the channel $Q_{S0,collector}$ is the mean value of sediment transport capacities found from the top equation at the initial time. The mean value of $Q_{S0,collector}$ is counted when $Q_{S,collector}$ is somehow constant in a particular time interval, and the bed is not affected significantly by the aggradation phenomenon.

Figure 2-69 shows terms $V(t)_{measured\_collector} \times (1-p)$ and $Q_{S0,collector}$in different times where p is porosity. By averaging the calculated $Q_{S,collector}$ between times t_1 and t_2 (red rectangle), where the values of the $Q_{S,collector}$ are almost constant, the initial sediment transport capacity of the channel, $Q_{S0,collector}$, can be found.

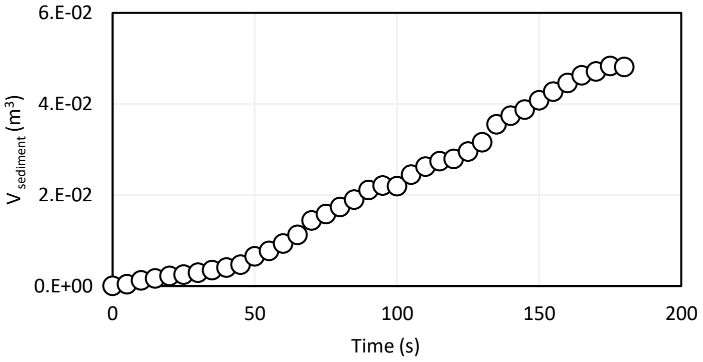

(a)

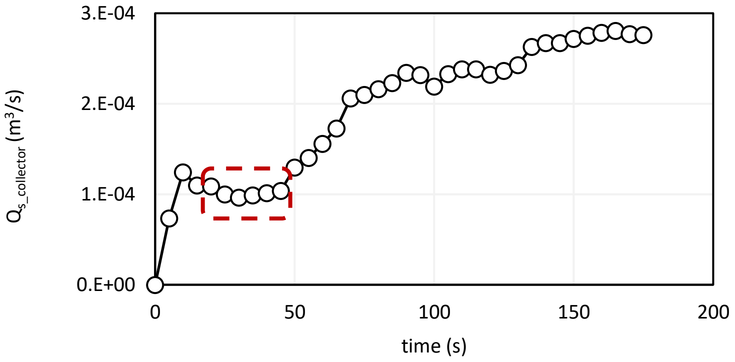

(b)

Figure 2-69 (a) Temporal evolution of sediment volume in collector method (b) Temporal evolution of sediment transport capacity in collector method

In this thesis, these two times (t_1 and t_2) are used in continuity method discussed in 2.4.3.

2.4.3 Continuity method

This method is used to calculate the initial sediment transport capacity of a channel. Based on the spatial sediment profiles at different times, the volume of sediment can be calculated by Equation 2-22.

$$V(t)_{measured\_bed} = A(t)_{bed} \times B \qquad \text{Equation 2-22}$$

Where $A(t)_{bed}$ is the side area of a depositional wedge, t is time and B is the width of the channel.

Like previous work, since the bed profiles are monitored starting at $x = 139.25\ cm$, the sediment volume deposited between the position of sediment inlet ($x = 25\ cm$) and the first coordinate of the monitored profile ($x = 139.25\ cm$) ($\Delta x = 114.25\ cm$) cannot be calculated. Therefore, two different scenarios are considered in these steps. These scenarios are like those used in previous works (Eslami et al.,2021). In the first scenario, which is called the "Constant Upstream" (CU) scenario, the bed elevation in the missing part is constant and equal to the bed elevation at $x = 139.25\ cm$ so that the slop would be equal to zero, and the second scenario that called "Inclined Upstream" (IU) scenario in which it is assumed that the bed elevation in the missing reach linearly increases, and the slope is equal to the same slope of the same interval ($\Delta x = 114.25\ cm$) after the missing reach from $x = 139.25\ to\ x = 253.5\ cm$. (Figure 2-70)

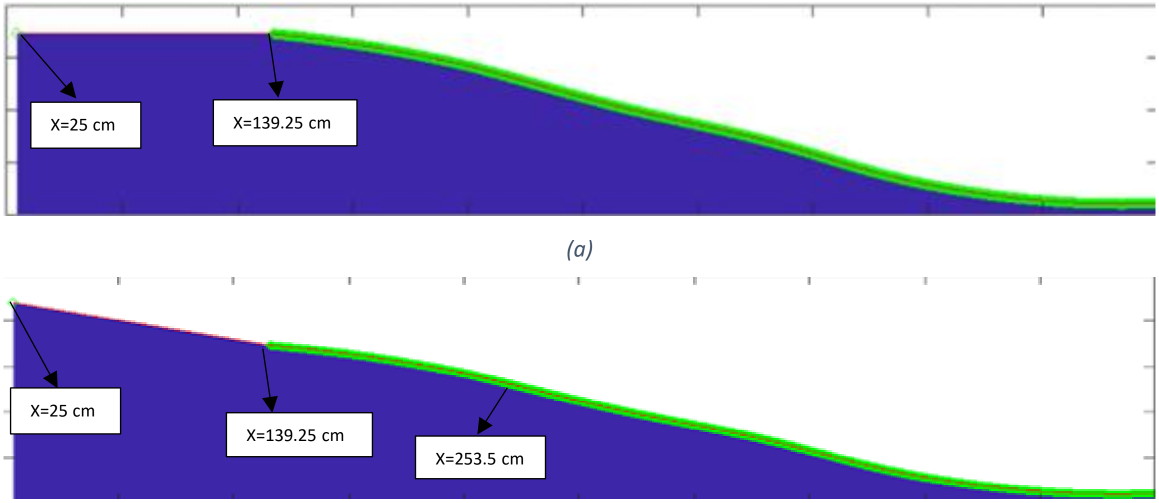

(a)

(b)

Figure 2-70 Different scenarios for volume calculation (a) "CU" scenario (b) "IU" scenario

By knowing $V(t)_{measured\_bed}$ at each time step and the sediment feeding rate Q_{sin}, the sediment transport capacity is illustrated as below.

$$Q_{s0,continuity} = Q_{sin} - m \times (1-p) \qquad \text{Equation 2-23}$$

Where:

$$m = \frac{\mathrm{d}V_{measured\_bed}}{\mathrm{d}t} \qquad \text{Equation 2-24}$$

Where m represents the slope of a linear function that is fitted to the values of $V(t)_{measured\_bed}$ in time, since the values of $V(t)_{measured\_bed}$ related to the initial times of the experiment must be considered in the calculations, time is a vital issue. Therefore, based on t_1 and t_2, which are highlighted in the collector method (2.4.2), two different scenarios are defined to obtain m and evaluate the initial sediment transport capacity of the channel; the first one is $0 - t_2$, and the second one is $t_1 - t_2$. (Figure 2-71)

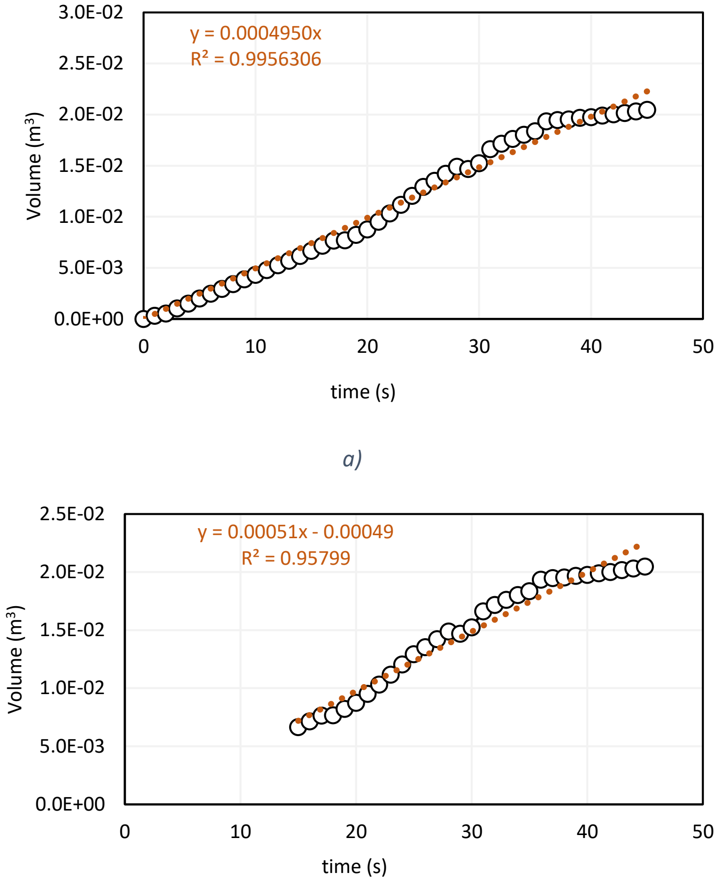

a)

b)

Figure 2-71 Two different scenarios considering time interval a) first scenario b) second scenario

Therefore, there would be two scenarios and four final different approach: IU1-CU1 and IU2-CU2. (Table 2-6)

Table 2-6 Four Final different considered scenarios for monitoring method

SCENARIOS		SLOPE	TIME
SCENARIO 1	IU 1	Inclined slope	time $0 - t_2$
	CU 1	Constant slope	time$0 - t_2$

SCENARIO 2	IU 2	Inclined slope	time $t_1 - t_2$
	CU 2	Constant slope	time $t_1 - t_2$

It is worth mentioning that the IU1 and CU1 scenarios are not reliable, because these scenarios consider the start of the experiment ($t = 0$) instead of the first time selected from the temporal evolution of sediment transport capacity in collector method (t_1) (See 2.4.2). Furthermore, based on this fact that the profiles on initial times of experiments are not reliable, the slope of the temporal evolution of volume at these times are different from reality.

2.4.3.1 Validation

As mentioned in the previous part, profiles possess some changes, particularly in the downstream and upstream and middle, due to the code modifications. To ensure that the monitoring method is not sensitive to code and experimental set up modification, the experimental numbers AE6, AE07, and AE08 from (Eslami et al., 2021) are redone (Figure 2-72) The results show that modification did not change the outcomes, and they are close.

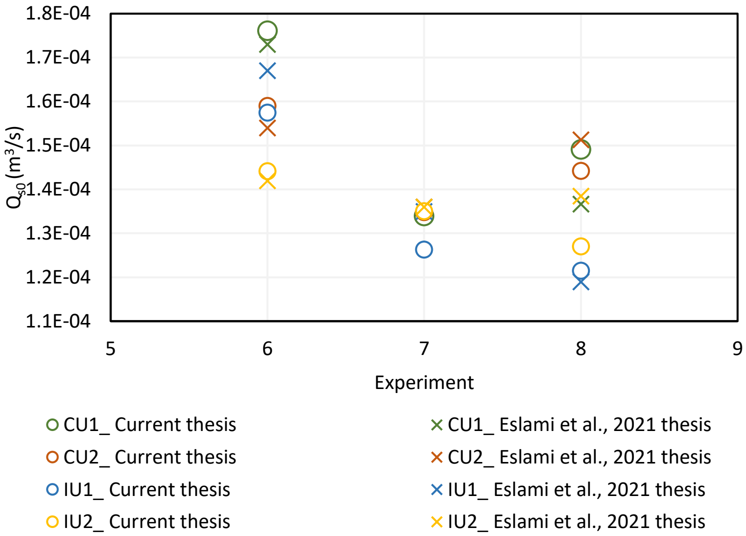

Figure 2-72 Sediment initial transport capacity for AE6, AE7, and AE8

2.5 Estimation of the celerity

The term “celerity” is used for the sediment front velocity of migration. When the flow speed is not high like subcritical flow, monitoring sediment front is possible, and in this situation, sediment front has a translating type. In contrast, monitoring sediment front is not possible yet in flow with high velocity such as supercritical flow and dispersive. Since the type of flow in this thesis is supercritical, the latter is happening. Some relations are employed to spot celerity. These relations are introduced in Figure 2-73.

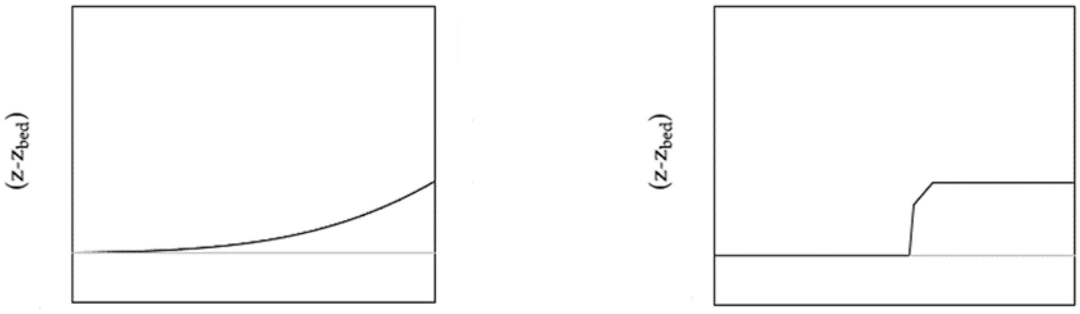

(a) *(b)*

Figure 2-73 Schematic representation of the two types of sediment front (Zanchi,2018) (a) Dispersive type (b) Translating type

In this work, two different methods are used to show the celerity in supercritical flow. The first one is related to calculating celerity locally, and the second one is belonged to solving the Equation 1-27 theoretically discussed as below.

$$A'(U) = \frac{\partial F(U)}{\partial U} + H(U) = \begin{bmatrix} 0 & 1 & 0 \\ -\frac{q^2}{h^2} + gh & 2\frac{q}{h} & gh \\ \frac{1}{1-p}\frac{\partial q_s}{\partial h} & \frac{1}{1-p}\frac{\partial q_s}{\partial q} & 0 \end{bmatrix}$$ *Equation 1-27*

2.5.1 Local celerity C equation

A definition of celerity can be used for finding this parameter based on spatial and temporal evolutions of sediment profile. As mentioned previously, in supercritical flow, the speed of sediment profile evolution in the length of the channel is different from the speed of evolution in time. (Figure 2-74) Therefore, it could be quite beneficial to use Equation 2-25 to spot celerity.

$$C = -\frac{\frac{\partial z}{\partial t}}{\frac{\partial z}{\partial x}}$$ *Equation 2-25*

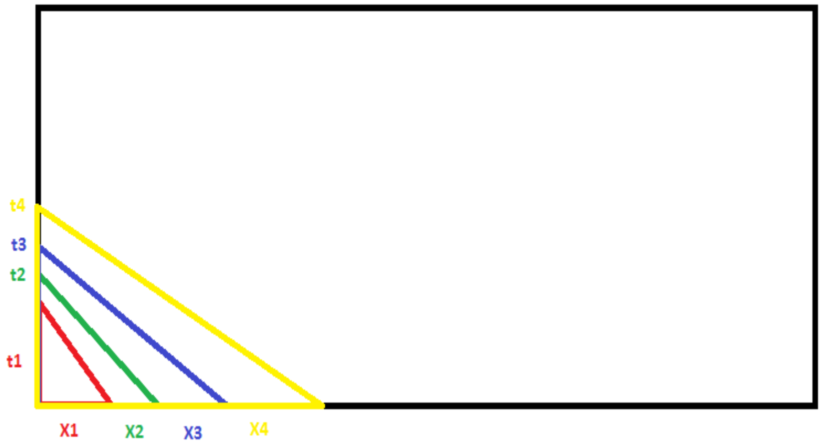

Figure 2-74 Evolution of slope in time and length

The finite element method is used to solve this equation for the supercritical flow. The discrete form of this equation would be as Equation 2-26.

$$\Delta \boldsymbol{C} = -\frac{\frac{\Delta \boldsymbol{z}}{\Delta \boldsymbol{t}}}{\frac{\Delta \boldsymbol{z}}{\Delta \boldsymbol{x}}}$$

Equation 2-26

It should be mentioned that two different matrices can be used for calculating celerity.

- Bed aggradation matrix: This matrix is related to the temporal and spatial evolution of bed aggradation absolute value
- Bed elevation matrix: This matrix is related to the temporal and spatial evolution of bed elevation, which means obtained results by motion bed detection are referenced concerning the slope.

However, because of time shortage, the second one is chosen for evaluating the celerity in the current thesis, and the first one can be done in future work.

So as mentioned, the matrix of sediment profile (Bed elevation matrix) in different times and locations is needed as an input to solve this equation. In this matrix, every column is spatial sediment profile at each time (t), and every row is temporal evolutions of sediment profile in each location in the x-direction.

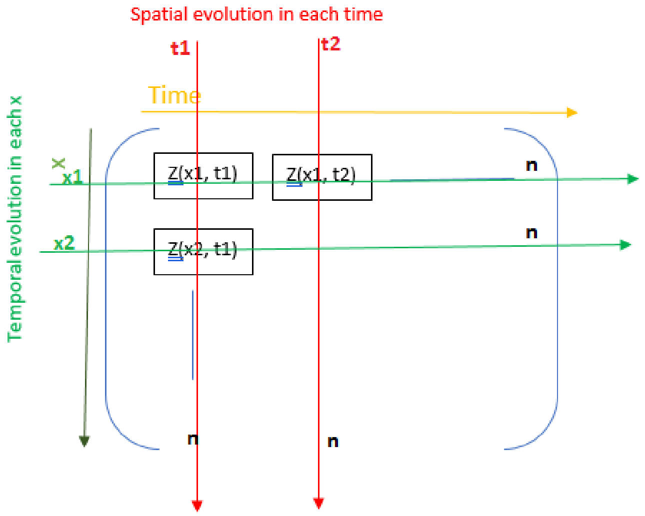

Figure 2-75 Schematic representation of sediment profile matrix

Equation 2-26 is divided into two equations to solve it more straightforwardly. Moreover, the forward finite difference method is used for discretization. Therefore, as evidenced below, Equation 2-27 solves the equation column by column, and Equation 2-28 solves it row by row.

$$\frac{\Delta z}{\Delta t} = \frac{z_{(xn,t2)} - z_{(xn,t1)}}{t_2 - t_1}$$

Equation 2-27

$$\frac{\Delta z}{\Delta x} = \frac{Z_{(X2,tn)} - Z_{(X1,tn)}}{X_2 - x_1}$$ Equation 2-28

In this way, each term has a matrix form, and by dividing the matrixes, each element by each element, the celerity matrix can be provided.

$$C = -\frac{Equation\ 2.16}{Equation\ 2.17}$$ Equation 2-29

A color map can be provided to show the celerity in each part of the channel, which illustrates the changes of celerity in various times and locations. It should be mentioned that the x and y-axis are based on the number of rows and columns.

2.5.2 Celerity based on eigenvalues λ

Eigenvalue analysis and approximation can approximate celerity (explained in 1.2.1). As mentioned previously, three eigenvalues λ can show the value of celerity of water and sediment. (Equation 2-30, Equation 2-31, and Equation 2-32)

$$\lambda_1 = \mathrm{u} + c$$ Equation 2-30

$$\lambda_2 \cong \frac{u}{1 - Fr^2}(\frac{1}{h}\frac{\partial q_s}{\partial u} - \frac{1}{u}\frac{\partial q_s}{\partial h})$$ Equation 2-31

$$\lambda_3 = \mathrm{u} - c$$ Equation 2-32

Where $Fr = u/\sqrt{gh}$ is the Froude number Fr, $c = \sqrt{gh}$ shows hydrodynamic wave celerity, $q = u \times h$ is unit flow discharge, h shows the water depth, u is the depth-averaged velocity, and q_s is sediment discharge.

Considering Equation 2-33, the q_s is a function of (u, h) so the term$(\frac{\partial q_s}{\partial u}, \frac{\partial q_s}{\partial h})$ can be calculated directly:

$$q_s(q,h) = 8\sqrt{g(s-1)d_{50}^3}\left(\frac{n^2 q^2}{(s-1)d_{50}h^{7/3}} - 0.047\right)^{3/2}$$ Equation 2-33

Where, n is the Manning's coefficient, $s = \rho_s/\rho_w$ shows the relative sediment density, and d_{50} denotes the median grain diameter.

Like the previous part, the initial input is a matrix of spatial and temporal evolution for sediment profiles. By using above formula, all the parameters can be calculated in matrix form. After finding λ_1, λ_2, and λ_3, the results can be shown as color gradian maps. The results will be discussed in **Error! Reference source not found.**.

2.6 Numerical Simulation

In general, numerical models are defined to relate the obtained experimental results to theoretical concepts, which causes the achievement of quantitative results. The final goal is to verify a concord between numerical simulation results and experimental results. Based on the degree of this compliance, the ability of the numerical model to predict the results can be determined. This adaptation can be increased by calibrating the numerical model with some parameters. Finally, when there is convenient accordance between the results, the numerical model can be used as a simulative tool in impracticable physical modeling.

2.6.1 Hydro-morphologic model and numerical solver used

For performing unsteady 1-D hydro-morphologic modeling of water surface and bed elevation, two Saint-Venant equations (SVEs), which contain the mass conservation and momentum of water, and one Exner equation, which demonstrates the sediment continuity (see 1.3), are used as the governing flow equations. (Equation 1-24)

$$\begin{cases} \dfrac{\partial h}{\partial t} + \dfrac{\partial q}{\partial x} = 0 \\ \dfrac{\partial q}{\partial t} + \dfrac{\partial}{\partial x}\left(\dfrac{q^2}{h}\right) + gh\left(\dfrac{\partial h}{\partial x} + \dfrac{\partial z_b}{\partial x}\right) = -ghS_f \\ (1-p)\dfrac{\partial z_b}{\partial t} + \dfrac{\partial q_s}{\partial x} = 0 \end{cases} \qquad \text{Equation 1-24}$$

Two closure equations are needed. The first is the Manning-Strickle used for the friction slope (Equation 2-17). The second one, the Meyer-Peter and Müller (1948) formula (Equation 2-10), is chosen among the formulas used to estimate bedload transport by providing the sediment discharge (see 1.3).

In this thesis, the BASEMENT software is used as a numerical solver to simulate the water flow and channel bed evolutions. (This software has been developed by ETH Zurich / Laboratory of Hydraulics, Glaciology, and Hydrology (VAW) (It is freely available at http://www.basement.ethz.ch). This software uses space discretization, Finite Volume Method (FV), and time discretization, Finite Difference Method (FD) with an Explicit Euler scheme to solve the PDE system of governing equation since this system is not analytically solvable for any general boundary condition (Zanchi, 2018 and Zucchi, 2018).

It should be mentioned that considering the theory, three boundary conditions are needed to solve the PDE system (Equation 1-24). These boundary conditions are different upstream and downstream, considering the flow type, subcritical or supercritical. The Table 2-7 shows the number and type of boundary conditions which should be imposed in the model.

Table 2-7 The required boundary conditions according to the theory to solve the SVE and Exner equations

FLOW TYPE	UPSTREAM	DOWNSTREAM
SUBCRITICAL ($Fr < 1$)	Q and Z_{bed}	h
SUPERCRITICAL ($Fr > 1$)	Q and h	Z_{bed}

2.6.1.1 Model parameterization

There are three different types of parameters that should be defined as the input of the model in the software. These parameters are detailed in the following.

1) **Geometry**

   The model's geometry should be the same as the actual channel used to conduct the experimental laboratory campaigns.

   - Section

     As highlighted in 2.1, a flume with a rectangular cross-section is chosen, with 30 cm width and 45 cm overall depth, while the initial 15 cm of this depth is filled with sediment. (Figure 2-76)

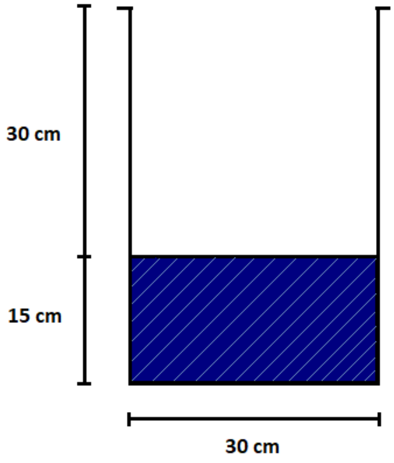

Figure 2-76 Schematic characteristics of the channel section reproduced for numerical modeling

   - Length

     The upstream of the simulated channel is considered to be at the location of the sediment inflow, which is 0.25 m far from the real channel upstream. Also downstream of this simulated channel is a fixed point at a 4.9 m from its upstream point. As a result, the length of the channel in numerical modeling is 4.9 m, while the actual length of the channel in experimental work is 5.2 m. Considering that every 5 cm is defined as a cross-section with mentioned properties above (Figure 2-76), 99 sections are needed to cover this length of 4.9 m. Furthermore, the slope of the simulated channel should be considered the same as the experimental channel and equal to 1.2%. The schematic presentation of the simulated channel is provided in Figure 2-77.

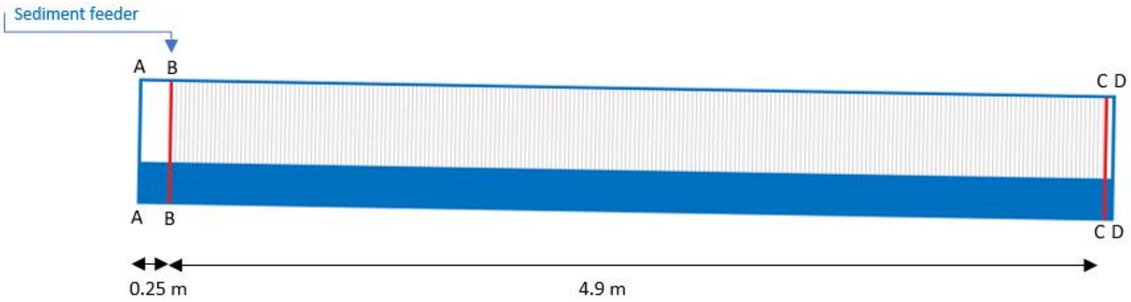

Figure 2-77 Schematic presentation of the simulated channel

Section A-A: Upstream section of the experimental channel

Section B-B: Upstream section of the simulated channel

Section C-C: Downstream section of the experimental channel

Section D-D: Downstream section of the simulated channel

2) Hydraulics

- Parameter

  In this part, some general numerical parameters for hydraulic simulation are defined.

  - Minimum water depth: The value of $0.001\ m$ is chosen for the minimum water depth, which illustrates the water depth for which the channel is considered dry.
  - Section computation: In this part, the type and some parameters for measuring hydraulic characteristics in a cross-section are defined. "Iteration" is chosen as the determination type for the hydraulic state variable in the cross-section. Also, precision of $0.045\ m^2$ is used as the maximum difference between given and calculated wetted areas in iterative determination of water surface elevation.

- Manning's coefficient n

  The value of Manning's coefficient n is considered equal to $0.015\ s/m^{\frac{1}{3}}$, wwhich is the experimental value obtained by Unigarro (Unigarro Villota, 2017). This value is the reference one, and it will be changed to calibrate the simulated model with the experimental one (2.6.3).

- Boundary condition (upstream)

  Considering that the water flow rate is known upstream, the "Hydrograph" type has been defined as the upstream boundary condition of the hydraulic part. The water flow rate, which is a constant value during each experiment, is provided below. (Table 2-8)

Table 2-8 The water discharge in each experiment and its corresponding duration

EXPERIMENT	Q (l/s)	DURATION (sec)
AE 06	7	255

AE 07	7	360
AE 08	7	230
AE 10	7	181
AE 11	7	179
AE 13	6	376
AE14	6	240

- Boundary condition (downstream)

  As mentioned in 2.6.1 and Table 2-7, in supercritical flow, defining two boundary conditions upstream (Q and h) for the hydraulics part (For solving SVEs) is needed. But there is a contradiction between this theoretical concept and the software requirement. Indeed, although it is known that no information arrives from downstream, the software requires a boundary condition downstream, which is defined here as the "*Hqrelation*" type instead of upstream. Considering this type of boundary condition, the water elevation downstream is calculated based on the relationship between water depth and water flow rate by considering the uniform state. And then, by defining the upstream slope and assuming the flow resistance law for a uniform flow, the water elevation upstream is calculated. It is worth mentioning that this assumption is not entirely correct because the flow is not a uniform flow upstream during the experimental work since the slope is changing and backwater is induced by sediment feeding upstream, which results in the transition of the critical depth upstream.

- Initial condition

  It is assumed that the behavior of the flow in the channel before the sediment feeding is steady. This behavior is remarked as the channel's initial condition, and it is needed to be reproduced for the numerical modeling. Therefore, a water profile by assuming the existence of clear water and non-erodible bed and developing an initial fictitious model without any sediment inflow discharge that has enough time to reach the steady flow state from a dry condition is provided as the initial condition in this part.

3) Morphology

- Parameter

  Some general parameters based on the material type (cylindrical PVC grain) for morphological computation are defined in this part which is essential for bedload and suspended load transportation.

Table 2-9 The properties of the sediment material as an input for numerical model

POROSITY (%)	**DENSITY** (kg/m^3)
45	**1443**

- Bed material

In this part, the material diameter is defined as 3.8 mm.

- Bedload formula
  The required closure equation for solving the PDE system (Equation 1-24) is defined here.

$$\begin{cases} \frac{\partial \mathrm{h}}{\partial \mathrm{t}} + \frac{\partial \mathrm{q}}{\partial \mathrm{x}} = 0 \\ \frac{\partial \mathrm{q}}{\partial \mathrm{t}} + \frac{\partial}{\partial \mathrm{x}}\left(\frac{\mathrm{q}^2}{\mathrm{h}}\right) + \mathrm{gh}\left(\frac{\partial \mathrm{h}}{\partial \mathrm{x}} + \frac{\partial \mathrm{z_b}}{\partial \mathrm{x}}\right) = -\mathrm{ghS_f} \\ (1-\mathrm{p})\frac{\partial \mathrm{z_b}}{\partial \mathrm{t}} + \frac{\partial \mathrm{q_s}}{\partial \mathrm{x}} = 0 \end{cases} \quad \text{Equation 1-24}$$

As mentioned before, the Meyer-Peter and Müller formula (Equation 2-10) is chosen through all the formulas suggested by BASEMENT.

It is worth mentioning that τ_c^* , the critical shields number, can be obtained by the user or the software. In this thesis, it is evaluated by the software through transformed shields diagram (Figure 1-2) by considering Van Rijn (1984) approach (see 2.4.1).

- Boundary condition (upstream)
  There is an actual upstream boundary condition in experimental work which should be imposed in this part. This boundary condition is a sediment graph consisting of the Q_{sin} obtained by the PIV algorithm and transfer functions, explained in 2.2 , with corresponded time. (Table 2-10)

Table 2-10 The initial sediment discharge in each experiment and its corresponding duration

EXPERIMENT	$Q_{sin}\ (\frac{m^3}{s})$	$Duration\ t\ (sec)$
AE 06	2.30E-04	255
AE 07	1.43E-04	360
AE 08	2.55E-04	230
AE 10	4.16E-04	181
AE 11	4.01E-04	179
AE 13	1.49E-04	376
AE14	2.58E-04	240

In principle, the value of Q_{sin} is not constant during the experiment, but it can be assumed that the behavior of the hopper is uniform during the experiment, so it is appropriate if someone considers a constant value for Q_{sin} during the experiment.

It should be highlighted that this upstream boundary condition is not needed based on theory (explained in 2.6.1), but it is imposed since it exists in real experimental work. It affects the bed evolution from upstream to downstream.

- Boundary condition (downstream)
  In this part, the downstream boundary condition Z_{bed} is specified by considering the "IODown" type. In this boundary condition, all sediment entering the last computational section will leave the section over the downstream boundary. If any downstream boundary condition is not defined here, there is no sediment transport over the downstream boundary since the software assumed a wall as a downstream boundary condition.

2.6.2 Comparison of initial numerical results with experimental results

After defining the input parameters, the simulation starts, and the initial result is compared with the experimental results. These results are presented in 3.6.1.

2.6.3 Calibration of the numerical model

A calibration process of the numerical model is needed to increase the concordance between the numerical and experimental results. The following parts explain this calibration process concerning Manning's coefficient n and Bedload factor α_{MPM}.

2.6.3.1 Modification of the Bedload factor α_{MPM}

The inconsistency between numerical and experimental results can be related to underestimating the initial sediment transport capacity estimated by the software concerning the experimental initial sediment transport capacity. It is possible to increase this quantity to have more consistency between results by increasing the multiplier coefficient of the Meyer-Peter and Müller formula (also known as Bedload factor α_{MPM}) in the software (Equation 2-34). It should be mentioned that generally, this value is equal to 1.

$$\Phi = \alpha_{MPM} 8(\tau^{*} - \tau_{c}^{*})^{1.5}$$ *Equation 2-34*

For having an initial estimation of this value, one can divide the initial sediment transport capacity estimated by experimental work on the initial sediment transport capacity calculated by software considering the Meyer-Peter and Müller formula and Van Rijn approach. (Equation 2-35)

$$\alpha_{MPM} = \frac{Q_{s0}(Experimental)}{Q_{s0}(MPM\ formula)}$$ *Equation 2-35*

For this calculation, the results of Q_{s0} (Experimental) and Q_{s0} (MPM formula are used.

2.6.3.2 Modification of Manning's coefficient n

As mentioned previously (in 2.6.1.1-Hydraulics), the value of $n = 0.015\ s/m^{\frac{1}{3}}$ is selected as the Manning's coefficient n in numerical modeling. Another way to make more consistency between numerical and experimental results is by increasing Manning's coefficient n. Indeed, by rising in

Manning's coefficient n, the water elevation increases while the bed elevation declines since the shear stress in the bed increases, leading to more sediment transport capacity of the channel.

2.6.3.3 Combination of Modification of Bedload factor αMPM and Manning's coefficient n as the final calibration

To find a proper consistency between numerical and experimental results, one must modify both Bedload factor α_{MPM} and Manning's coefficient n. Several trials have been considered to find the best combination of these two factors for each experiment. The best trial is chosen by considering the human judgment and evaluating the mean square error.

The mean square error (Equation 2-8) has been performed for some specific times in spatial profiles (see Table 2-11) for each experiment and then it is summed over all of these times for each trial. As a result, two single values, one for bed profiles and one for water profiles, are obtained. The best trial had been chosen by considering the average value of these two single values (see Table 2-12).

Table 2-11 Mean square error (cm^2) of a) bed elevation b) water surface elevation for some specific times in spatial profiles (AE14)

TRIAL	T=0 SEC	T= 40 SEC	T= 80 SEC	T= 120 SEC	T= 160 SEC	T= 200 SEC	T= 240 SEC
1	0.33	0.61	1.46	2.80	4.49	5.85	7.38
2	0.33	0.48	0.73	1.01	1.33	1.41	1.55
3	0.33	0.44	0.60	0.75	0.93	0.92	0.97
4	0.33	0.40	0.48	0.54	0.63	0.59	0.59
5	0.33	0.35	0.35	0.33	0.34	0.29	0.28
6	0.33	0.33	0.32	0.28	0.27	0.23	0.22
7	0.33	0.31	0.28	0.23	0.22	0.19	0.19
8	0.33	0.29	0.26	0.20	0.18	0.18	0.19
9	0.33	0.32	0.30	0.25	0.24	0.20	0.20
10	0.33	0.34	0.33	0.29	0.29	0.24	0.23
11	0.33	0.32	0.31	0.27	0.26	0.22	0.21
12	0.38	0.49	0.66	0.79	0.93	0.89	0.91
13	0.33	0.38	0.43	0.46	0.51	0.46	0.46
14	0.33	0.33	0.32	0.28	0.28	0.24	0.23

(a)

TRIAL	T=0 SEC	T= 40 SEC	T= 80 SEC	T= 120 SEC	T= 160 SEC	T= 200 SEC	T= 240 SEC
1	1.27	0.03	0.16	0.61	1.31	2.11	3.10
2	1.27	0.04	0.05	0.09	0.14	0.18	0.26
3	1.27	0.04	0.03	0.04	0.05	0.06	0.10
4	1.27	0.04	0.03	0.02	0.02	0.02	0.04
5	1.27	0.05	0.04	0.04	0.04	0.06	0.07
6	1.58	0.09	0.07	0.06	0.06	0.08	0.11
7	1.93	0.17	0.12	0.10	0.09	0.12	0.15
8	2.29	0.27	0.20	0.16	0.14	0.17	0.20
9	1.75	0.13	0.09	0.08	0.08	0.10	0.13
10	1.75	0.13	0.09	0.07	0.06	0.08	0.10
11	1.93	0.17	0.12	0.10	0.08	0.10	0.12
12	2.22	0.25	0.26	0.27	0.27	0.27	0.32
13	1.27	0.04	0.03	0.02	0.02	0.02	0.03

14	1.27	0.05	0.04	0.05	0.06	0.09	0.11

(b)

Table 2-12 Sum of the mean square error (cm^2) *for bed and water in each trial and then its average as an indicator for choosing the best trial (AE14)*

TRIAL	SUM OF THE BED ERROR (CM²)	SUM OF THE WATER ERROR (CM²)	AVERAGE OF ERRORS (CM²)
1	21.990	7.302	14.646
2	6.042	0.720	3.381
3	4.166	0.287	2.226
4	2.829	0.129	1.479
5	1.593	0.252	0.923
6	1.307	0.382	0.845
7	1.106	0.585	0.846
8	1.012	0.875	0.944
9	**1.193**	**0.474**	**0.833**
10	1.383	0.403	0.893
11	1.258	0.517	0.888
12	4.166	1.393	2.780
13	2.326	0.129	1.228
14	1.342	0.362	0.852

2.7 Dimensionless analysis

This part explains making the Celerity and the Manning's coefficient n dimensionless to plot them based on the Froude number Fr and Loading ratio Lr.

2.7.1 Dimensionless Manning's coefficient n

The dimension of Manning's coefficient n is $(time/length^{\frac{1}{3}})$, which can be dimensionless if it is multiplied by $\frac{v}{h^{\frac{2}{3}}}$. Where v is the water velocity, and h is the water depth. So, the n', which is the dimensionless Manning's coefficient, is calculated by Equation 2-36.

$$n' = \frac{n \times v}{h^{\frac{2}{3}}}$$

Equation 2-36

For defining the flow velocity v, water depth h, and Froude number Fr, four different scenarios are considered:

First scenario: This scenario is defined based on the theory of calculating the water discharge for a uniform open channel flow. On the one hand, by considering the calibrated Manning's coefficient n and final slope of the profile, the water discharge can be calculated by Equation 2-37.

$$Q_{water,calculated} = \frac{1}{n} A \sqrt{S_f} R^{\frac{2}{3}}$$

Equation 2-37

Where, n is calibrated Manning's coefficient, A is the cross-sectional area of flow normal to the flow direction,S_f is the final bottom slope of the channel and R is the hydraulic radius and equal to $R = \frac{A}{P}$ where P is the wetted perimeter of the cross-sectional area of flow
On the other hand, the water discharge $Q_{water,experiment}$ is known during the experiment $(5, 6, or\ 7\ l/s)$.
Then, the correspondence water depth h is found by making equality between $Q_{water,experiment}$ and $Q_{water,calculated}$, the correspondence water depth h is found. Afterward, by using Equation 2-38, the flow velocity v is calculated.

$$v = \frac{Q}{A}$$ Equation 2-38

Where, A is the cross-sectional area of flow normal to the flow direction.
At the end, the value of the Froude number Fr is calculated by considering this v and h and using Equation 2-39.

$$Fr = \frac{v}{\sqrt{gh}}$$ Equation 2-39

Where g is the gravitational acceleration.

Second Scenario: In this scenario, the values of water depth h, flow velocity v, and Froude number Fr are calculated by taking an average of their correspondence matrices spatially for the first time that the sediment profile is stable.

Third scenario: In this scenario, the values of water depth h, flow velocity v, and Froude number Fr are calculated by taking an average of their correspondence matrices spatially for the last time.

Fourth scenario: In this scenario, the values of water depth h, flow velocity v, and Froude number Fr are calculated by taking an average of their correspondence matrices spatially for the time interval between the first-mentioned time in second scenario and the last time mentioned in third scenario.

These scenarios also will be used for dimensionless analysis of Bedload factor α in 3.7.2 and final slope in 3.7.3.

2.7.2 Dimensionless celerity

The dimension of celerity is $(length/time)$, which can be dimensionless if it is divided by $\sqrt{g}h$. Where g is the gravitational acceleration, and h is the water depth. In this thesis, two different types of methods for finding celerity are introduced (Local celerity C and eigenvalues λ) discussed in 2.5. The below equations are used for making C and λ dimensionless.

$$C' = \frac{C}{\sqrt{g}h}$$ Equation 2-40

$$\lambda' = \frac{\lambda}{\sqrt{g}h}$$ Equation 2-41

Where C' is Dimensionless local celerity and λ' is dimensionless eigenvalue.

For defining the water depth h two different scenarios are defined:

First scenario: In this scenario, the values of celerity, water depth h, and Froude number Fr are calculated by taking an average of their correspondence matrices spatially for time interval $t = 50\ sec\ to\ t = 100\ sec$.

Second scenario: In this scenario, the values of celerity, water depth h, and Froude number Fr are calculated by taking an average of their correspondence matrices spatially for time interval same as the first scenario but for the half of the space interval. This decision of considering the half of the space interval for the second scenario is made since by considering the entire length of the channel, the positive celerity on upstream and negative celerity downstream more or less neutralize each other and results in less average celerity value.

Chapter 3:

RESULTS AND DISCUSSION

3.1 introduction

This chapter discusses and analyzes results obtained from the coupling of experimental and numerical work. The supercritical flow campaign consists of AE experimental series and their simulations from AE01 to AE14. Each experiment has a specific boundary condition, highlighted in Figure 3-1. It should be mentioned that experiments number AE9 to AE14 are run and conducted in this research. The images belonging to experiments AE06 to AE08 related to previous works (Eslami et al., 2021) are reprocessed with a newly modified measurement method (explained in 2.3.3). Results are employed for a better understanding of the process. Furthermore, some results of experiments number AE01, AE02, and AE05 (Heydari, 2020) are employed for dimensional and dimensionless analysis discussed at the end of this chapter. It is worth mentioning that due to failure (crash) in experiment AE12, the data of this experiment is just used for validation. Moreover, since experiment AE09 is the first trial, the value of some results, such as Q_{s0}, has a significant difference from previous results (Eslami et al., 2021). Therefore, another experiment with the same boundary condition as AE09 is performed. It should be mentioned that the results belonging to this experiment can be reprocessed again since the measurement method are clear now.

Table 3-1Summary of experiment

	EXPERIMENTS	**QWATER** (l/s)	$Q_{sin}(m^3/s)$	$Q_{s0}(m^3/s)$	Lr
USED AS PRODUCED IN PREVIOUS WORKS (RUN BY Heydari & RECOMPUTED BY Eslami ET., AL)	AE01	5	1.42E-04	8.31E-05	1.71
	AE02	5	1.01E-04	8.31E-05	1.22
	AE03	5	8.67E-05	8.31E-05	1.04
	AE04	5	8.70E-05	8.31E-05	1.05
	AE05	5	2.43E-04	8.31E-05	2.92
RUN BY (Eslami ET., AL) RECOMPUTE IN THIS THESIS	AE06	7	2.30E-04	1.41E-04	1.63
	AE07	7	1.43E-04	1.29E-04	1.11
	AE08	7	2.55E-04	1.29E-04	1.97
RUN, EXTRACT AND COMPUTE DATA IN THIS THESIS	AE09	7	4.04E-04	-	-
	AE10	7	4.16E-04	1.20E-04	3.46
	AE11	7	4.01E-04	1.19E-04	3.37
	AE12	7	2.92E-04	-	-
	AE13	6	1.50E-04	1.39E-04	1.07
	AE14	6	2.58E-04	1.46E-04	1.76

3.2 Spatial and temporal evolution of bed and water elevation

Spatial evolution profiles illustrate the water and bed surface elevation along the flume at a particular time. In contrast, temporal evolution profiles indicate the water and bed surface elevation during the experiment at specific locations along the flume.

Two points need to be mentioned; First, when the sediments start vibrating along the feeder channel to feed into the flume is considered as the start time of the experiment ($t = 0\ sec$). In fact, no sediment has yet entered the flume, and it takes some while for the sediment to start moving within it. In these early times, there was no combination of water and sediment fed along the flume, so the profiles obtained at these times will not be our desired profiles. Second, at the beginning of the test, the actual water discharge in the channel differs from the nominal water flow rate ($Q_{nominal}$ can be $5, 6$, and $7\ l/s$ considering the current campaign). This difference is due to two main reasons. On the one hand, the flow rate of water increases gradually over time to reach the $Q_{nominal}$, so at $t = 0\ sec$, the water flow rate in the channel is less than the $Q_{nominal}$. This difference is related to the fact that water must first fill the tank and then enter the channel, so that this process will take some time. On the other hand, shortly after the start of the test (after $t = 0\ sec$), the falling sediment hinders the flow of water, so some backwater is induced. Part of the flow rate coming from the delivery pipe is then spent to fill the upstream tank to meet the backwater and this reduces the flow into the flume. After some transient, steady flow is achieved again. It is required to develop some investigations considering these issues.

Based on two mentioned above points, the interval between $t = 0\ sec$ and $t = 50\ sec$ is considered as the initial times, and the water and sediment profiles related to this range are not fully considered in this thesis, as an example, for calculation of some parameters like celerity and Froude number Fr (see Figure 3-1).

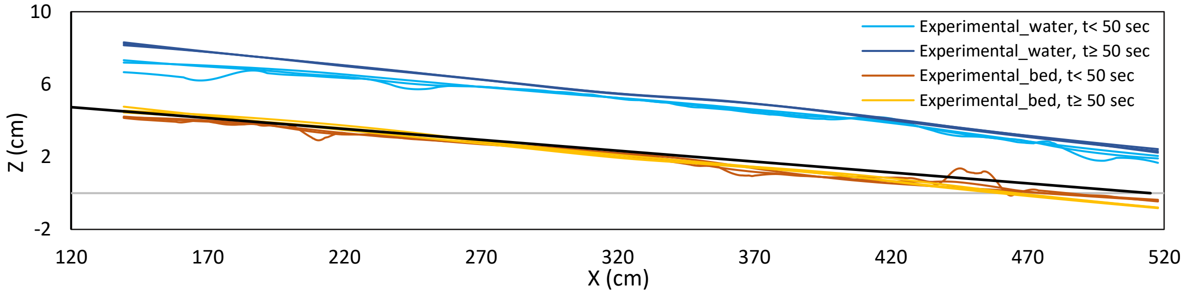

Figure 3-1 Comparing the generated profiles before and after $t = 50\ sec$ *_ AE13*

Moreover, in all experiments, an unavoidable degradation occurs downstream before starting the experiment when the discharge increases to reach the nominal value. This degradation may occur because of a sill located outlet of the flume. Indeed, the water movement is blocked along the flume near the outlet, resulting in the tendency of water to have an upward movement. As a result, the lifting force increases, leading to a growth in sediment transport capacity in that area, which means the occurrence of degradation downstream. (Eslami et al., 2021).

For instance, Figure 3-2 from AE14 shows that the elevation of the sediment downstream at the first time ($t = 0\ sec$) is already eroded; in other words, the experiment starts with existent degradation, which may be caused due to sill effect.

During the experiments, sediment profiles remain more or less constant downstream. However, one may consider this behavior during the experiment as a degradation process concerning the reference line, which is an assumed ideal sediment profile at the initial time ($t = 0\ sec$) considering the slope of 1.2% in all experiments. More studies can be conducted to that which line should be assumed as the reference line in the future.

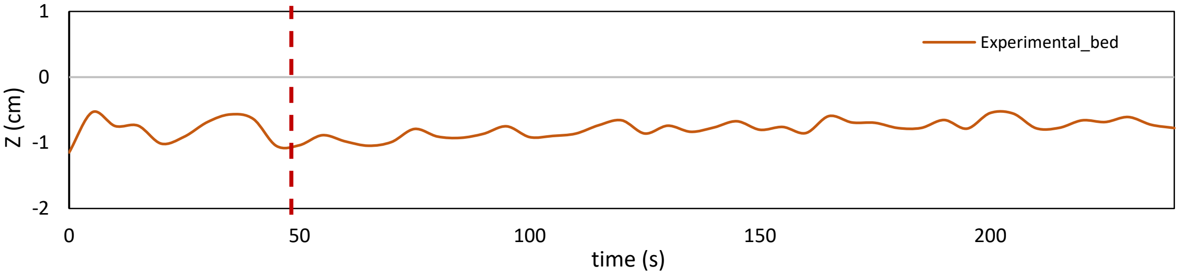

(a)

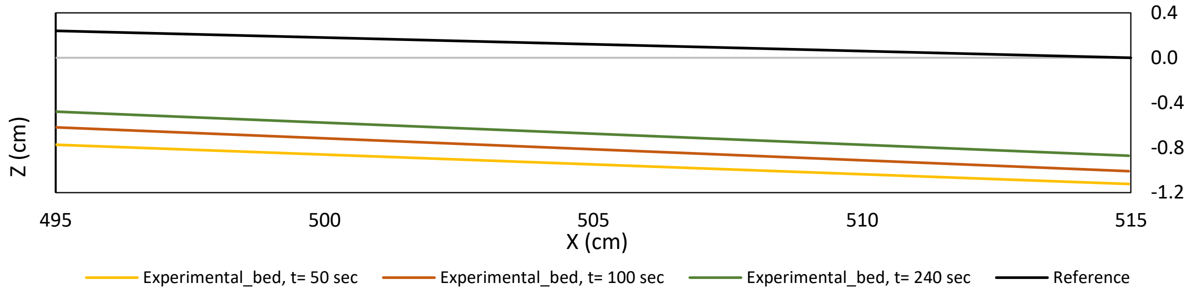

(b)

Figure 3-2 Sediment profile downstream in experiment AE14 a) Temporal evolution b) Spatial evolution

In the following, spatial and temporal evolutions of water and sediment profiles are discussed. It should be mentioned that plots related to experiment numbers AE13 and AE14 are shown as examples, and other plots belonging to other experiments are shown in Appendix_6.

3.2.1 Spatial evolution

The evolution of sediment and water profiles is discussed spatially in this part. Figure 3-3 and Figure 3-4 show the longitudinal profiles for experiments AE13 and AE14, respectively, at different times.

In experiment AE13, the elevation of the water and sediment surface remains constant during the experimental time. In another way, the aggradation and degradation process does not occur clearly through the channel. Therefore, from this aspect, it can be concluded that the volume of sediment that comes from upstream may be equal to the volume of sediment which goes out of the flume outlet from downstream, which can be the definition of equilibrium. So, it can be said that this experiment is run in nearly equilibrium conditions.

In contrast, in experiment AE14, the results show that the aggradation and degradation processes occur in the channel during the experiment.

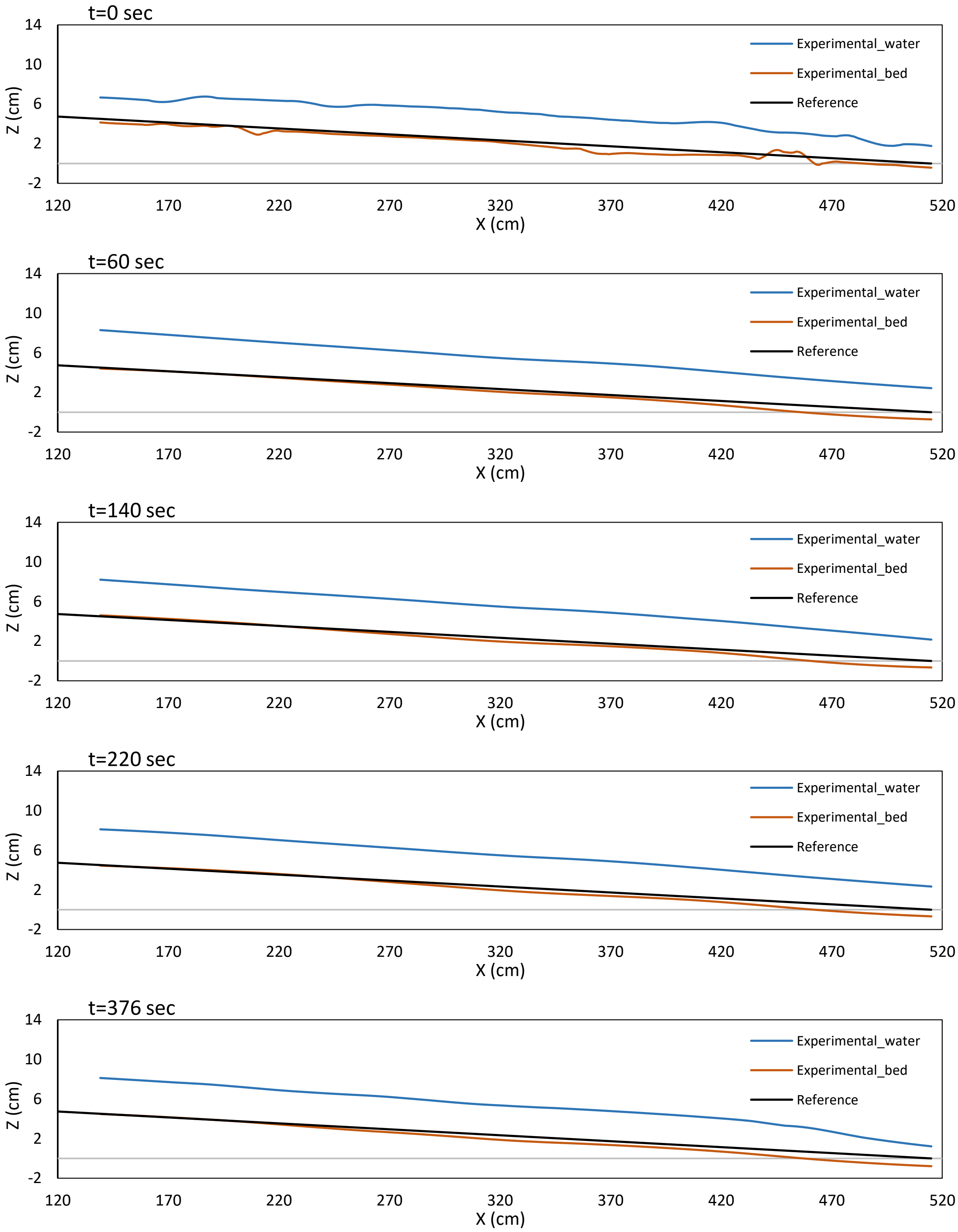

Figure 3-3 Spatial evolution of water surface and bed elevation for AE13 (Loading ratio L_r= 1.07)

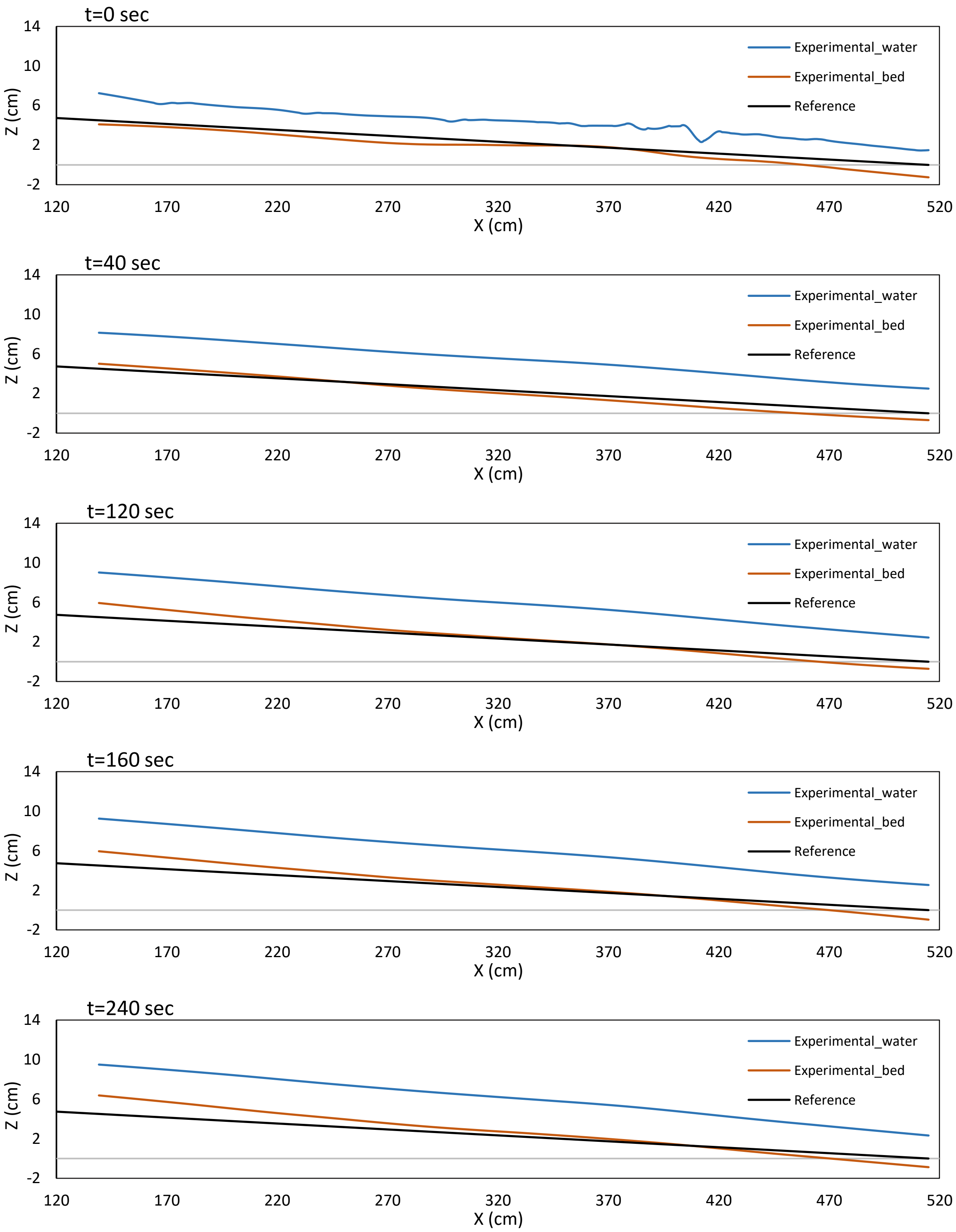

Figure 3-4 Spatial evolution of water surface and bed elevation for AE14 (Loading ratio L_r= 1.76)

3.2.1.1 Temporal evolution of slope

Based on different boundary conditions applied for every experiment, such as water discharge Q_{water} and sediment feeding discharge Q_{sin} (Table 3-1), the slope of the sediment profile can change or stay constant during trials. Therefore, the temporal evolution of the slope is used to recognize the aggradation and degradation process. For calculating the slope of the sediment profile, employing a linear approximation trend is considered reasonable since the slope variations are not detectable by the eye. When equilibrium in sediment transport capacity happens, the slope remains constant, like in experiments AE13 and AE07. On the other hand, while aggradation and degradation occur, slope changes continuously during experiments similar to experiment AE14. Therefore, it can be deduced that the slope changes during the time, and it remains fixed when there is an equilibrium. Furthermore, by analyzing the slope, it can be clear how the sediment transport capacity is close to equilibrium in each experiment. Figure 3-5 shows different slopes at various times for all experiments from AE01 to AE14 (except AE09 and AE12). In this figure, three types of behaviors can be seen:

1. Experiments in which the slope of the sediment profiles remains constant (AE02, AE03, AE04, AE07, and AE13); these experiments experience a slight growth at the beginning for a short time which is followed by an almost constant slope. This situation can be noted as a near-equilibrium condition.
2. Experiments need a longer time to reach nearly equilibrium conditions (AE01, AE06, AE08, and AE14); these experiments started with different slopes, and it can be seen that as they are close to the end of experiments, they tend to reach a same constant slope. It may happen because they are close to equilibrium as they get close to the end of the experiment.
3. Experiments with a short duration compared to others (AE05, AE10, and AE11); these experiments possess a higher Loading ratio Lr, and they have the shortest duration among these three groups (due to the fast process and limited volume of sediment fed). They need more time to reach the equilibrium condition.

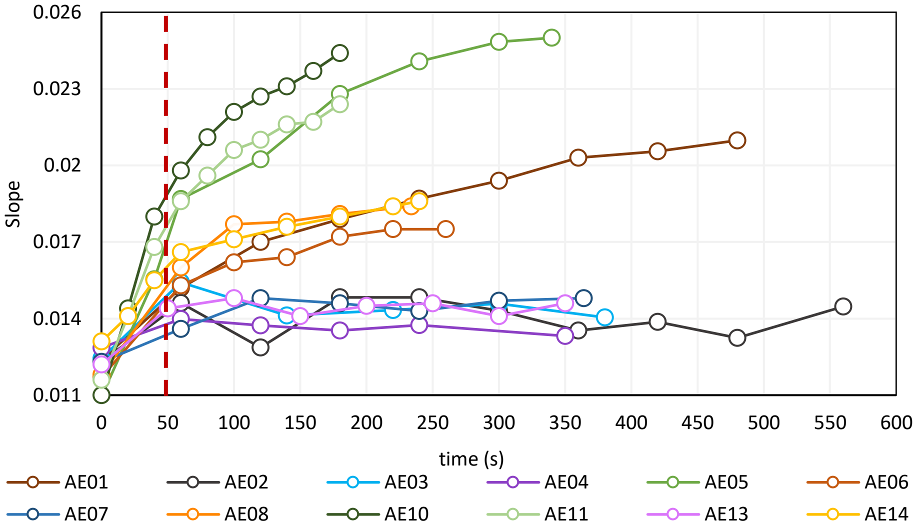

Figure 3-5 Temporal evolution of linear slope in various experiment

3.2.2 Temporal evolution

In this part, the evolutions of sediment and water profiles are discussed temporally. For instance, Figure 3-5 and Figure 3-6 illustrate how the elevation of water and sediment change during the time in experiments AE13 and AE14.

The profiles related to AE13 (Figure 3-5) show that the elevation of various locations during the experiment does not change significantly. Instead, in experiment AE14 (Figure 3-6), aggradation along the channel is evident. Furthermore, water depth almost keeps a constant value in both runs, showing a uniform flow during experimental work.

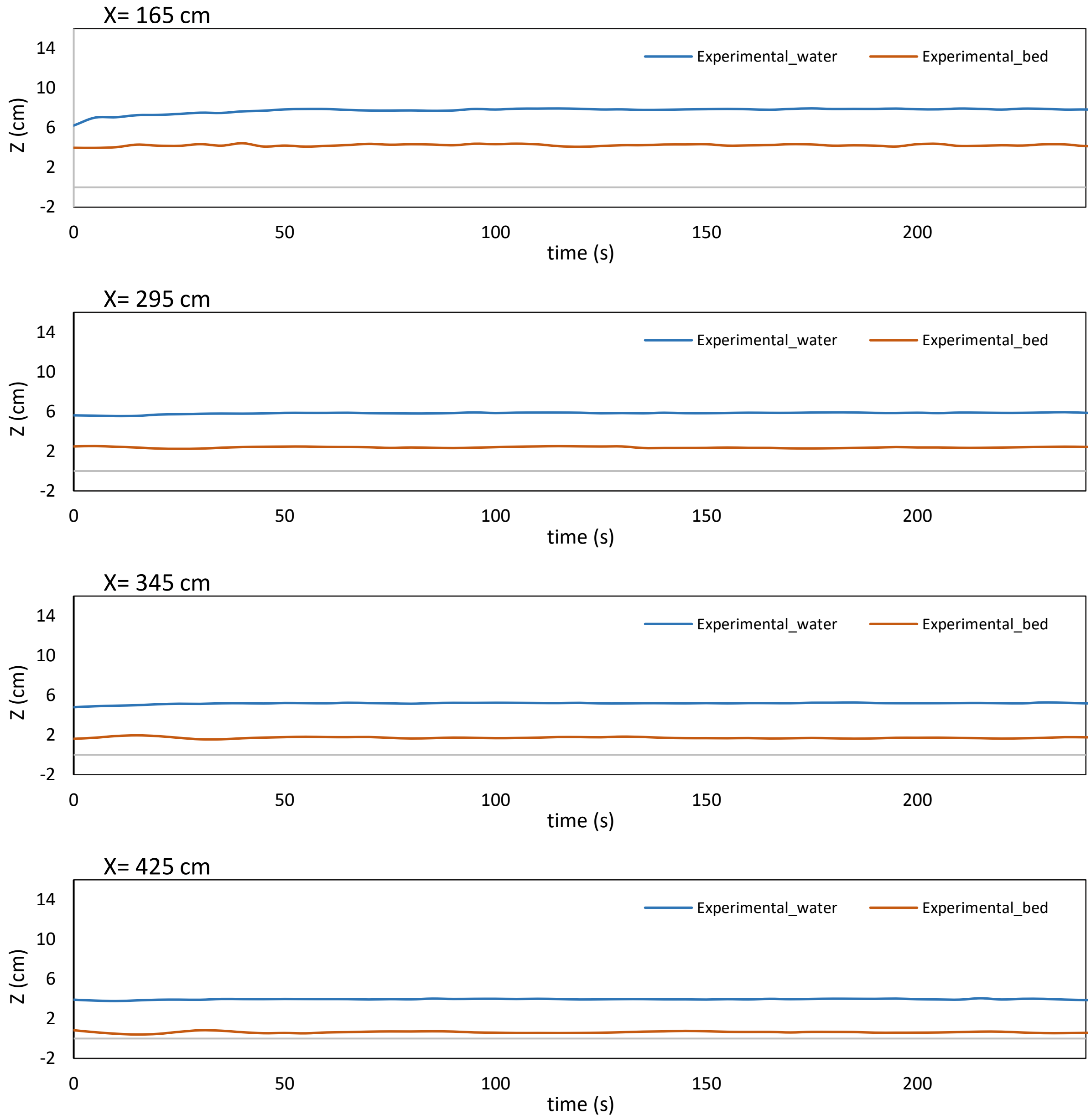

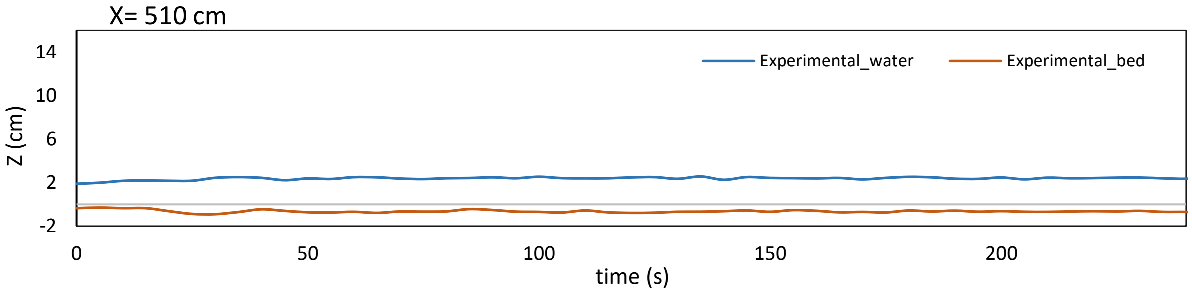

Figure 3-6 Temporal evolution of water surface and bed elevation in AE13(Loading ratio L_r= 1.07)

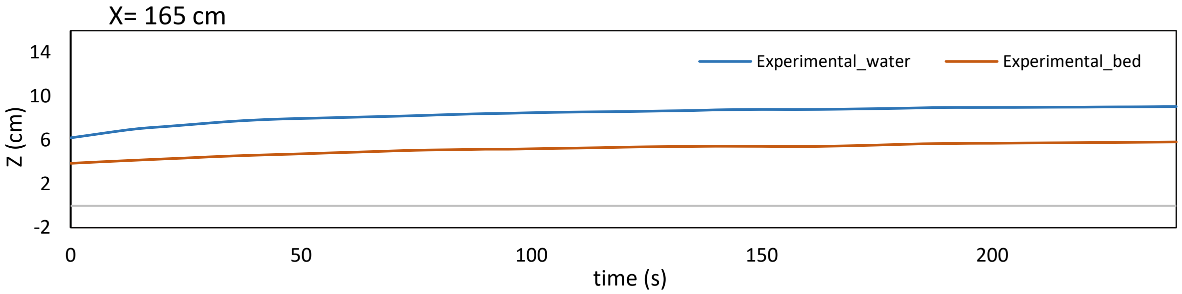

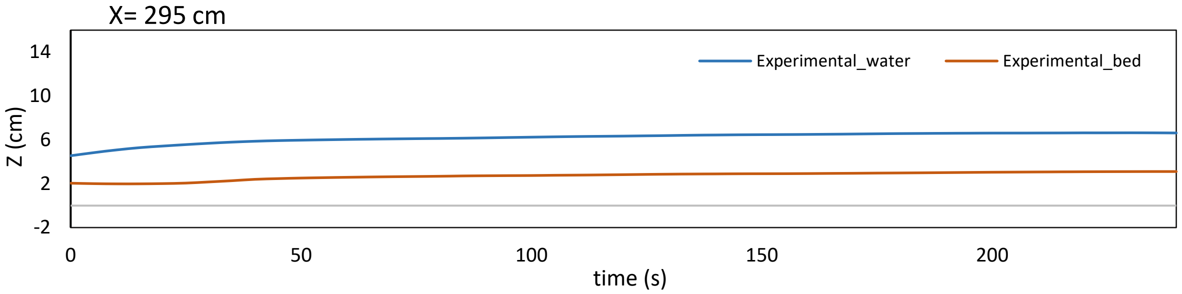

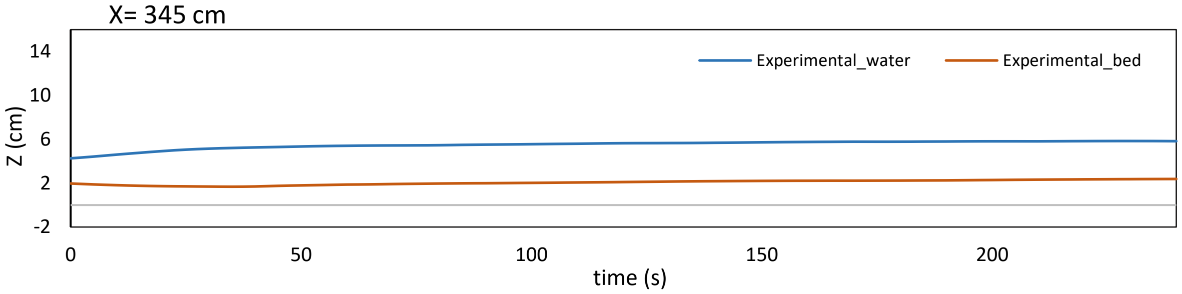

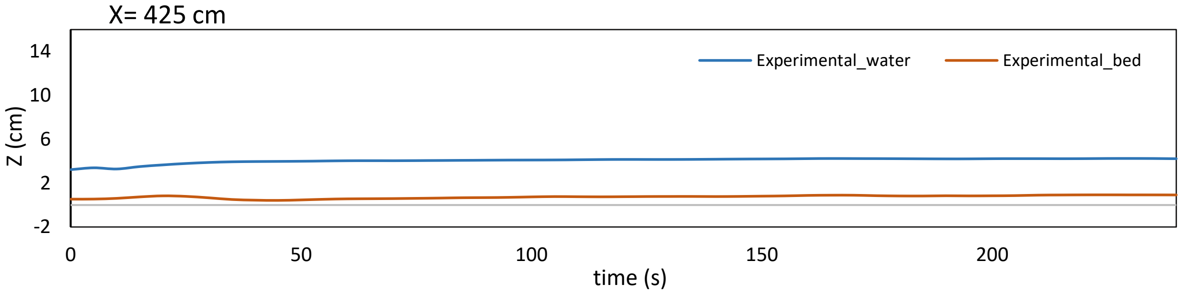

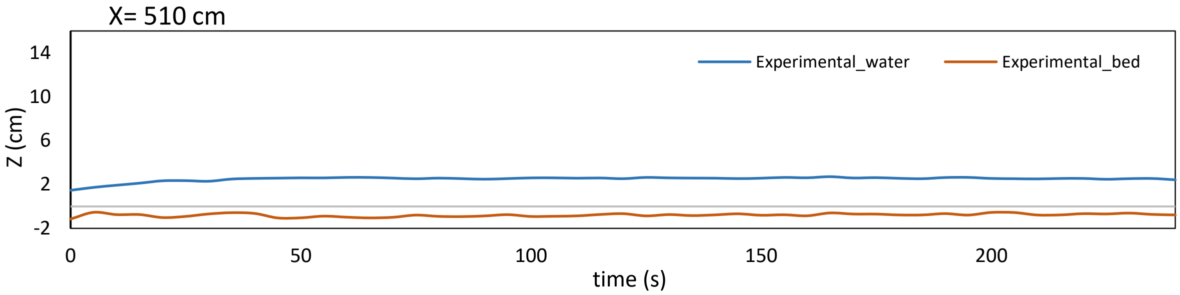

Figure 3-7 Temporal evolution of water surface and bed elevation in AE14 (Loading ratio Lr= 1.76)

3.2.3 Color map gradient for water and sediment elevation

This part shows the color gradient maps of sediment and water elevation. Color gradient maps can provide the opportunity to illustrate the spatial and temporal evolution of water and sediment profiles simultaneously.

Figure 3-8 shows the color gradient map of experiment AE13. A little temporal change can be pointed after the mentioned initial time ($t > 50\ sec$) by eye-averaging contour lines returning to vertical stripes. Therefore, a near equilibrium condition can be confirmed in this experiment. Moreover, the elevation of sediment and water decreases from upstream to downstream.

In the color gradient map of experiment AE14 (Figure 3-9), the elevation of water and sediment profiles increases during the experiment, and the aggradation pattern is evident. In the bed color gradient map, the white color shows the zero elevation for sediment, and there is degradation below this range.

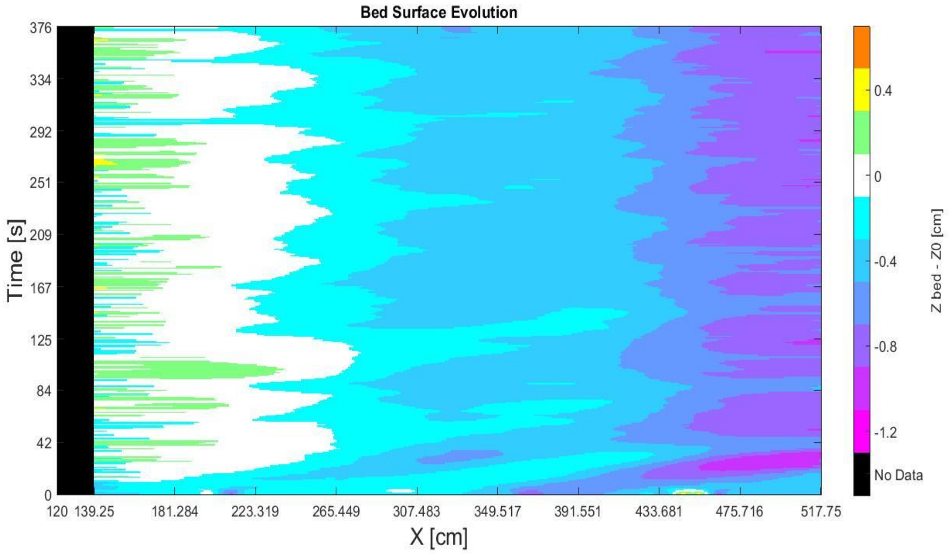

a)

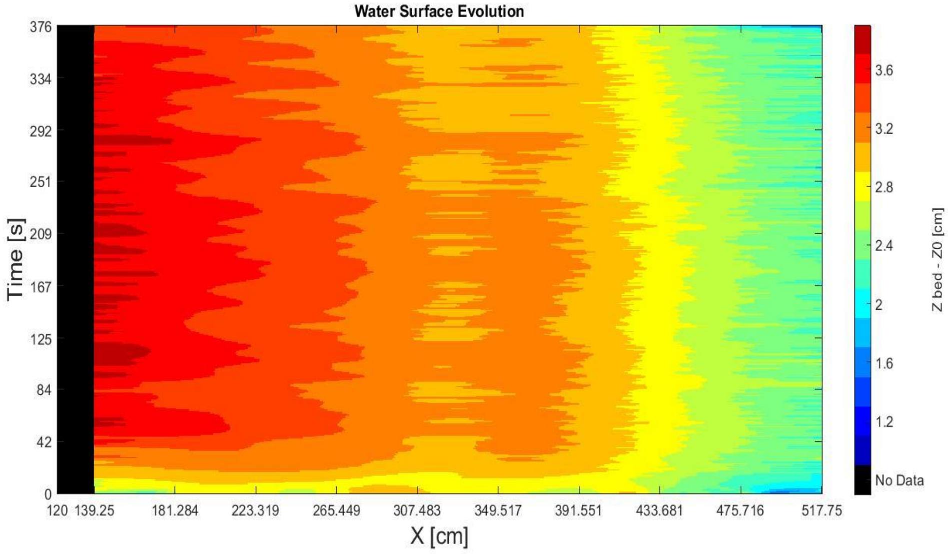

b)

Figure 3-8 Elevation color gradian map_AE13. a) Bed surface elevation. b) Water surface elevation.

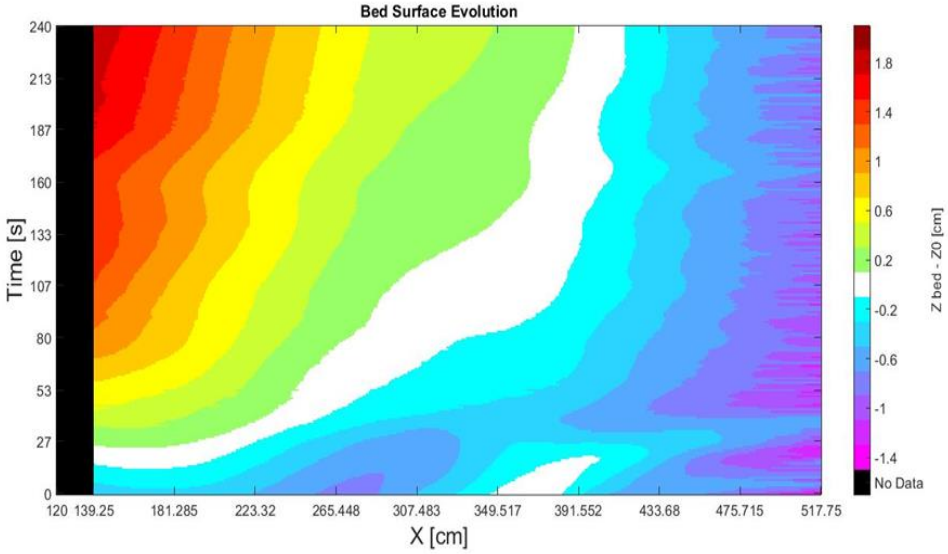

a)

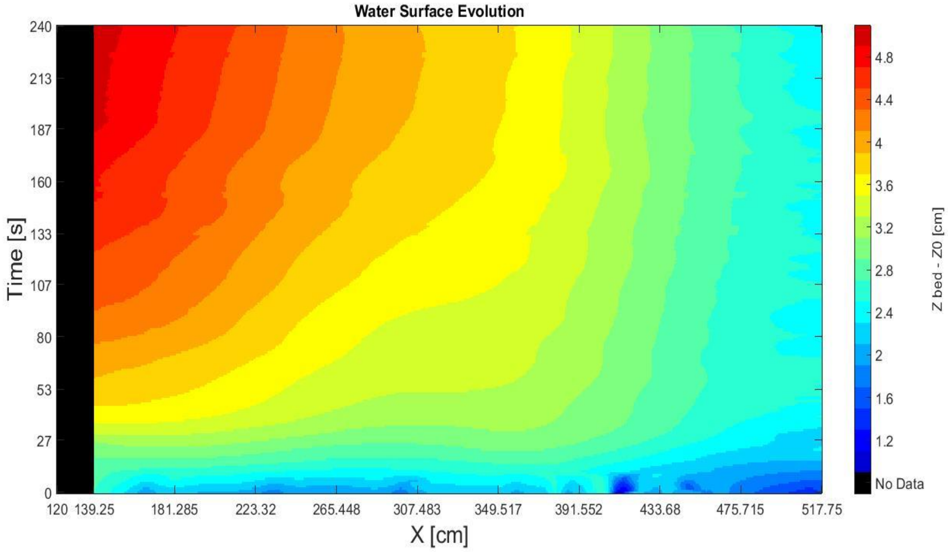

b)

Figure 3-9 Elevation color gradian map_AE14. a) Bed surface elevation. b) Water surface elevation.

3.3 Estimation of the initial sediment transport capacity of the channel

Based on three different methods (MPM, collector and continuity method) with various scenarios, and their combinations (see 2.4), the initial sediment transport capacity Q_{s0} values for each experiment are highlighted. It should be mentioned that calculating the value of Q_{s0} is vital since it is used for determining Loading ratio Lr. Table 3-2 shows the value of Q_{s0} for different experiments.

3.3.1 MPM method

The value of Q_{s0} can be estimated by employing the MPM method based on two different formulas discussed in 2.4.1. Figure 3-10 shows that the value of Q_{s0} for each specific discharge is same; for example, in experiment AE01 to AE05, with the water discharge equal to $Q_{water} = 5\ {}^{l}/_{s}$, Q_{s0} is the same. It similarly happens in experiment AE06 to AE011 ($Q_{water} = 7\ {}^{l}/_{s}$) and AE13 to AE14 ($Q_{water} = 6\ {}^{l}/_{s}$). Considering different water discharge, it becomes clear that by increasing the water discharge Q_{water}, the initial sediment transport capacity Q_{s0} rises. Furthermore, experiment AE09 and AE12 have the value for Q_{s0} in this part since their discharge is clear, so the corresponding values of Q_{s0} can be found by using MPM formula.

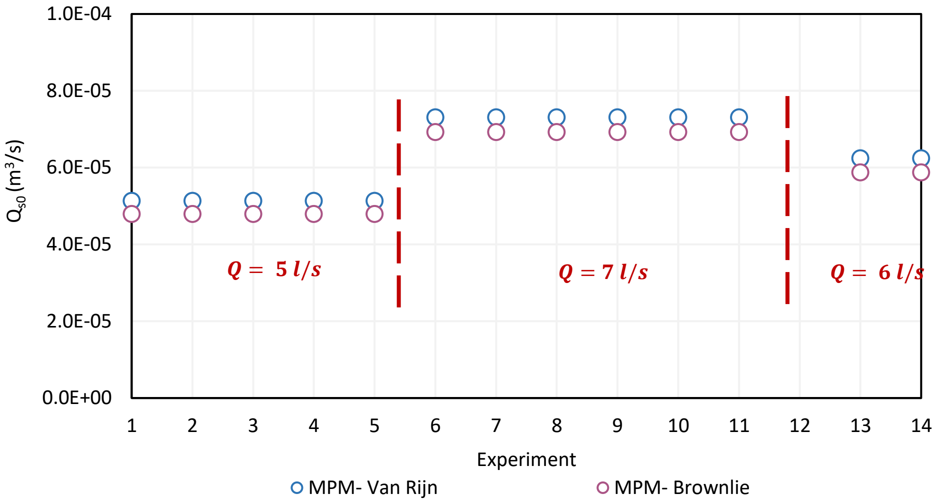

Figure 3-10 The value of Q_{s0} using MPM method for different experiments.

3.3.2 Collector method

Based on collector method the value of $\mathrm{Q}_{\mathrm{s,collector}}$ can be illustrated in different time. As discussed in 2.4.2, at time interval in which $\mathrm{Q}_{\mathrm{s,collector}}$ remains approximately constant, the first time and the last time of interval is considered as t_1 and t_2, respectively. By averaging the value of $\mathrm{Q}_{\mathrm{s,collector}}$in this time interval, the $\mathrm{Q}_{\mathrm{s0,collector}}$can be calculated. Furthermore, t_1 and t_2 are used in continuity method.

Based on the collector method, the value of $\mathrm{Q}_{\mathrm{s0,collector}}$ can be illustrated at different times. As discussed in 2.4.2, there is an interval in which $Q_{s0,collector}$ remains approximately constant and the first time and the last time of interval are considered as t_1 and t_2, respectively. By averaging the value of $Q_{s0,collector}$ in this time interval, the final value of $Q_{s0,collector}$can be calculated. Furthermore, t_1 and t_2 are used in the continuity method.

Figure 3-11 and Figure 3-12 show the temporal evolution of sediment volume in the collector and the corresponding sediment transport rate for runs AE13 and AE14. It is clear that the range of $Q_{s,collector}$ in experiment AE13 stays constant for a long duration, and this issue can confirm previous parts and that sediment transport capacity is at the equilibrium stage.

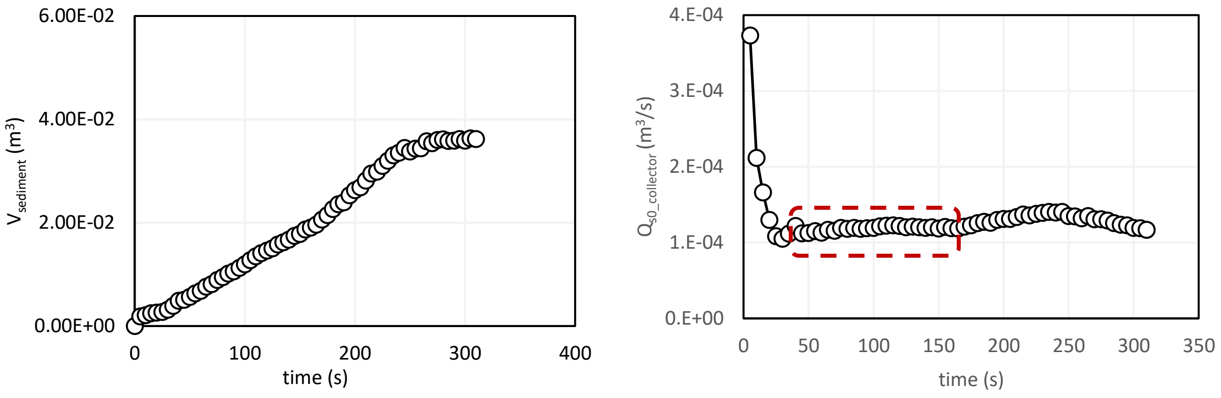

a) *b)*

Figure 3-11 Experiment AE13_ a) Temporal evolution of sediment volume in collector method. b) The corresponding sediment transport rate

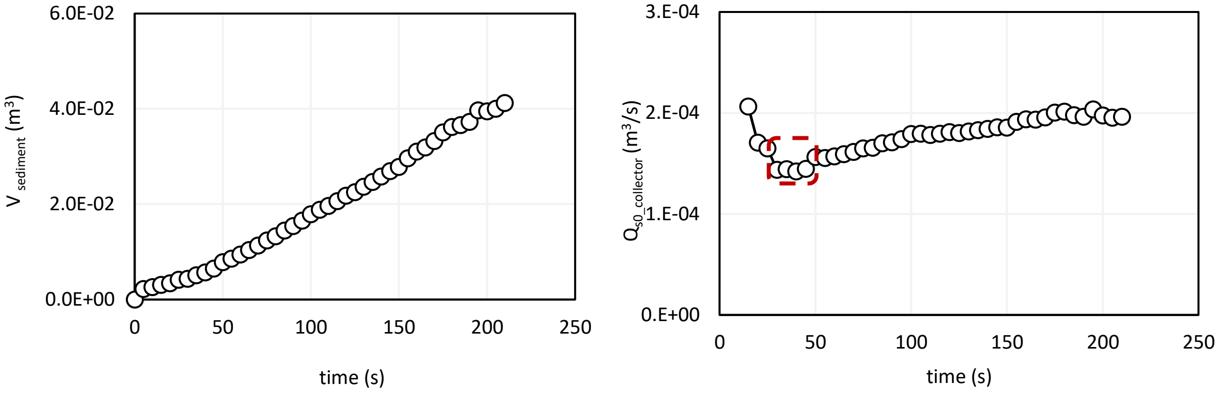

a) *b)*

Figure 3-12 Experiment AE14_ a) Temporal evolution of sediment volume in collector method. b) The corresponding sediment transport rate

Figure 3-13 shows the value of $Q_{S0,Collector}$ for all experiments. $Q_{S0,Collector}$ from AE01 to AE05, in which the water discharge Q_{water} is equal to $5\,{}^{l}/_{s}$, possess the values close to each other. The same happens for the experiments number AE06 to AE11 ($Q_{water} = 7\,{}^{l}/_{s}$) as well as AE13 and AE14 ($Q_{water} = 6\,{}^{l}/_{s}$).

Based on MPM Formulae, it is expected that by increasing the water discharge Q_{water}, the value of $Q_{S0,Collector}$ grows. This issue happens for experiments AE01 to AE05 and AE06 to AE11, but it is not true in experiments AE13 and AE14. Therefore, it is an inconsistency that could be discussed in the future work.

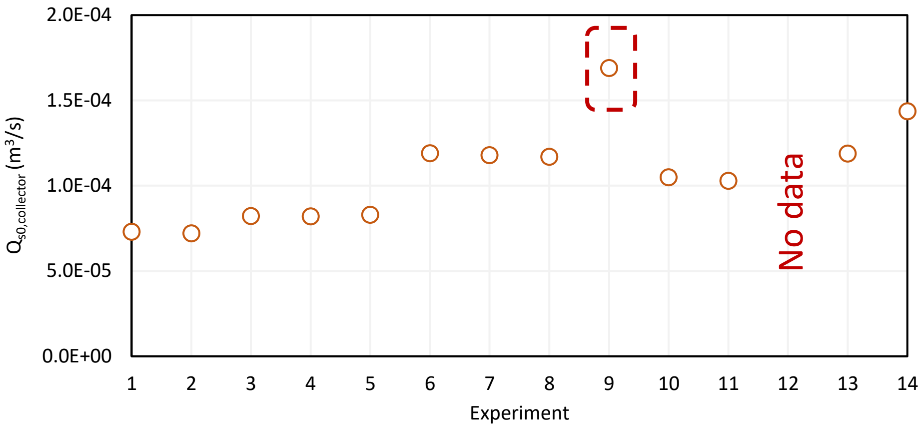

Figure 3-13 Value of $Q_{s0,collector}$ for experiments AE01 to AE14.

3.3.3 Continuity method

Based on four scenarios (IU1-CU1 and IU2-CU2) discussed in 2.4.3, the values of initial sediment transport capacity (Q_{s0}) are illustrated by the continuity method for AE06 to AE14 (except AE09 and AE12) (Figure 3-14). The results show that values coming from these scenarios are close, except for AE05 and AE11. In these two runs, the values related to scenario number one (IU1-CU1) vary from those belonging to scenario number two (IU2-CU2). The range for each discharge is close likewise the MPM and collector method results, and by increasing discharge, the value rises except for experiments AE13 and AE14. Therefore, this contradiction exists in the continuity method.

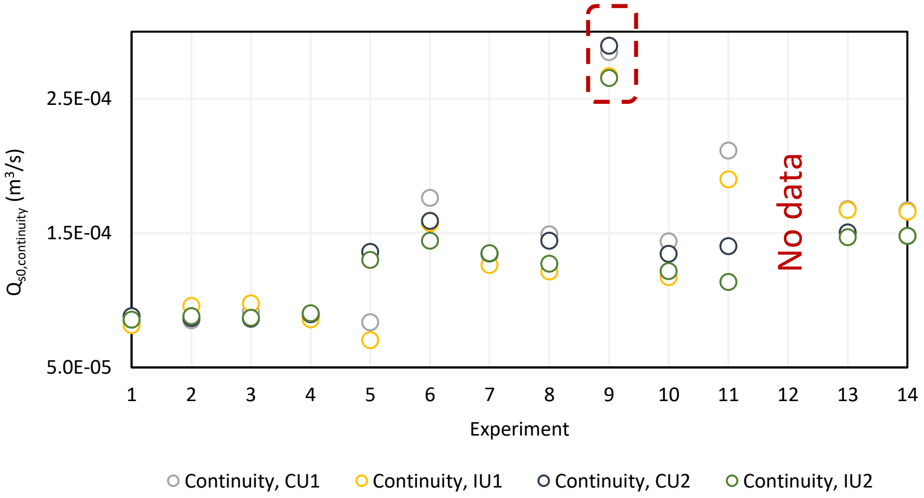

Figure 3-14 Value of $Q_{s0,continuity}$ for experiments AE01 to AE14.

3.3.4 Comparison of Q_{S0} value from different methods:

Figure 3-15 shows Q_{S0} for all the experiments which are obtained considering all the methods.

The results illustrate that, in all experiments, the value of $Q_{S0,Collector}$ is smaller than other values estimated from the continuity method. This issue can be rooted in the fact that the changes in sediment volume in the flume are considered in the continuity model. In contrast, the volume of sediment entries to the collector is assumed in the collector method. Moreover, During the experiments, all the particles may not go through the collector, so the value of $Q_{S0,\text{collector}}$ method is less than the value of $Q_{S0,\text{continuity}}$. Furthermore, this overestimation of the sediment going out in the continuity method could be due to ignoring either porosity between sediment particles in the bed or suspension.

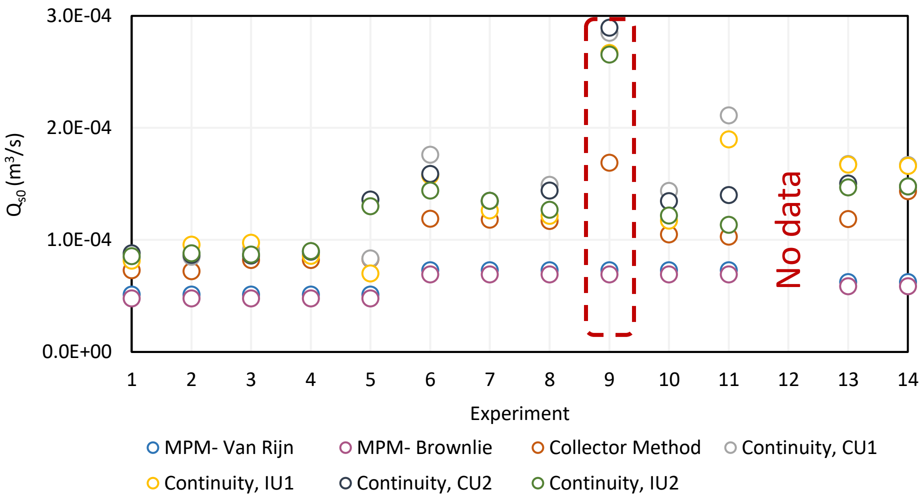

Figure 3-15 Comparison between different values of Qs0 obtained from different methods

3.3.5 Reference value of Q_{S0} for each experiment

In this part, according to the previous mentioned methods, the final value of Q_{S0} is reported for each experiment. Among them, MPM methods are calculated theoretically, and as explained earlier in 2.4.3, the first scenario of continuity method (IU1 and CU1), is less reliable in comparison with second scenario (IU2 and CU2). However, it can be highlighted that just in the experiment AE05, the first scenario is more harmonized with the results of experiments with the same water discharge (AE01 to AE04). This happens due to a failure related to forming a dam upstream that occurred during this experiment. So, for calculating the initial sediment transport capacity for each experiment, from different obtained Q_{S0} values, the average value of the collector method and second scenario of the continuity method (CU2 and IU2) is counted as a result of Q_{S0}. (See Table 3-2)

Table 3-2 Different obtained values of Qs0 (m³⁄s)

EXPERIMENT	Q_{S0} MPM, VAN RIJIN	Q_{S0} MPM, BROWNLIE	Q_{S0} CALLECTOR	Q_{S0} CONTINUITY (CU1)	Q_{S0} CONTINUITY (IU1)	Q_{S0} CONTINUITY (CU2)	Q_{S0} CONTINUITY (IU2)	Q_{S0} (m^3/s)
AE01	5.14E-05	4.80E-05	7.31E-05	8.38E-05	8.15E-05	8.80E-05	8.55E-05	8.31E-05
AE02	5.14E-05	4.80E-05	7.20E-05	8.49E-05	9.58E-05	8.66E-05	8.82E-05	8.31E-05
AE03	5.14E-05	4.80E-05	8.22E-05	9.15E-05	9.76E-05	8.61E-05	8.69E-05	8.31E-05
AE04	5.14E-05	4.80E-05	8.20E-05	8.75E-05	8.57E-05	8.96E-05	9.02E-05	8.31E-05
AE05	5.14E-05	4.80E-05	8.30E-05	8.35E-05	7.02E-05	1.36E-04	1.30E-04	8.31E-05
AE06	7.31E-05	6.92E-05	1.19E-04	1.76E-04	1.57E-04	1.59E-04	1.44E-04	1.41E-04
AE07	7.31E-05	6.92E-05	1.18E-04	1.34E-04	1.26E-04	1.35E-04	1.35E-04	1.29E-04

AE08	7.31E-05	6.92E-05	1.17E-04	1.49E-04	1.22E-04	1.44E-04	1.27E-04	1.29E-04
AE10	7.31E-05	6.92E-05	1.05E-04	1.44E-04	1.17E-04	1.35E-04	1.22E-04	1.20E-04
AE11	7.31E-05	6.92E-05	1.03E-04	2.11E-04	1.90E-04	1.40E-04	1.14E-04	1.19E-04
AE13	6.24E-05	5.88E-05	1.19E-04	1.68E-04	1.67E-04	1.50E-04	1.47E-04	1.39E-04
AE14	6.24E-05	5.88E-05	1.44E-04	1.67E-04	1.66E-04	1.48E-04	1.48E-04	1.46E-04

Also, to have an overview of all experiments, the sediment transport capacity in each water discharge can be calculated. In this way, the average Q_{S0} obtained considering all experiments with similar discharge can be noted as the sediment transport capacity of that water discharge (Table 3-3).

Table 3-3 the average value of Q_{S0} for each discharge

QWATER (l/s)	Q S0, AVERAGE (m^3/s)
5	8.31E-05
6	1.43E-04
7	1.28E-04

It should be highlighted that there is a contradiction between the estimated average value of Q_{S0} for each discharge. The average value of Q_{S0} belonging to water discharge equal to 6 l/s is more significant than that of 7 l/s. One reason for this is that the actual water discharge in the experimental work is different from the nominal water discharge ($Q_{nominal} = 5, 6, and\ 7\ l/s$) while conducting the experiment.

3.4 Froude number Fr analysis

Froude number Fr can play a significant role in recognizing some parameters such as eigenvalues λ and Local celerity C discussed in 2.5.

3.4.1 Froude number Fr

Since the Froude number Fr changes spatially and temporally, it would be helpful to see the Froude number color gradient map. Froude number Fr is influenced by two parameters: velocity and water depth. To better understand these parameters and their variations, the color maps of the average velocity and the water depth are shown and discussed in the following.

3.4.1.1 Water depth color gradient map

Water depth can be calculated by subtracting sediment surface elevation from water elevation. For example, Figure 3-16 shows the water depth value for experiments AE13 and AE14. It is clear that in AE13, water depth approximately stays in the same stage and has a minimum value downstream. It is happening for experiment AE14 similarly, but the water depth is not a minimum value downstream.

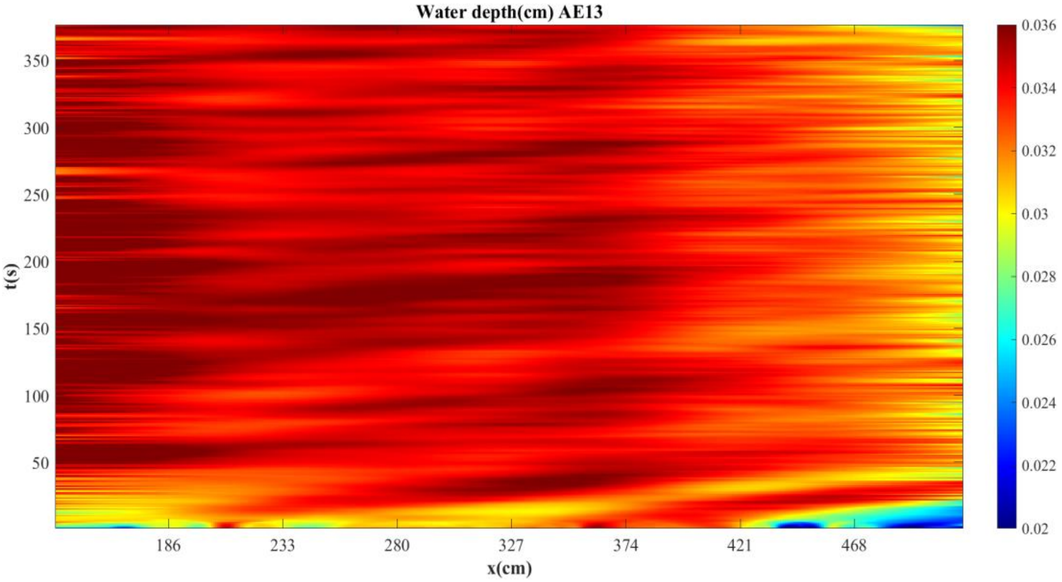

a)

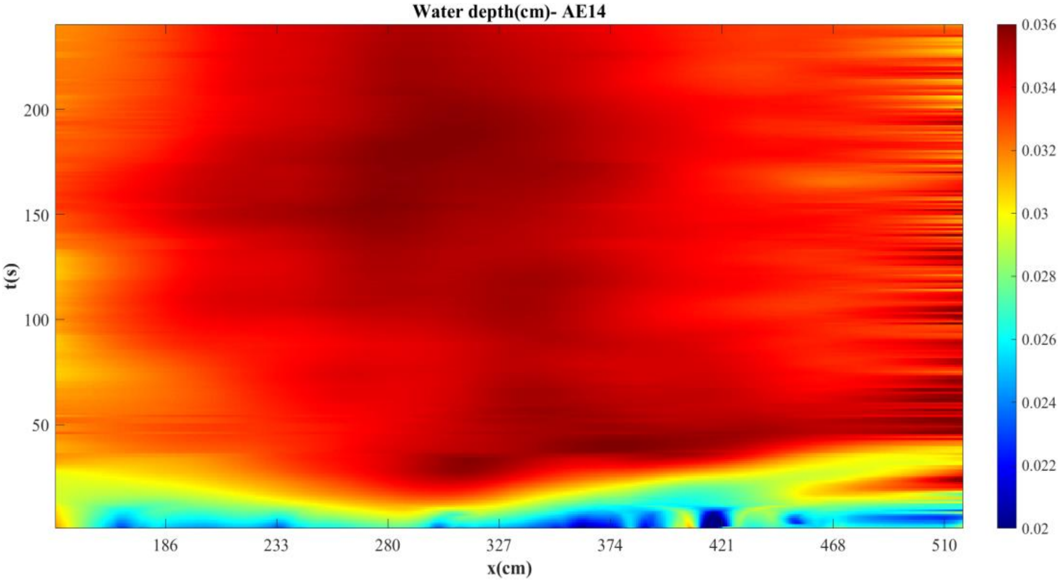

b)

Figure 3-16 Water depth color map gradient. a) experiment AE13. b) experiment AE14.

3.4.1.2 Average velocity color gradient map

Figure 3-17 illustrates the average velocity, calculated by dividing a constant flow discharge by the cross-section area. The maximum velocity value is related to initial times by considering the assumption of constant water discharge. However, this assumption is not fully correct due to the second reason that is discussed in 3.2. Furthermore, in Figure 3-17.a (AE13), related to a near-equilibrium situation, the velocity downstream is higher than in other parts. The reason behind this phenomenon needs more investigation in the future.

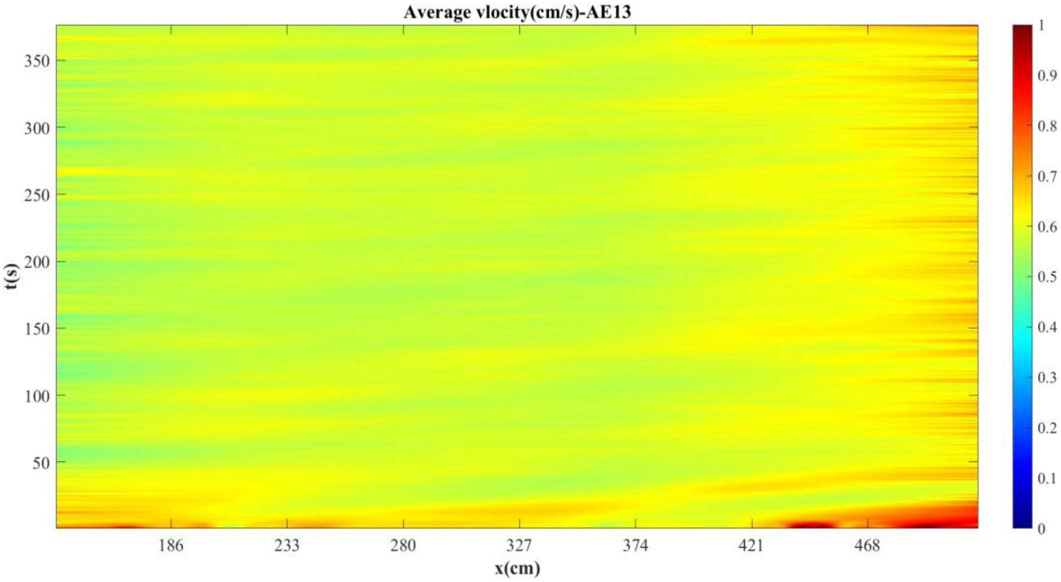

a)

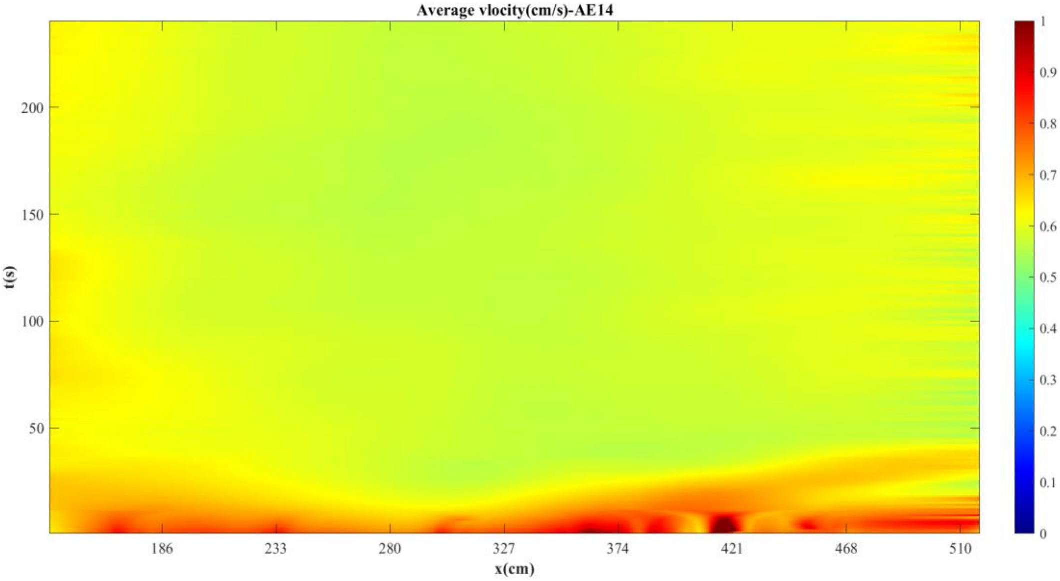

b)

Figure 3-17 Average velocity of flow. a) experiment AE13. b) experiment AE14.

3.4.1.3 Froude number Fr color gradient map

The color gradient maps of Froude number Fr for experiments AE13 and AE14 are shown in Figure 3-18. In experiment AE13, the value of the Froude number Fr fluctuates around one upstream and middle of the channel; however, it reaches the maximum value downstream. In experiment AE14, the Froude number Fr value correspondence to upstream and downstream are the maximum value while around one in the middle of the channel. Also, it should be highlighted that in both experiments (AE13 and AE14), the values of the Froude number Fr are the highest at initial times due to the reason that is discussed in 3.2.

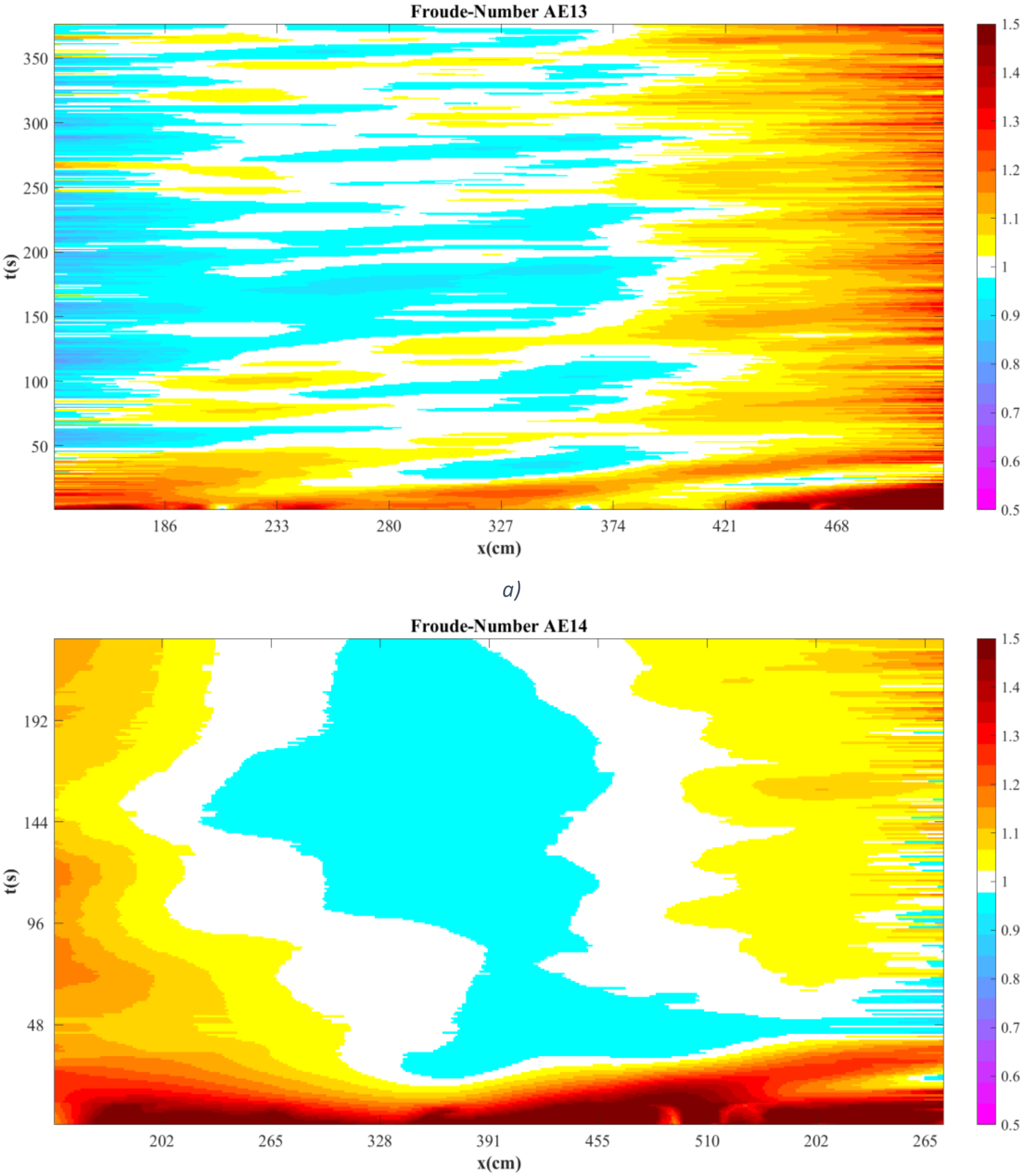

a)

b)

Figure 3-18 Froude number Fr color gradient map. a) experiment AE13. b) experiment AE14.

3.4.2 Average Froude number Fr

By considering Figure 3.18, the Froude number Fr changes in time and space. In order to convert this continuous space-time variable to one representative value, one can take the average in various ways (the entire map, by rows, by columns, and by a rectangle). It is worth mentioning that the region over which the average is taken is crucial.

Figure 3-19 shows the average Froude number Fr considering rows and columns, respectively. Results illustrate that experiments AE10 and AE11 have average Froude number Fr of more than one ($Fr > 1$), while other experiments possess average Froude number Fr around one ($Fr \approx 1$). The high value of this parameter in experiments AE10 and AE11 can be due to the high value of the Loading ratio Lr. In experiments with a high Loading ratio Lr, the variation of sediment profiles is higher, and the slope is more; therefore, the flow velocity in these experiments is more than in the experiment with less Loading ratio Lr and leads to higher Froude number Fr. This relation is also illustrated by results of Froude number Fr versus Loading ratio Lr plot that provided in 3.7.

There is a point in Figure 3-19, in trial AE07, the discharge is larger than AE13, so it is expected to have a more significant Froude number Fr; instead, the results show smaller values average of Froude number Fr. By comparing the water depth related to these experiments, it can be understood that it happens since the water depth of AE07 is larger than AE13.

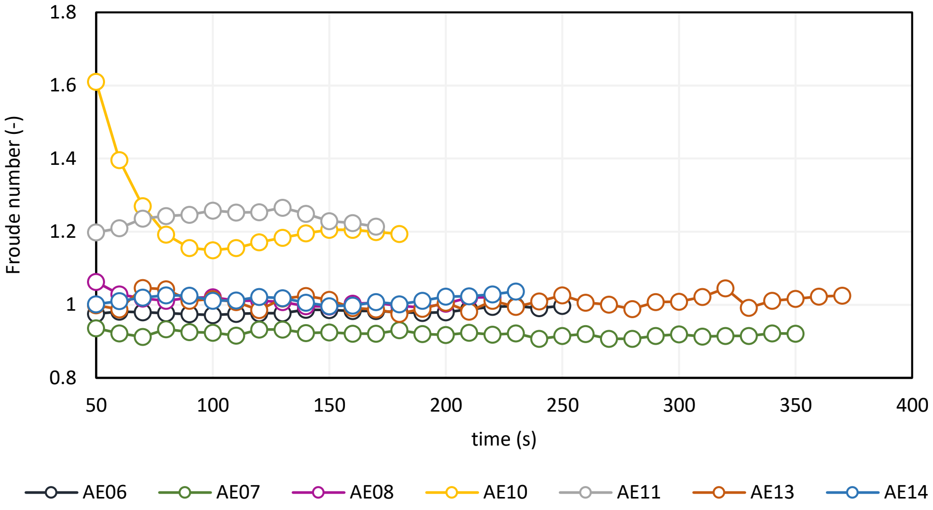

a)

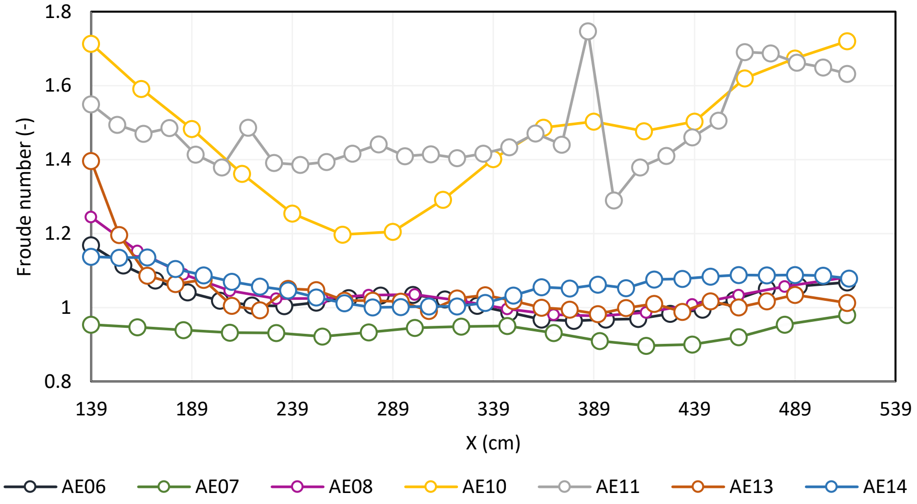

b)

Figure 3-19 Average Froude number Fr. a) by rows. b) by columns.

Moreover, comparing figures (a) and (b) in Figure 3-19 illustrates that averaging by rows shows more stable trends than by columns. This is reasonable considering that a temporal response would be swifter than a spatial one.

Therefore, by considering this plot of averaging by rows and Froude number gradient colormap, one may conclude that in experiments AE06 and AE07, the Froude number Fr is smaller than one ($Fr < 1$), which shows that the subcritical flow is dominant in these experiments. In contrast, in experiments AE10 and AE11, the flow type is supercritical. Moreover, in experiments AE08, AE13, and AE14, the Froude number Fr is almost equal to one ($Fr \approx 1$), which shows that the critical flow is dominant in these experiments.

The type of flow for experiments AE01 to AE04 were considered as supercritical flow by Heydari (Heydari, 2020), and then in Eslami thesis (Eslami et al., 2021), due to changing the measurement method of bed profile , the type of flow for these experiments was changed to subcritical flow. However, in this current thesis, these experiments are not considered in Figure 3-19 due to lack of time needed to recompute the data.

In the current thesis, based on the modification of measurement methods, the type of flow in experiments AE06 and AE07 is changed to subcritical, and AE08 is changed to almost critical flow; experimentally, however, these experiments are considered as supercritical flow by Eslami and his colleagues (Eslami et al., 2021).

It is worth mentioning that, in the previous thesis (Eslami et al., 2021) and (Heydari, 2020), no specific Froude number Fr was reported experimentally while the gradient maps were produced. However, the type of flow was reported visually. Table 3-4 shows the summary of this issue.

Table 3-4 The type of flow reported during the campaign

EXPERIMENT	HEYDARI, 2020	ESLAMI ET AL., 2021	CURRENT THESIS (Fr)	
AE 01	Supercritical	Subcritical	-	
AE 02	Supercritical	Subcritical	-	
AE 03	Supercritical	Subcritical	-	
AE 04	Supercritical	Subcritical	-	
AE 05	Supercritical	Supercritical	-	
AE 06	-	Supercritical	Subcritical	(0.934)
AE 07	-	Supercritical	Subcritical	(0.893)
AE 08	-	Supercritical	Critical	(0.974)
AE 10	-	-	Supercritical	(1.191)
AE 11	-	-	Supercritical	(1.231)
AE 13	-	-	Critical	(1.016)
AE 14	-	-	Critical	(1.013)

3.5 Celerity analysis

In this part, the value of celerity is found in two different scenarios discussed in 2.5, and the results are shown as color gradient maps. Then the results of the two scenarios compare with each other, and the comparison aims to know how two different concepts are similar. As mentioned before, the value of Local celerity C is based on referenced profiles, elevation profiles referenced concerning the channel slope (1.2%), in this research.

3.5.1 Local celerity C

As mentioned in 2.5.1, the Local celerity C can be calculated by dividing two equations $\frac{\partial Z}{\partial t}$ and $-\frac{\partial Z}{\partial x}$. In discrete form, equations are equal to $\frac{\Delta z}{\Delta t}$ and $-\frac{\Delta z}{\Delta x}$, in which Δt and Δx always possess positive value but $\Delta z = (z_2 - z_1)$ can be positive or negative. It would be positive if $Z_2 > Z_1$ and it is negative in another way. Therefore, Local celerity C can possess either positive or negative value depend on Δz.

3.5.1.1 *Color* gradient *of local celerity*

In this part, Local celerity C related to AE13 and AE14 is shown in Figure 3-20 as an example.

Figure 3-20.a shows that in experiment AE13, in which the channel is close to equilibrium condition, the value of Local celerity C changes slightly and fluctuates around zero.

For experiment AE14 (Figure 3-20.b), the generated profiles in initial times show the aggradation and degradation upstream and downstream, respectively. The Local celerity map shows the maximum value in these locations. While, after the initial times when the channel is close to equilibrium condition, the Local celerity C has a value around zero. However, the value of Local celerity C in this condition could be infinite.

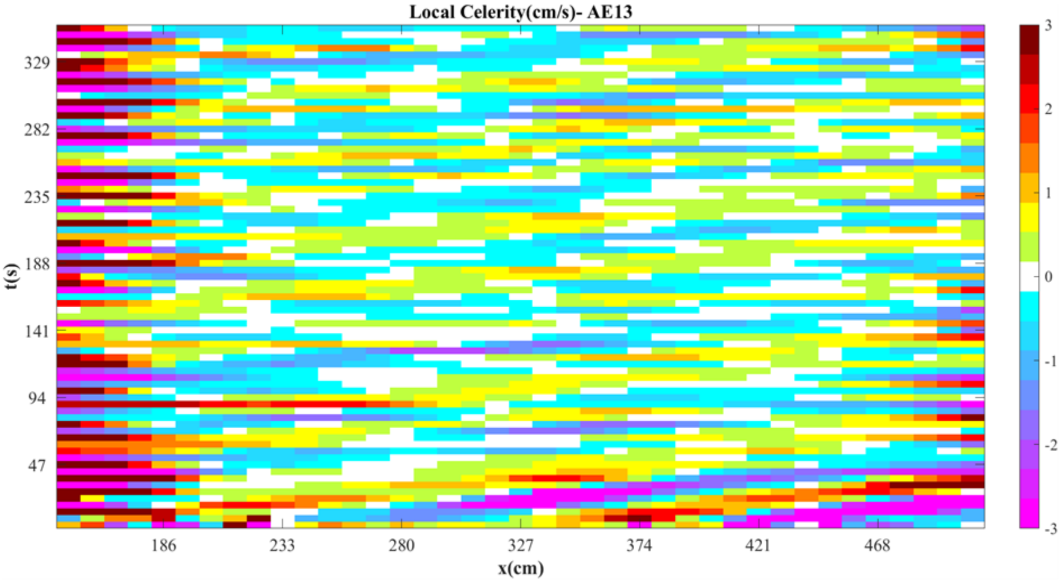

a)

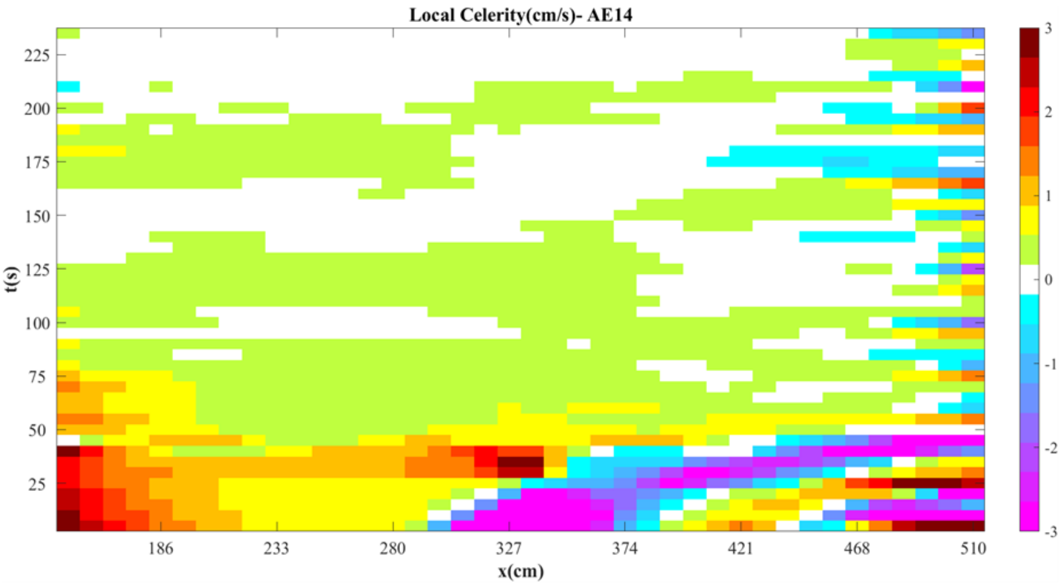

b)

Figure 3-20 Color gradient map of Local celerity C. a) experiment AE13. b) experiment AE14.

3.5.1.2 Average of local celerity

In this part, the average values of Local celerity C in each row after the initial time and in each column are calculated from the time-space local celerity matrix. Therefore, the comparison of Local celerity C is more facilitated. Figure 3-21 and Figure 3-22 show the temporal and spatial evolution of this value for experiments AE13 and AE14, respectively.

Figure 3-21 shows that, the Local celerity C periodically changes from upstream to downstream during experiment AE13. Additionally, this value decreases to around zero during the experiment AE14.

Figure 3-22 illustrates that the Local celerity C is close to zero from upstream to downstream in experiment AE13. In contrast, , this value is maximum upstream and decreases to zero downstream in experiment AE14.

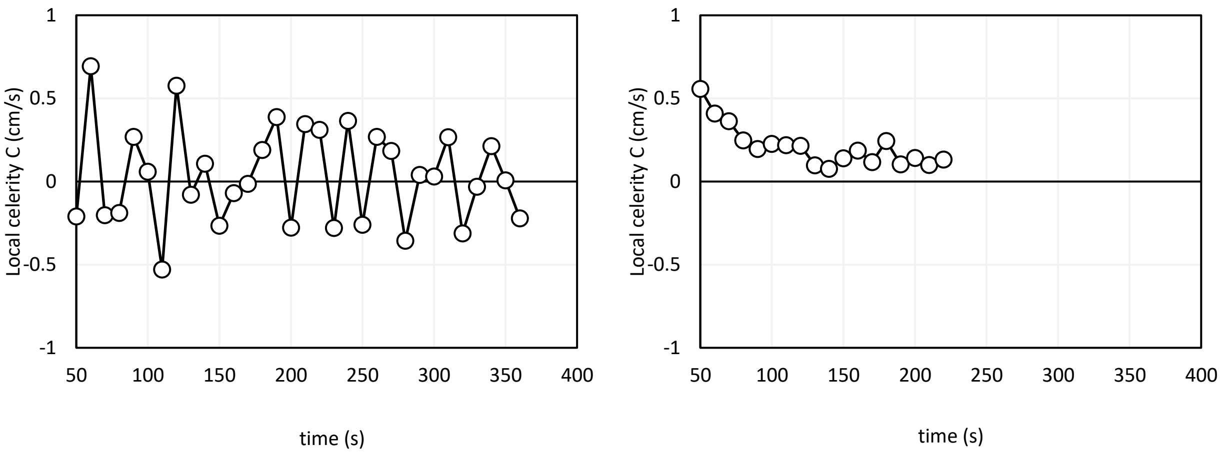

a) *b)*

Figure 3-21 Temporal evolution of average Local celerity C. a) experiment AE13. b) experiment AE14.

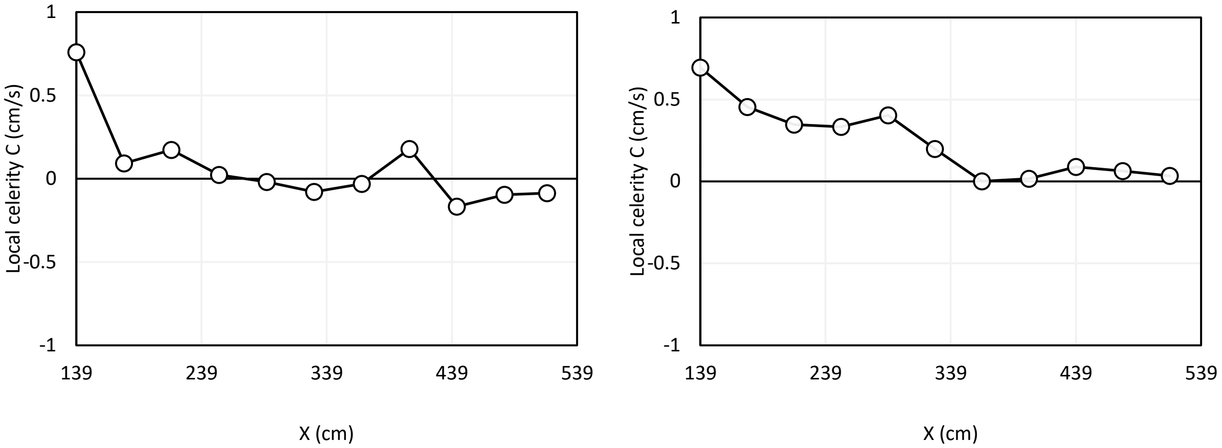

a) *b)*

Figure 3-22 Spatial evolution of average Local celerity C. a) experiment AE13. b) experiment AE14.

Figure 3-23 illustrates the temporal and spatial evolution of Local celerity C in all experiments. The results show that in most times and spaces, the Local celerity C in experiments AE10 and AE11 is higher than in other experiments. This issue may be rooted in the fact that these two trials have the highest Loading ratio Lr. The trend of experiments AE07 and AE13 are almost similar because both are in nearly equilibrium conditions. The average Local celerity C for both fluctuates around zero as there may not be evident aggradation or degradation in nearly equilibrium conditions. This issue can confirm that the method for Local celerity calculation works correctly.

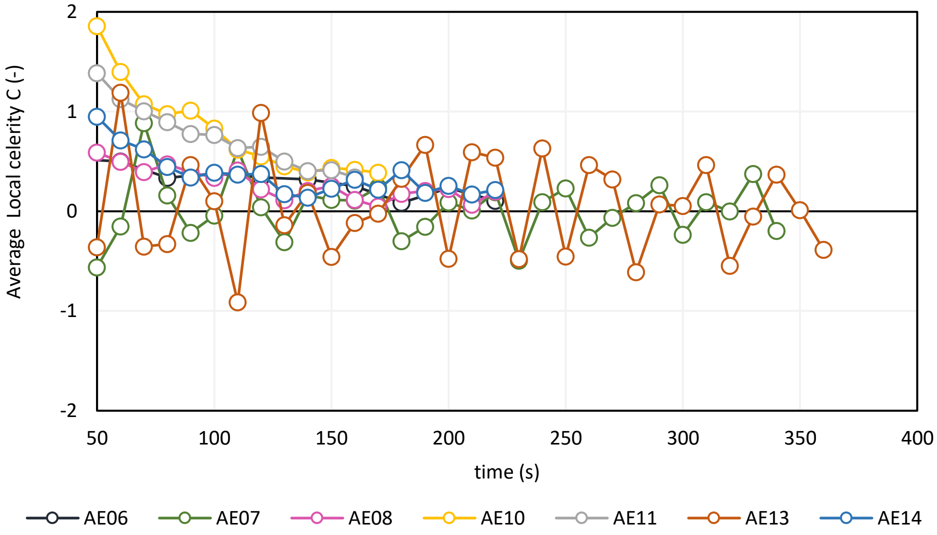

a)

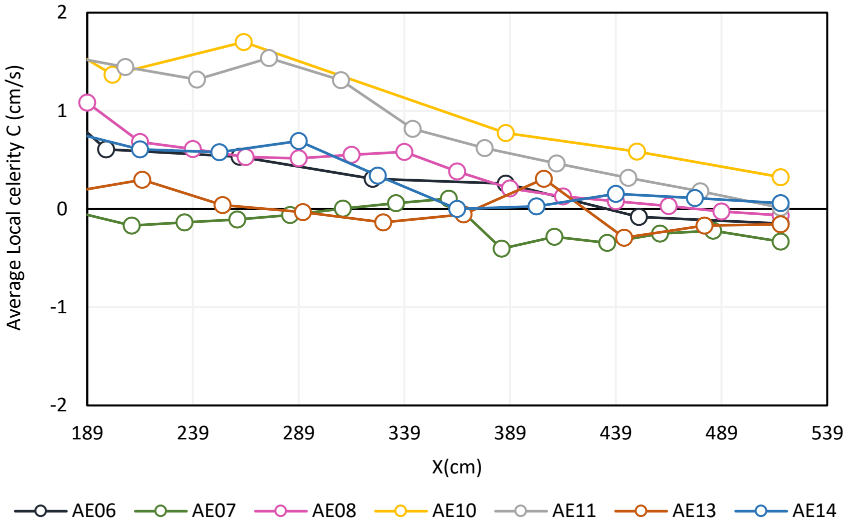

b)

Figure 3-23 Comparison of dimensionless average Local celerity during a) time b) Space

3.5.2 Eigenvalues λ

As mentioned in 2.5.2, the eigenvalues λ are estimated by solving the Equation 2-30, Equation 2-31 and Equation 2-32. These parameters might somehow show the values of celerity theoretically (Lyn and Altinakar, 2002).

3.5.2.1 Color gradient maps of eigenvalues λ

Figure 3-24, Figure 3-25 and Figure 3-26 show the value of $\lambda_1, \lambda_2, and\ \lambda_3$ belonged to experiments number AE13 and AE14 at different times and in various spaces, respectively . The results show that the value of $\lambda_1\ and\ \lambda_3$ do not change significantly, but the value of λ_2 have variation in times and spaces. λ_1 has the highest value in most experiments because it calculates using the equation V+$\sqrt{gd}$ which is summing up two positive quantities. While λ_3 results from the equation V-$\sqrt{gd}$ which subtract the two quantities, so it has smaller value. Both of them are related to water.

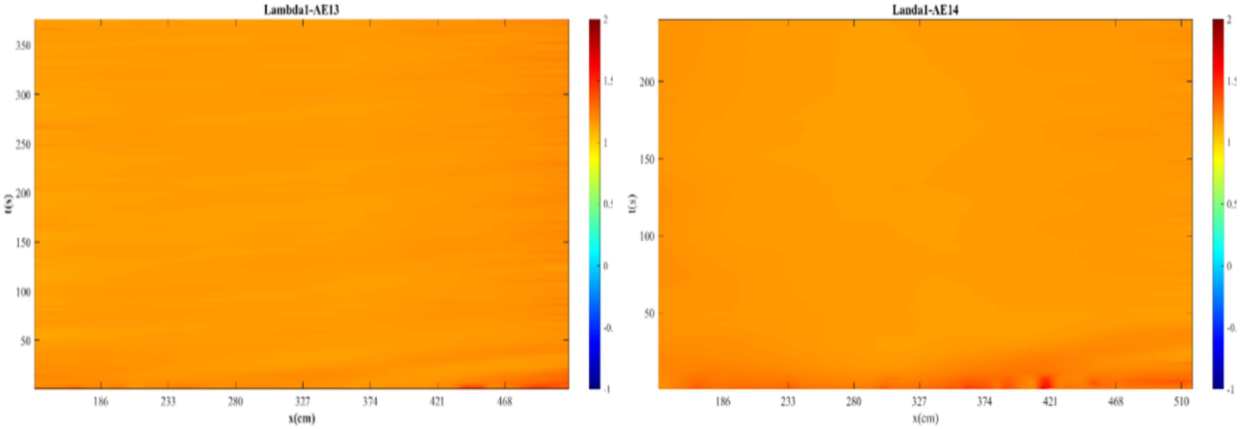

a) *b)*

Figure 3-24 Color gradian map of λ1. a) experiment AE13. b) experiment AE14.

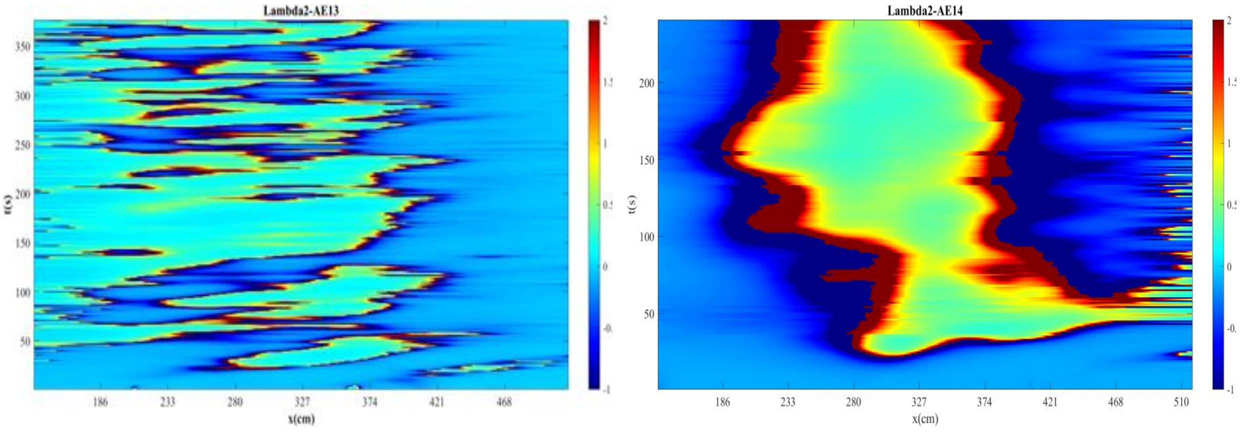

a) *b)*

Figure 3-25 Color gradian map of λ2. a) experiment AE13. b) experiment AE14.

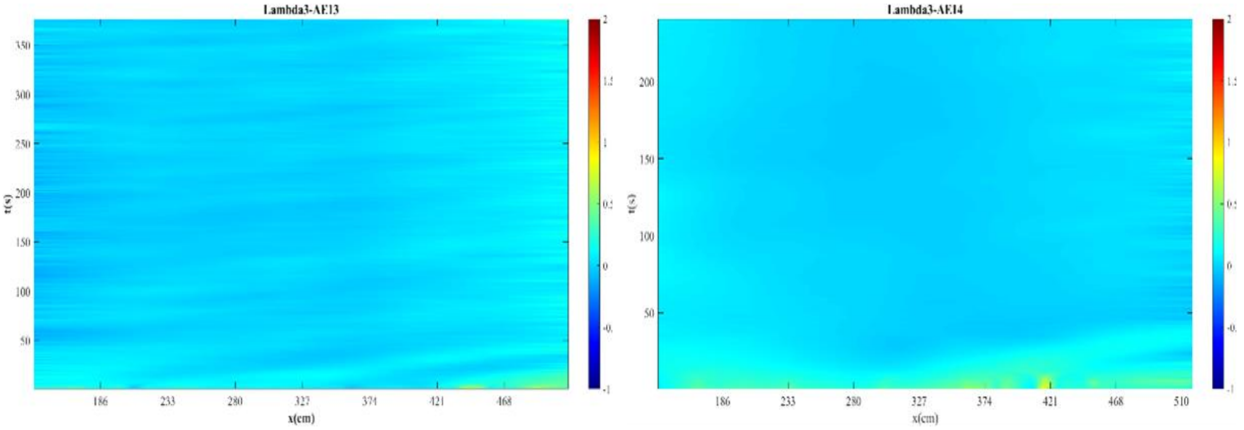

a) *b)*

Figure 3-26 Color gradian map of λ3. a) experiment AE13. b) experiment AE14.

3.5.2.2 Average of eigenvalues λ

Like the Local celerity C , the average value of different eigenvalues λ can be calculated; so, comparing them could be eased in this way. It is worth presenting average Local celerity C and eigenvalues λ in the same plot to detect any possible relations. So that, Figure 3-27 and Figure 3-28 Presentation of average local celerity C and eigenvalues λ of experiments in different spaces. Show the average eigenvalues λ and average Local celerity C of experiments at various times and spaces, respectively. As mentioned in previous part (3.5.2.1), the average value of λ_1 is mostly larger than two other eigenvalues λ. Moreover, λ_2 fluctuates and it is rarely larger than λ_1 but mostly larger than λ_3 during time and space, except in experiments AE10 and AE11, which λ_2 is mostly constant and smaller than $\lambda_3$over the time and in different spaces.

It is required to highlight that there is a significant gap between average Local celerity C and λ_1 in most experiments, while it is closer to λ_2 and λ_3, specifically when averaging is done at different times. In experiments AE07 and AE13 which are close to equilibrium condition, the values of λ_2 are close to the value of average Local celerity C in different times.

Although there might be some similarities between Local celerity C and eigenvalues λ in some situations, differences are significant, which can be rooted in the fact that these two parameters are conceptually different; estimation of the Local celerity C is based on the elevation matrices, while the evaluating of eigenvalues λ are based on taking derivate of the characteristic line which may be related to many parameters.

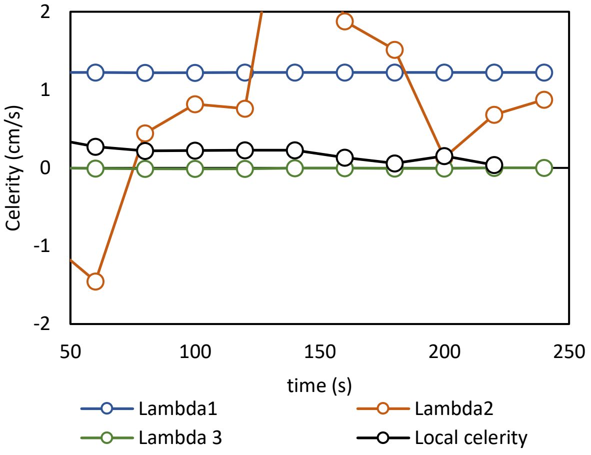

AE06

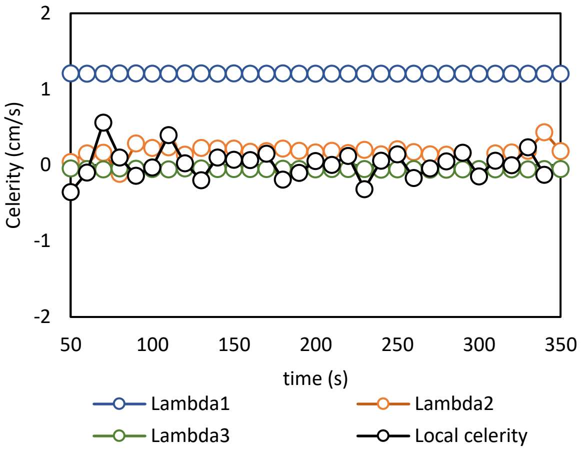

AE07

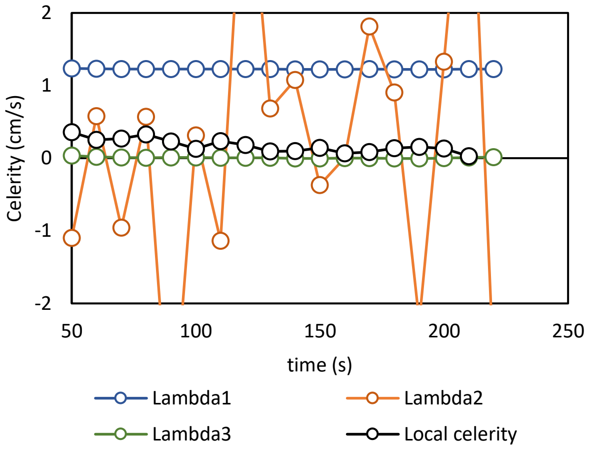

AE08

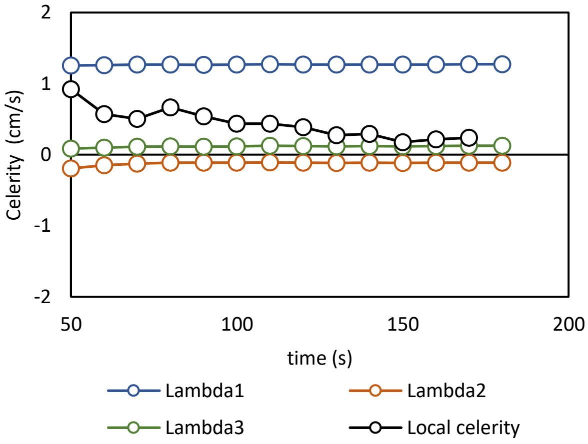

AE10

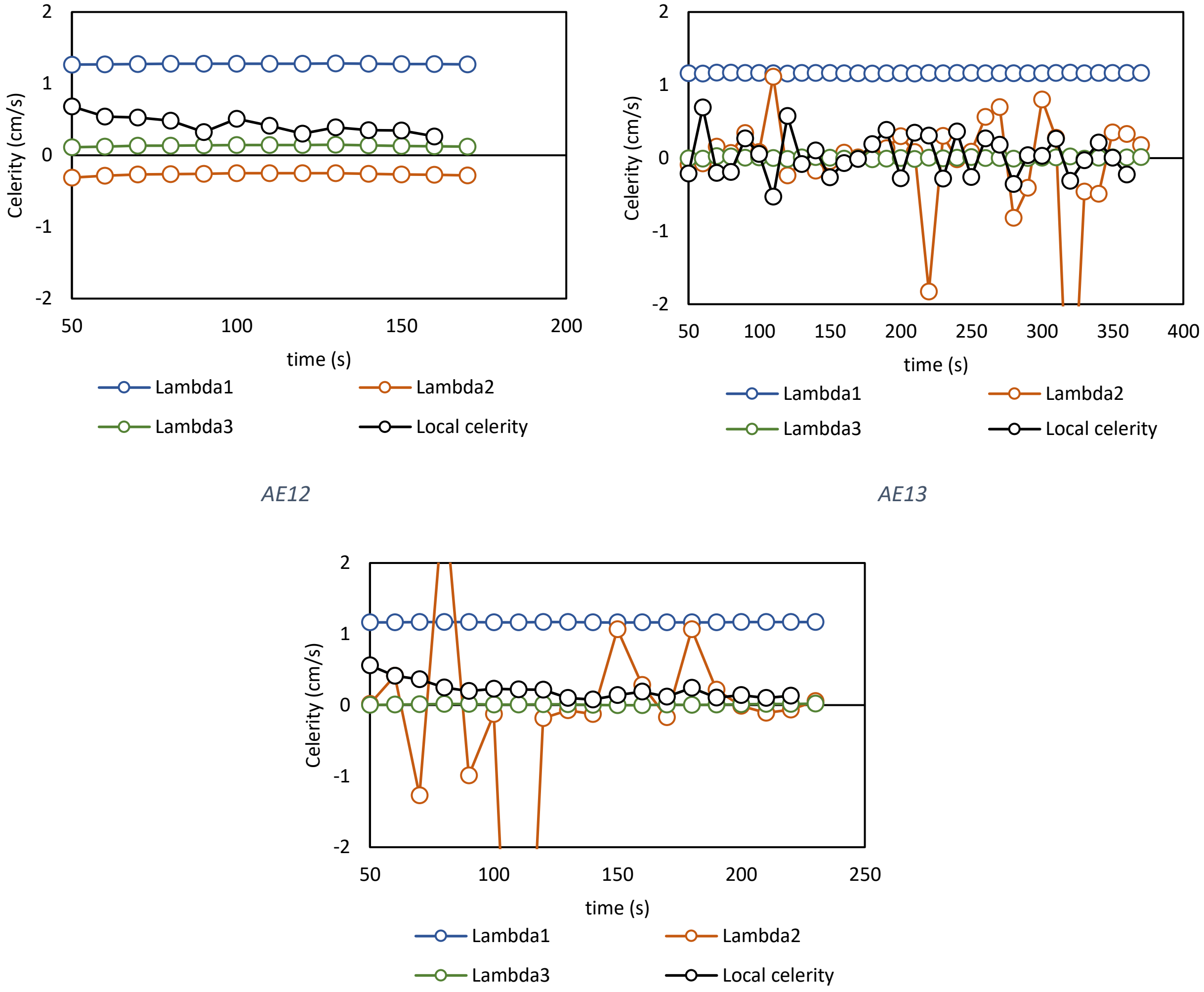

AE12

AE13

AE14

Figure 3-27 Presentation of average local celerity C and eigenvalues λ of experiments at different times.

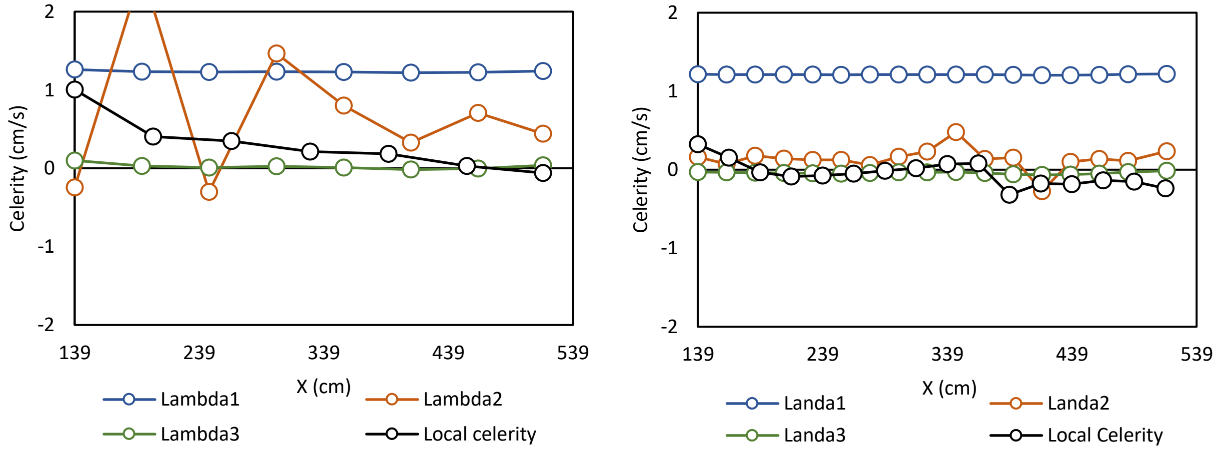

AE06

AE07

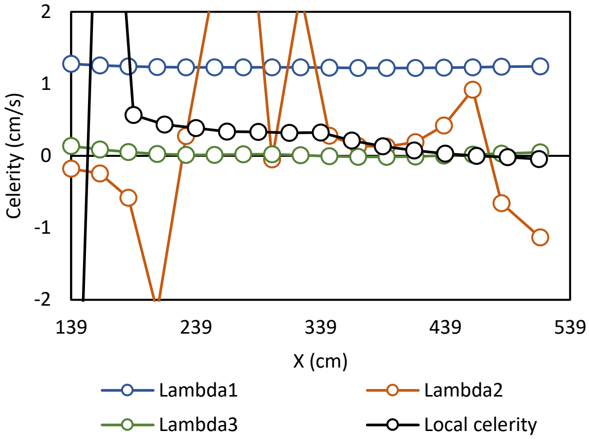

AE08

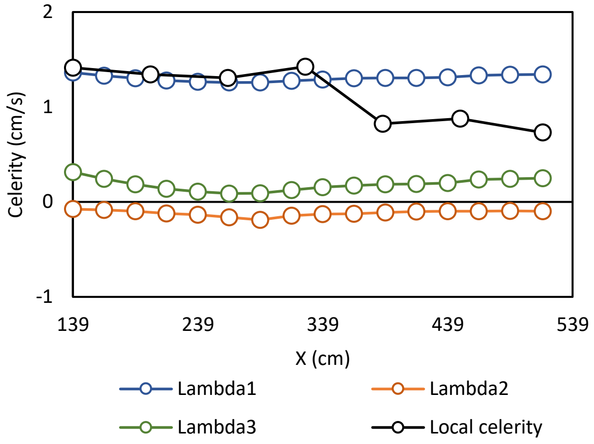

AE10

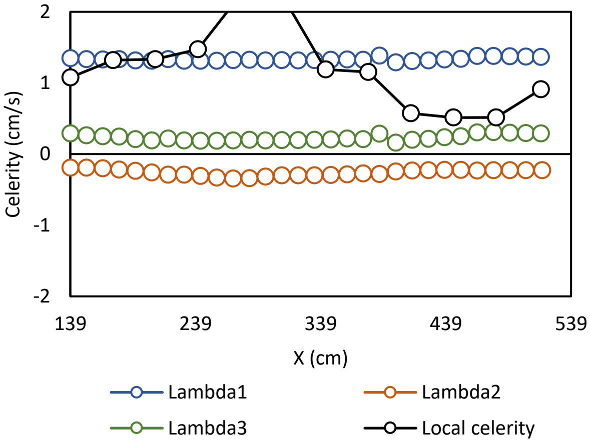

AE11

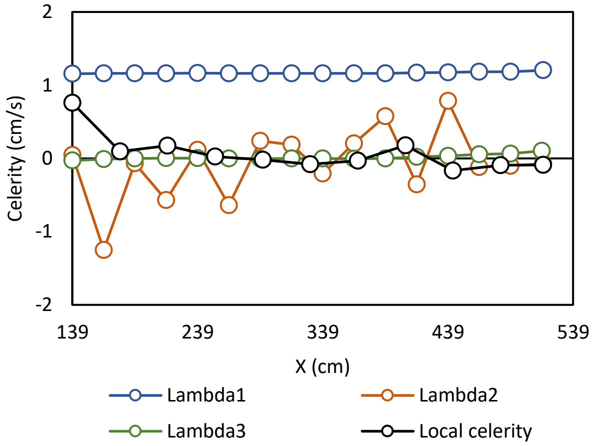

AE13

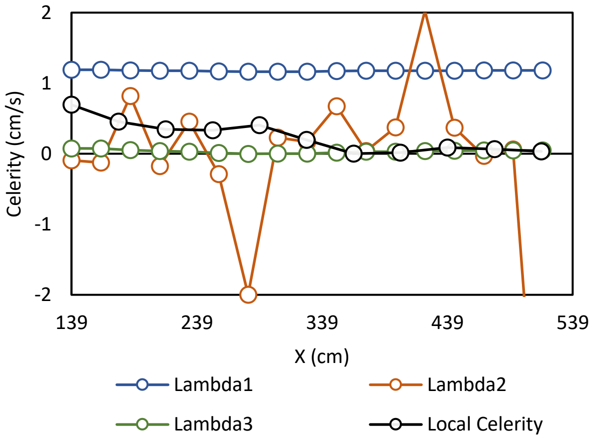

AE14

Figure 3-28 Presentation of average local celerity C and eigenvalues λ of experiments in different spaces.

3.6 Numerical analysis

In this part, the outcomes of numerical simulations are presented, which compare the uncalibrated and calibrated numerical model with experimental results, respectively. Furthermore, the values of equivalent parameters are provided for all experiments. Moreover, the obtained Manning's coefficient n are plotted based on Froude number Fr and Loading ratio Lr.

3.6.1 Determination of equivalent parameters based on numerical simulation

The numerical simulation results before calibration (considering Manning's coefficient n is equal to $0.015\ s/m^{\frac{1}{3}}$ and Bedload factor α is equal to 1) are compared with the experimental work. Figure 3-29 and Figure 3-30 compare the spatial evolution of bed and water surface in experimental and uncalibrated numerical works at selected times in AE13 and AE14.

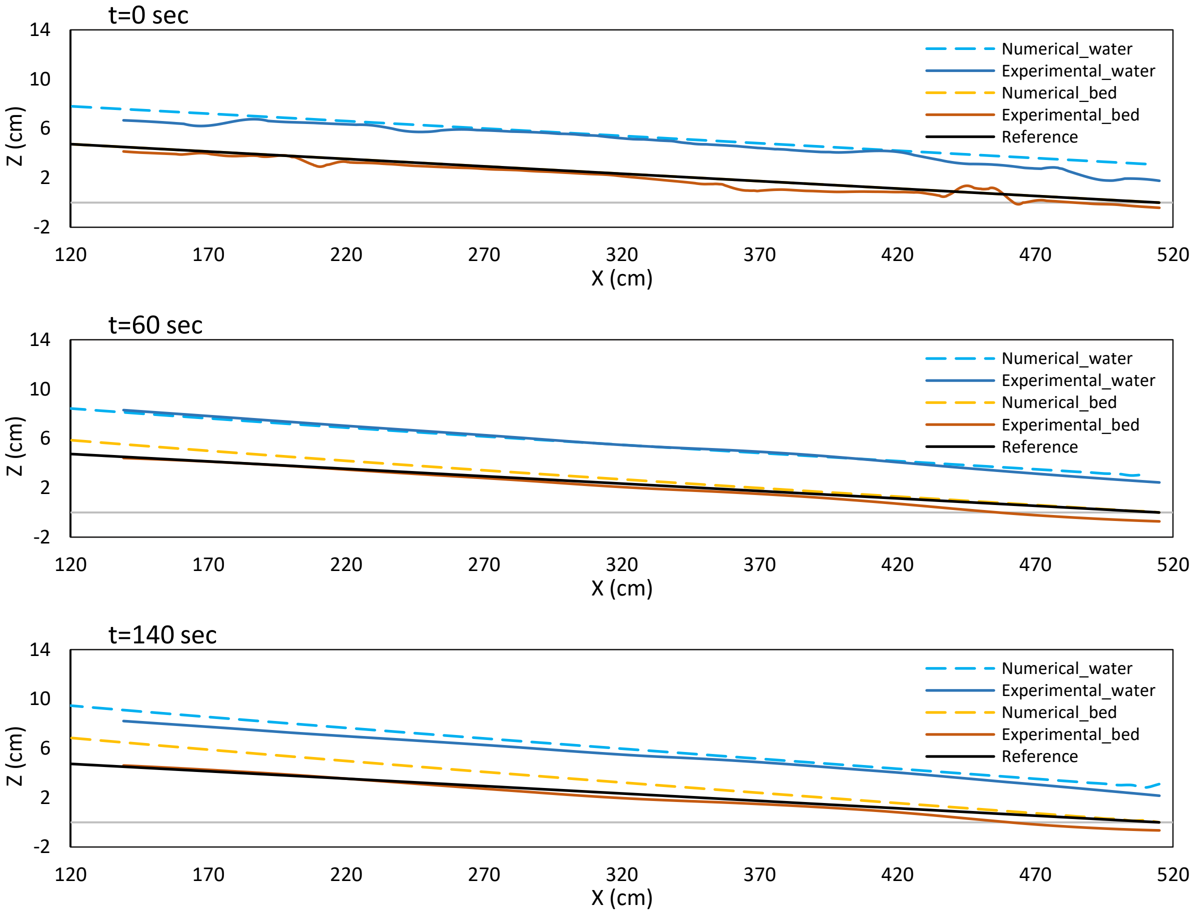

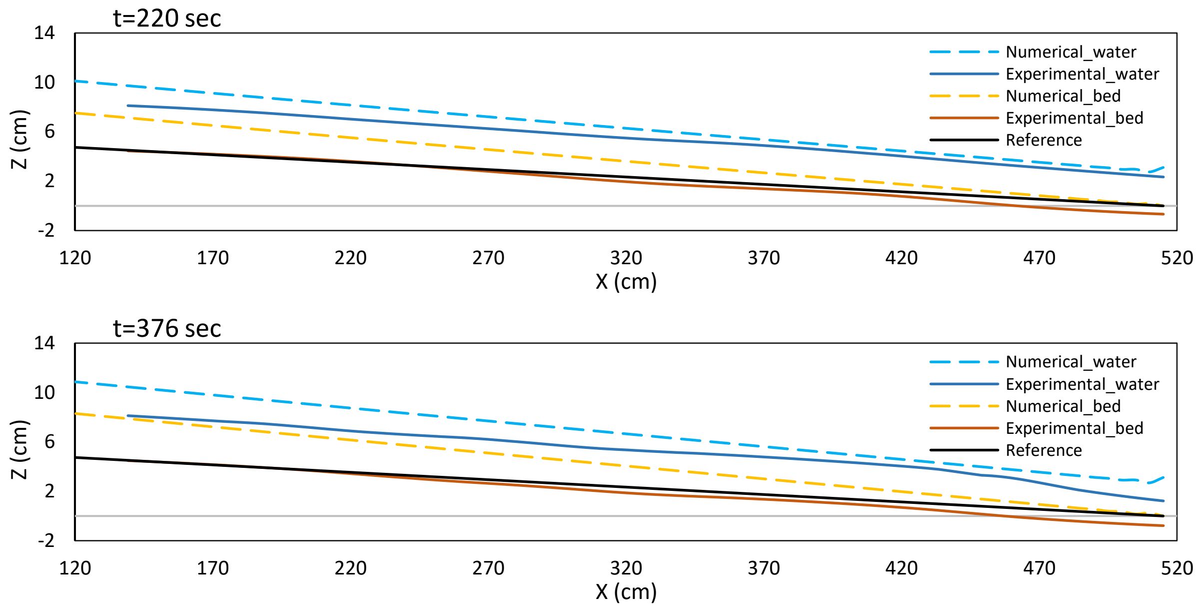

Figure 3-29 Comparison between experimental and uncalibrated numerical results- Spatial evolution of bed and water surface at selected times for AE13 (Loading ratio Lr *= 1.07)*

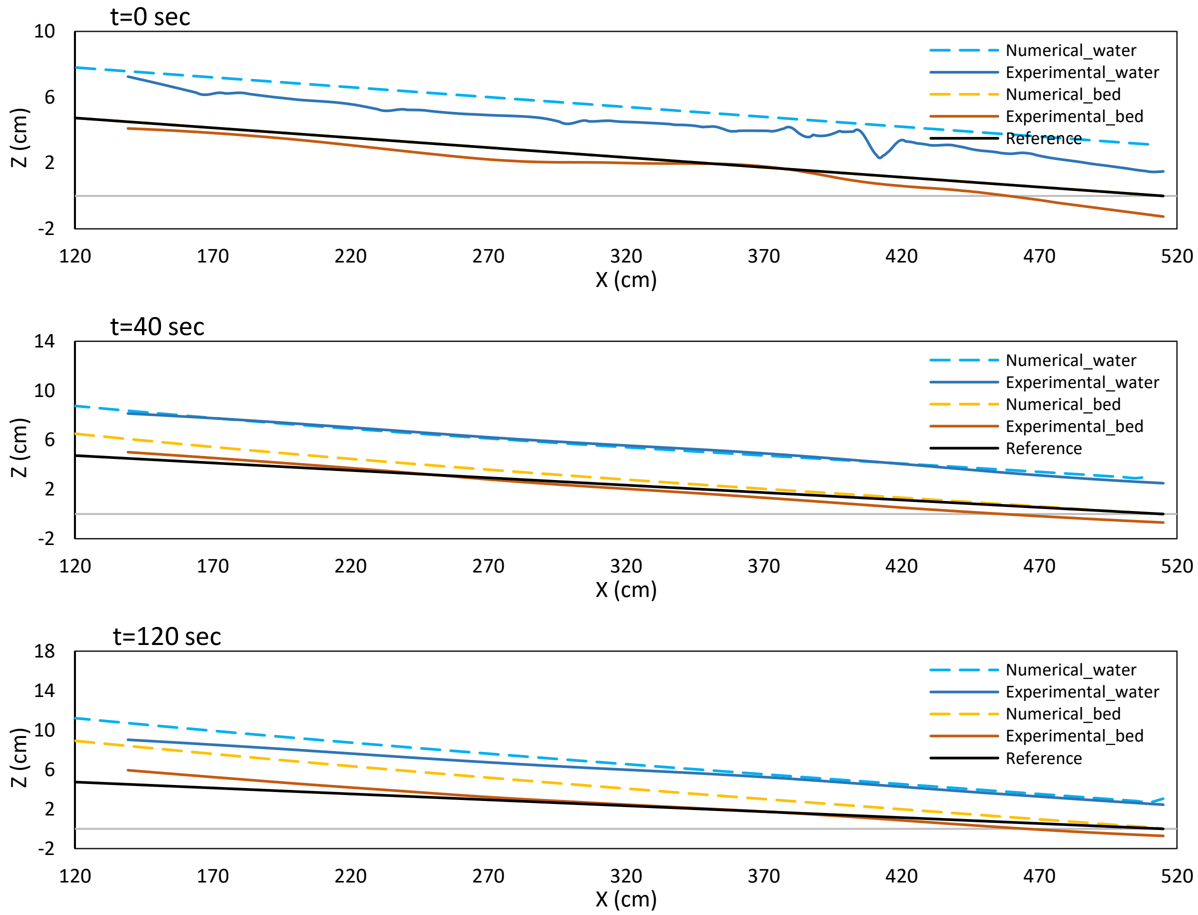

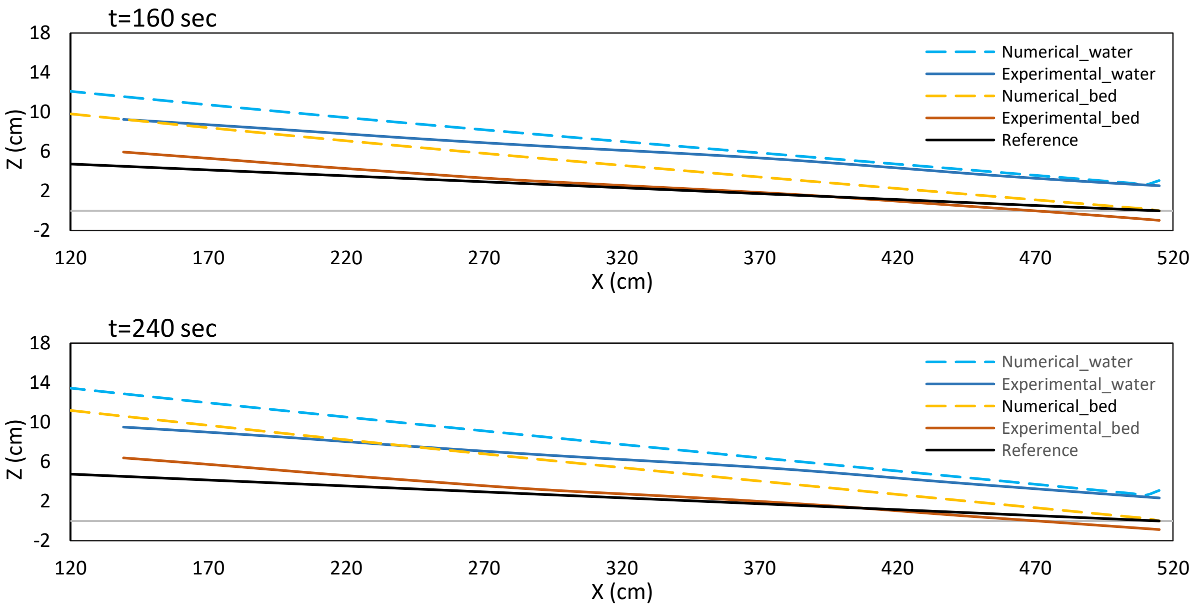

Figure 3-30 Comparison between experimental and uncalibrated numerical results- Spatial evolution of bed and water surface at selected times for AE14 (Loading ratio Lr= 1.76)

Figure 3-31 and Figure 3-32 compare the temporal evolution of bed and water surface in experimental and uncalibrated numerical works at selected locations in AE13 and AE14.

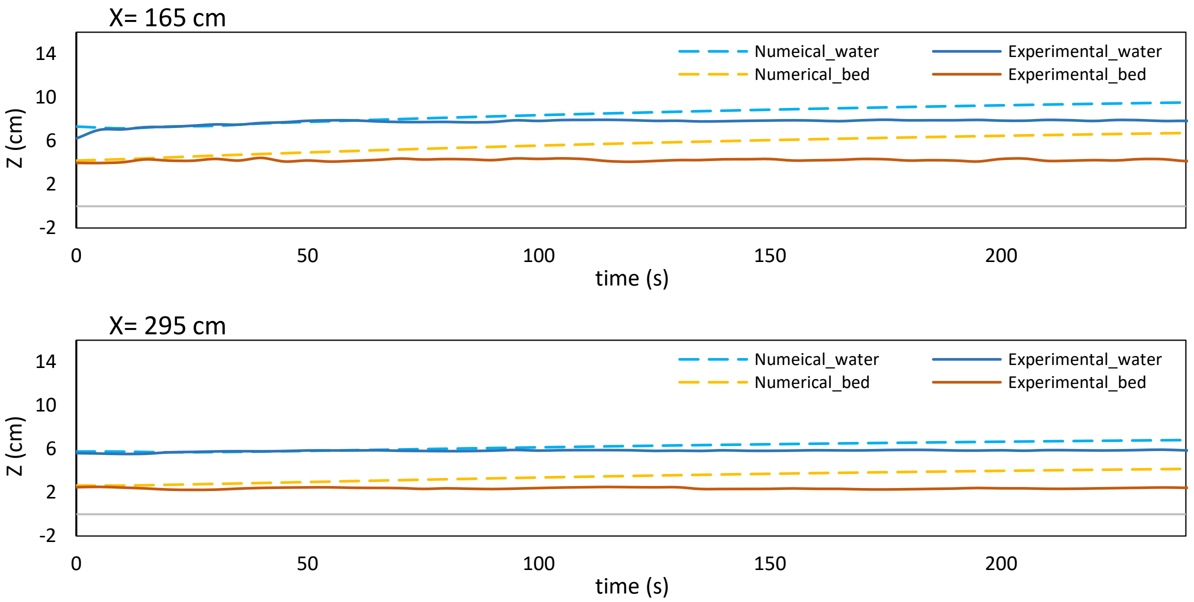

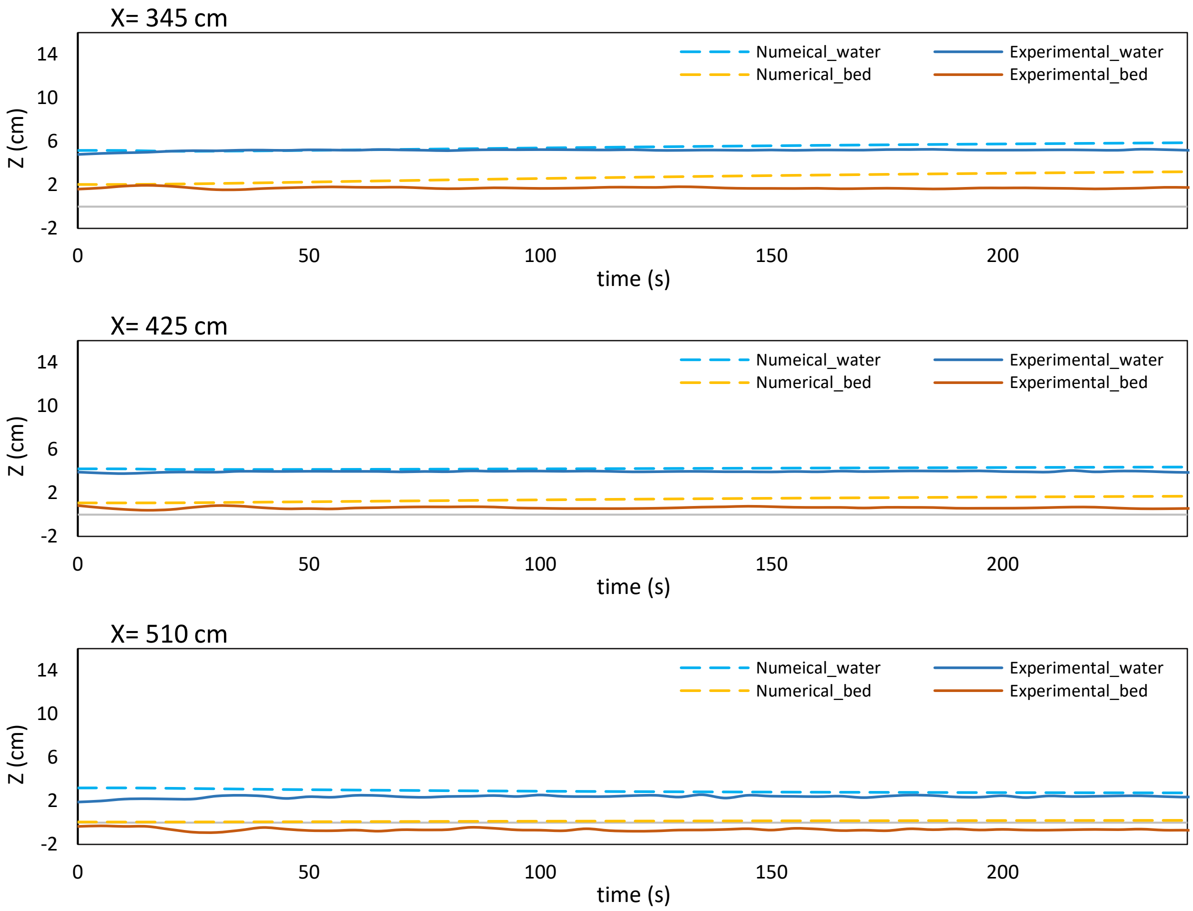

Figure 3-31 Comparison between experimental and uncalibrated numerical results- Temporal evolution of bed and water surface at selected locations for AE13 (Loading ratio L_r= 1.07)

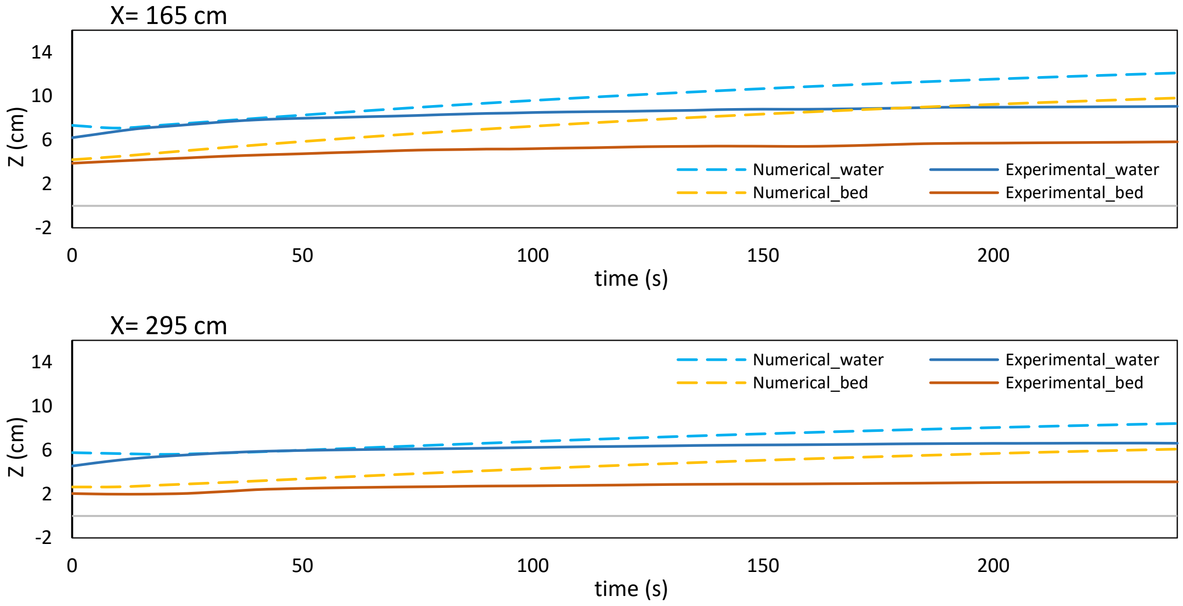

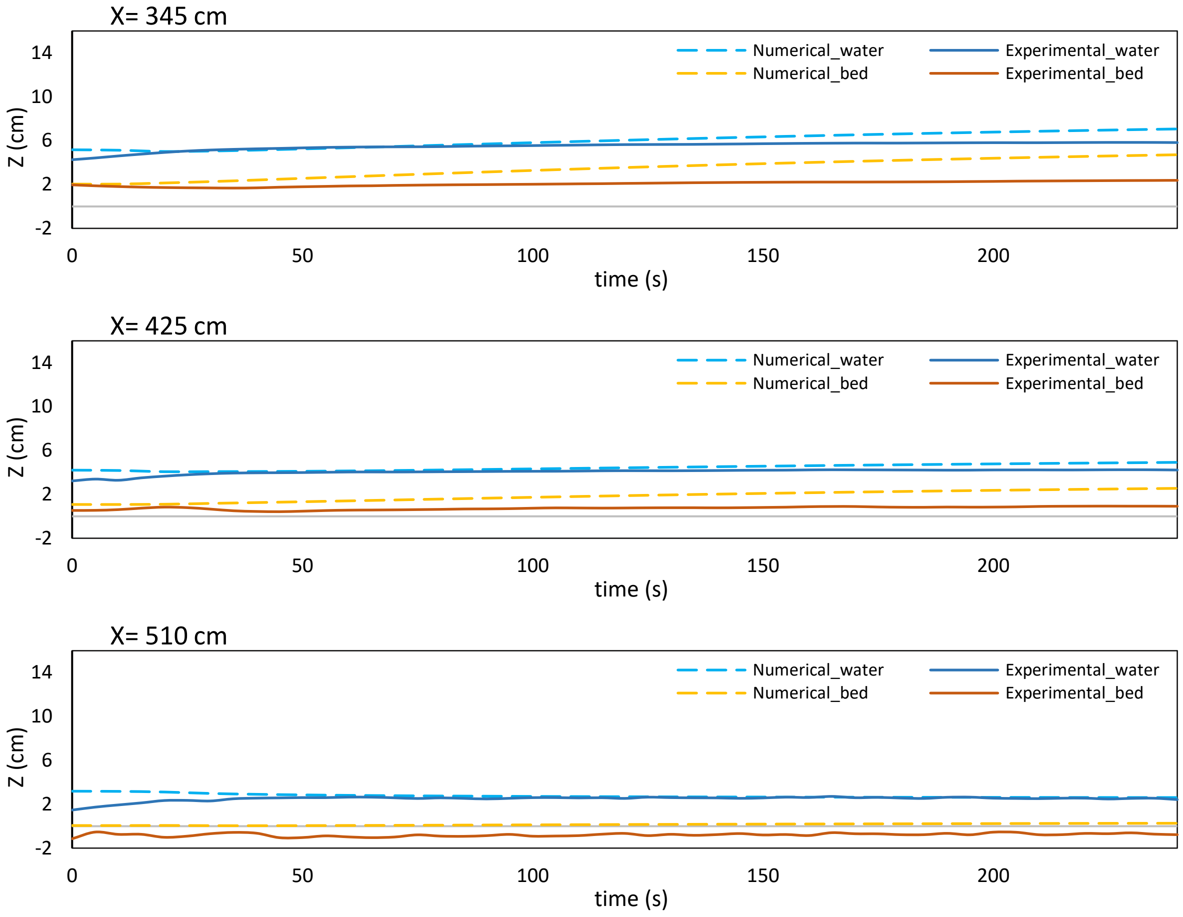

Figure 3-32 Comparison between experimental and uncalibrated numerical results- Temporal evolution of bed and water surface at selected locations for AE14 (Loading ratio Lr= 1.76)

By considering these comparisons, some points need to be highlighted.

First, bed elevations in the initial numerical analysis (uncalibrated model) are always higher than those in the experimental one. This inconsistency between results has happened since the initial sediment transport capacity Q_{s0} calculated by the software is much less than the experimental one. For instance, the initial sediment transport capacity from the experimental work AE14 has been obtained $Q_{s0} = 1.46E - 04\ m^3/s$, while this quantity is calculated as$Q_{s0} = 6.24\text{E} - 05\ m^3/s$ using the Meyer-Peter and Müller formula and Van Rijn approach (Table 3-5) by software which is 2.34 times less than the experimental one.

Second, the discrepancy between numerical and experimental profiles grows over the time. Therefore, the maximum difference is observed at the end of the experiments.

As mentioned in 2.6.3, a calibration process based on changing the Manning’s coefficient n and Bedload factor α has been done to reduce the mentioned inconsistency.

Based on Equation 2-35, the first estimation of the Bedload factor α is calculated and reported in Table 3-5.

Table 3-5 First estimation of Bedload factor α for different experiments, obtained from equality between the experimental Q_{s0} and the theoretical one.

EXPERIMENT	$Q_{water}\ (l/s)$	$Q_{so}\ (m^3/s)$ (EXPERIMENTAL)	$Q_{so}\ (m^3/s)$ (MPM FORMULA)	α_{MPM}
AE06	7	1.41E-04	7.31E-05	1.75
AE07	7	1.29E-04	7.31E-05	1.76
AE08	7	1.29E-04	7.31E-05	1.76
AE10	7	1.20E-04	7.31E-05	1.64
AE11	7	1.19E-04	7.31E-05	1.63
AE13	6	1.39E-04	6.24E-05	2.23
AE14	6	1.46E-04	6.24E-05	2.34

Then, several trials are developed by simultaneously changing the Bedload factor α and Manning's coefficient n. And as mentioned in 2.6.3.3, the best equivalent parameters are based on the mean square error calculated for water and bed profiles. These errors and the selected trials as the best ones for AE13 and AE14 are reported below.

Table 3-6 Mean square error (cm^2) of a) bed elevation b) water surface elevation for some specific times in spatial profiles (AE13)

TRIAL	$t=\ 0$ sec	$t=60$ sec	$t=100$ sec	$t=140$ sec	$t=180$ sec	$t=220$ sec	$t=260$ sec	$t=300$ sec	$t=340$ sec
1	0.14	0.48	0.81	1.42	2.02	2.50	3.05	3.98	3.95
2	0.14	0.25	0.28	0.36	0.43	0.46	0.53	0.60	0.60
3	0.14	0.21	0.21	0.25	0.28	0.29	0.33	0.36	0.37
4	0.14	0.18	0.18	0.18	0.19	0.19	0.22	0.22	0.24
5	0.14	0.16	0.16	0.14	0.14	0.14	0.16	0.16	0.18
6	0.14	0.19	0.19	0.21	0.23	0.23	0.27	0.28	0.30
7	0.14	0.16	0.17	0.16	0.16	0.16	0.18	0.17	0.20
8	0.14	0.17	0.17	0.17	0.18	0.18	0.21	0.21	0.22
9	0.14	0.17	0.18	0.16	0.15	0.16	0.17	0.16	0.18
10	0.14	0.23	0.26	0.32	0.38	0.40	0.46	0.51	0.52
11	0.14	0.16	0.16	0.15	0.15	0.15	0.18	0.17	0.19
12	0.14	0.17	0.17	0.16	0.16	0.16	0.19	0.18	0.20

a)

TRIAL	$t=\ 0$ sec	$t=60$ sec	$t=100$ sec	$t=140$ sec	$t=180$ sec	$t=220$ sec	$t=260$ sec	$t=300$ sec	$t=340$ sec
1	0.43	0.05	0.09	0.29	0.40	0.71	1.23	1.50	1.50
2	0.43	0.08	0.06	0.09	0.05	0.08	0.10	0.11	0.13
3	0.43	0.10	0.07	0.10	0.06	0.08	0.09	0.08	0.10
4	0.43	0.11	0.09	0.13	0.10	0.11	0.10	0.09	0.11
5	0.43	0.13	0.12	0.16	0.14	0.15	0.14	0.13	0.15
6	0.43	0.11	0.08	0.11	0.08	0.09	0.09	0.08	0.10

7	0.78	0.21	0.25	0.34	0.27	0.31	0.33	0.31	0.35
8	0.59	0.14	0.12	0.17	0.12	0.15	0.15	0.14	0.17
9	0.78	0.28	0.30	0.39	0.30	0.37	0.36	0.36	0.40
10	1.26	0.39	0.41	0.54	0.43	0.54	0.64	0.65	0.69
11	0.59	0.14	0.13	0.18	0.14	0.16	0.16	0.15	0.18
12	0.43	0.12	0.11	0.14	0.12	0.13	0.12	0.11	0.13

b)

As mentioned in 3.2, the obtained profiles through experimental work are not considered at times less than $t = 50\ sec$. So, the errors related to $t \leq 50\ sec$ in Table 3-6 are not considered in the sum of the errors calculated in Table 3-7.

Table 3-7 Sum of the mean square error (cm^2) *for bed and water in each trial and then its average as an indicator for choosing the best trial (AE13)*

TRIAL	SUM OF THE BED ERROR (cm^2)	SUM OF THE WATER ERROR (cm^2)	AVERAGE OF ERRORS (cm^2)
1	18.195	5.778	11.987
2	3.510	0.710	2.110
3	2.308	0.682	1.495
4	1.595	0.844	1.219
5	**1.239**	**1.128**	**1.184**
6	1.899	0.744	1.322
7	1.371	2.366	1.869
8	1.509	1.148	1.329
9	1.322	2.766	2.044
10	3.079	4.287	3.683
11	1.314	1.241	1.277
12	1.392	0.978	1.185

Table 3-7 illustrates that trial number 5, with a mean square error equal to $1.18\ cm^2$, is the best trial among those developed. So, the corresponding Manning's coefficient n and Bedload factor α of this trial are chosen as the final ones for experiment AE13.

In the following, the calibrated results based on these equivalent parameters and experimental results are compared together for AE13.

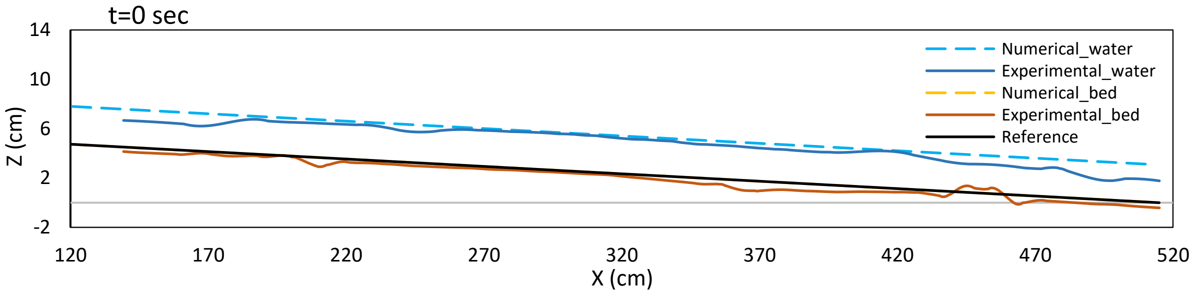

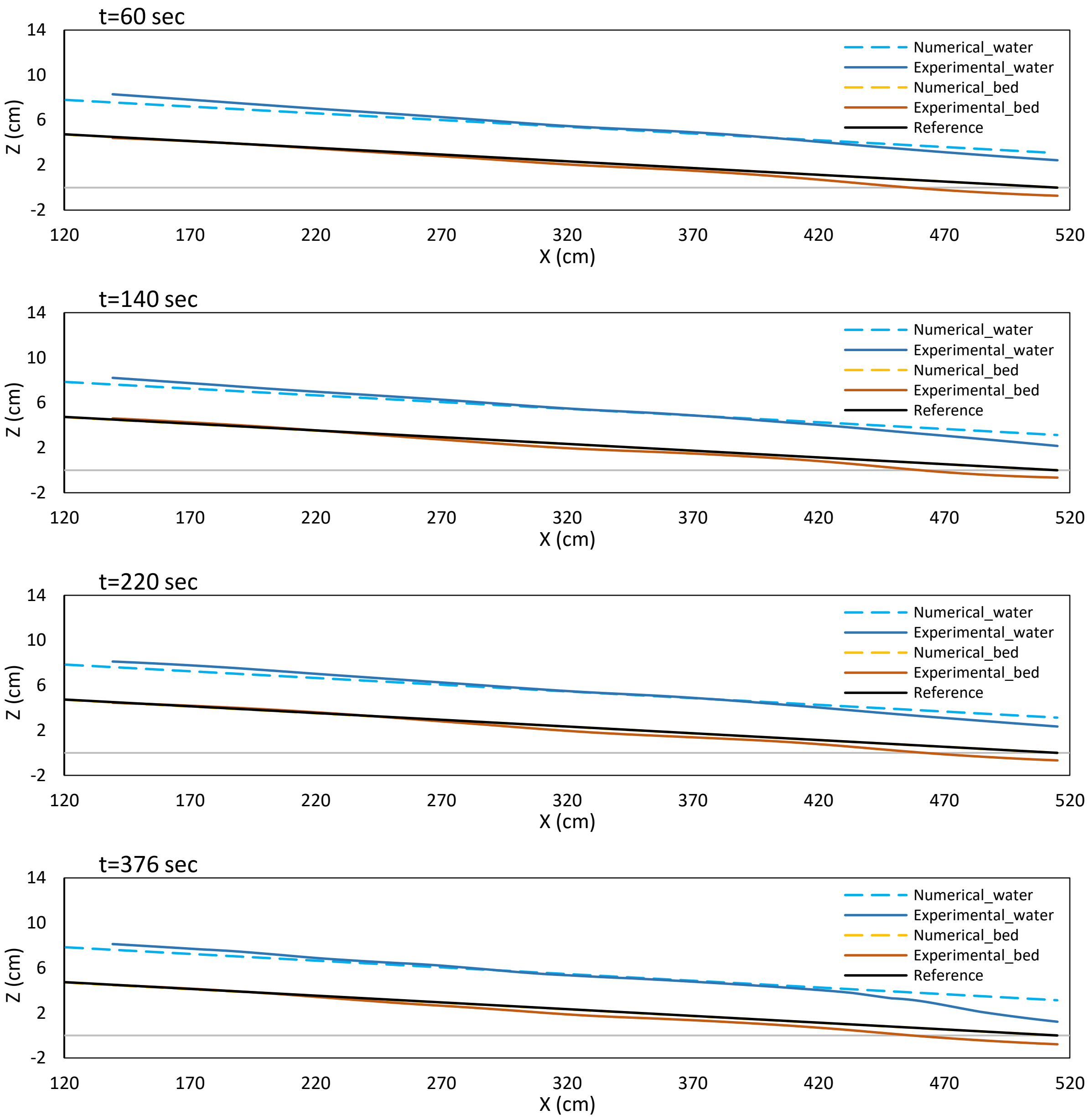

Figure 3-33 Comparison between experimental and calibrated numerical results- Spatial evolution of bed and water surface at selected times for AE13 (Loading ratio L_r= 1.07)

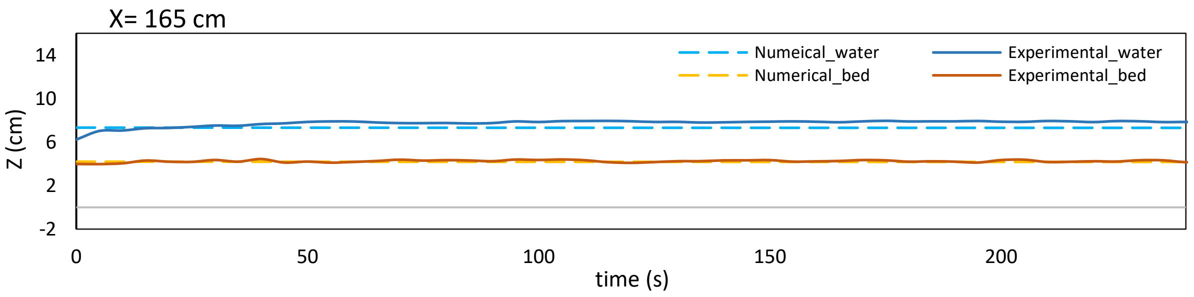

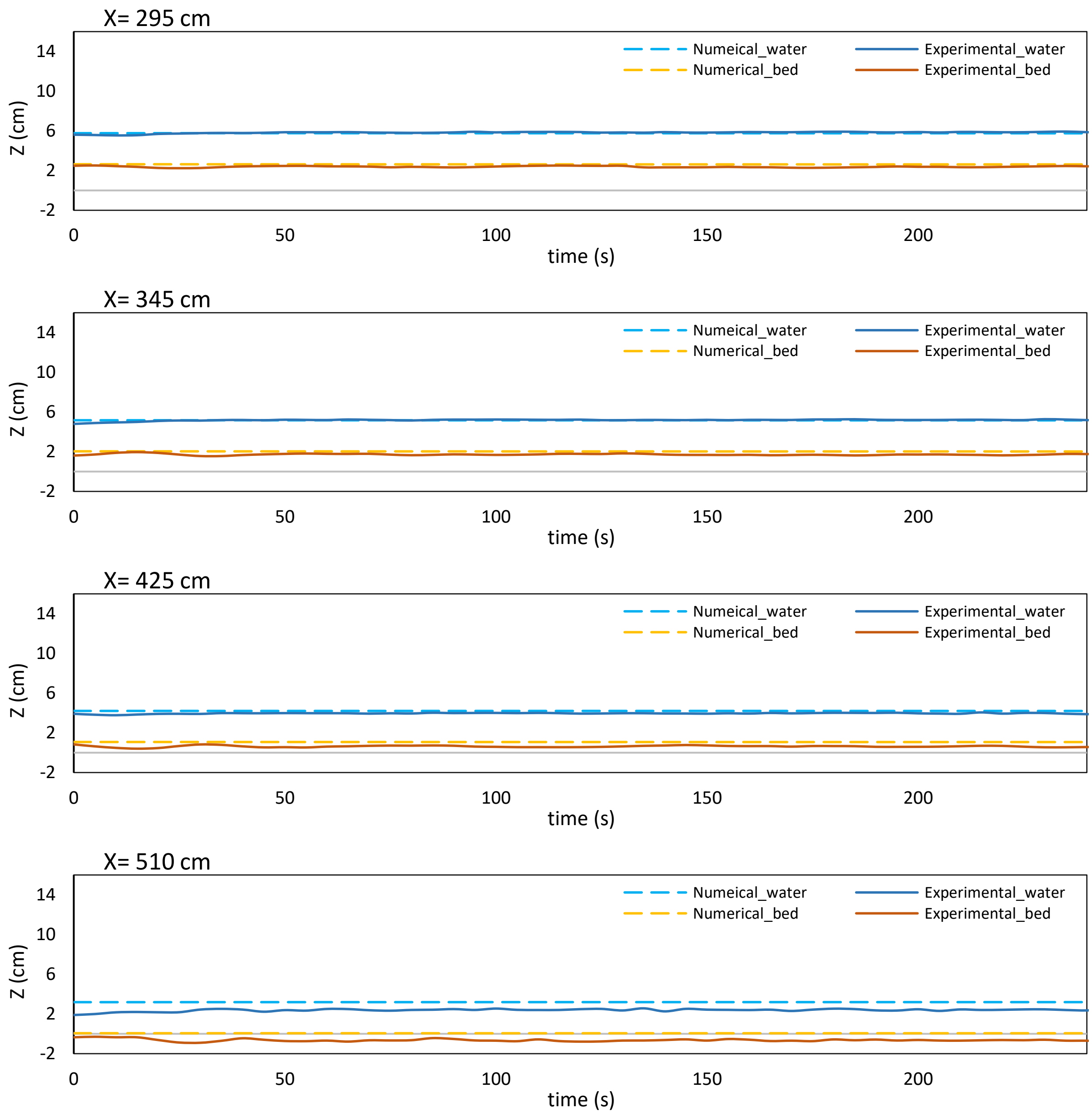

Figure 3-34 Comparison between experimental and calibrated numerical results- Temporal evolution of bed and water surface at selected locations for AE13 (Loading ratio L_r= 1.07)

The same procedure is reported in the following for AE14.

Table 3-8 Mean square error (cm^2) of a) bed elevation b) water surface elevation for some specific times in spatial profiles (AE14)

TRIAL	$t = 0$ sec	$t = 40$ sec	$t = 80$ sec	$t = 120$ sec	$t = 160$ sec	$t = 200$ sec	$t = 240$ sec
1	0.33	0.61	1.46	2.80	4.49	5.85	7.38
2	0.33	0.48	0.73	1.01	1.33	1.41	1.55
3	0.33	0.44	0.60	0.75	0.93	0.92	0.97
4	0.33	0.40	0.48	0.54	0.63	0.59	0.59
5	0.33	0.35	0.35	0.33	0.34	0.29	0.28
6	0.33	0.33	0.32	0.28	0.27	0.23	0.22
7	0.33	0.31	0.28	0.23	0.22	0.19	0.19
8	0.33	0.29	0.26	0.20	0.18	0.18	0.19
9	0.33	0.32	0.30	0.25	0.24	0.20	0.20
10	0.33	0.34	0.33	0.29	0.29	0.24	0.23
11	0.33	0.32	0.31	0.27	0.26	0.22	0.21
12	0.38	0.49	0.66	0.79	0.93	0.89	0.91
13	0.33	0.38	0.43	0.46	0.51	0.46	0.46
14	0.33	0.33	0.32	0.28	0.28	0.24	0.23

a)

TRIAL	$t = 0$ sec	$t = 40$ sec	$t = 80$ sec	$t = 120$ sec	$t = 160$ sec	$t = 200$ sec	$t = 240$ sec
1	1.27	0.03	0.16	0.61	1.31	2.11	3.10
2	1.27	0.04	0.05	0.09	0.14	0.18	0.26
3	1.27	0.04	0.03	0.04	0.05	0.06	0.10
4	1.27	0.04	0.03	0.02	0.02	0.02	0.04
5	1.27	0.05	0.04	0.04	0.04	0.06	0.07
6	1.58	0.09	0.07	0.06	0.06	0.08	0.11
7	1.93	0.17	0.12	0.10	0.09	0.12	0.15
8	2.29	0.27	0.20	0.16	0.14	0.17	0.20
9	1.75	0.13	0.09	0.08	0.08	0.10	0.13
10	1.75	0.13	0.09	0.07	0.06	0.08	0.10
11	1.93	0.17	0.12	0.10	0.08	0.10	0.12
12	2.22	0.25	0.26	0.27	0.27	0.27	0.32
13	1.27	0.04	0.03	0.02	0.02	0.02	0.03
14	1.27	0.05	0.04	0.05	0.06	0.09	0.11

b)

As mentioned before, the errors related to $t \leq 50\ sec$ are not considered when the sum of the errors is calculated.

Table 3-9 Sum of the mean square error (cm^2) for bed and water in each trial and then its average as an indicator for choosing the best trial (AE14)

TRIAL	SUM OF THE BED ERROR ($\mathbf{cm^2}$)	SUM OF THE WATER ERROR ($\mathbf{cm^2}$)	AVERAGE OF ERRORS ($\mathbf{cm^2}$)
1	21.990	7.302	14.646
2	6.042	0.720	3.381
3	4.166	0.287	2.226
4	2.829	0.129	1.479
5	1.593	0.252	0.923
6	1.307	0.382	0.845

7	1.106	0.585	0.846
8	1.012	0.875	0.944
9	**1.193**	**0.474**	**0.833**
10	1.383	0.403	0.893
11	1.258	0.517	0.888
12	4.166	1.393	2.780
13	2.326	0.129	1.228
14	1.342	0.362	0.852

As indicated in Table 3-9 the best trial is number 9, with the minimum mean square error of $0.83\ cm^2$. The water surface and bed elevation profiles related to this trial are presented below as the final numerical results compared with experimental results.

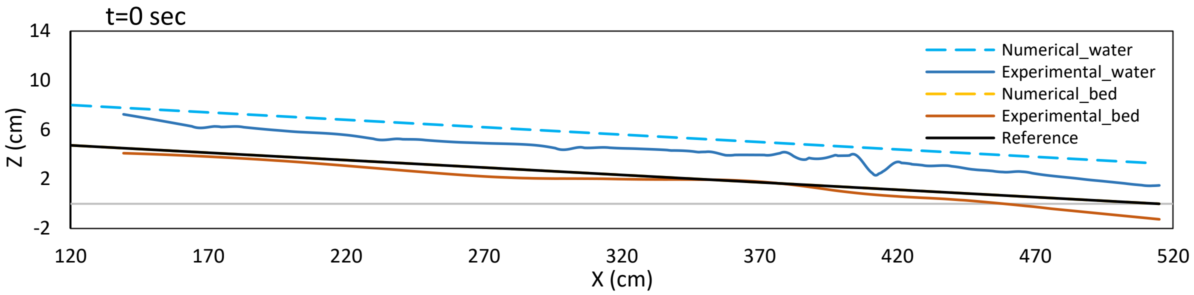

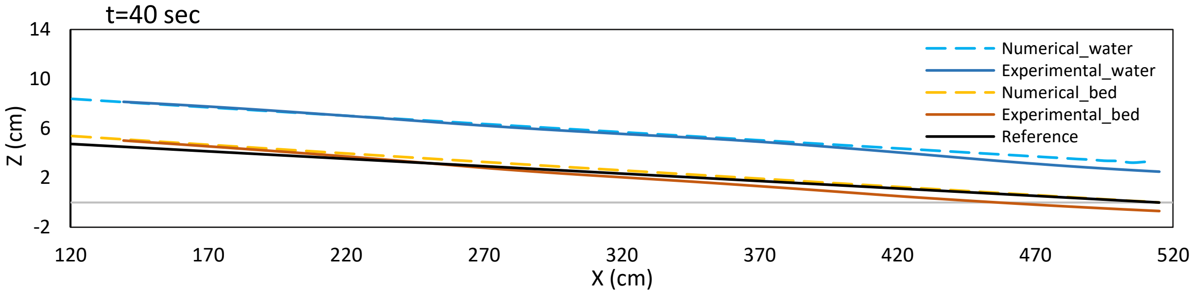

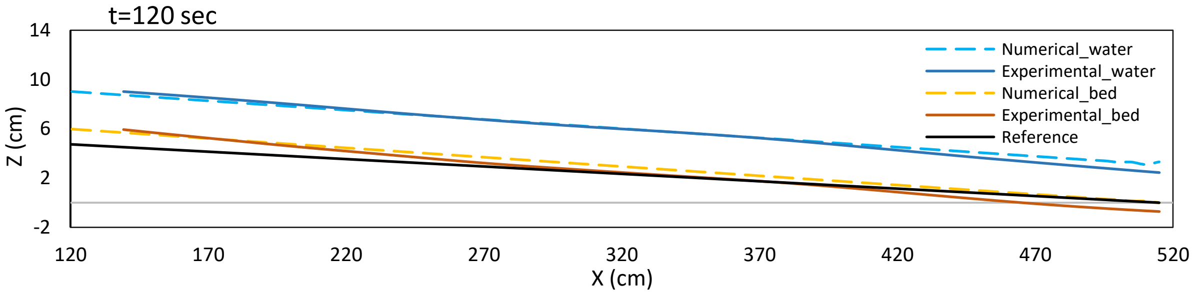

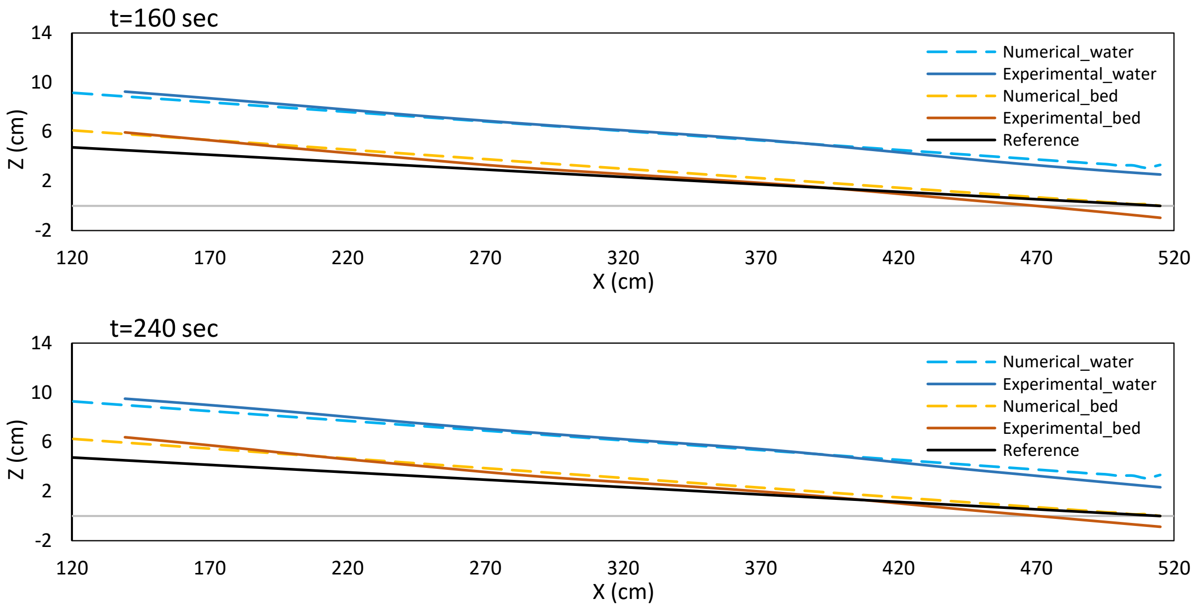

Figure 3-35 Comparison between experimental and calibrated numerical results- Spatial evolution of bed and water surface at selected times for AE14 (Loading ratio L_r= 1.76)

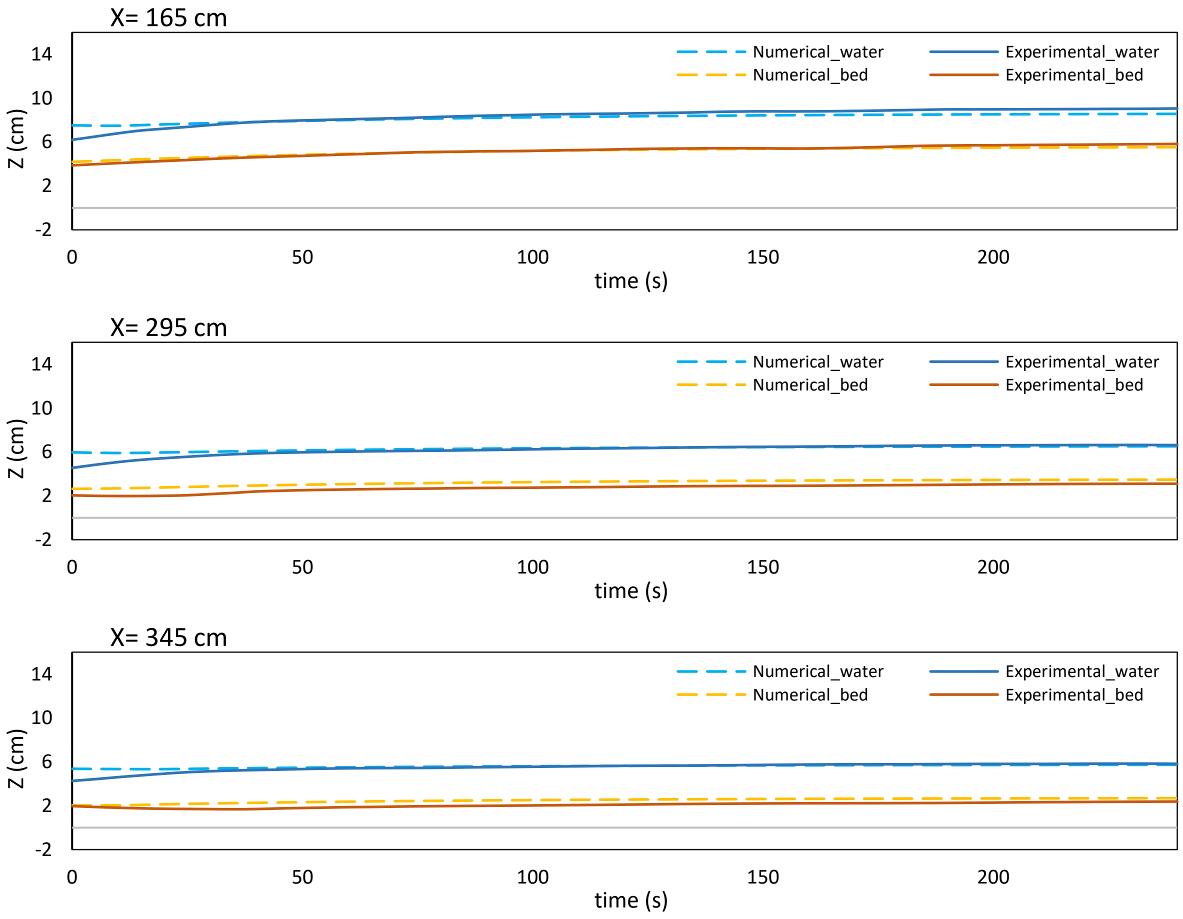

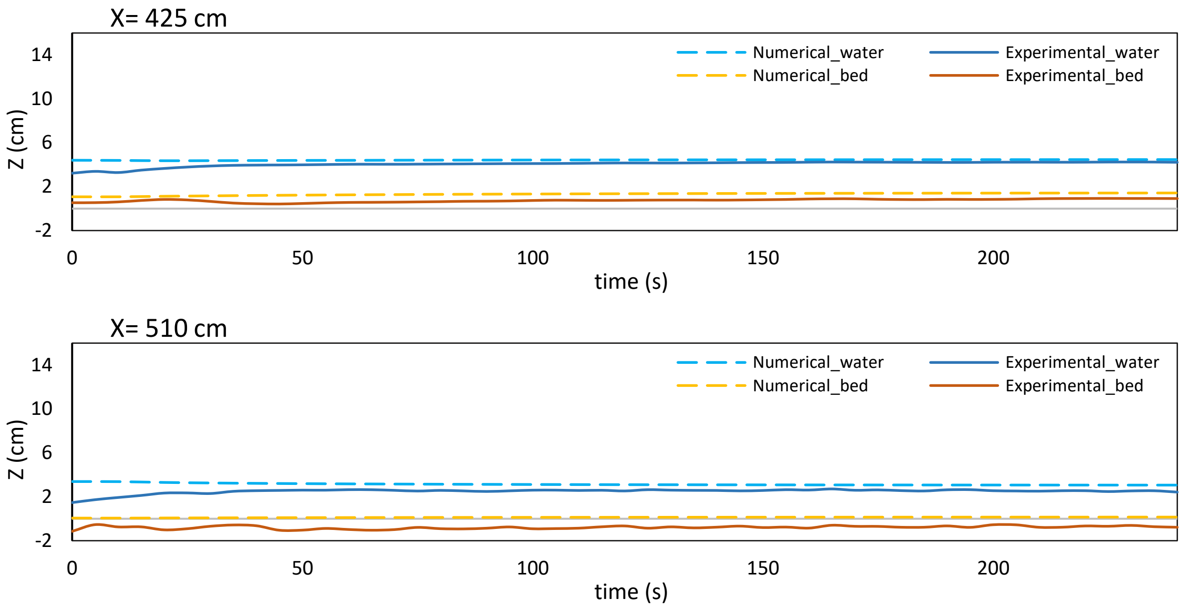

Figure 3-36 Comparison between experimental and calibrated numerical results- Temporal evolution of bed and water surface at selected locations for AE14 (Loading ratio L_r= 1.76)

It should be noted that other tools or types of error can be developed to choose the best trial. However, in this thesis, the mean square error and human judgment simultaneously are employed for this selection.

By considering the results, one can understand that the numerical model cannot completely cover the experimental results downstream and sometimes upstream. This problem happens downstream because a sill is located at the outlet of the actual channel in experimental work (Figure 2-1), resulting in degradation downstream of the profiles. While, in the numerical modeling, an “IODown” boundary condition (2.6.1.1) is defined downstream, which means all the sediment entered the last computational section will leave it; as a result, a bed elevation remains constant downstream of the simulated channel, and numerical model cannot simulate the effect of the sill. So, the behavior of numerical results is different from the experimental results downstream. The reason for different behaviors of profiles upstream should be investigated more in the future.

Also, another point is to be discussed here, considering the profiles at initial times ($t < 50\ sec$) in both calibrated and uncalibrated models. It is observed that at this time, the experimental water elevations are almost less than those of numerical. As mentioned in 3.2, the reason behind it is related to the value of water discharge at initial times, which is not a constant nominal value ($Q_{nominal} = 5, 6, and\ 7\ l$/s) in experimental work. At the same time, the numerical solver considers this value equal to the nominal one during the experiment.

In the following table (Table 3-10), the final results of equivalent parameters for each experiment are reported.

Table 3-10 Obtained Manning's coefficient n and Bedload factor α for each experiment

EXPERIMENT	Q_{water} (l/s)	LOADING RATIO $Lr\ (-)$	FROUDE NUMBER $Fr\ (-)$	MANNING'S COEFFICIENT $n\ (s/m^{\frac{1}{3}})$	BEDLOAD FACTOR $\alpha\ (-)$
AE06	7	1.63	0.934	0.017	1.90
AE07	7	1.11	0.893	0.015	1.85
AE08	7	1.97	0.974	0.017	1.80
AE10	7	3.46	1.191	0.017	2.40
AE11	7	3.37	1.231	0.016	2.50
AE13	6	1.07	1.016	0.015	2.40
AE14	6	1.76	1.013	0.0165	2.50

In Table 3-10, the reported Froude number Fr is related to the fourth scenario which is explained in 2.7.1

One may consider that the optimized values of Bedload factor α (Table 3-10) and those values estimated by considering Q_{s0} (Table 3-5) are not fully sound comparison because the optimum values of Bedload factor α also depend on Manning's coefficient n.

3.6.2 Manning's coefficient n analysis

By considering Table 3-10, Manning's coefficient n are plotted based on Loading ratio Lr and Froude number Fr to find a relationship between them.

One may conclude that, by considering Figure 3-37.a, when the Loading ratio Lr is less than 1.5 (Lr<1.5), there is not any relation between Manning's coefficient n and Froude number Fr. Moreover, an insignificant decreasing trend can be observed by increasing the Loading ratio Lr. Figure 3-37.b illustrates that Manning's coefficient n slightly rises by growth in Loading ratio Lr. However, these correlations could be considered a neglectable trend.

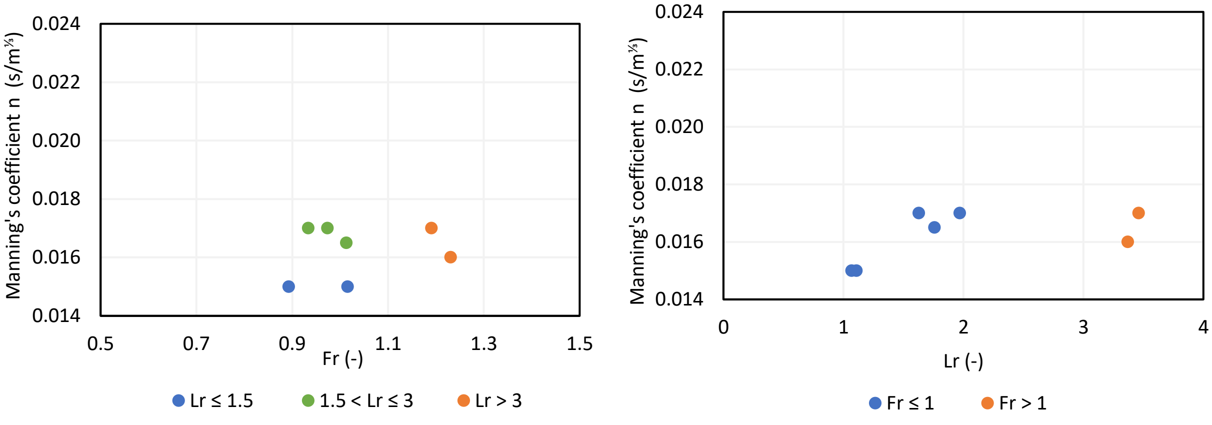

a) *b)*

Figure 3-37 Scenario 4 _ Manning's coefficient n versus: a) Froude number Fr. b) Loading ratio Lr.

Also, it is required to develop Dimensionless Manning's coefficient n', as is explained in 2.7.1 to discuss these trends better. This parameter is obtained by multiplying the term $\frac{v}{d^{\frac{2}{3}}}$ by obtained Manning's coefficient n through calibration.

3.7 Dimensionless analysis

For conducting dimensionless analysis of parameters, Froude number Fr and Loading ratio Lr are selected because these two variables distinguish experiments AE1 to AE14 from each other.

Figure 3-38 show that by increasing the Loading ratio Lr, the Froude number Fr rises moderately.

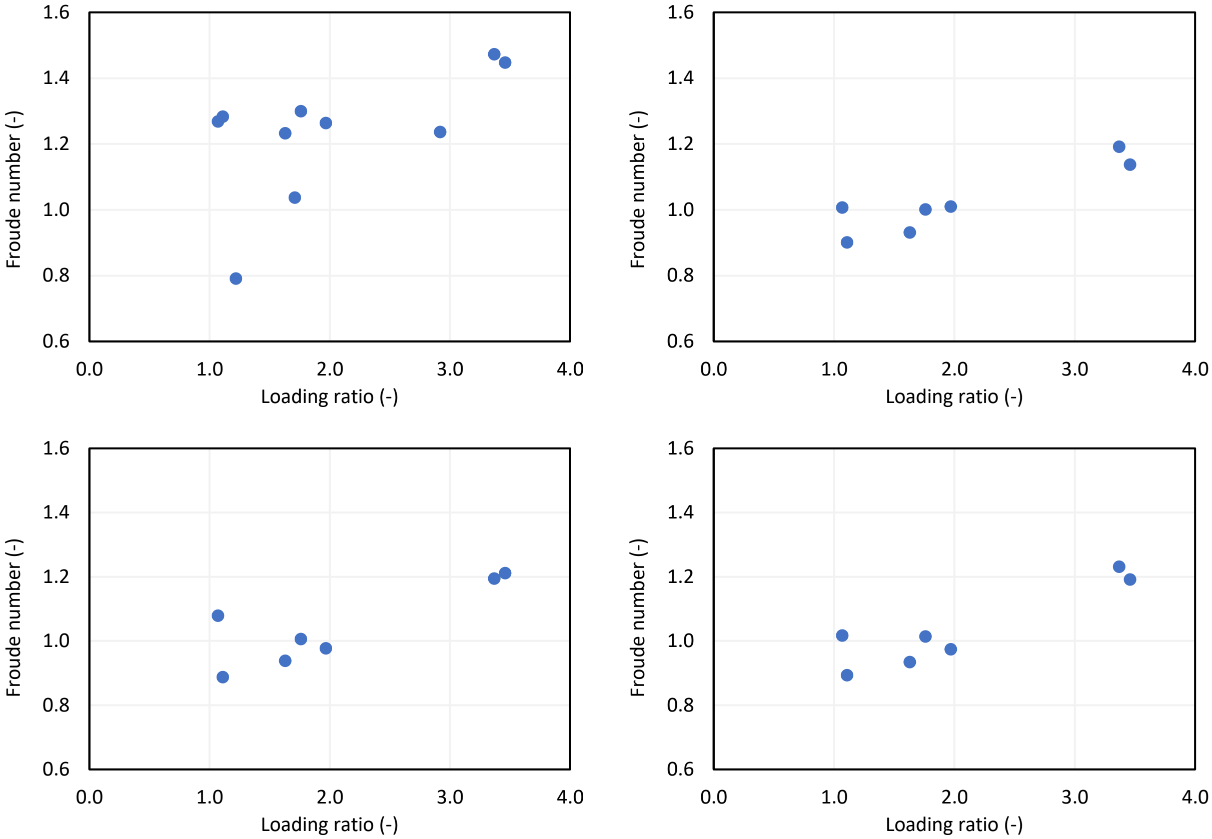

Figure 3-38 Froude number Fr versus Loading ratio Lr. a) scenario 1. b) scenario 2. c) scenario 3. d) scenario 4.

The dimensionless analysis is developed for four parameters. Manning's coefficient n, Bedload factor α, Final slope, and Celerity (both Local celerity C and eigenvalues λ). Between mentioned parameters, Manning's coefficient n and Bedload factor α are obtained from numerical analysis, while Celerity and final slope are related to experimental results.

Among the following parameter, Dimensionless Manning's coefficient n', Bedload factor α and Final slope are analyzed considering four mentioned scenarios (see 2.7.1). The first scenario is defined based on the theory of calculating the water discharge for a uniform open channel flow. In the scenario, the required parameters are calculated by taking an average of their correspondence matrices spatially for the first time that the sediment profile is stable. In the third scenario, the required parameters are calculated by taking an average of their correspondence matrices spatially for the last time of the experiment. Furthermore, in the fourth scenario, the required parameters are calculated by taking an average of their correspondence matrices spatially for the time interval between the first stable time mentioned in the second scenario and the last time of experiments mentioned in the third scenario.

For analyzing the Dimensionless Local celerity C' and eigenvalues λ, two scenarios are considered (see 2.7.2). The required values are calculated in the first scenario by taking an average of their correspondence matrices spatially for the time interval between $t = 50\ sec\ to\ t = 100\ sec$. In the second scenario, the required values are calculated by taking an average of their correspondence matrices spatially for the time interval same as in the first scenario but the half of the space interval.

Dimensionless analysis related to these parameters considering mentioned scenarios is discussed in the following.

3.7.1 Dimensionless Manning's coefficient n'

Based on what is explained in 2.7.1, the Dimensionless Manning's coefficient n' for four different scenarios are calculated.

It should be highlighted in Table 3-11 that the Dimensionless Manning's coefficient n' in the experiments AE01, AE02, and AE05 are just calculated for the first scenario because, in other scenarios, it is required to redo the bed detection procedure for these experiments to find the profiles based on newly modified method (see 2.3.3) and then calculate the Froude number Fr for them which is not developed in this thesis due to the lack of time. It is worth mentioning that experiments AE03 and AE04 are not considered in this analysis due to a lack of data.

Table 3-11 Manning's coefficient n' and Froude number Fr for four different scenarios

EXPERIMENT	1ST SCENARIO		2ND SCENARIO		3RD SCENARIO		4TH SCENARIO	
	n'	Fr	n'	Fr	n'	Fr	n'	Fr
AE 01	41.787	1.037	-	-	-	-	-	-
AE 02	24.316	0.791	-	-	-	-	-	-
AE 05	53.989	1.236	-	-	-	-	-	-
AE 06	32.582	1.233	18.572	0.931	18.845	0.938	18.662	0.934
AE 07	31.150	1.283	15.330	0.901	14.868	0.887	15.086	0.893
AE 08	34.206	1.263	22.048	1.01	20.411	0.977	20.311	0.974
AE 10	44.934	1.448	27.517	1.137	31.252	1.211	30.286	1.191
AE 11	43.772	1.473	28.411	1.191	28.614	1.194	30.391	1.231
AE 13	35.492	1.268	22.307	1.007	24.973	1.078	22.670	1.016
AE 14	41.026	1.300	24.238	1.001	25.979	1.005	24.866	1.013

Then, the obtained Dimensionless Manning's coefficient n' is plotted based on Froude number Fr. Considering Figure 3-39, it can be seen that the Dimensionless Manning's coefficient n' almost increases by rising the Froude number Fr in all scenarios. Moreover, considering the second, third, and fourth scenarios, almost linear increasing relations between Dimensionless Manning's coefficient n' and Froude number Fr can be induced.

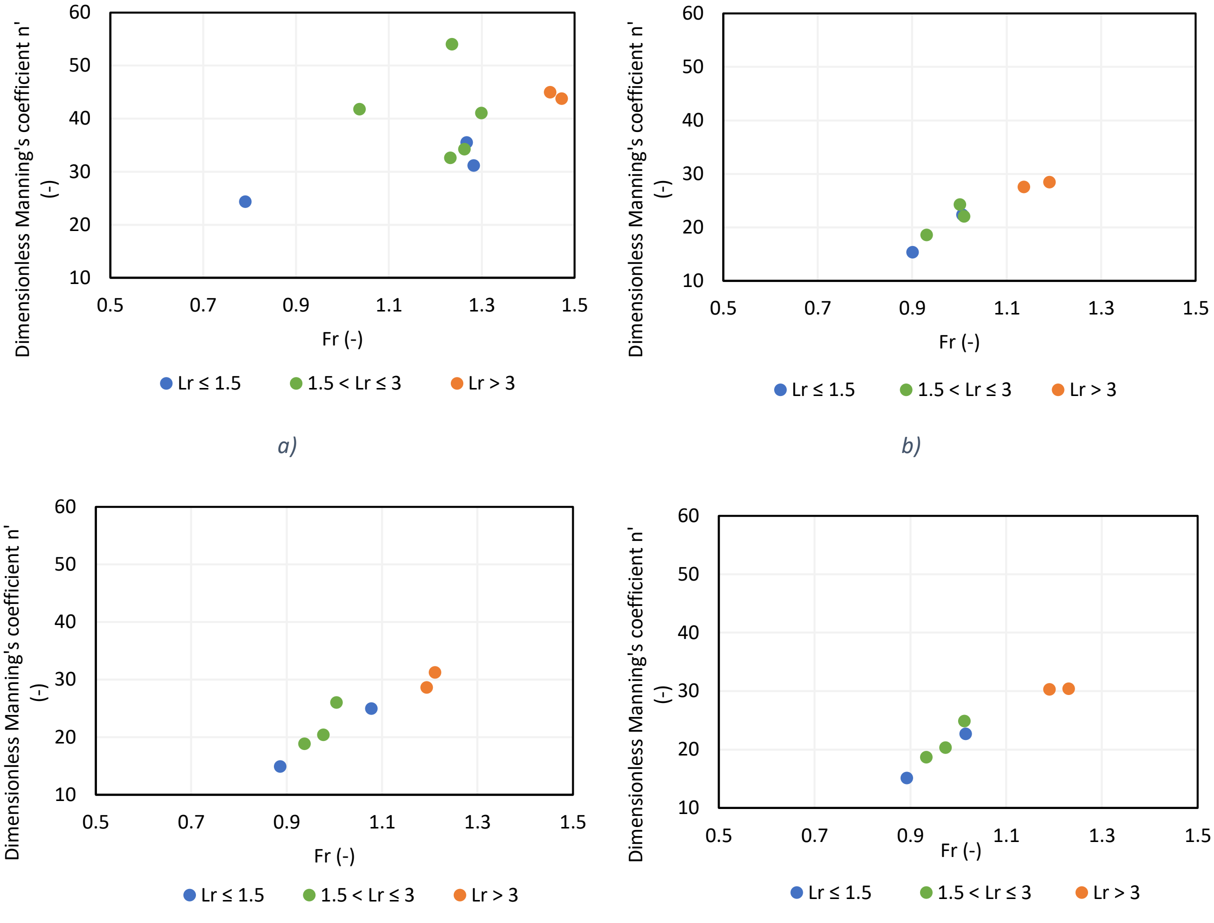

a) *b)*

c) *d)*

Figure 3-39 Dimensionless Manning's coefficient n' versus Froude number Fr considering a) Scenario 1. b) Scenario 2. c) Scenario 3. d) Scenario 4.

One may assume that this observed trend is not real since both Dimensionless Manning's coefficient $n'$and Froude number Fr are calculated by multiplying flow velocity v. However, it should be mentioned that considering the relation between Froude number Fr and Loading ratio Lr, and the correlation of both Dimensionless Manning's coefficient with Loading ratio, it might be that the observed trend is not spurious. It can be concluded that there is uncertainty about this trend. by considering these two points,

Afterward, the obtained Dimensionless Manning's coefficient n' are plotted based on Loading ratio Lr. Regarding Figure 3-40, it can be seen that the trend between the Dimensionless Manning's coefficient n' and the Loading ratio Lr can be interpreted the same as the relation between Dimensionless Manning's coefficient n' and Froude number Fr

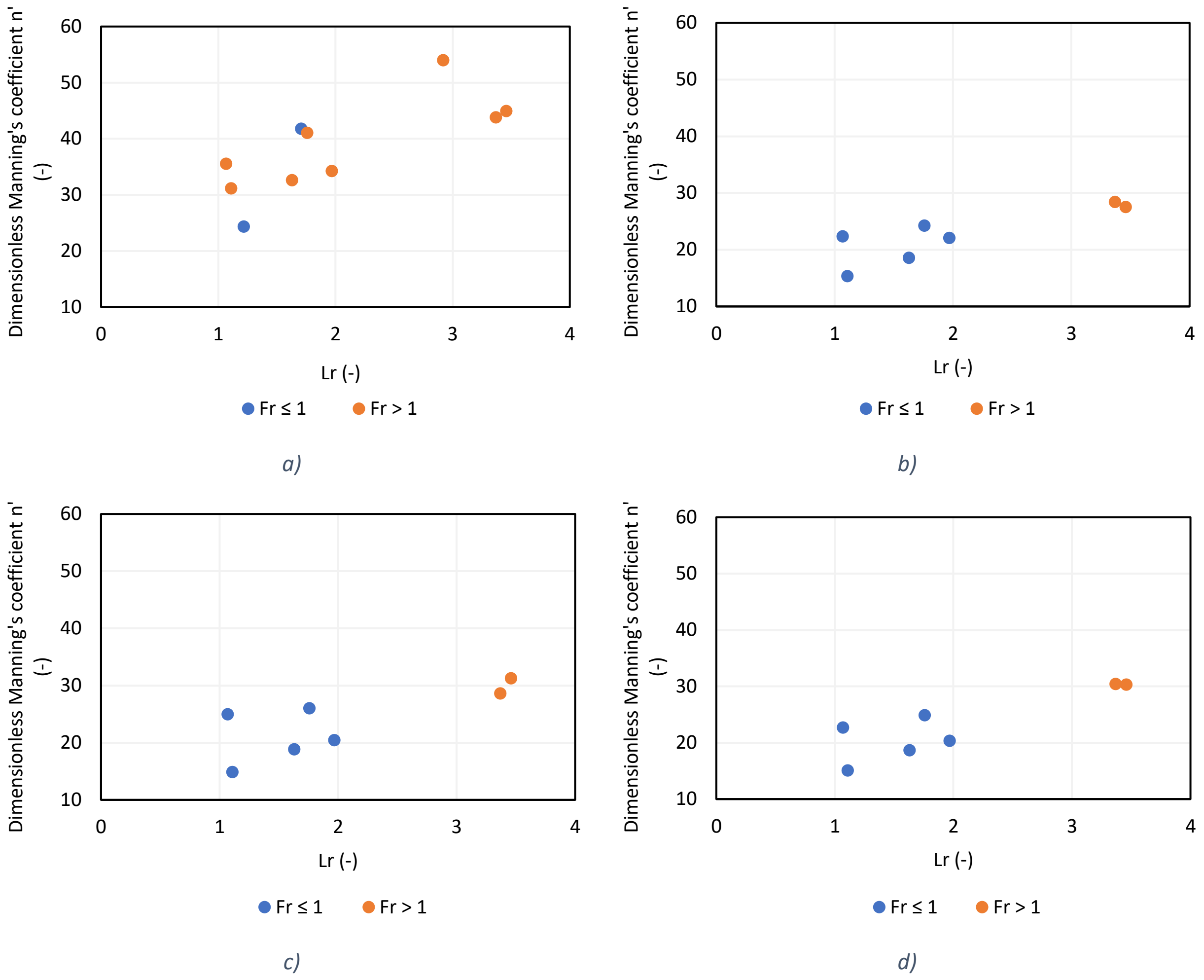

Figure 3-40 Dimensionless Manning's coefficient n' *versus Loading ratio* Lr *considering a) Scenario 1. b) Scenario 2. c) Scenario 3. d) Scenario 4.*

3.7.2 Bedload factor α

Bedload factor α as a dimensionless factor can be plotted based on Froude number Fr and Loading ratio Lr. For this sake, just scenarios number one and four are considered because the second and third scenarios are embedded in scenario four (see 2.7.1).

Regarding Figure 3-41 one can understand that the two different scenarios show approximately similar increasing trends.

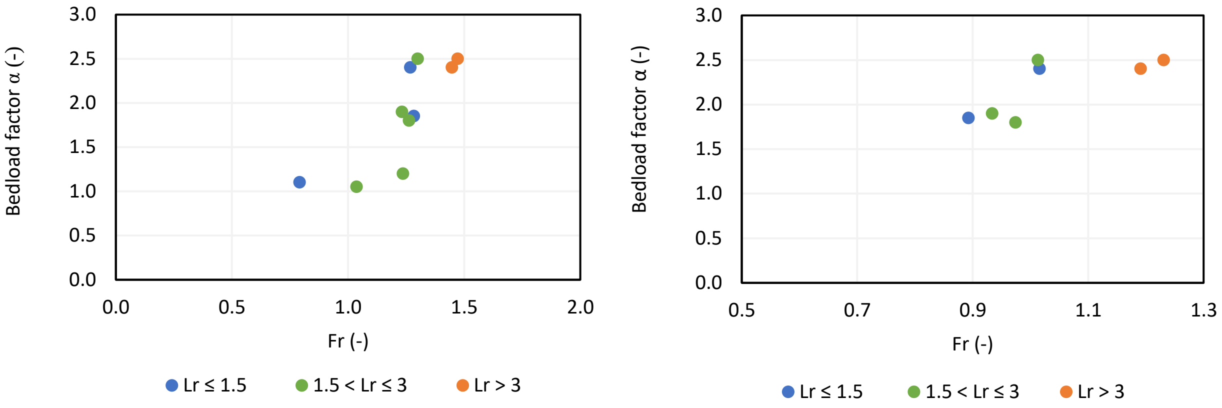

a) *b)*

Figure 3-41 Bedload factor α versus Froude number Fr considering a) Scenario 1. b) Scenario 4.

It can be highlighted by considering Figure 3-42 that the two scenarios almost show the same trend for Bedload factor α versus Loading ratio Lr. One can understand that the Loading ratio Lr does not affect the Bedload factor α by considering the fourth scenario.

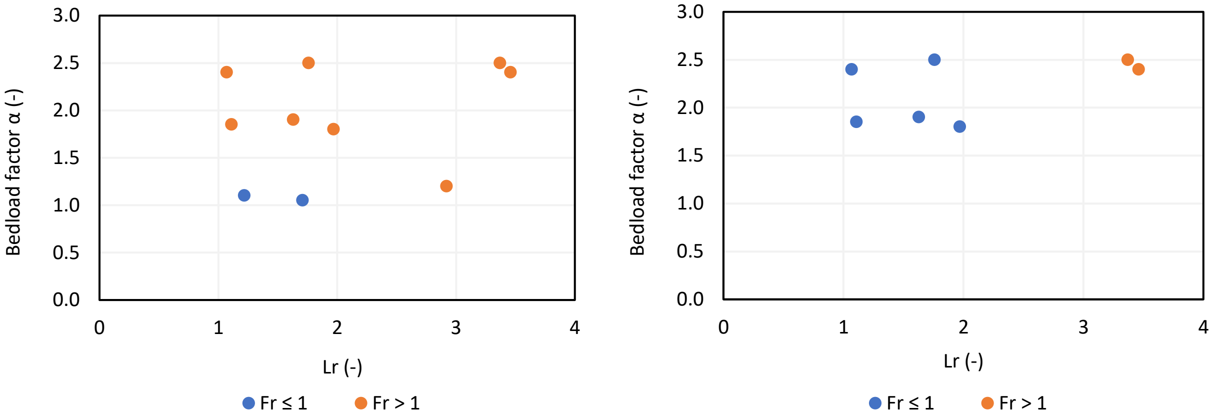

a) *b)*

Figure 3-42 Bedload factor α versus Loading ratio Lr considering a) Scenario 1. b) Scenario 4.

3.7.3 Final Slope

In this part, the results of the final slope versus the Froude number Fr and Loading ratio Lr are provided.

Figure 3-43 generally shows an increasing trend between the final slope and Froude number Fr.

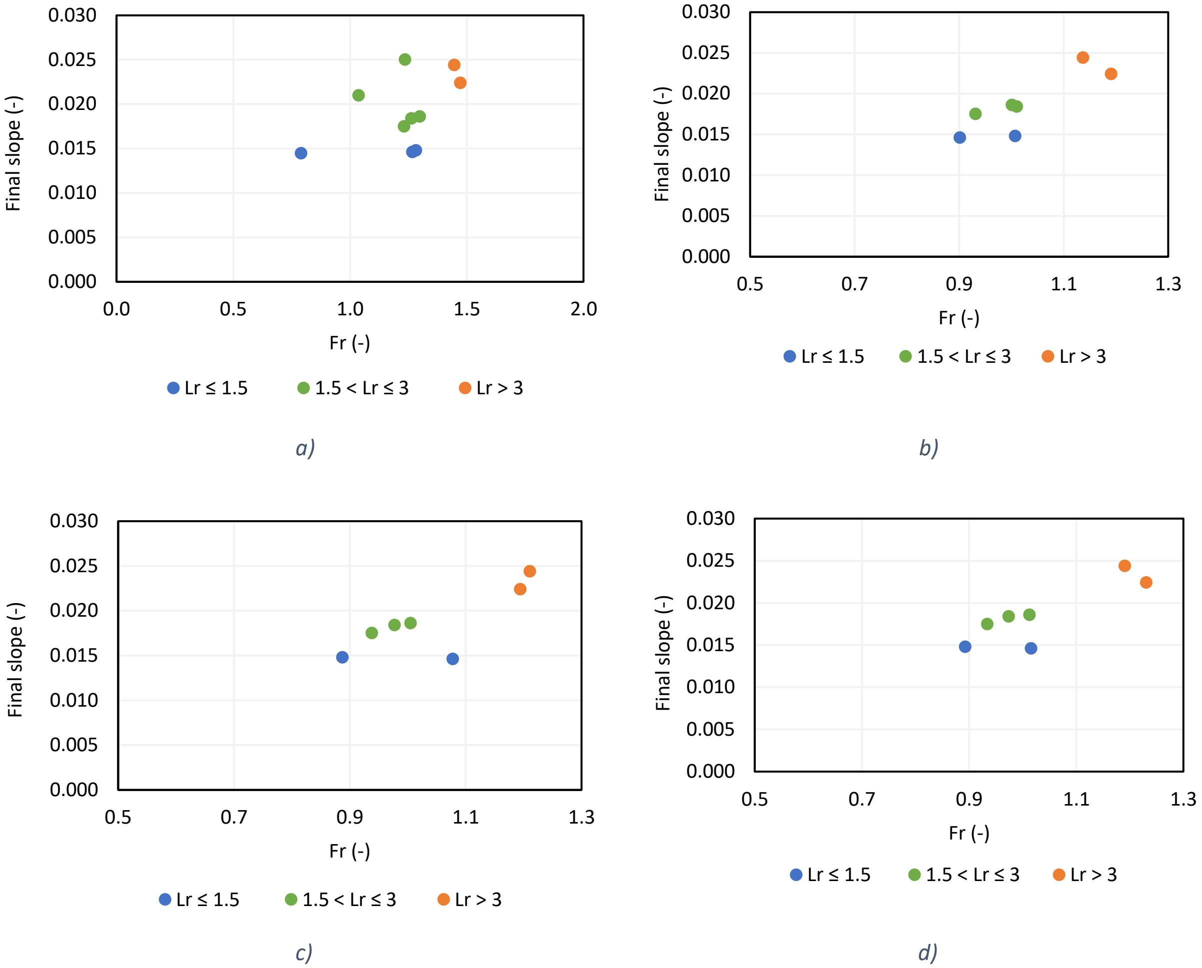

a)

b)

c)

d)

Figure 3-43 Final slope versus Froude number Fr considering a) Scenario 1. b) Scenario 2. c) Scenario 3. d) Scenario 4

Figure 3-44 illustrate that there is a direct correlation between Final slope and Loading ratio Lr.

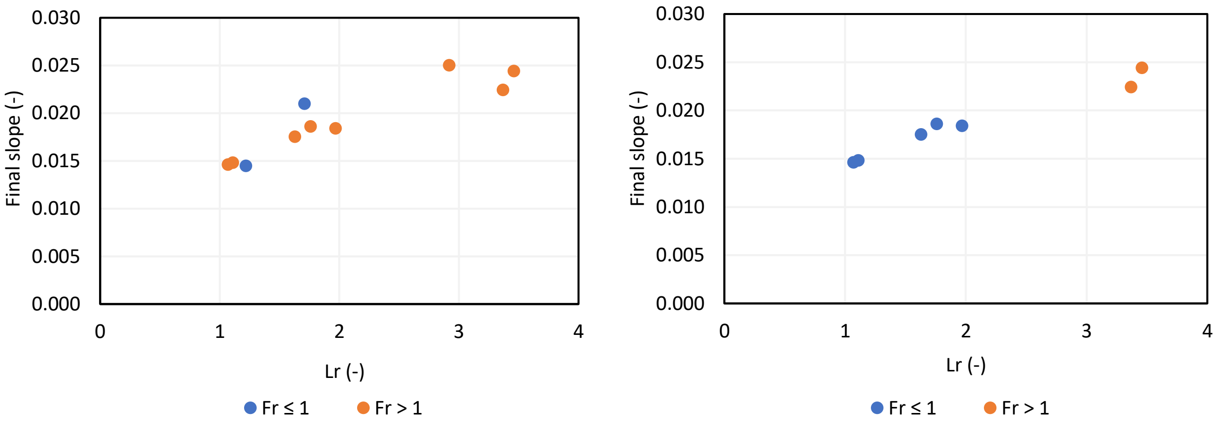

a)

b)

Figure 3-44 Final slope versus Loading ratio Lr considering a) scenario1 b) Scenario 2, Scenario 3 and Scenario 4.

Therefore, it may be concluded that the final slope depends on Loading ratio Lr more than Froude number Fr.

3.7.4 Dimensionless celerity

As mentioned in 2.5, there are two types of celerity, consist of Local celerity C and eigenvalues λ, which can be presented as dimensionless parameters by two scenarios for averaging different types of celerity (see 2.7.2).

3.7.4.1 Dimensionless local celerity C'

Figure 3-45 shows that there is almost an upward trend between Dimensionless local celerity C' and both Loading ratio Lr and Froude number Fr in the first scenario.

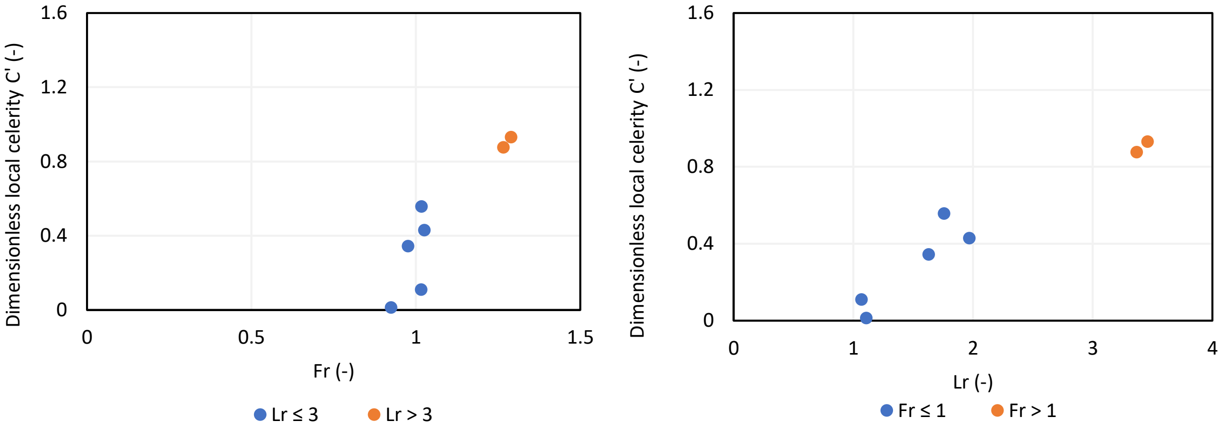

a) *b)*

Figure 3-45 Scenarios 1 _ Dimensionless local celerity C' versus: a) Froude number Fr. b) Loading ratio Lr.

The second scenario (Figure 3-46) approximately follows a pattern same as scenario one.

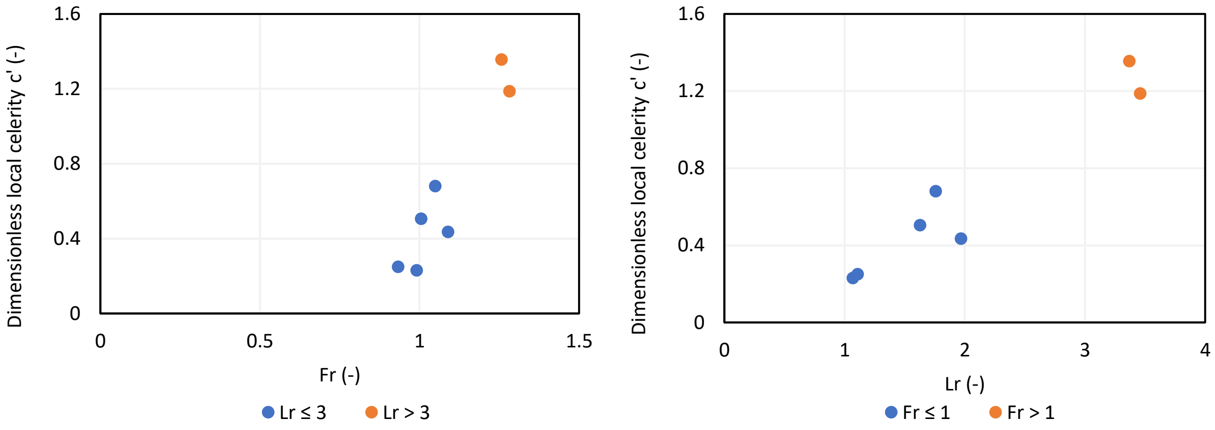

a) *b)*

Figure 3-46 Scenarios 2 _ Dimensionless local celerity C' versus: a) Froude number Fr. b) Loading ratio Lr.

3.7.4.2 Dimensionless eigenvalue λ'

Figure 3-47, Figure 3-48 and Figure 3-49 illustrate the value of $\lambda'_1,\ \lambda'_2,\ and\ \lambda'_3$ (Dimensionless eigenvalues λ) for both scenarios discussed before (see 2.7.2). The value of $\lambda'_1, and\ \lambda'_3$ in both scenarios almost increase linearly by rising both Froude number Fr and Loading ratio Lr. Figure 3-48 shows that λ'_2 can have different value when Froude number Fr is around one and Loading ratio Lr less than three ($Lr < 3$). When $Lr > 3$ and $Fr > 1$, the λ'_2 increases by rising the Froude number Fr and Loading ratio Lr respectively. Furthermore, it seems that λ'_2 is not continuous when Froude number Fr is almost equal to one and it tends to infinity.

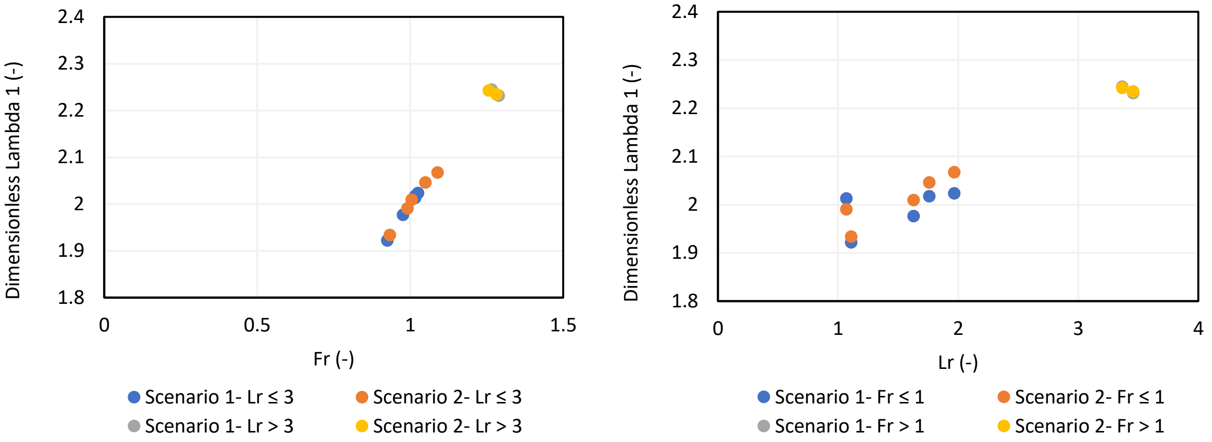

a) *b)*

Figure 3-47 Comparison all scenarios _ Dimensionless Lambda 1 λ'_1 versus: a) Froude number Fr. b) Loading ratio Lr.

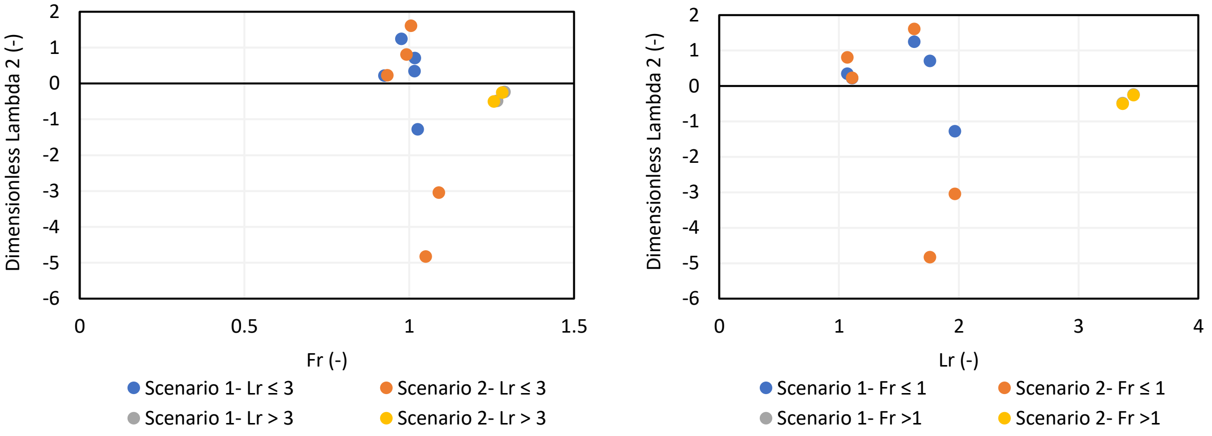

a) *b)*

Figure 3-48 Comparison all scenarios _ Dimensionless Lambda 2 λ'_2 versus: a) Froude number Fr. b) Loading ratio Lr.

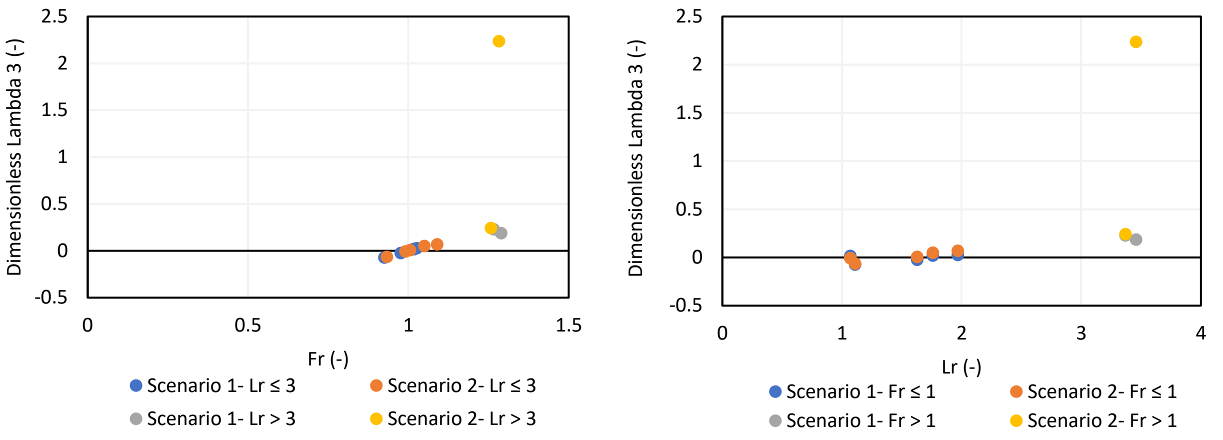

a) *b)*

Figure 3-49 Comparison all scenarios _ Dimensionless Lambda 3 λ'_3 versus: a) Froude number Fr. b) Loading ratio Lr.

3.7.4.3 Comparison between the Dimensionless local celerity C' and Dimensionless eigenvalues λ'

The results related to different Dimensionless eigenvalues λ' can be compared with Dimensionless local celerity C' concerning different Lr and Fr for both scenarios. This comparison aims to figure out any possible relation between these two parameters.

Figure 3-51 shows that the values of λ'_2 and Dimensionless local celerity C' for experiments with Froude number Fr around one ($Fr \approx 1$) and Loading ratio Lr less than three ($Lr < 3$) are almost similar during the first scenario. The results related to λ'_1 follow a pattern similar to the results of Dimensionless local celerity C', except that the range of their numbers is higher than the range of Dimensionless local celerity C' numbers.

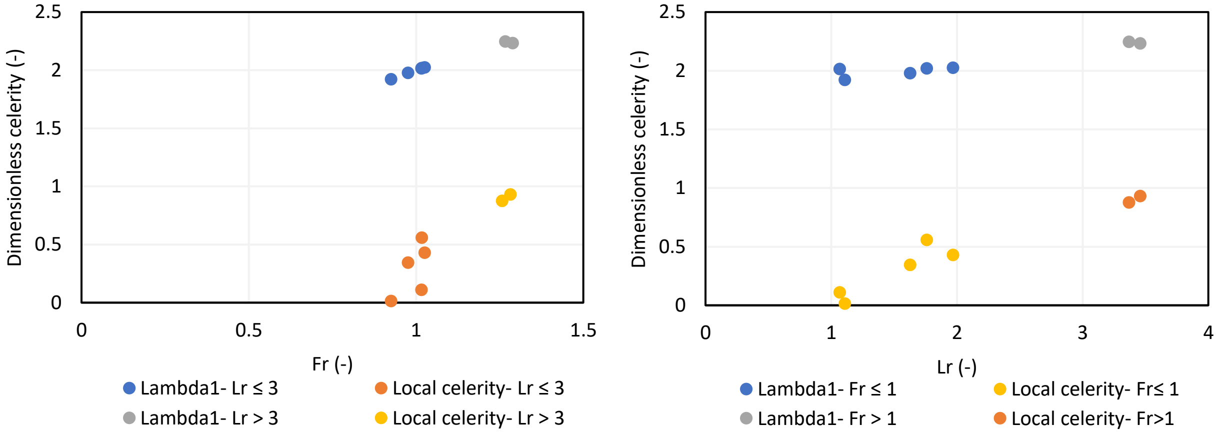

a) *b)*

Figure 3-50 Scenario1 _ Comparison Dimensionless Lambda 1 λ'_1 and Dimensionless local celerity C' versus: a) Froude number Fr. b) Loading ratio Lr.

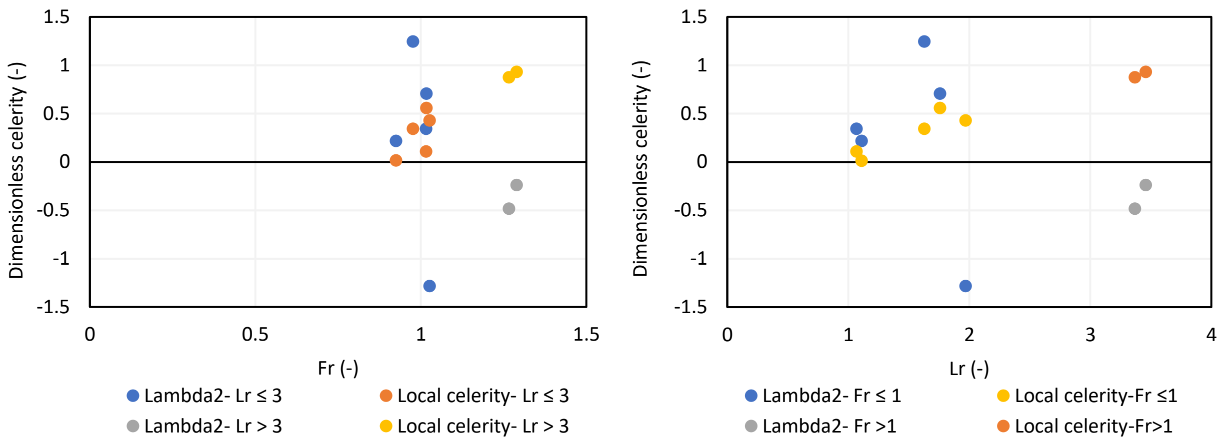

a) *b)*

Figure 3-51 Scenario1 _ Comparison Dimensionless Lambda 2 λ'_2 and Dimensionless local celerity C' versus: a) Froude number Fr. b) Loading ratio Lr.

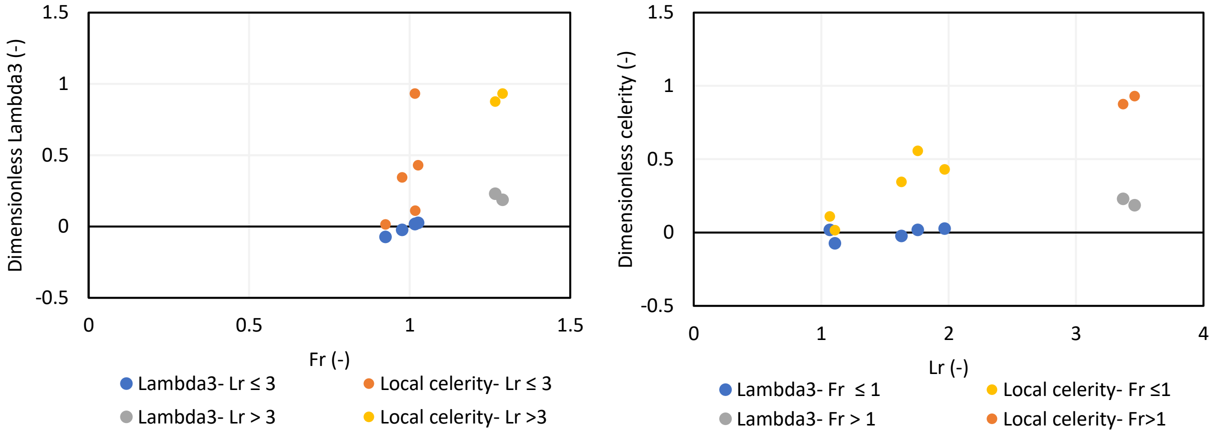

a) *b)*

Figure 3-52 Scenario1 _ Comparison Dimensionless Lambda 3 λ'_3 and Dimensionless local celerity C' versus: a) Froude number Fr. b) Loading ratio Lr.

In Figure 3-53, Figure 3-54 and Figure 3-55, the value of λ'_1, λ'_2, $and\ \lambda'_3$ belonging to second scenario are shown, respectively. This scenario almost follows a pattern same as scenario one.

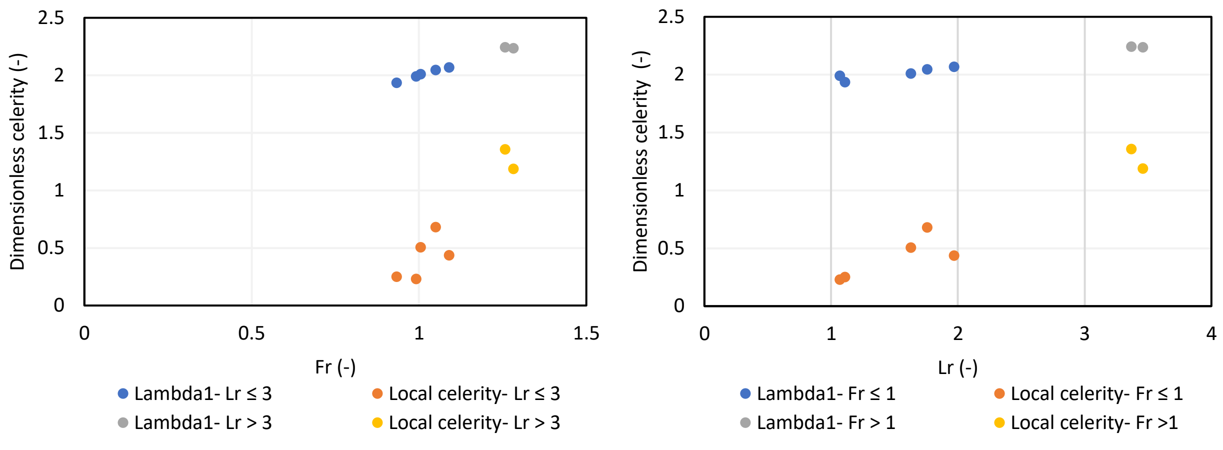

a) *b)*

Figure 3-53 Scenario2 _ Comparison dimensionless Lambda 1 λ'_1 and Dimensionless local celerity C' versus: a) Froude number Fr. b) Loading ratio Lr.

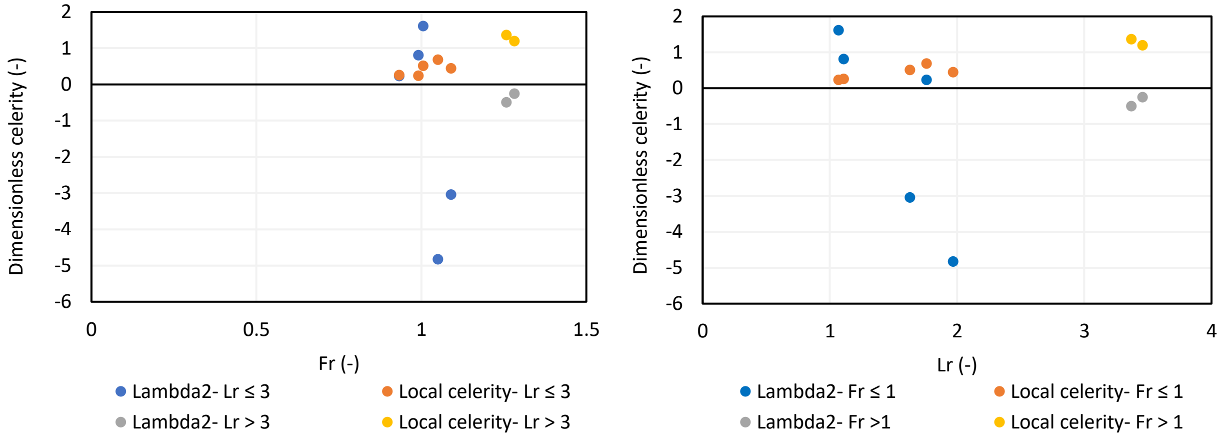

a) *b)*

Figure 3-54 Scenario2 _ Comparison dimensionless Lambda 2 and dimensionless local versus: a) Froude number Fr. b) Loading ratio Lr.

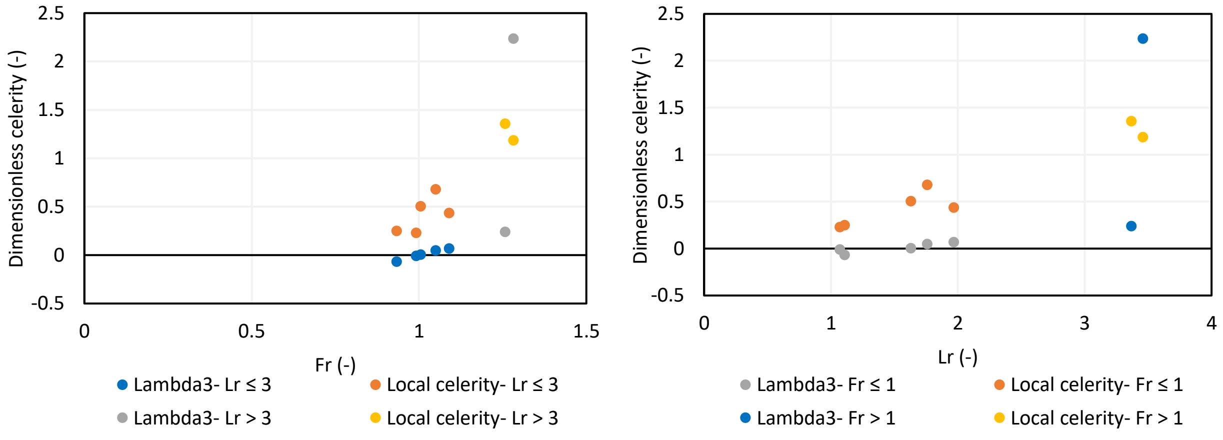

a) *b)*

Figure 3-55 Scenario2 _ Comparison Dimensionless Lambda 3 λ'_3 *and Dimensionless local celerity* C' *versus: a) Froude number* Fr*. b) Loading ratio* Lr*.*

Based on the above comparison, it could be considered that although there might be some similarities in pattern between Dimensionless local celerity $C'$and Dimensionless eigenvalues λ, the range of their values are different. Therefore, it would be helpful to find out whether there is any possible relationship between them. So that Figure 3-56 are provided to fulfill this demand.

Figure 3-56 show that it does not seem there is any relation between Dimensionless local celerity C' and λ'_2. In contrast, there is an almost linear relation between Dimensionless local celerity C' and both λ'_1 and λ'_3. Some research could be conducted in the future to find possible relations between these two parameters for more reliable comparison.

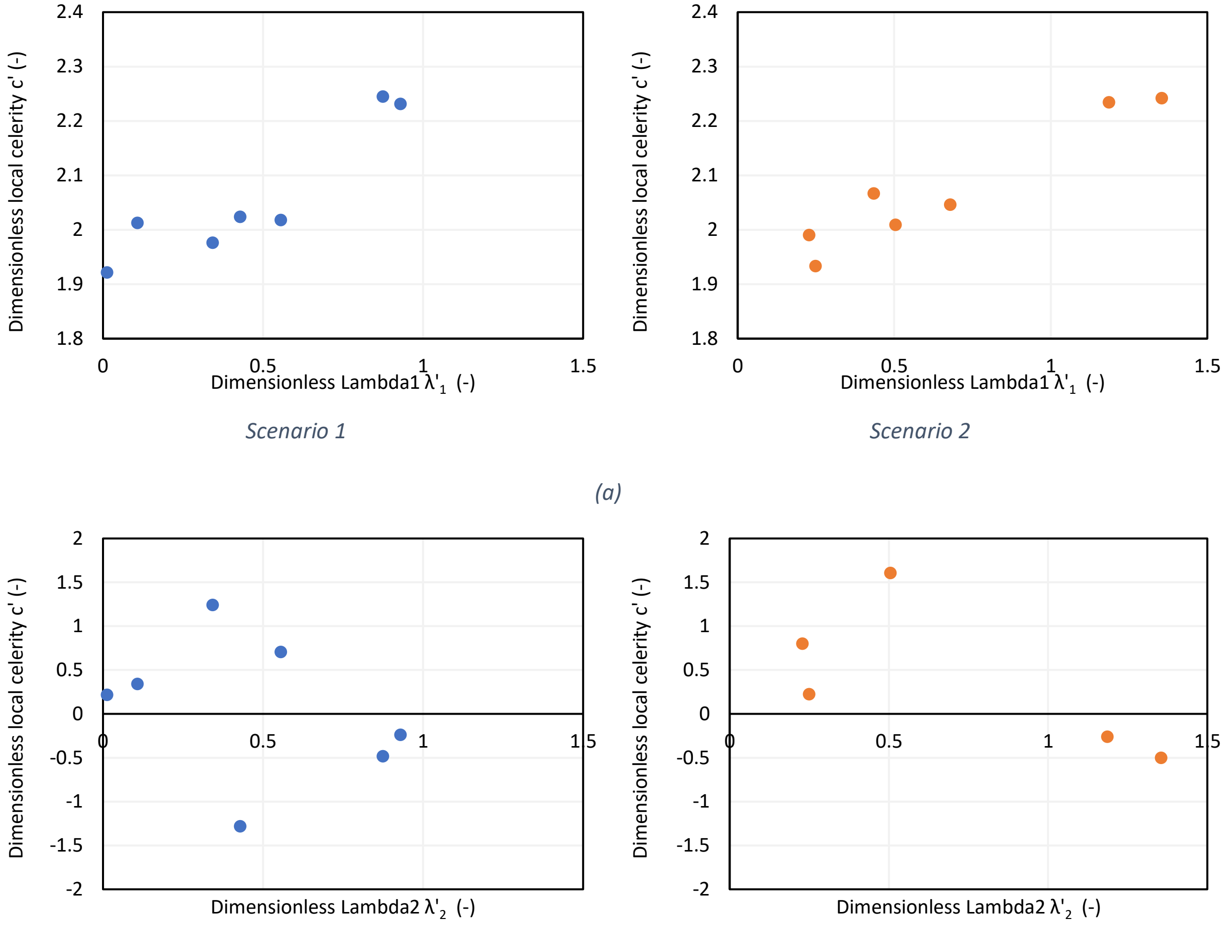

Scenario 1 *Scenario 2*

(a)

Scenario 1 *Scenario 2*

(b)

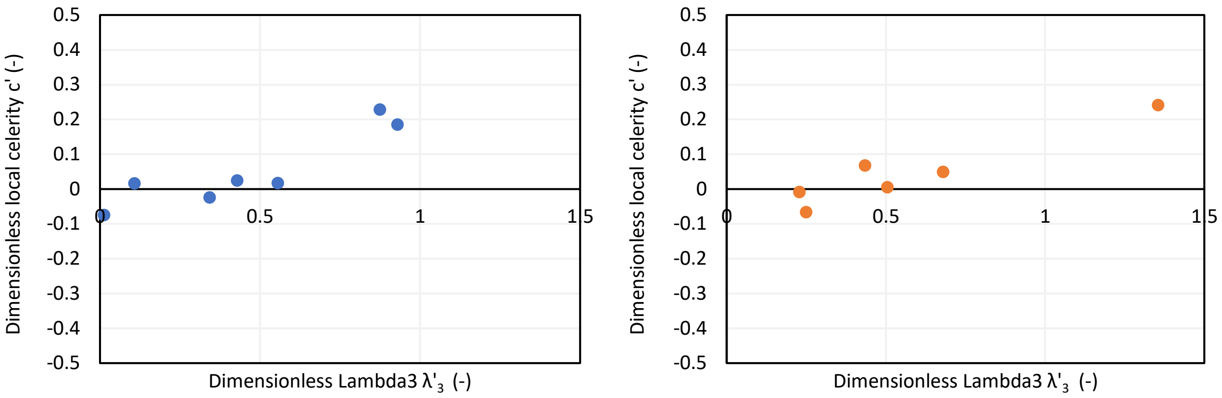

Scenario 1

Scenario 2

(c)

Figure 3-56 Both scenarios of Dimensionless local celerity C' versus Dimensionless a) Lambda 1 λ_1'. b) Lambda 2 λ_2'. c) Lambda 3λ_3'.

Chapter 4:

SUMMARY AND CONCLUSIONS

The river's conveyance is prone to fall during a flood event because of the aggradation phenomena of the riverbed, where the morphologic evolution is determined by the balance between the solid material supply and the sediment transport capacity. It should be mentioned that since there is mostly a steep slope in the mountainous areas, the type of flow during flood events is supercritical mainly. Analyzing the aggradation phenomena in this type of flow experimentally and numerically is considered as a helpful tool for assessing the flood risk.

Specifically, the main topic is the propagating sediment properties along a channel in non-equilibrium conditions. Since the flow velocity is high in supercritical flow, the sediment front is dispersive and unrecognizable, so analyzing the sediment propagation is momentous. This factor is characterized by considering the evolution of deposition phenomena temporally and spatially. Employing an experimental model in the laboratory may allow determining properties of the morphologic evolution process (aggradation process). Furthermore, developing a numerical model validated by using experimental results can be employed as a predictive tool for flood risk assessment in physically infeasible situations. Fundamentally, the reported study aims to deepen the knowledge of channel aggradation phenomena by coupling numerical and experimental approaches.

The aggradation process experiments in supercritical flow formed the experimental campaign are executed in the Mountain Hydraulics Laboratory (located in the Lecco campus, Politecnico di Milano). The current study continues previous theses (Heydari, 2020 and Eslami et al., 2021) by modifying measurement methods related to the experimental setup, MATLAB code, and developing new methods for analyzing the celerity of the aggradation wave. The mentioned campaign consists of 14 aggradation experiments (AE), varying in the water and inflow sediment discharges. It should be noted that trials AE01 to AE05 and AE06 to AE08 were performed by Heydari, 2020, and Eslami et al., 2021 respectively. During this campaign, the aggradation process as a dynamic event is recorded by various cameras installed at different parts of the experimental setup. Then data acquisition is executed by image processing.

The sediment inflow discharge Q_{sin} is estimated by implying proper transfer functions based on experiment characteristics on the mean velocity of sediment fed in the channel u_{mean} obtained through a PIV algorithm. The mentioned functions are induced through a calibration process for different vibration levels and opening heights. Notably, the procedure of obtaining the transfer function related to the opening height of 3 cm is conducted in this thesis.

The channel’s bed and water surface levels change continuously during the experiment due to the aggradation process. Therefore, it is required to record sediment and water elevations to be capable of analyzing this dynamic behavior. Water and sediment profiles at different times of each experiment are used as one of the significant inputs for developing the analysis of hydro-morphological parameters, so these profiles should be reliable and accurate as much as possible. Moreover, measuring these profiles with a low computational cost is beneficial. Accordingly, the factors leading to some errors in generating profiles in previous works (Eslami et al., 2021) are identified. These error factors are divided into four groups; noises, objects that obstruct the cameras view along the channel, image distortions, and discontinuity in the final profile. Some modifications and innovations related to the laboratory setups, measuring devices, and MATLAB code are executed to address the mentioned errors and generate more accurate profiles with the minimum computational cost. One solution is to use one single camera instead of multiple cameras for recording, followed by modifications and innovations in the MATLAB code to address the other errors and analyze the images that are compatible with the new conditions. Moreover, to use the data of previous experiments performed with two cameras, modifications were made in MATLAB code to reduce the mentioned errors as much as possible. So, analysis is performed again with newly generated profiles for experiments AE06, AE07, and AE08 from previous work. Also, for this transition from the previous method to the new modified method, validation analyses confirmed the results obtained in the new modified method.

The maximum sediment passing through a specific river section is defined as sediment transport capacity Q_{s0}. This parameter is characterized by the flow properties, channel's physical properties, and sediment material' properties. Three main methods are employed for estimating this value in this thesis. The first one is the Meyer-Peter and Müller formula (MPM formula), one of the most common formulae for estimating the Q_{s0}. The second one is the collector method which is defined based on the concept of discharge definition as a volume in time in the collector. Indeed, the deposition rate of the sediment particles trapped in the collector at the initial times of the experiment gives the initial sediment transport capacity. The last one is the continuity method based on the mass conservation law. This method finds the initial sediment transport capacity by subtracting the calculated initial sediment deposition rate from the sediment feeding rate. The reference value for final sediment transport capacity Q_{s0} for each experiment in this work is represented as the average value of the collector method and the second scenario of the continuity method (CU2 and IU2). Also, the sediment transport capacity for each discharge is calculated by taking the average of Q_{s0} obtained from all experiments with similar discharge. The values of Q_{s0} belonging to the water discharges of $5\ l/s$,$6\ l/s,\ and\ 7\ l/s$ are gained equal to $8.31 \times 10^{-5}\ m^3/s,\ 1.43 \times 10^{-4}\ m^3/s,$ and $1.28 \times 10^{-4}\ m^3/s$ respectively. It should be highlighted that there is a contradiction among the estimated value of Q_{s0} for each discharge. The Q_{s0} belonging to water discharge 6 l/s is larger than that of Q_{s0} related to 7 l/s.

After evaluating sediment feeding discharge Q_{sin} and initial sediment transport capacity Q_{s0}, the loading ratio is calculated by $Lr = Q_{sin}/Q_{s0}$ for each experiment. When the loading ratio is around one ($Lr \approx 1$), a near-equilibrium condition, the slope of sediment and water profiles remains almost constant during the experiment. Furthermore, the aggradation process occurs along the channel when the loading ratio is more significant than one ($Lr > 1$).

The conducted experiments are divided into three groups considering their temporal evolution of the slope. First, experiments in which the slope of the sediment profiles remains almost constant after a short time (AE02, AE03, AE04, AE07, and AE13). These experiments have an approximately same slope after a slight growth at the beginning. This situation can be noted as a near-equilibrium condition. Second, experiments that need a longer time to reach a near-equilibrium situation rather than the previous group (AE01, AE06, AE08, and AE14). These experiments possess diverse slopes at the beginning, which tend to reach the same constant slope as they get close to the end of the experiments. Third, experiments with a shorter duration of the experiment than others (AE05, AE10, and AE11). These experiments hold the highest loading ratio and have the shortest duration among these three groups (due to the fast process and limited sediment volume fed). Consequently, they need more time to reach the near-equilibrium condition.

The elevation color gradient maps are provided for each experiment to analyze the water and sediment profiles in detail. Color gradient maps can provide the opportunity to illustrate the spatial and temporal evolution of profiles simultaneously.

In the current thesis, the first 50-sec span of the experiments is supposed as initial times, and the water and sediment profiles related to this interval are not fully considered in the calculation of some parameters such as celerity and Froude number. This decision is made concerning two points. First, in the initial times, although the experiment commences ($t = 0\ sec$), no sediment had yet arrived in the flume, and the experiment is run just with water flow. So, the profiles obtained at these times are not our demanded profiles. Second, the actual water discharge in the experiment differs from the nominal water flow rate ($Q_{nominal}$ can be $5, 6$, and $7\ l/s$ considering the current campaign). This difference is due to two main reasons. On the one hand, the water flow rate moderately increases from the beginning of the test to reach the nominal value; therefore, it is not the same as the nominal water discharge at the beginning of the experiment. On the other hand, an alteration of flow rate and depth happens considering the dam-like effect of sediment falling upstream.

Froude number Fr is obtained as a function of water depth and the average water velocity in each cross-section. The water depth is calculated from generated profiles at different times and locations. Moreover, the average water velocity in different times and spaces is calculated by dividing the nominal water discharge, which is constant, by the cross-section area. Then the Froude number Fr is evaluated as a time-space matrix. Results illustrate that in near-equilibrium conditions (AE07 and AE13), the maximum value of the Froud number Fr is related to the downstream location, and this is due to the smaller value of the water depth downstream. In contrast, upstream almost possess the maximum value of the Froude number in other experiments. To represent a reference value of the Froude number Fr for each experiment out of its continuous space-time, averaging with multiple patterns is done. Considering the results from these averaging, while experiments AE10 and AE11 have average Froude number Fr of more than one ($Fr > 1$), others possess average Froude number Fr around one ($Fr \approx 1$). The high value of this parameter in experiments AE10 and AE11 can be due to the high value of the loading ratio Lr. Indeed, in experiments with a high loading ratio Lr, the variation of sediment profiles is more, and the slope is more comparing other experiments. Therefore, the flow velocity in these experiments is more than the experiment with less loading ratio Lr and leads to a higher

Froude number Fr. Therefore, it can be concluded that the loading ratio Lr might affect the Froude number Fr directly.

Since the aggradation happens in a dispersive way when dealing with higher flow velocities, it gets almost impossible to detect any aggradation front; therefore, it is not possible to obtain celerity by studying the sediment front location in different time instants. An attempt is made to overcome this problem by using two different methods, which are calculating the Local celerity C and estimating the eigenvalues λ by applying some literature methods.

In the first method, by dividing the matrix of $\frac{\partial Z}{\partial t}$ by matrix related to $-\frac{\partial Z}{\partial x}$, the Local celerity matrix is calculated and shown as a color gradient map of Local celerity. It is worth mentioning that the value of Local celerity C is calculated based on the referenced bed elevation matrix in this thesis. Considering the obtained values for Local celerity C, one can figure out values change during time and space, and Local celerity C is not a unique value. Furthermore, the value of Local celerity C decreases for all experiments over time because the channel tends to reach the equilibrium condition, in which the Local celerity C could be around zero, by passing the time. Moreover, the pattern of the Local celerity C from upstream to downstream differs in experiments by considering the Loading ratio Lr. In the experiment with $Lr \approx 1$ (such as AE07 and AE13), the value of local celerity fluctuates slightly around zero. In contrast, in the experiment with a loading ratio larger than one ($Lr > 1$), the local celerity map shows the maximum value upstream and downstream since the generated profiles show aggradation and degradation in these locations, respectively, at initial times. Furthermore, local celerity shows a value around zero after the initial times when the channel is close to the equilibrium condition. The average Local celerity C during time and space is calculated as a representative value of this parameter for each experiment, then this value of experiments is compared with each other. In this way, results show that the Local celerity C in experiments AE10 and AE11 is the highest. This issue may be rooted in the fact that these two experiments have the highest loading ratio Lr. Moreover, the average Local celerity C during time and space in experiments AE07 and AE13 are similar and are close to zero, and it confirms that these experiments are in nearly equilibrium condition.

The second method is related to solving the Saint-Venant-Exner equations. This system has three eigenvalues λ which might somehow show the values of celerity, theoretically. The matrix form of water depth and average velocity are used as input for solving this system. The results show that the value of λ_1 *and* λ_3 are somehow constant, but the value of λ_2 changes. λ_1 has the highest value in most experiments because it calculates using the equation V+$\sqrt{gd}$ in which two positive quantities are summed up. In contrast, λ_3 results as the lower values are calculated from equation V-$\sqrt{gd}$ in which two quantities are subtracted. To comparing the results obtained in this part, the average value of different eigenvalues λ is calculated. The calculated average value of eigenvalues λ shows that the value of λ_1 is almost more than λ_2 and λ_3 . Furthermore, λ_2 fluctuates and it is rarely larger than λ_1 but mostly larger than λ_3 during time and space except in experiments AE10 and AE11, where λ_2 is mostly constant and smaller than λ_3 during times and spaces.

Typically, experimental results are related to theoretical concepts by numerical modeling. If there is proper coordination between the results of this numerical model and the experimental results, this numerical model can be used to predict and simulate physically unfeasible conditions. In this thesis, numerical modeling is performed by BASEMENT software. BASEMENT solves a hydro-morphologic system of PDEs, including two SVEs and one Exner equation, to numerically model a situation similar to the experimental work with similar characteristics and boundary conditions. The assigned boundary conditions in the software are water discharge and sediment inflow discharge upstream and water and bed elevations downstream. These defined boundary conditions are different from the theoretical concepts considering the supercritical flow. Indeed, the water elevation is a boundary condition required by software downstream. By considering this boundary condition, the slope of the upstream, and using a flow resistance law for a uniform flow, the software calculates the water depth upstream. Moreover, the sediment inflow discharge is an actual boundary condition defined for software upstream. The numerical simulation has been performed for AE06 to AE14 except for AE09 and AE12. After comparing the initial results of these models with experimental outcomes, it can be observed that there is no consistency between profiles. So, the numerical model has been calibrated by simultaneously changing the two coefficients of Manning's coefficient n and bedload factor α (the Meyer-Peter and Müller formula's multiplier coefficient). Several trials have been developed by considering different combinations of these two coefficients for each experiment. Finally, the best trial has been selected by considering the minimum least square errors calculated for both bed and water surface elevation. Its coefficients are reported as the corresponding coefficient for that experiment.

After obtaining the final slope, Local celerity C, eigenvalues λ, Manning's coefficient n, and Bedload factor α for each experiment, two types of analysis have been done to determine whether they are affected by Froude number Fr and Loading ratio Lr as two significant characteristics of each experiment.

The first type of analysis is dimensional analysis. In this type, Manning's coefficient n is studied versus Froude number Fr and Loading ratio Lr. It can be concluded that the Froude number Fr and the Loading ratio Lr cannot impact Manning's coefficient n.

The second types of analysis are dimensionless analysis. In this type of analysis, while the bedload factor α and final slope are already dimensionless, Manning's coefficient n and celerity are converted to dimensionless parameters.
As the first parameters, Dimensionless Manning's coefficients n' are plotted based on the Froude numbers Fr and Loading ratios Lr. There is an upward, almost linear trend between dimensionless Manning's coefficients n' and both Froude number Fr and Loading ratio Lr. On the one hand, one might presume that the relationship between Manning's coefficients n' and Froude number Fr is spurious because they both depend on the average velocity of flow v. On

the other hand, Froude number Fr and Loading ratio Lr have an increasing linear relationship. So, considering this relationship and the increasing linear relationship between dimensionless Manning's coefficient and Loading ratio Lr, it can be said that this relationship may be real. Nevertheless, it is not possible to conclude with certainty whether the correlation between Dimensionless Manning's coefficient n' and Froude number Fr is genuine or spurious, and more research is needed.
Bedload factor α is analyzed as the second parameter. It can be deduced that while the Loading ratio Lr does not affect bedload factor α, there is an approximately increasing linear relation between Bedload factor α and Froude number Fr.
Results from the third parameter, the final slope, show that the final slope increases by rising the Froude number Fr and Loading ratio Lr.
The analysis of the fourth parameter which is Dimensionless average Local celerity C' shows that for all experiments, dimensionless average Local celerity C' increases by both parameters ($Fr\ and\ Lr$).
Results of the last parameter which is average eigenvalues λ' shows that, the value of λ'_1 and λ'_3 almost increase linearly by rising both Froude number Fr and Loading ratio Lr. Furthermore, λ'_2 can have different value when Froude number is around one and loading ratio less than three ($Lr < 3$). When $Lr > 3$ and $Fr > 1$, the λ'_2 rises by growing in the Froude number Fr and $Loading\ ratio\ Lr$. Moreover, it seems that λ'_2 is not continuous when the Froude number Fr is almost equal to one, and it tends to infinity.
All in all, by considering these two kinds of analyzes, there are three robust results. First, the Bedload factor α increases by growth in Loading ratio Lr. Second and third, the final slope is directly affected by increasing the Froude number Fr and Loading ratio Lr.

The values of Dimensionless average local celerity C' and Dimensionless eigenvalues λ' are plotted based on Fr and Lr to find any possible relation between these two parameters. Results show that values of λ'_2 and Dimensionless average local celerity C' for experiments with Froude number around one ($Fr \approx 1$) and Loading ratio less than three ($Lr < 3$) are approximately similar. The results related to λ'_1 follow a pattern similar to the results of Dimensionless average local celerity C', except that the range of their numbers is higher than the range of Dimensionless average local celerity C' numbers. Based on this comparison, it could be concluded that although there might be some similarities in pattern between Dimensionless average local celerity C' and Dimensionless eigenvalues λ', the range of their values is different.

Based on this comparison, it could be concluded that although there might be some similarities in pattern between Dimensionless average local celerity C' and eigenvalues λ', the range of their values are different. Therefore, it might be not completely correct to compare the Dimensionless eigenvalues λ' with Local celerity C' values of elevation. In fact, the eigenvalues will be the slope of the characteristic lines (dx/dt), but actually not necessary the ratio of (dx/dt) with respect to elevation, and they can be the (dx/dt) of other parameters. To make it clearer, Lambdas are the eigenvalue of St. Venant equations system in unsteady flow, and they are used to find the characteristic form of the equations (celerity). It means that if one applies the eigenvalues formula for finding celerity, the results would be different because the formula is different. When the eigenvalues λ are different from the celerity of system it might not correct to compare it with Local celerity C. Since the distribution of data belonging to local celerity and eigenvalues are different it is tried to find if there is a relationship between them or not.

Moreover, the relation between Dimensionless average local celerity C' and Dimensionless eigenvalues λ' is investigated by plotting them versus each other. The results show that it does not seem there is any relation between Dimensionless average local celerity C' and λ'_2. In contrast, there is an almost linear relation between dimensionless average local celerity C' and both λ'_1 and λ'_3.

There are some issues related to this work that should be handled somehow within future works.

1. There might be some experimental distortions affecting the results. In particular, the issue of the discrepancy between the actual initial discharge in the flume and the nominal one could be investigated better in the future to have a more trustful value for this parameter.
2. This one is related to averaging and considering different scenarios for conversion from a spatial-temporal distribution to a single value for estimating different parameters. In this matter, different scenarios calculated by averaging rows, columns, and rectangles are performed in this thesis. Finding the more reliable averaging method could be studied more in the future.
3. This one is related to calculating the local celerity. This work calculates local celerity based on referenced experimental profiles concerning the channel slope. However, calculating this parameter using absolute profiles and numerical model results could be done in the future.
4. This one is related to different concepts of celerity and eigenvalues, and some comparison between them was made in this thesis. Some research could be conducted in the future to find possible relations between these two parameters for a more reliable comparison.
5. This is about the contradiction among the estimated value of Q_{s0} for each discharge. The Q_{s0} belonging to water discharge 6 l/s is more significant than that of Q_{s0} related to 7 l/s. The reason for this inconsistency needs more studies in the future.
6. More experiments are needed to perform in the future, in particular experiments with a loading ratio of more than two ($Lr > 2$) and Froude number larger than 1.2 ($Fr > 1.2$) to validate the obtained results.
7. Considering a proper reference line used to define the occurrence of degradation and aggradation can be investigated more in the future. In this thesis, before the start of the experiments, the reference bed was already eroded by water flow, especially in downstream.
8. Using the collector and continuity methods to estimate the Qs0 could result in either overestimation or underestimation of this parameter. A different method for improving the accuracy of estimating the Q_{s0} could be investigated more in the future.

9. There is a contradiction among the estimated value of Q_{s0} for each discharge. The Q_{s0} belonging to water discharge 6 l/s is larger than that of Q_{s0} related to 7 l/s. More studied can be conducted to figure out the reason behind this problem.
10. All experiments in this campaign are done by one channel slope; performing experiments with different channel slopes could be done in the future.
11. The equivalent coefficients in numerical modeling (Manning's coefficient n and Bedload α) can be chosen based on the development of other methods or kinds of errors. So, more research can be done to find the best tool to select these coefficients.
12. The reason for different behaviors of numerically calibrated profiles with respect to experimental ones upstream should be investigated more in the future.
13. Experiments AE01 to AE05 are not recomputed in this thesis due to the lack of time that could be done in the future.

Bibliography

Alves, E., & Cardoso, A. H. (1999). Experimental study on aggradation. *International journal of sediment research*, *14*(1), 1-15.

Buffington, J. M., & Montgomery, D. R. (1999). Effects of hydraulic roughness on surface textures of gravel-bed rivers. *Water Resources Research*, *35*(11), 3507-3521.

Chaudhry, M. H. (2007). *Open-channel flow*. Springer Science & Business Media.

Chien, N., & Wan, Z. (1999, June). Mechanics of sediment transport. American Society of Civil Engineers.

Dey, S. (2014). *Fluvial hydrodynamics* (pp. 529-562). Berlin: Springer.

Du Boys, M. P. (1879). The Rhone and streams with movable beds. *Annals des Pontes et Chaussees*, *18*, 22.

Exner, F. M. (1925). *Dynamische meteorologie*. Springer.

Goutière, L., Soares-Frazão, S., Savary, C., Laraichi, T., & Zech, Y. (2008). One-dimensional model for transient flows involving bed-load sediment transport and changes in flow regimes. *Journal of Hydraulic Engineering*, *134*(6), 726-735

Hager, W. H. (2005). Du Boys and sediment transport. *Journal of Hydraulic Research*, *43*(3), 227-233.

HEYDARI, E. (2020). Experimental analysis of channel overloading in supercritical condition. (Master's Thesis, Politecnico di Milano, Milan, Italy)

Jain, S. C. (1981). River bed aggradation due to overloading. In *Journal of the Hydraulics Division, Proceedings of the American Society of Civil Engineers* (Vol. 107).

Lyn, D. A. (1987). Unsteady sediment-transport modeling. *Journal of Hydraulic Engineering*, *113*(1), 1-15.

Lyn, D. A., & Altinakar, M. (2002). St. Venant–Exner equations for near-critical and transcritical flows. *Journal of Hydraulic Engineering*, *128*(6), 579-587.

Miglio, A., Gaudio, R., & Calomino, F. (2009). Mobile-bed aggradation and degradation in a narrow flume: Laboratory experiments and numerical simulations. *Journal of Hydro-environment Research*, *3*(1), 9-19.

Radice, A., & Villota, S. U. (2018). Propagation of aggrading sediment fronts in a laboratory flume. In *E3S Web of Conferences* (Vol. 40, p. 05055). EDP Sciences.

Radice, A., & Zanchi, B. (2018). Multicamera, multimethod measurements for hydromorphologic laboratory experiments. *Geosciences*, *8*(5), 172.

Radice, A., Malavasi, S., & Ballio, F. (2006). Solid transport measurements through image processing. *Experiments in fluids*, *41*(5), 721-734.

Radice, A., Rosatti, G., Ballio, F., Franzetti, S., Mauri, M., Spagnolatti, M., & Garegnani, G. (2013). Management of flood hazard via hydro-morphological river modelling. The case of the M allero in I talian A lps. *Journal of Flood Risk Management*, *6*(3), 197-209.

Shields, A. (1936). Application of similarity principles and turbulence research to bed-load movement.

Soni, J. P., Ranga Raju, K. G., & Garde, R. J. (1980). Aggradation in streams due to overloading. *Journal of the Hydraulics Division*, *106*(1), 117-132.

UNIGARRO VILLOTA, S. (2017). Laboratory study of channel aggradation due to overloading. (Master's Thesis, Politecnico di Milano, Milan, Italy)

Yen, C. L., Chang, S. Y., & Lee, H. Y. (1992). Aggradation-degradation process in alluvial channels. *Journal of Hydraulic Engineering*, *118*(12), 1651-1669.

ZANCHI, B. (2018). Experimental investigation of the deposit phenomenon in a supercharged moving floor channel. (Master's Thesis, Politecnico di Milano, Milan, Italy)

ZUCCHI, M. (2018). Experimental and numerical study of channel aggradation. (Master's Thesis, Politecnico di Milano, Milan, Italy)

YAVARY NIA, M., Yousefyani, H., & Eslami, H. (2021). Experimental and numerical analysis of overloaded channel in supercritical condition. (Master's Thesis, Politecnico di Milano, Milan, Italy)

Appendix

Experiment AE06

Vibration level	Opening height (cm)	S_0 (%)	t (sec)	Q_{water} (l/s)	Q_{sin} (m^3/s)	Q_{s0} (m^3/s)	Froude number Fr	Loading ratio Lr
8.3	2	1.2	255	7	2.3E-04	1.41E-04	0.93	1.63

AE06 - 1 Experimental parameters

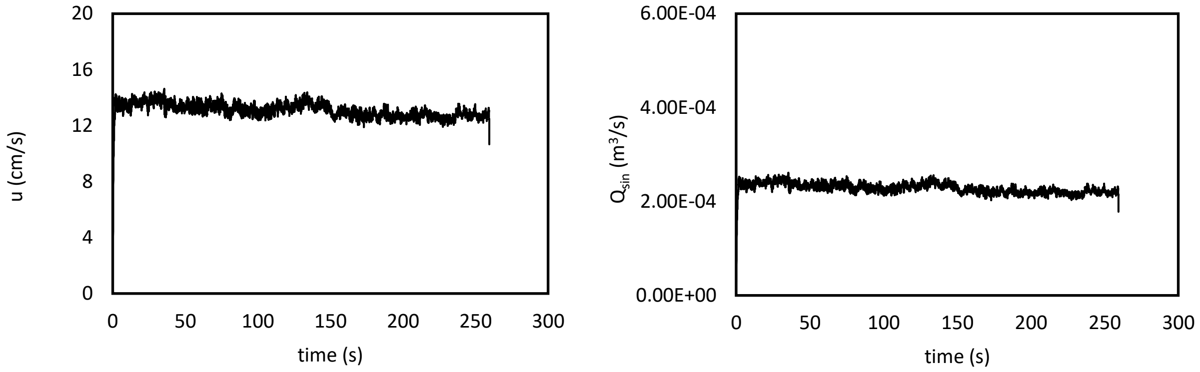

AE06 - 2 Temporal evolution of velocity and sediment discharge for the inflow material

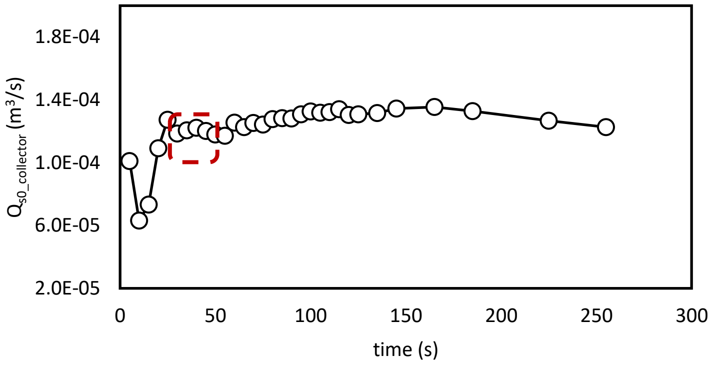

AE06 - 3 Temporal evolution of sediment transport capacity considering the collector method. The average of the constant values of Qs0 is considered as the $Q_{s0,\ collector}$

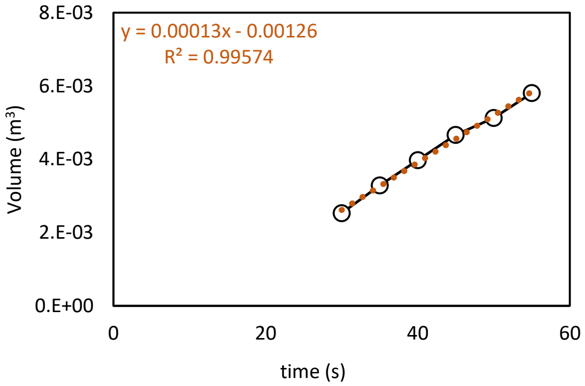

(a) CU2 Scenario

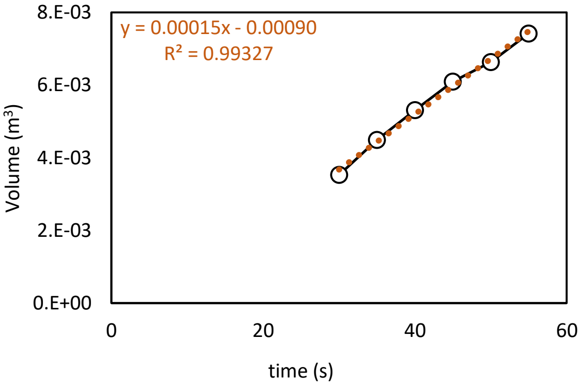

(b) IU2 Scenario

AE06 - 4 Temporal evolution of sediment transport capacity considering the continuity method and second scenario. The average of the slope of the interpolating lines is used to calculate Qs0, monitored.

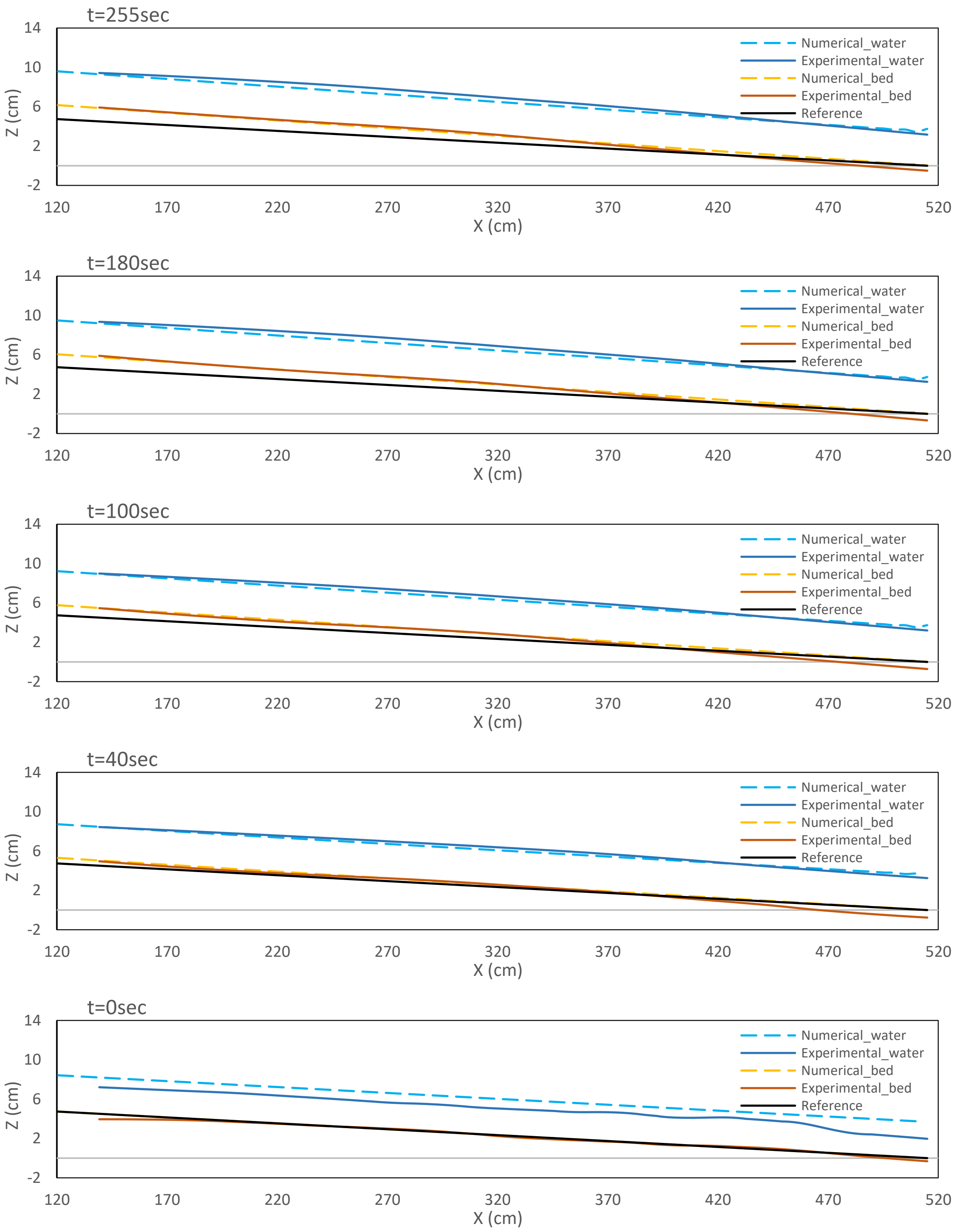

AE06 - 5 Spatial evolution of bed and water

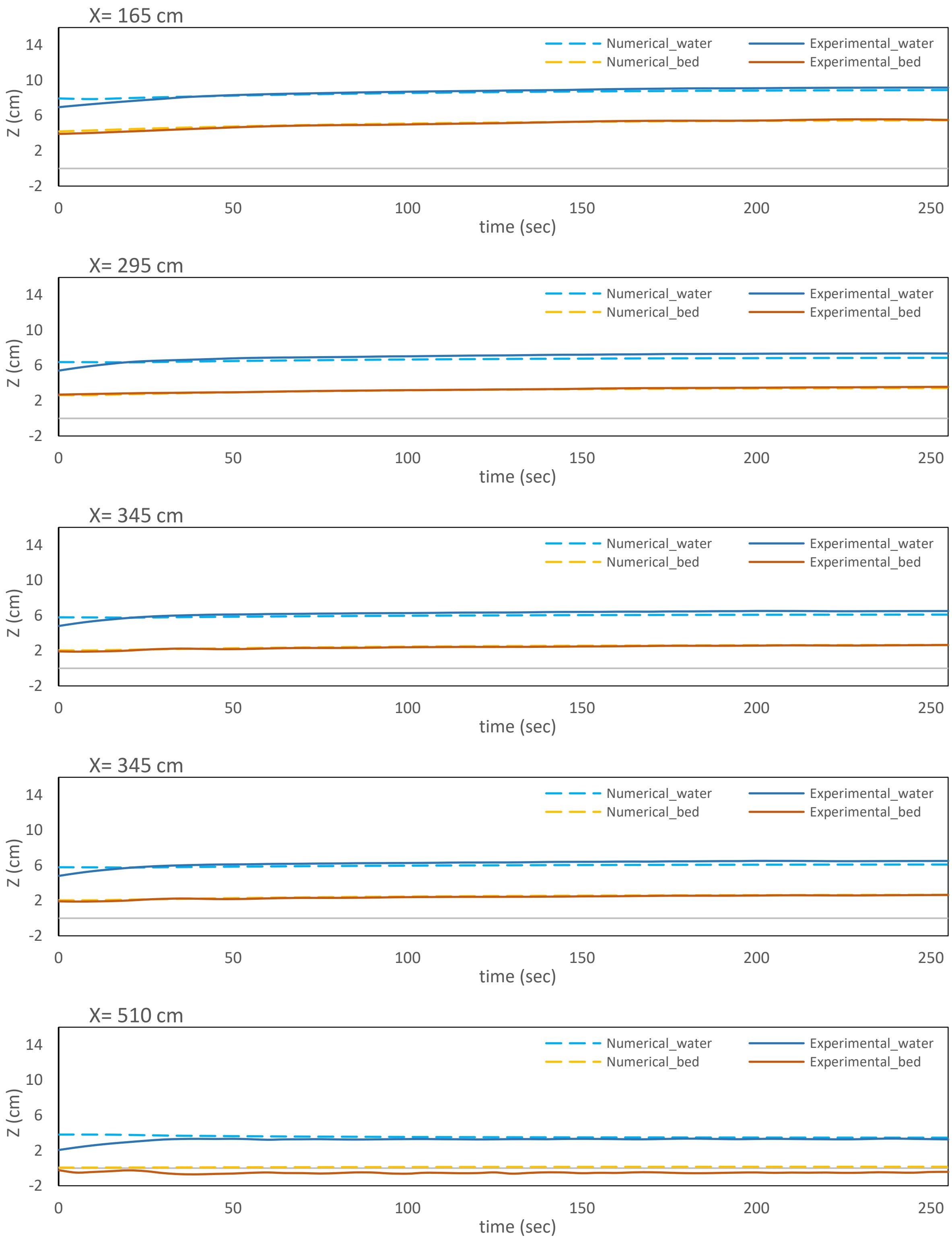

AE06 - 6 Temporal evolution of bed and water

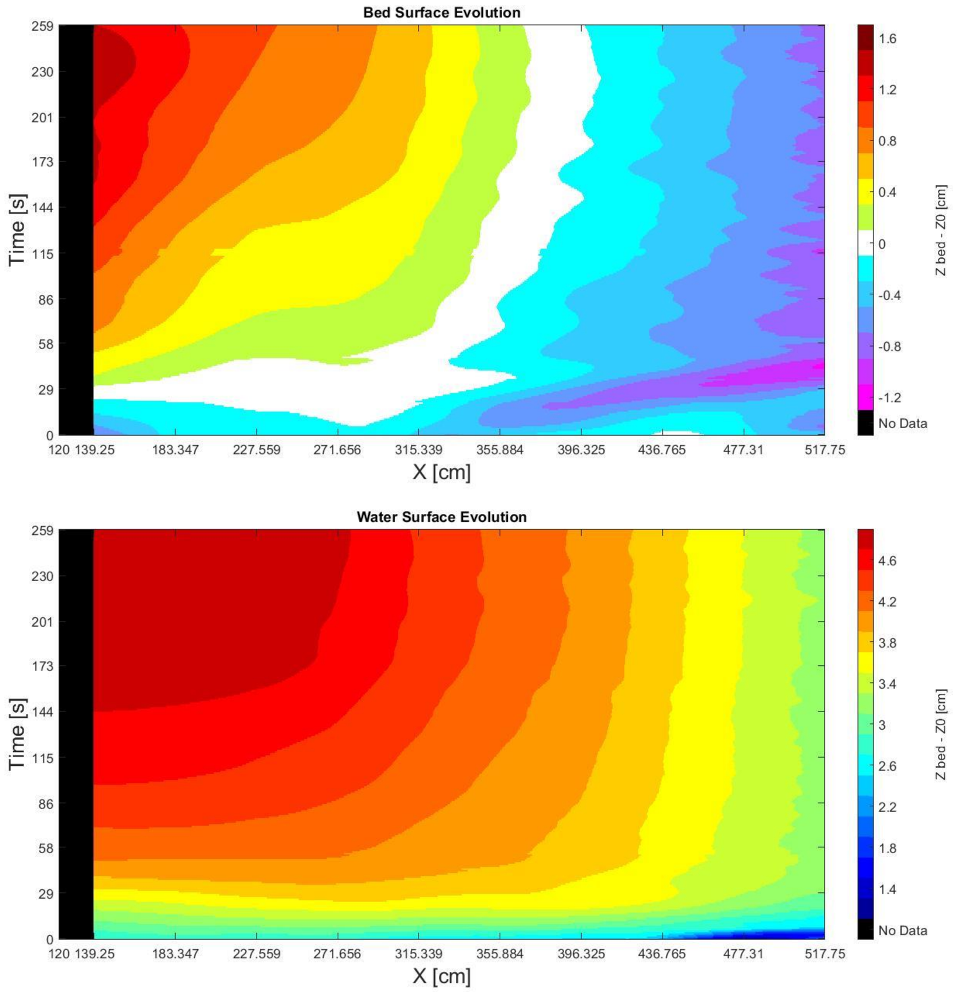

AE06 - 7 Color gradient maps for bed and water surface elevation evolution in space and time

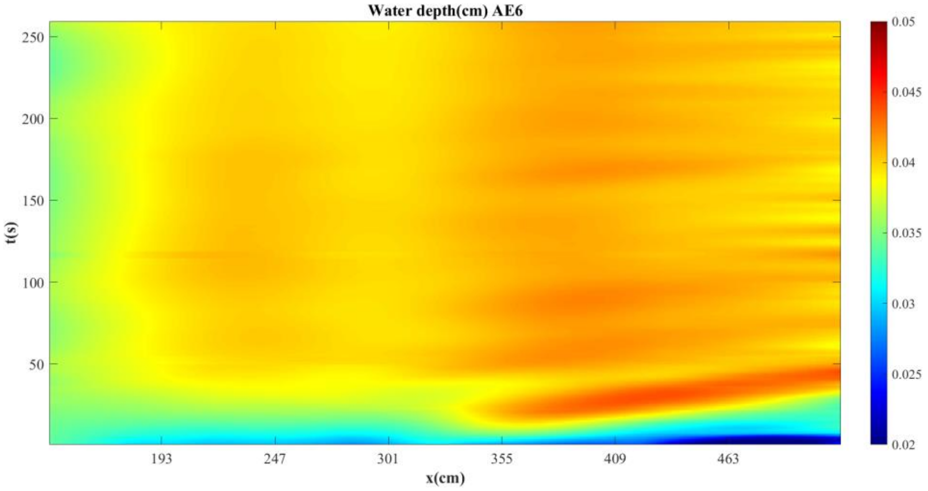

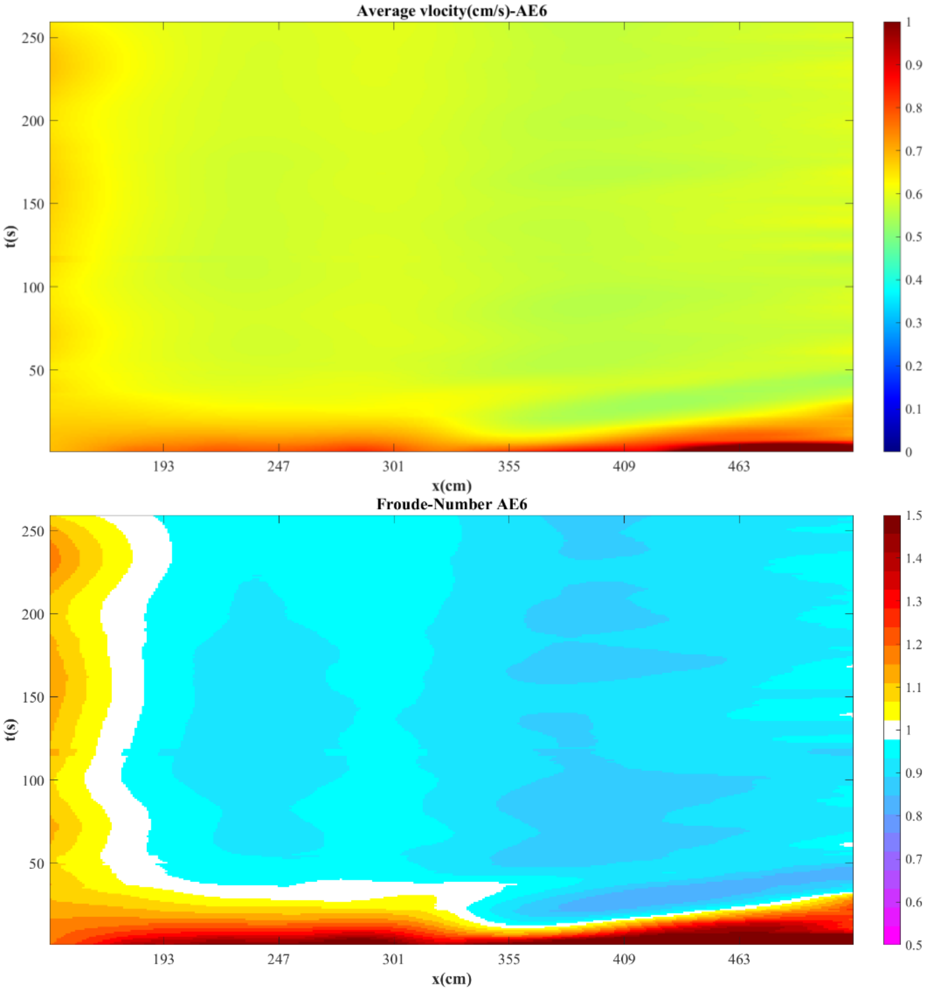

AE06 - 8 Color gradient maps for water depth, water average velocity, and Froude number Fr evolution in space and time

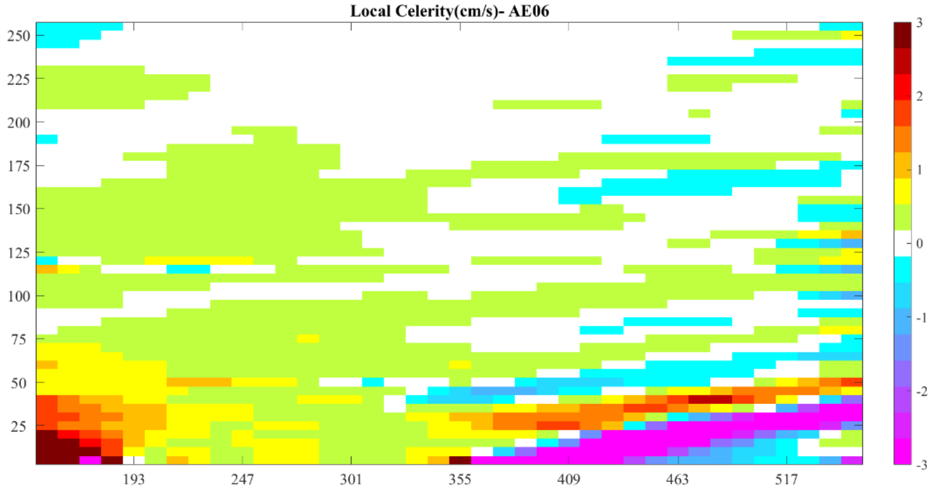

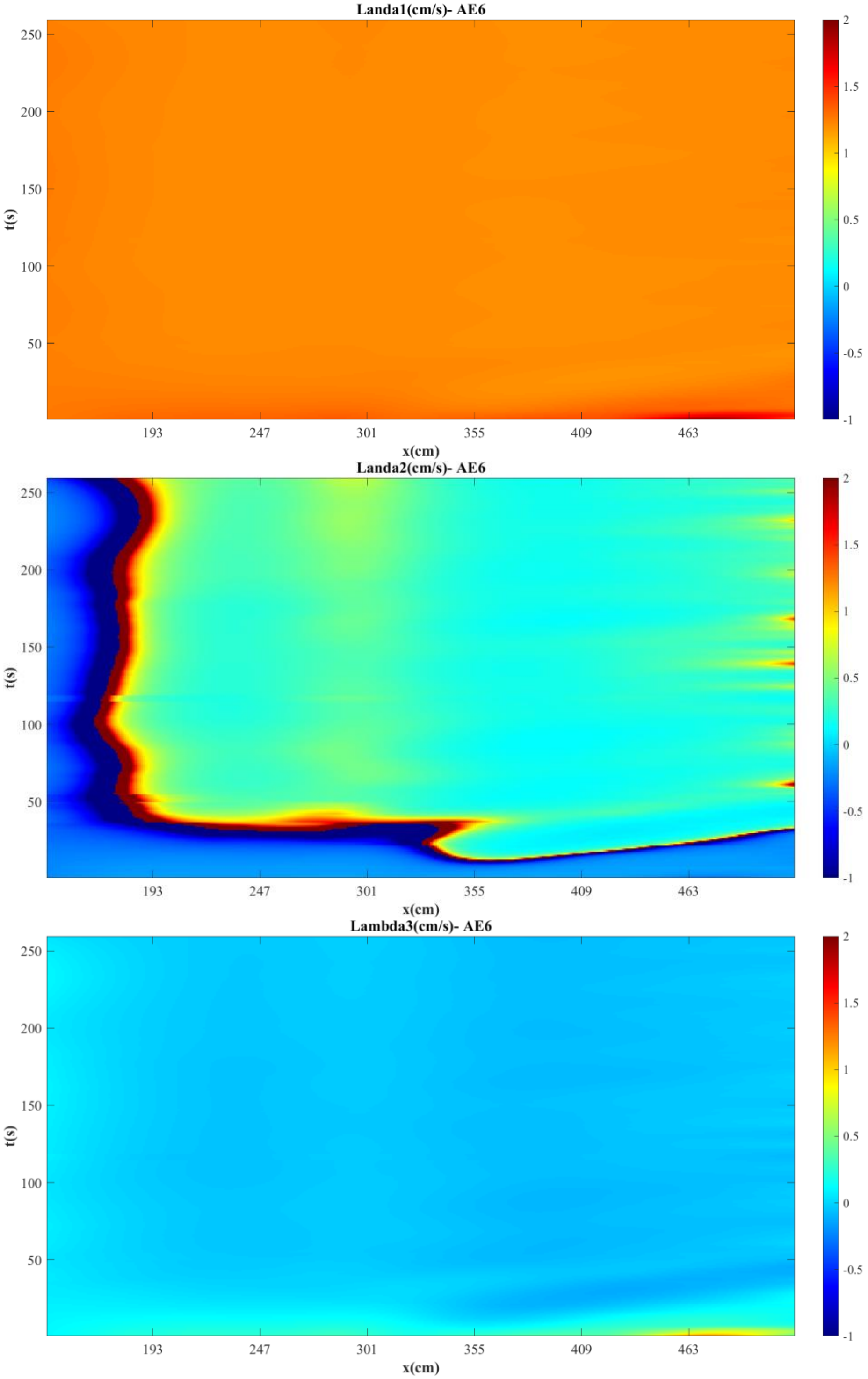

AE06 - 9 Color gradient maps for local celerity, Lambda 1, Lambda 2, and Lambda 3 evolution in space and time

Experiment AE07

Vibration level	Opening height (cm)	S_0 (%)	t (sec)	Q_{water} (l/s)	Q_{sin} (m^3/s)	Q_{s0} (m^3/s)	Froude number Fr	Loading ratio Lr
8	2	1.2	360	7	1.43E-04	1.29E-04	0.89	1.11

AE07 - 1 Experimental parameters

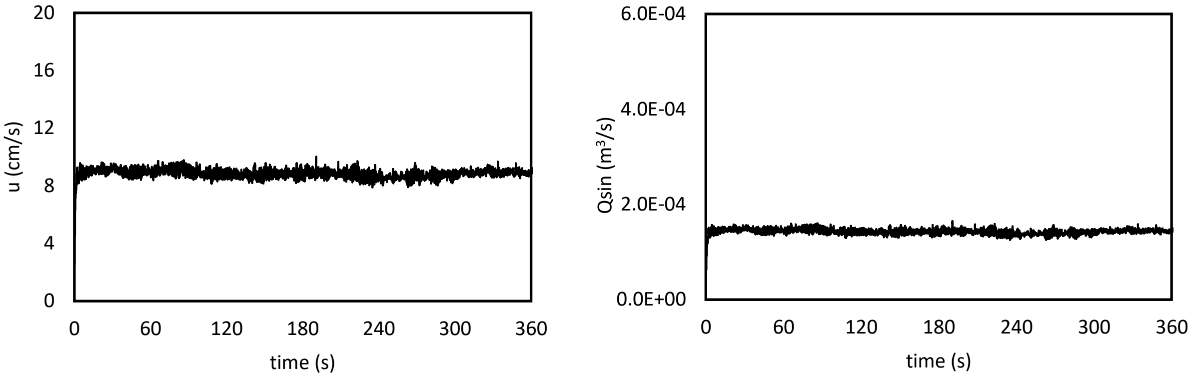

AE07 - 2 Temporal evolution of velocity and sediment discharge

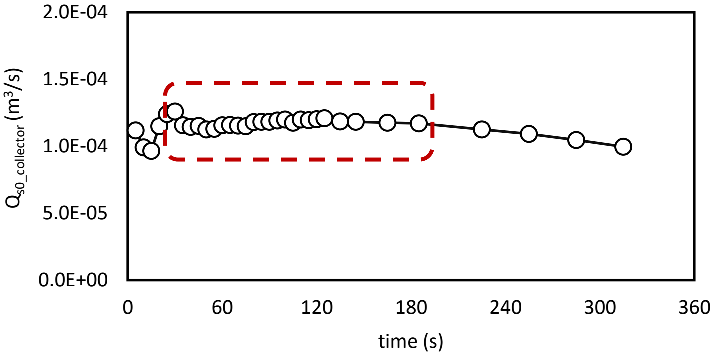

AE07 - 3 Temporal evolution of sediment transport capacity considering the collector method. The average of the constant values of Qs0 is considered as the Qs0, collector.

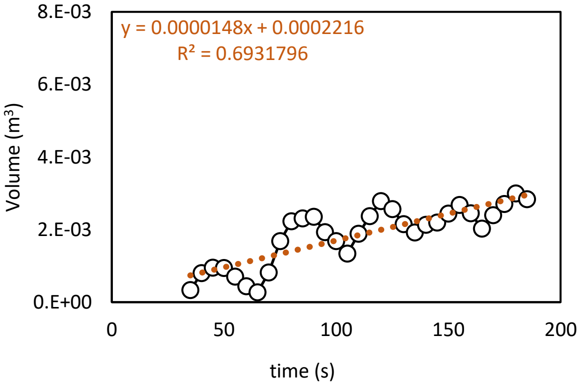

(a) CU2 Scenario

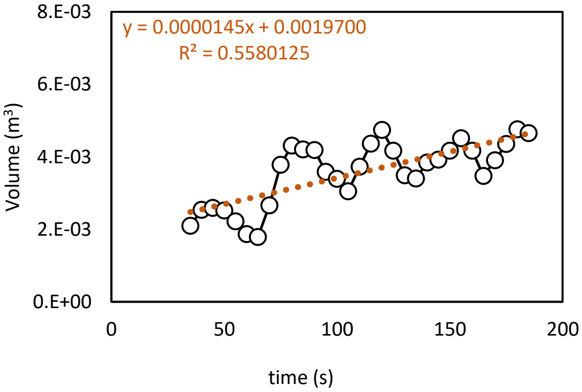

(b) IU2 Scenario

AE07 - 4 Temporal evolution of sediment transport capacity considering the continuity method and second scenario. The average of the slope of the interpolating lines is used to calculate Qs0, monitored.

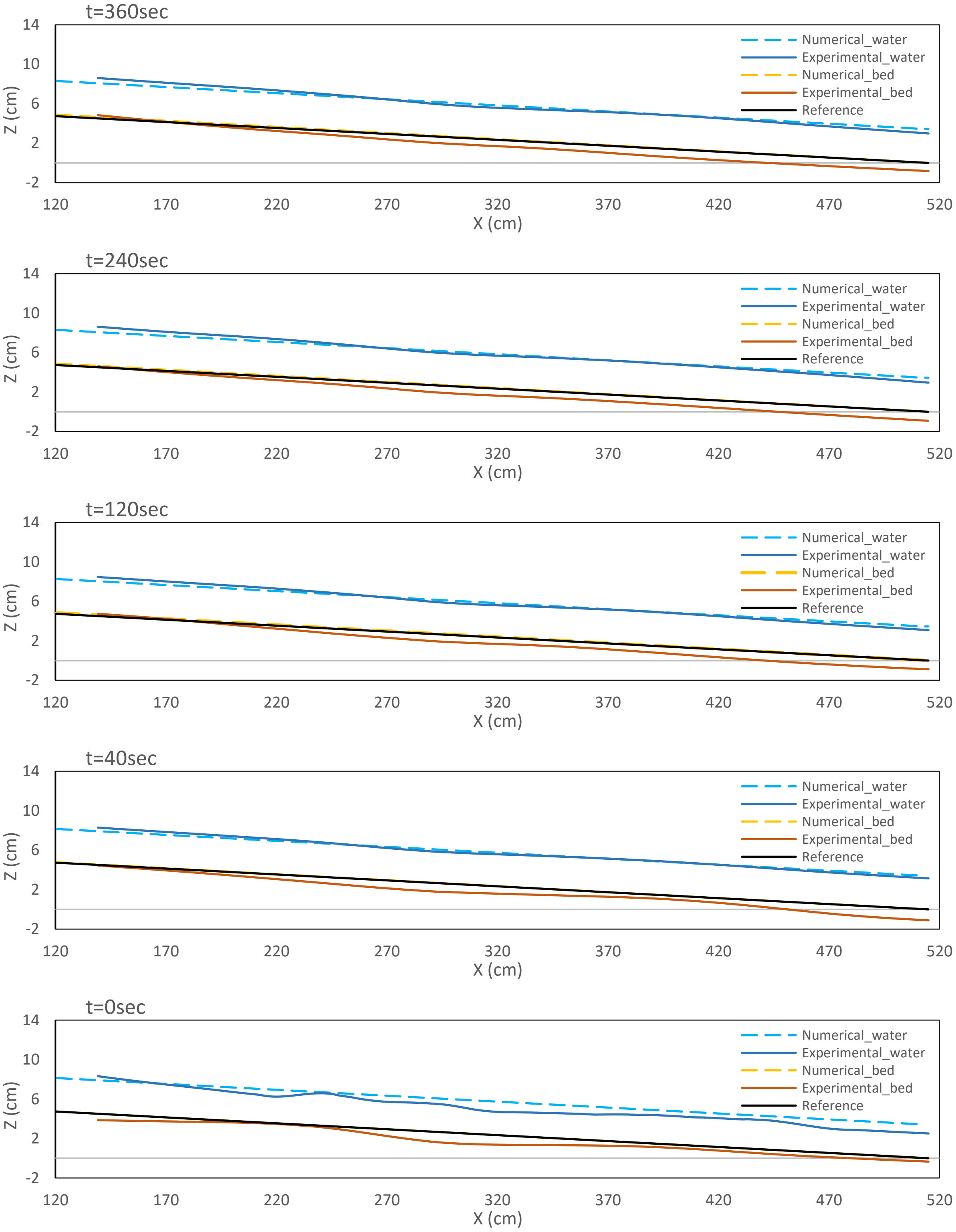

AE07 - 5 Spatial evolution of bed and water

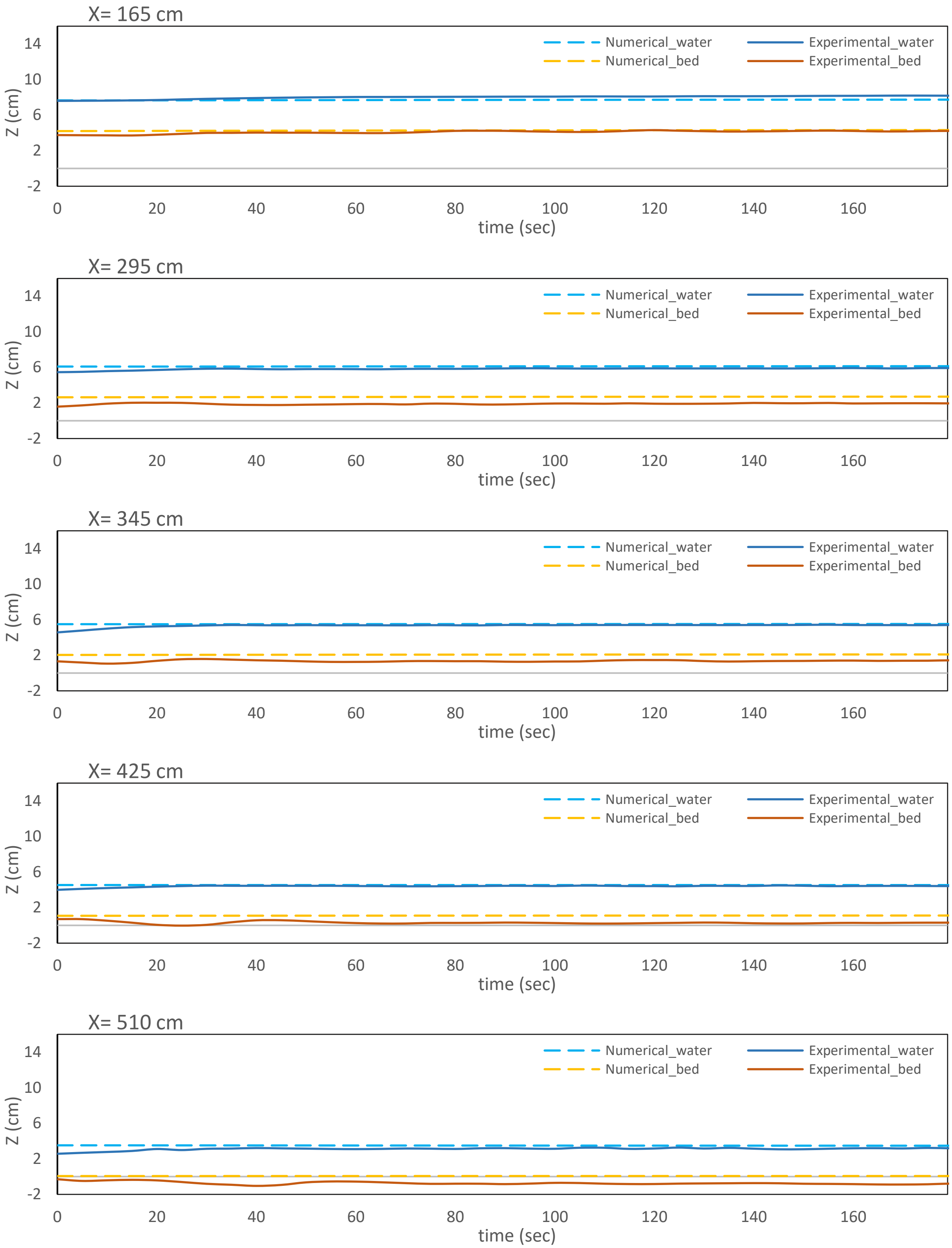

AE07 - 6 Temporal evolution of bed and water

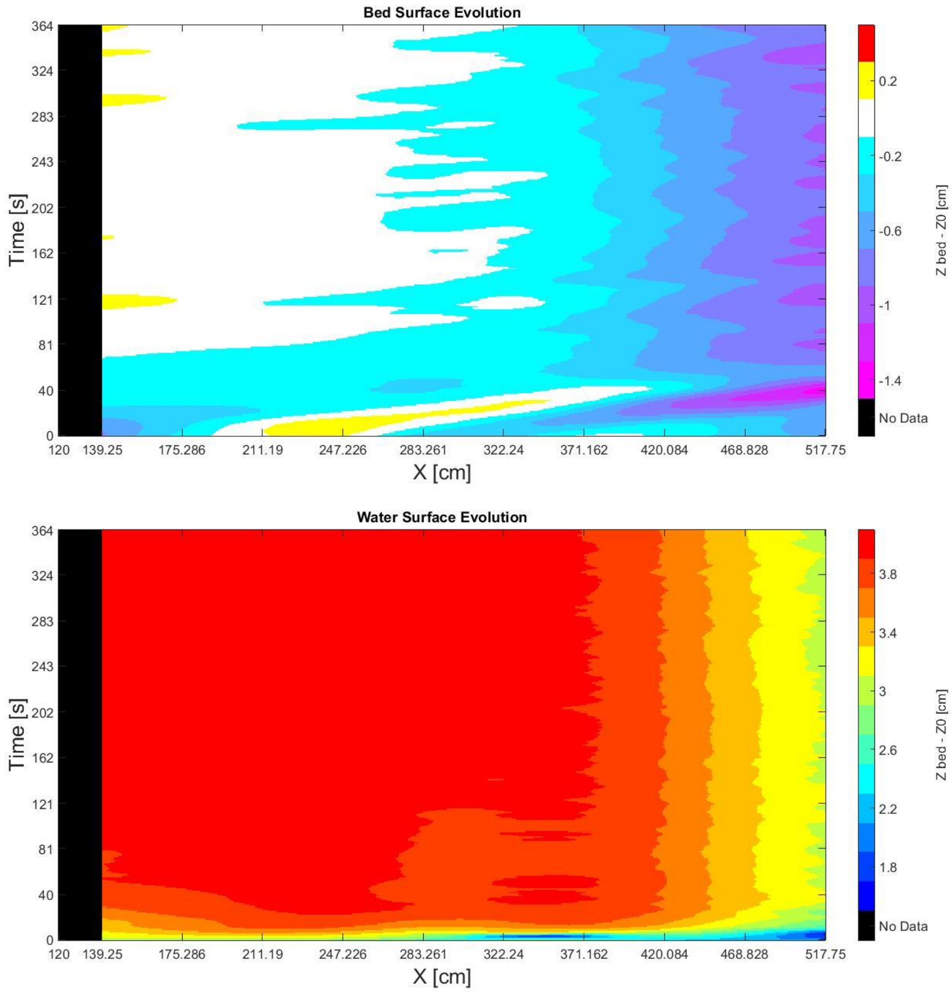

AE07 - 7 Color gradient maps for bed and water surface evolution in space and time

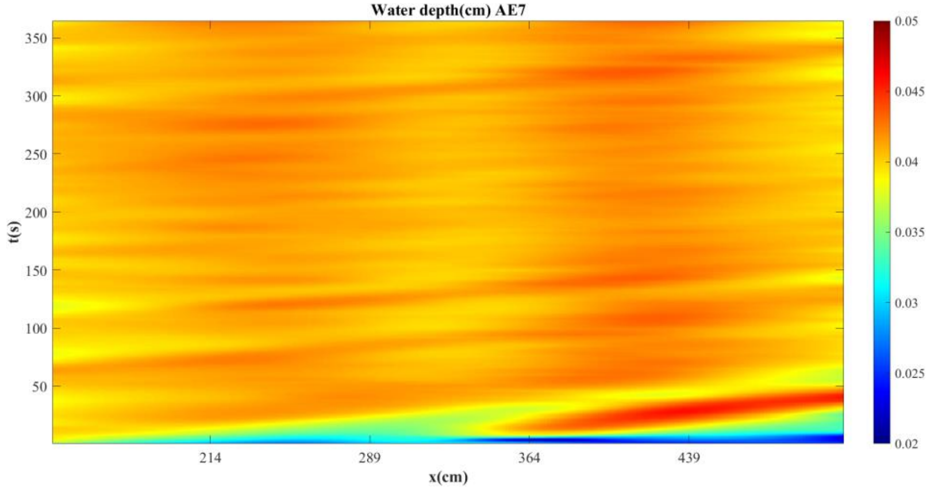

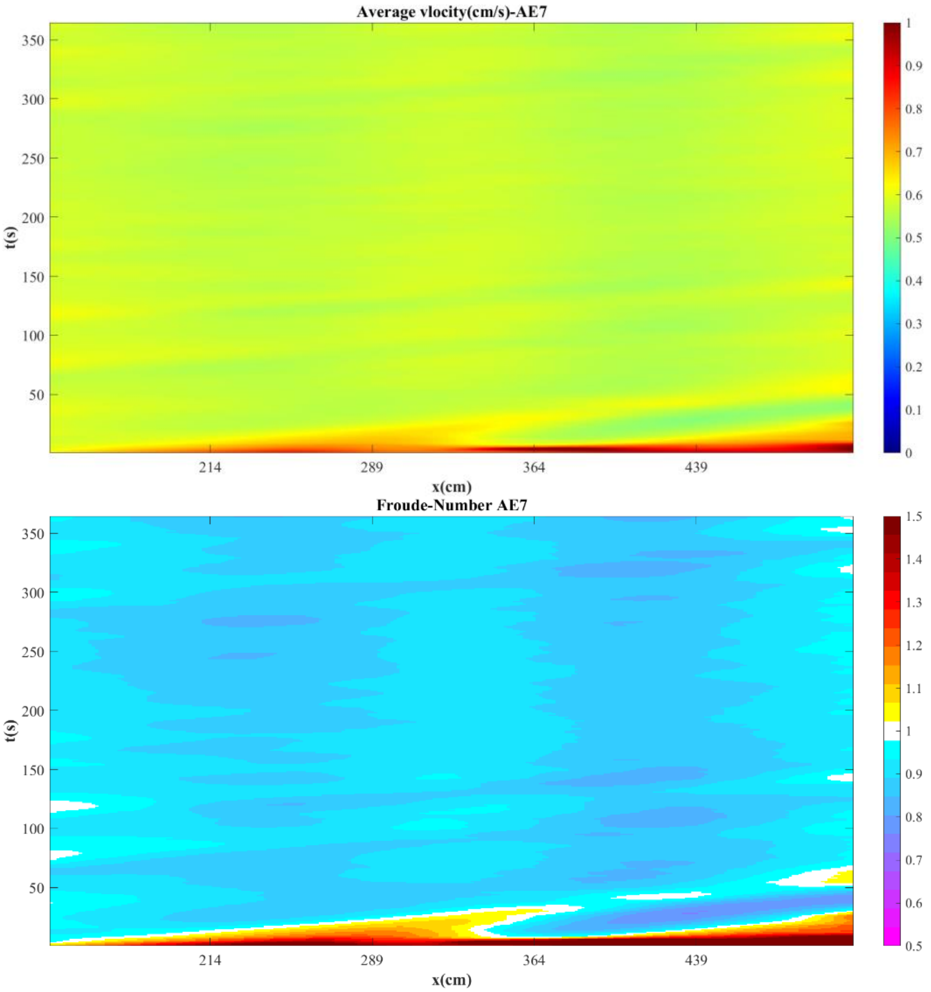

AE07 - 8 Color gradient maps for water depth, water average velocity, and Froude number Fr evolution in space and time

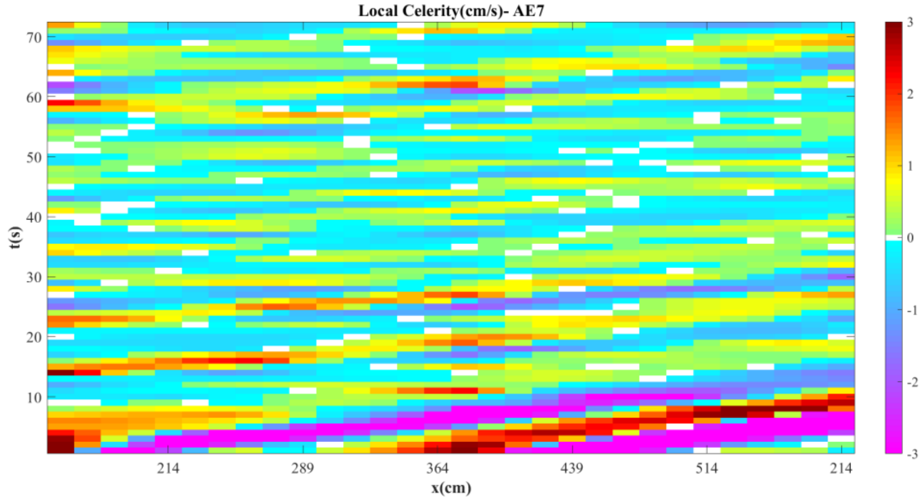

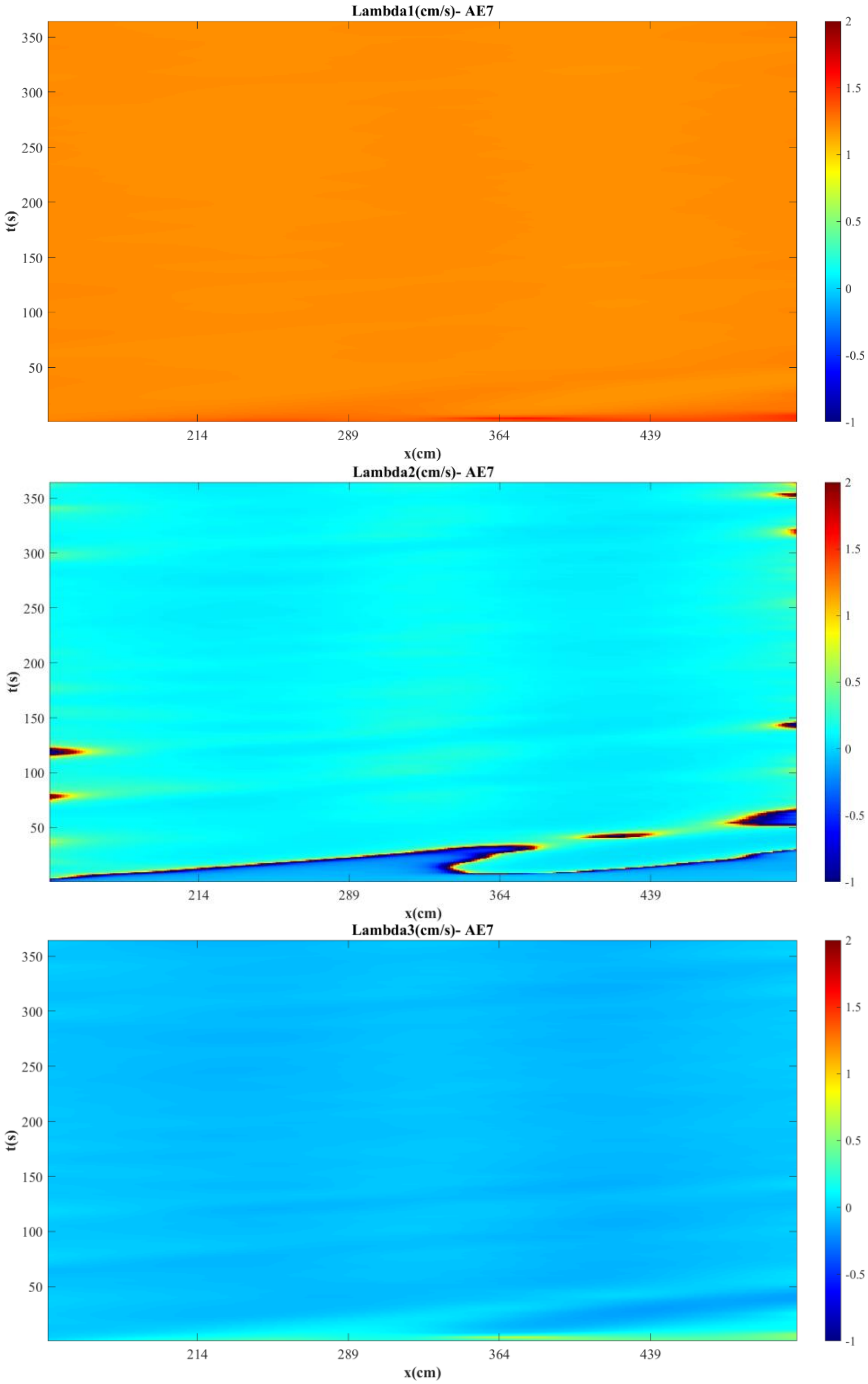

AE07 - 9 Color gradient maps for local celerity, Lambda 1, Lambda 2, and Lambda 3 evolution in space and time

Experiment AE08

Vibration level	Opening height (cm)	S_0 (%)	t (sec)	Q water (l/s)	Q_{sin} (m^3/s)	Q_{s0} (m^3/s)	Froude number Fr	Loading ratio Lr
8.75	2	1.2	230	7	2.55E-04	1.29E-04	0.97	1.97

AE08 - 1 Experimental parameters

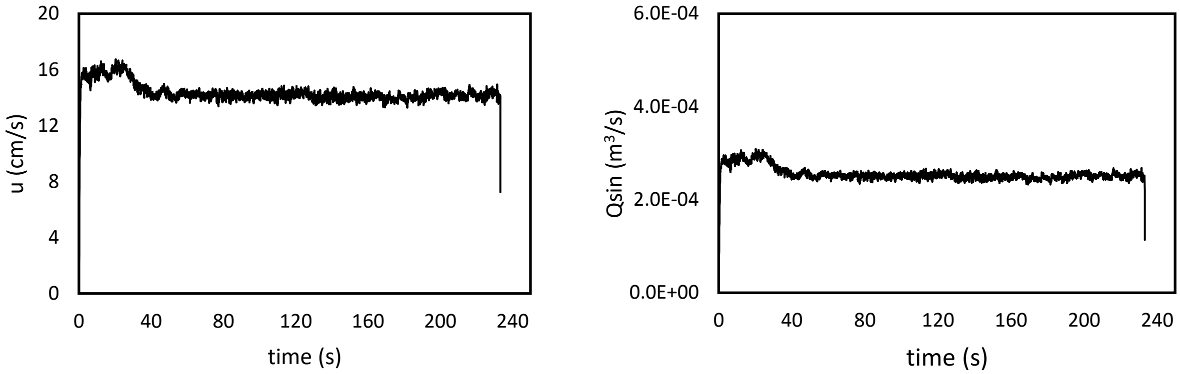

AE08 - 2 Temporal evolution of velocity and sediment discharge

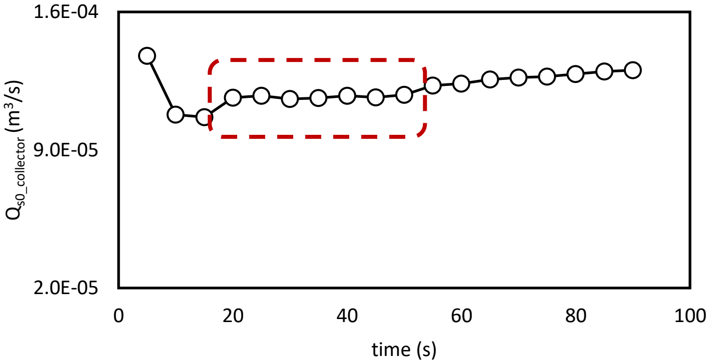

AE08 - 3 Temporal evolution of sediment transport capacity considering the collector method. The average of the constant values of Qs0 is considered as the Qs0, collector.

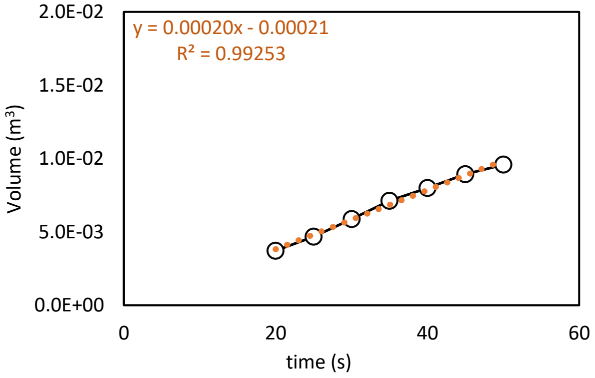

(a) CU2 Scenario

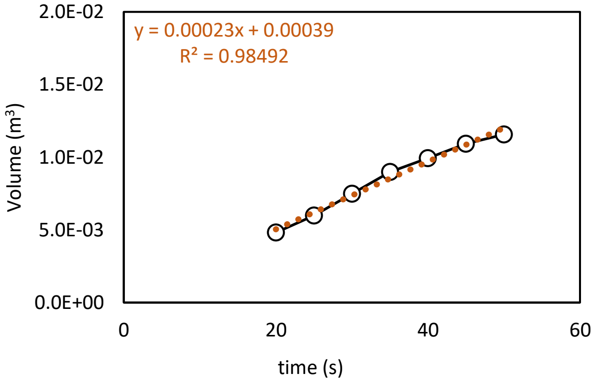

(b) IU2 Scenario

AE08 - 4 Temporal evolution of sediment transport capacity considering the continuity method and second scenario. The average of the slope of the interpolating lines is used to calculate Qs0, monitored.

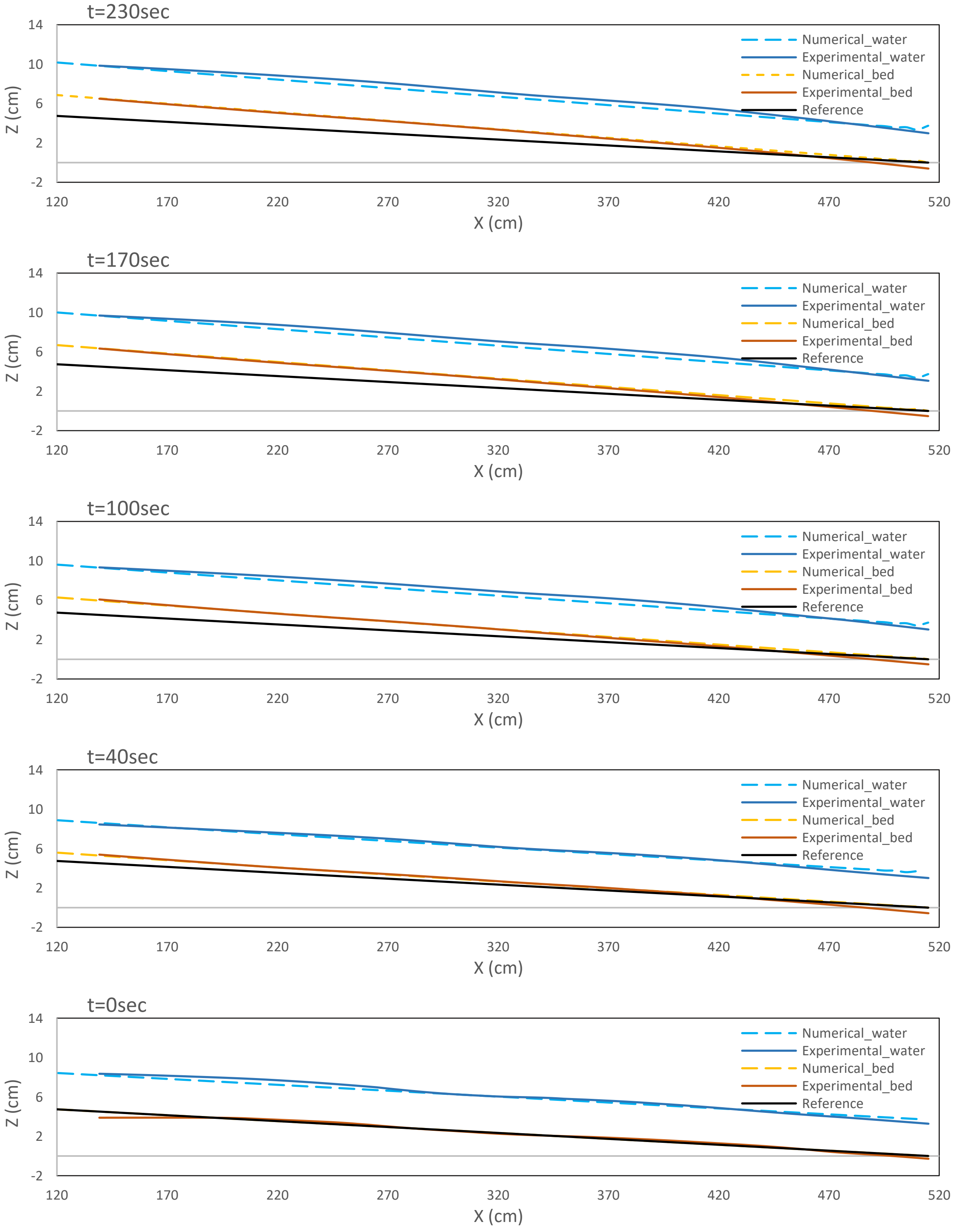

AE08 - 5 Spatial evolution of bed and water

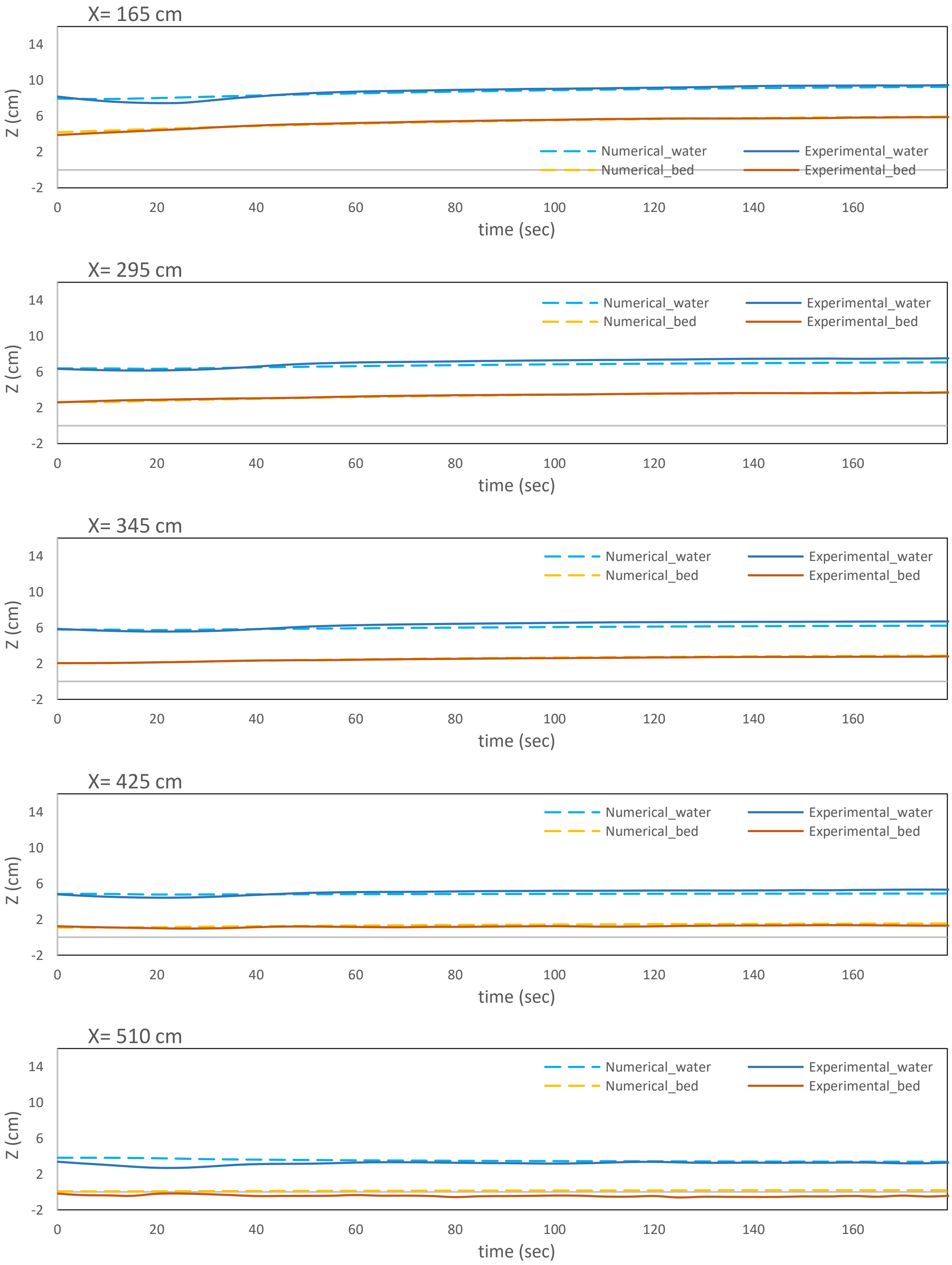

AE08 - 6 Temporal evolution of bed and water

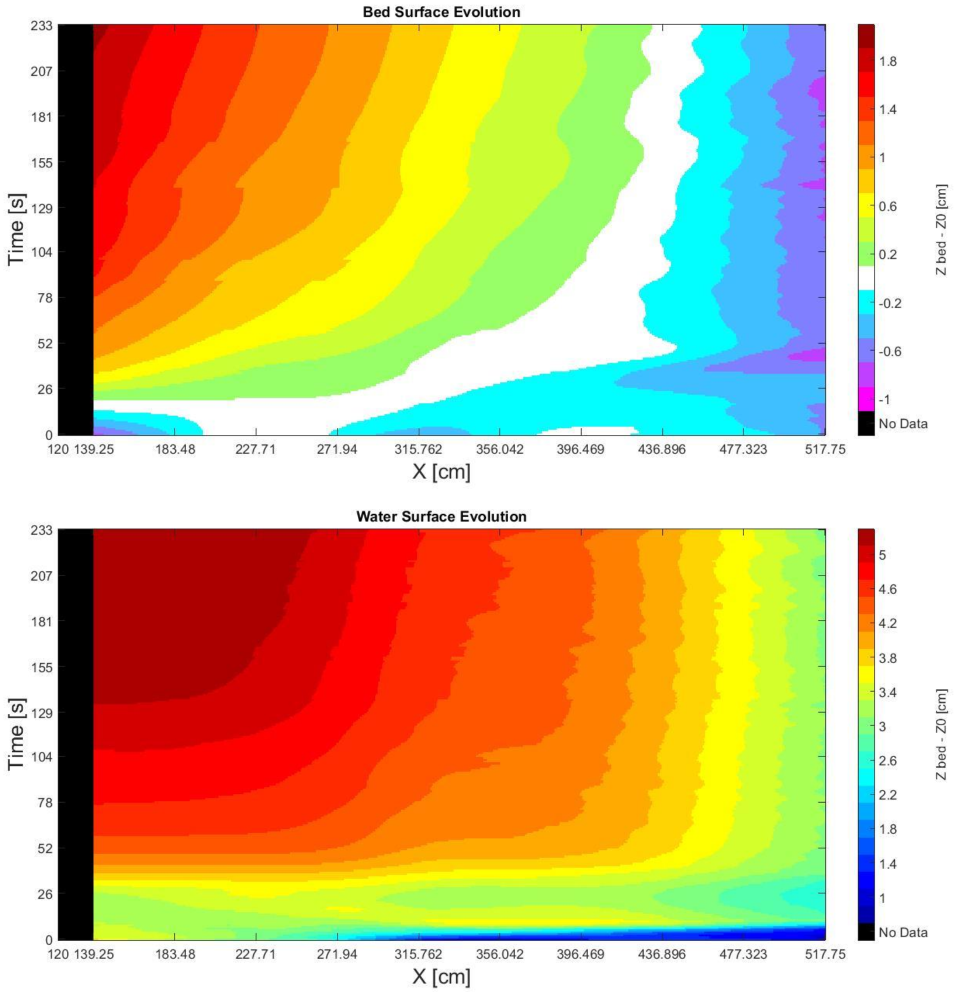

AE08 - 7 Color gradient maps for bed and water surface evolution in space and time

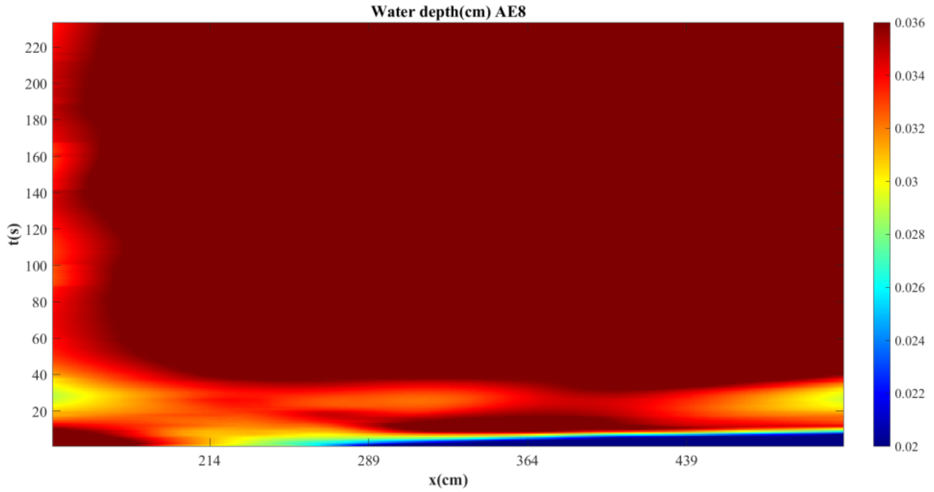

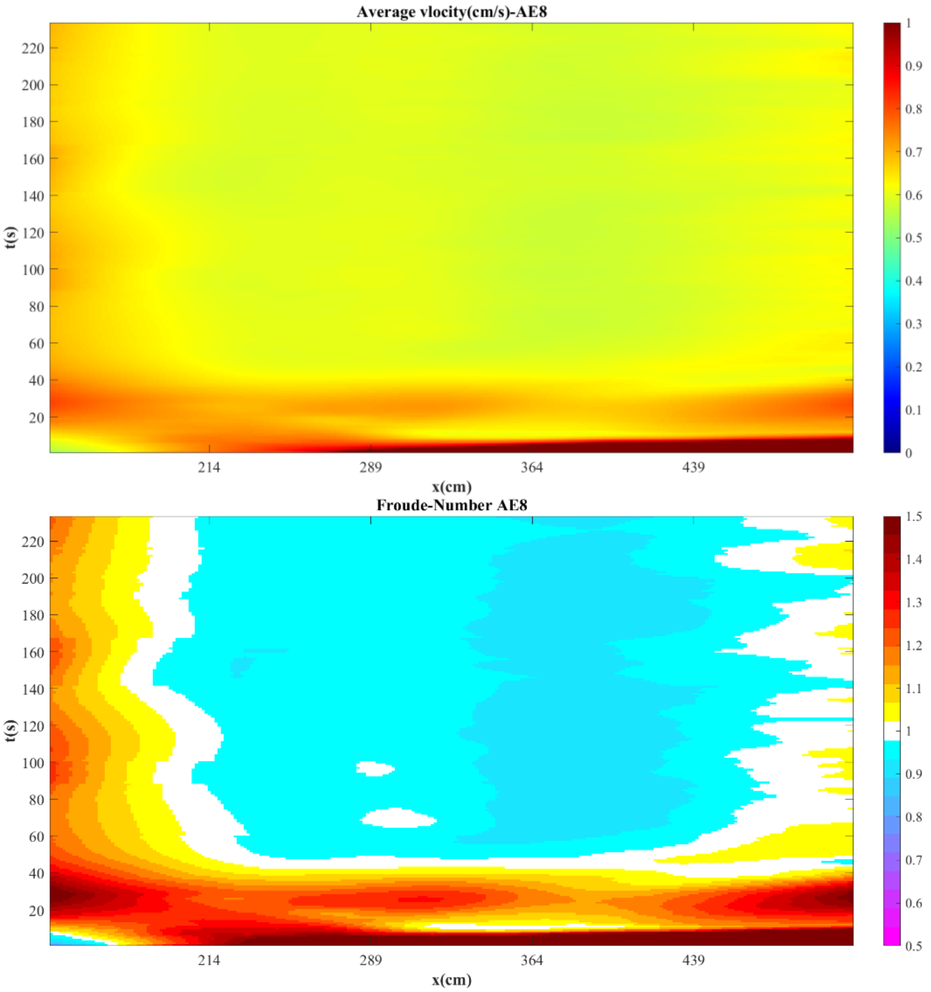
Average vlocity(cm/s)-AE8

Froude-Number AE8

AE08 - 8 Color gradient maps for water depth, water average velocity, and Froude number Fr evolution in space and time

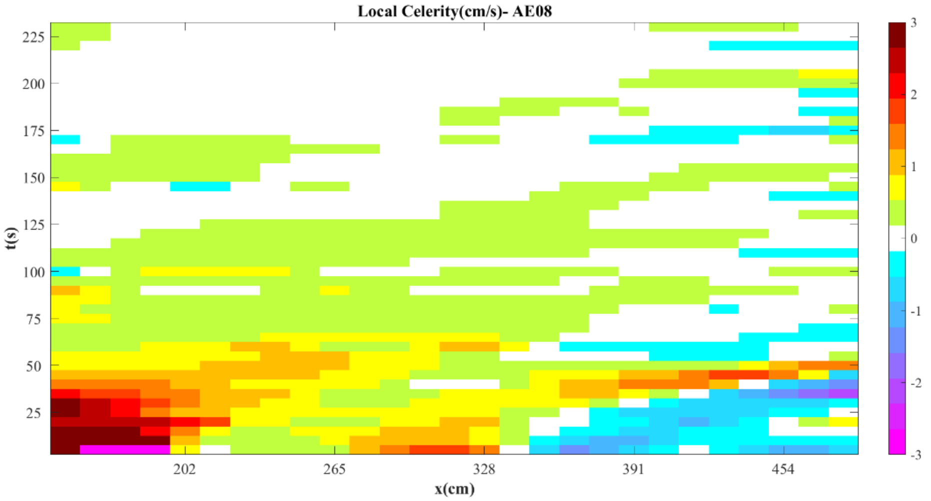
Local Celerity(cm/s)- AE08

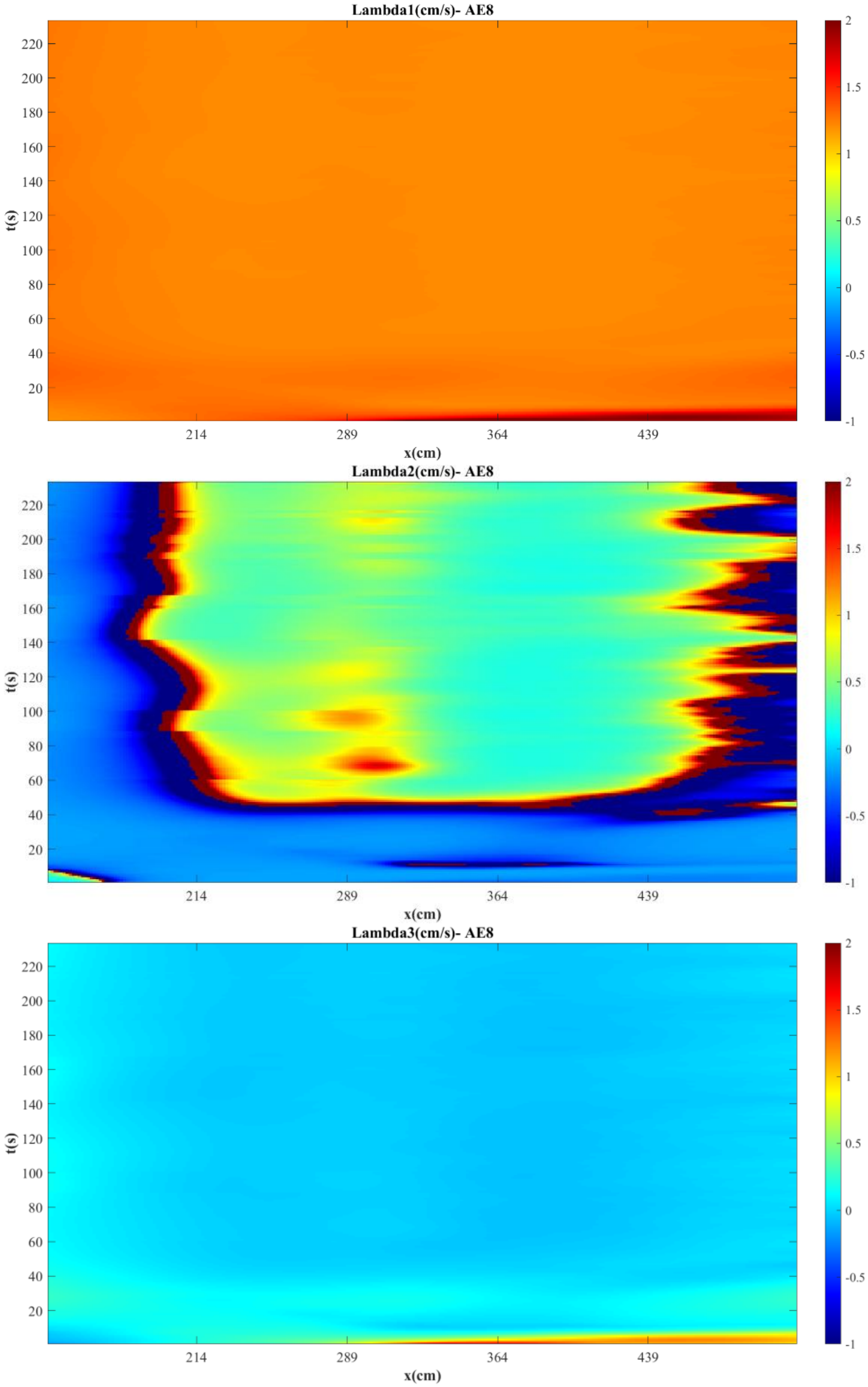

AE08 - 9 Color gradient maps for local celerity, Lambda 1, Lambda 2, and Lambda 3 evolution in space and time

Experiment AE10

Vibration level	Opening height (cm)	S_0 (%)	t (sec)	Q water (l/s)	Q_{sin} (m^3/s)	Q_{s0} (m^3/s)	Froude number Fr	Loading ratio Lr
8.75	3	1.2	181	7	4.16E-04	1.20E-04	1.19	3.46

AE10 - 1 Experimental parameters

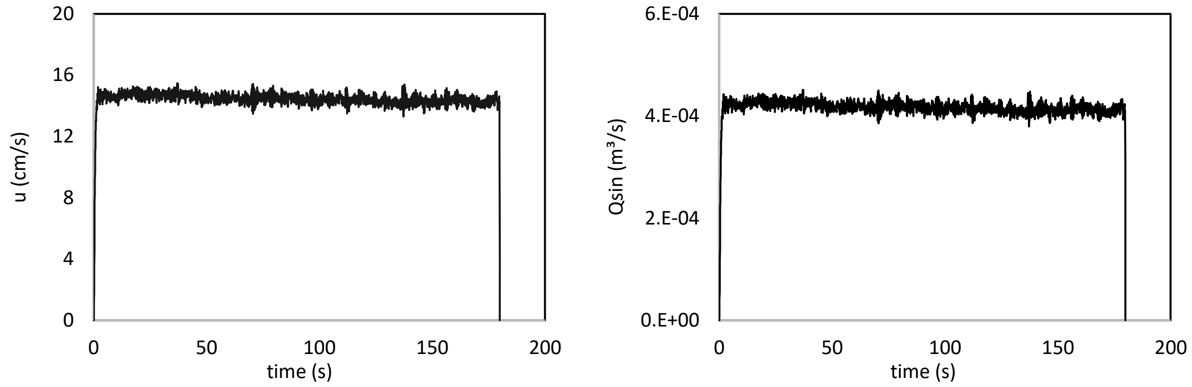

AE10 - 2 Temporal evolution of velocity and sediment discharge

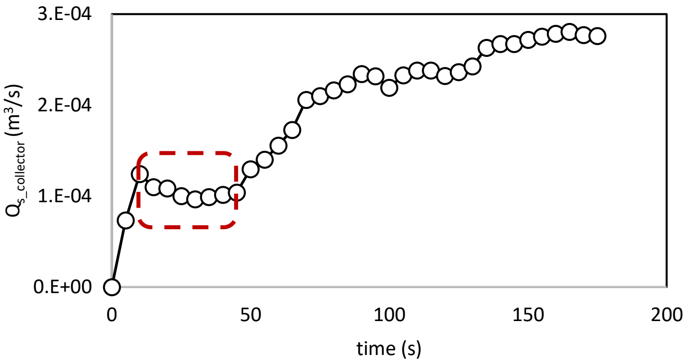

AE10 - 3 Temporal evolution of sediment transport capacity considering the collector method. The average of the constant values of Qs0 is considered as the Qs0, collector.

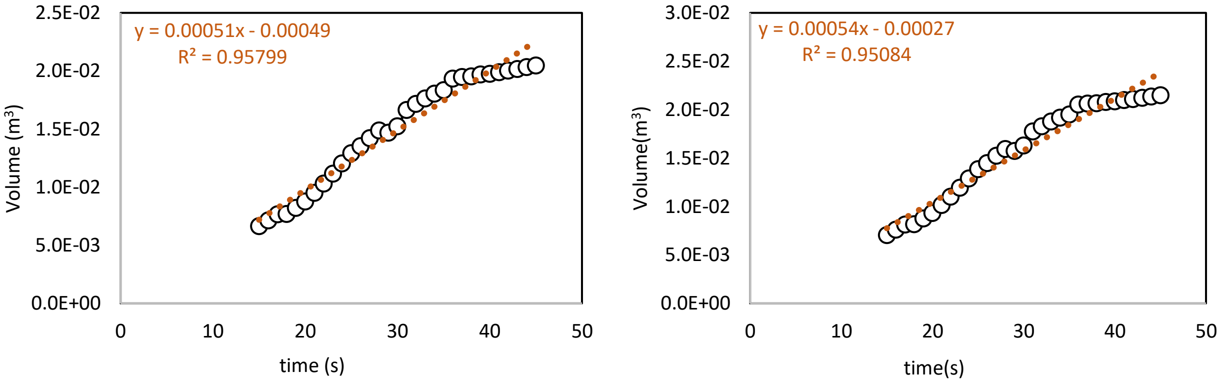

(a) CU2 Scenario

(b) IU2 Scenario

AE10 - 4 Temporal evolution of sediment transport capacity considering the continuity method and four scenarios. The average of the slope of the interpolating lines is used to calculate Qs0, monitored.

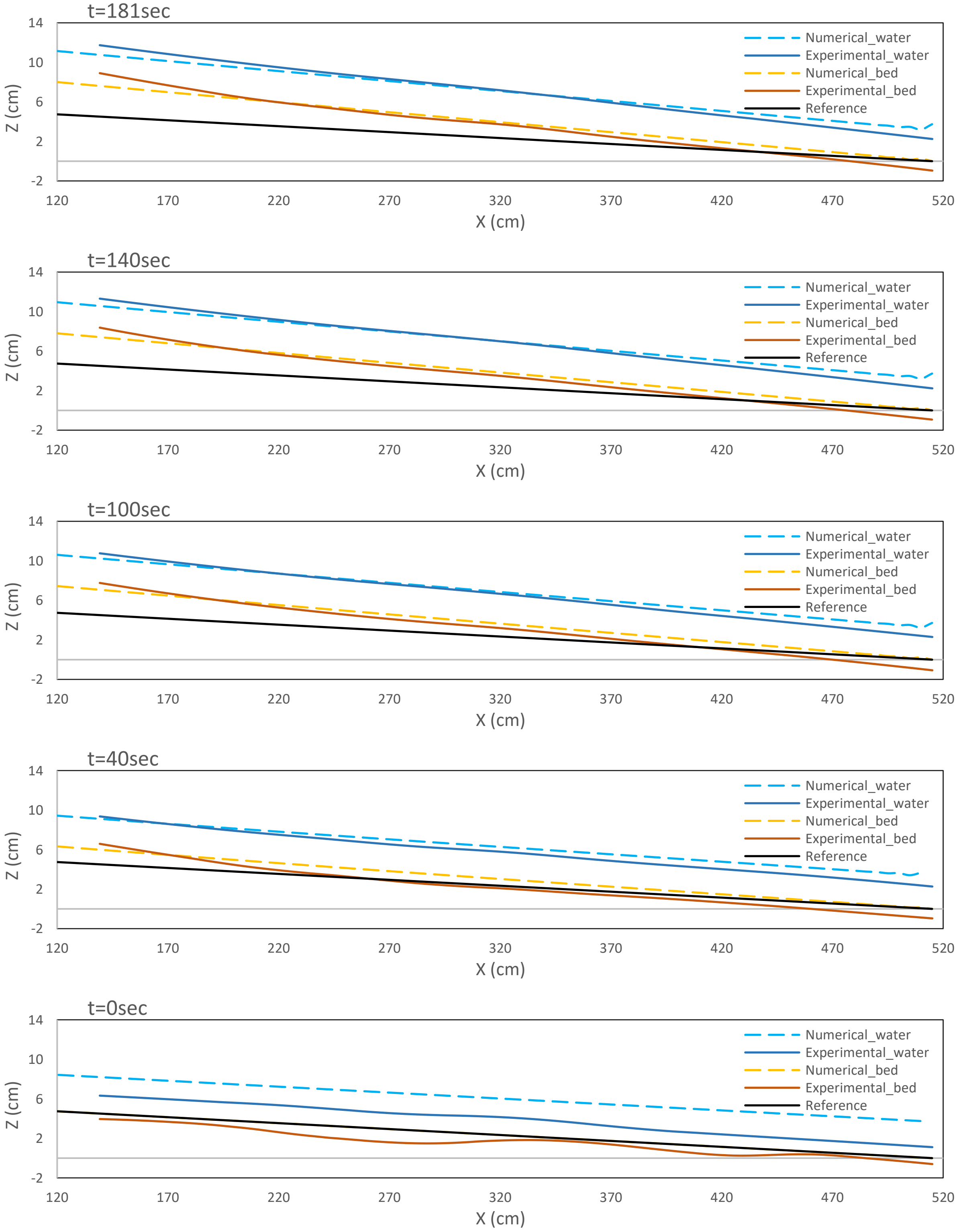

AE10 - 5 Spatial evolution of bed and water

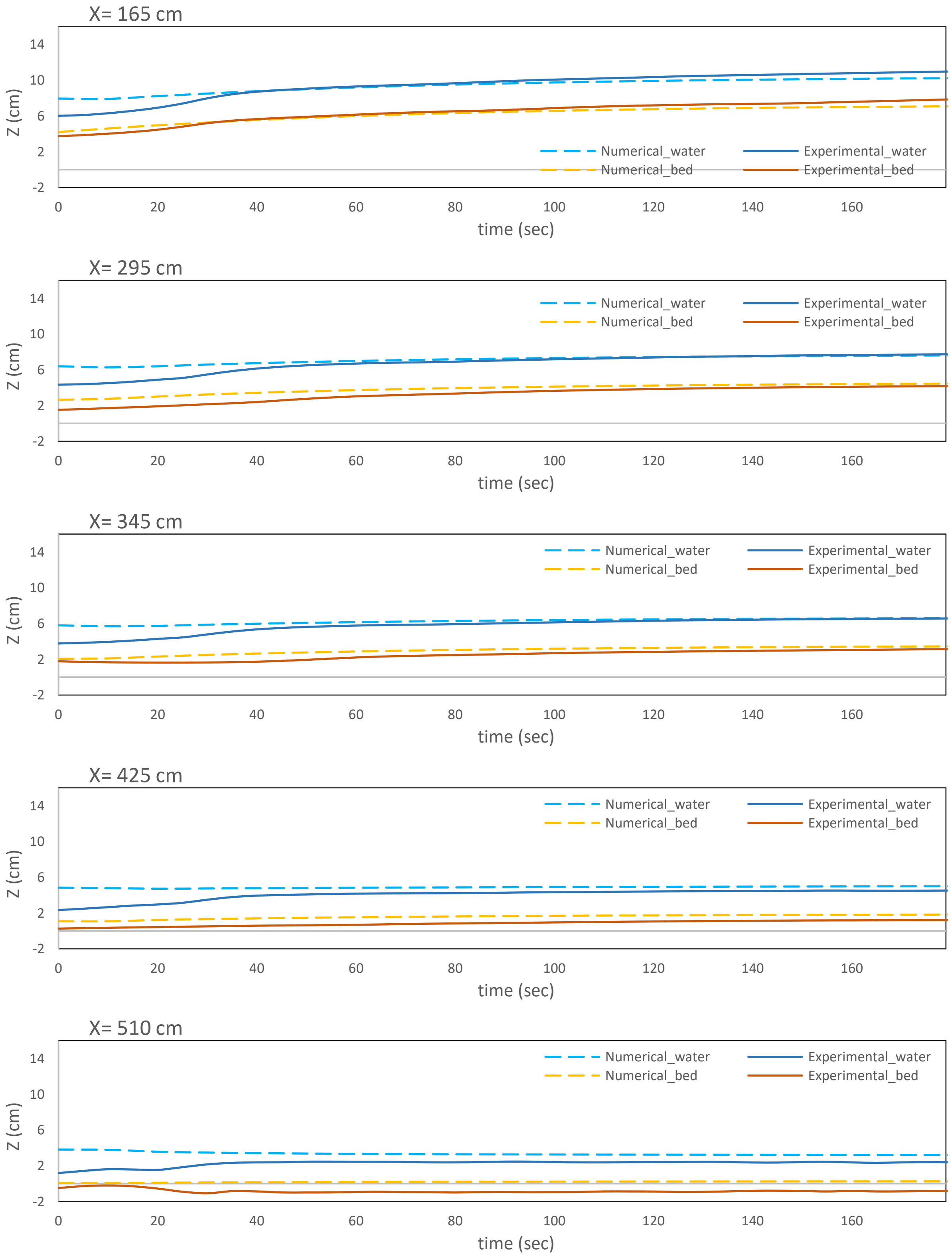

AE10 - 6 Temporal evolution of bed and water

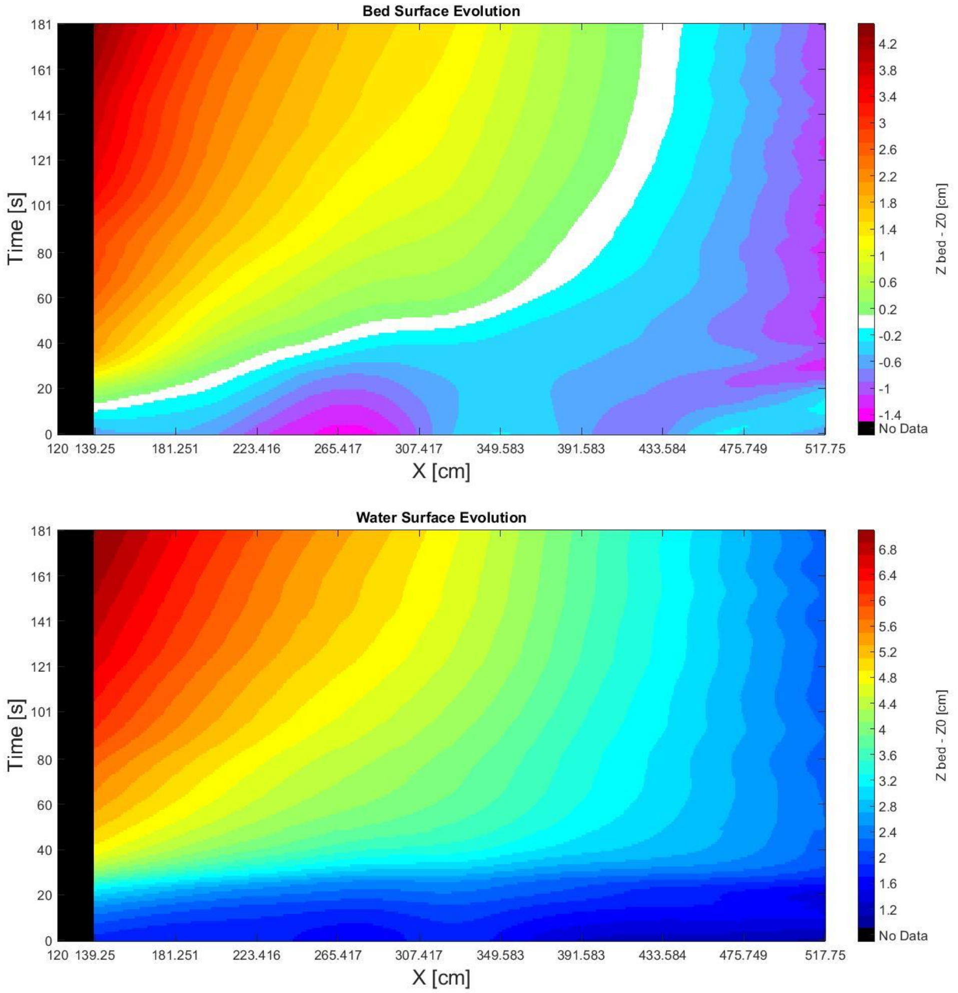

AE10 - 7 Color gradient maps for bed and water surface evolution in space and time

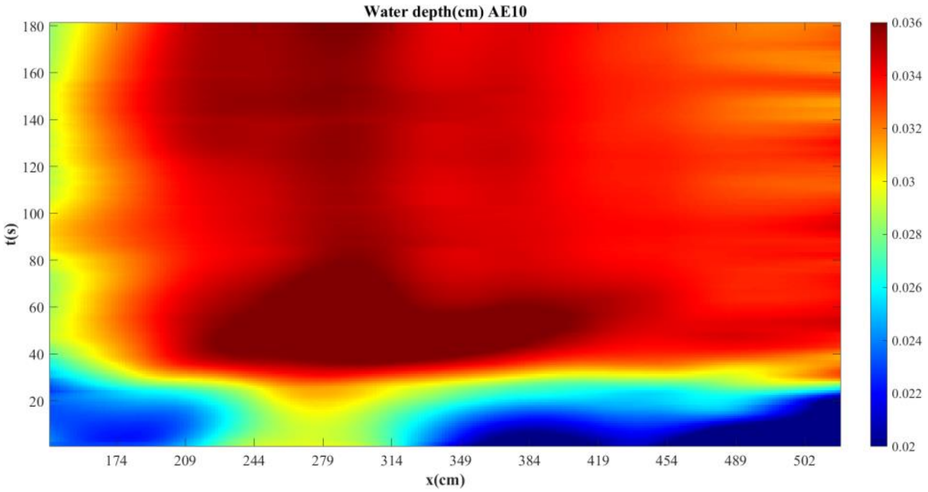

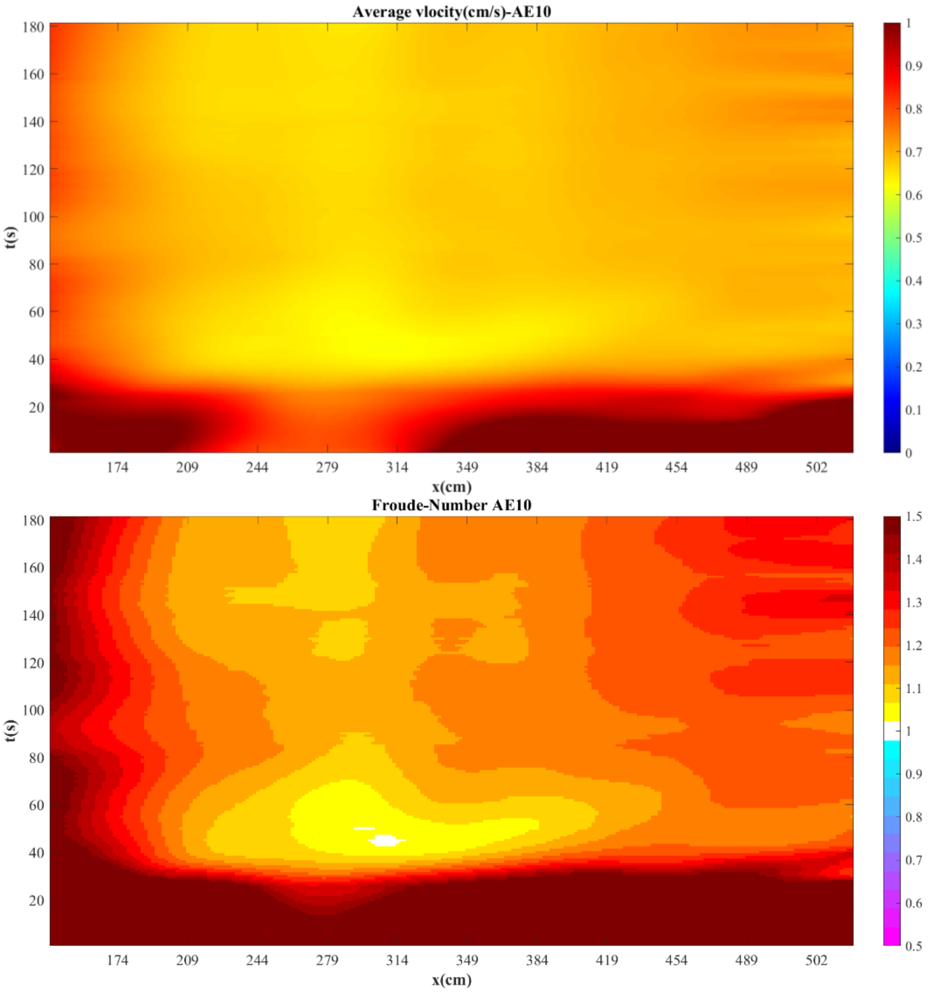

AE10 - 8 Color gradient maps for water depth, water average velocity, and Froude number Fr evolution in space and time

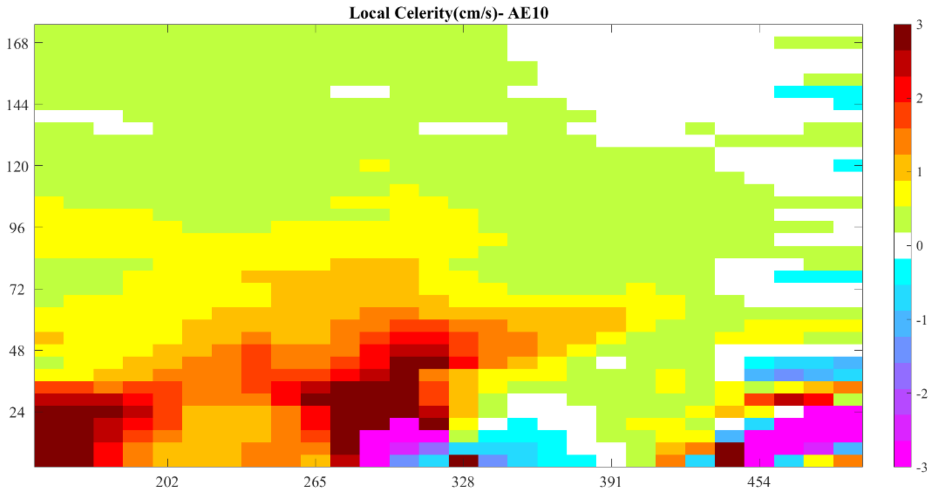

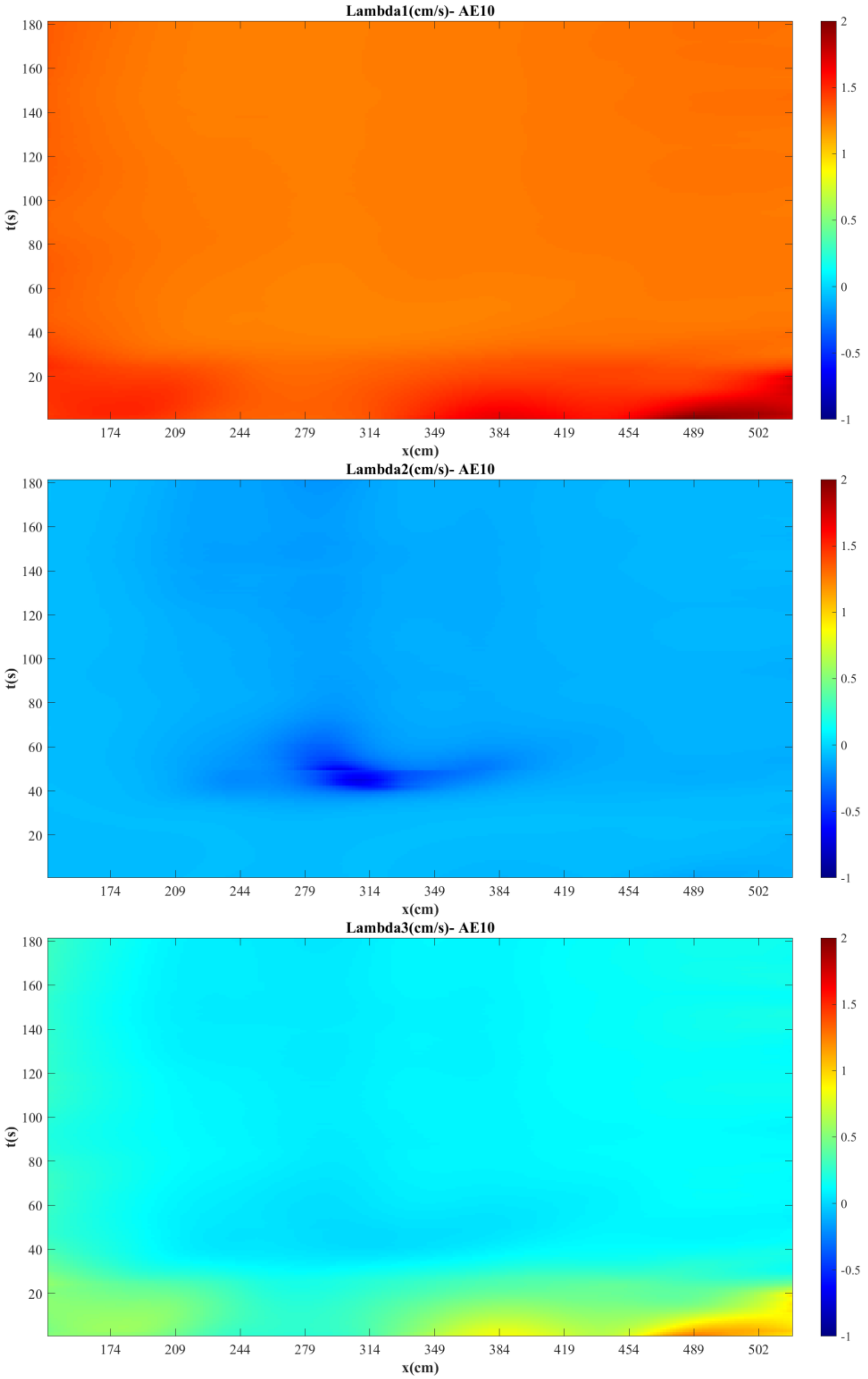

AE10 - 9 Color gradient maps for local celerity, Lambda 1, Lambda 2, and Lambda 3 evolution in space and time

Experiment AE11

Vibration level	Opening height (cm)	S_0 (%)	t (sec)	Q water (l/s)	Q_{sin} (m^3/s)	Q_{s0} (m^3/s)	Froude number Fr	Loading ratio Lr
8.75	3	1.2	179	7	4.01E-04	1.19E-04	1.23	3.37

AE11 - 1 Experimental parameters

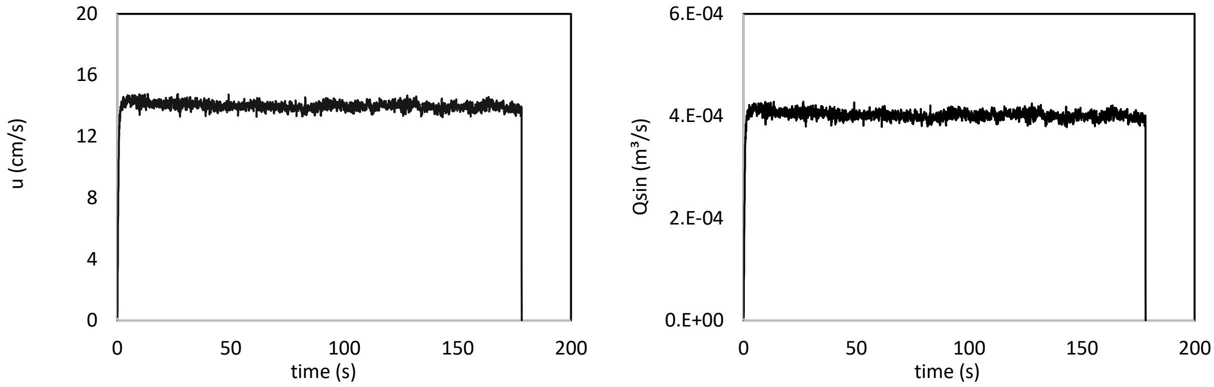

AE11 - 2 Temporal evolution of velocity and sediment discharge

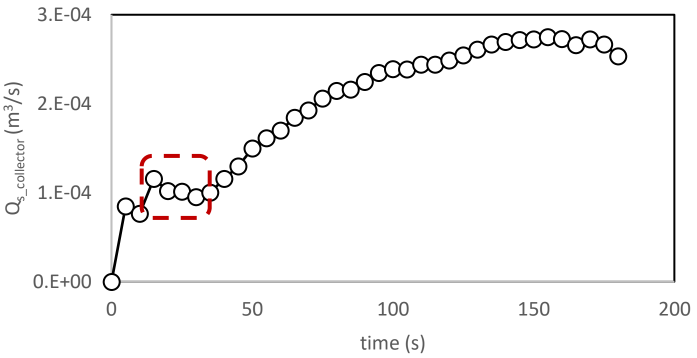

AE11 - 3 Temporal evolution of sediment transport capacity considering the collector method. The average of the constant values of Qs0 is considered as the Qs0, collector.

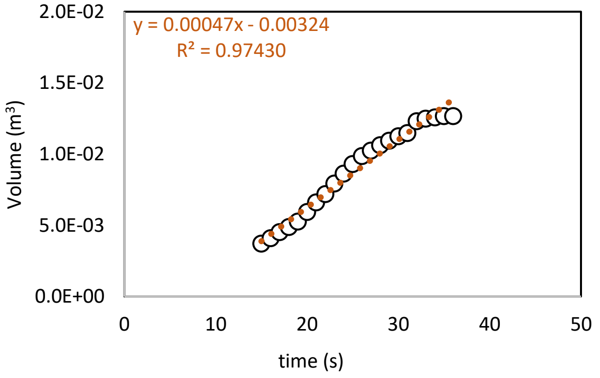

(a) CU2 Scenario

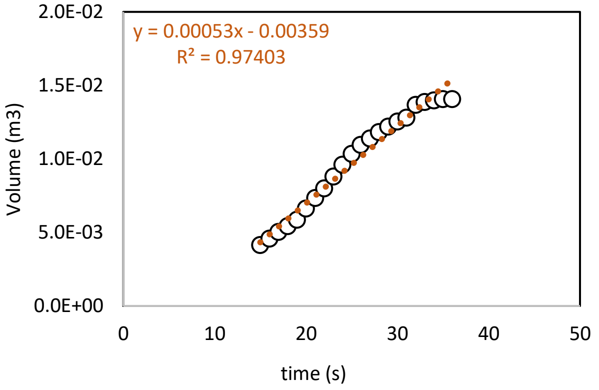

(b) IU2 Scenario

AE11 - 4 Temporal evolution of sediment transport capacity considering the continuity method and four scenarios. The average of the slope of the interpolating lines is used to calculate Qs0, monitored.

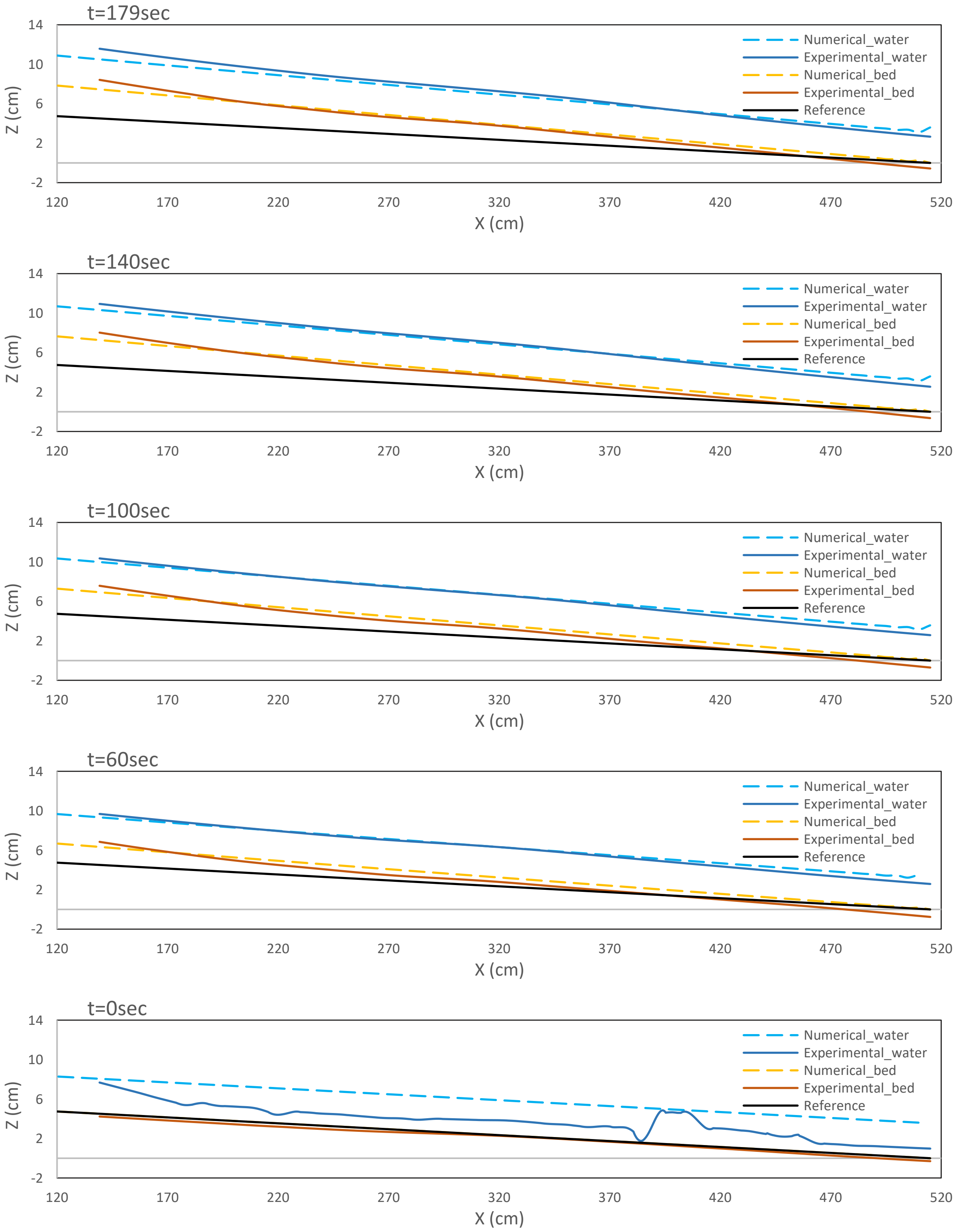

AE11 - 5 Spatial evolution of bed and water

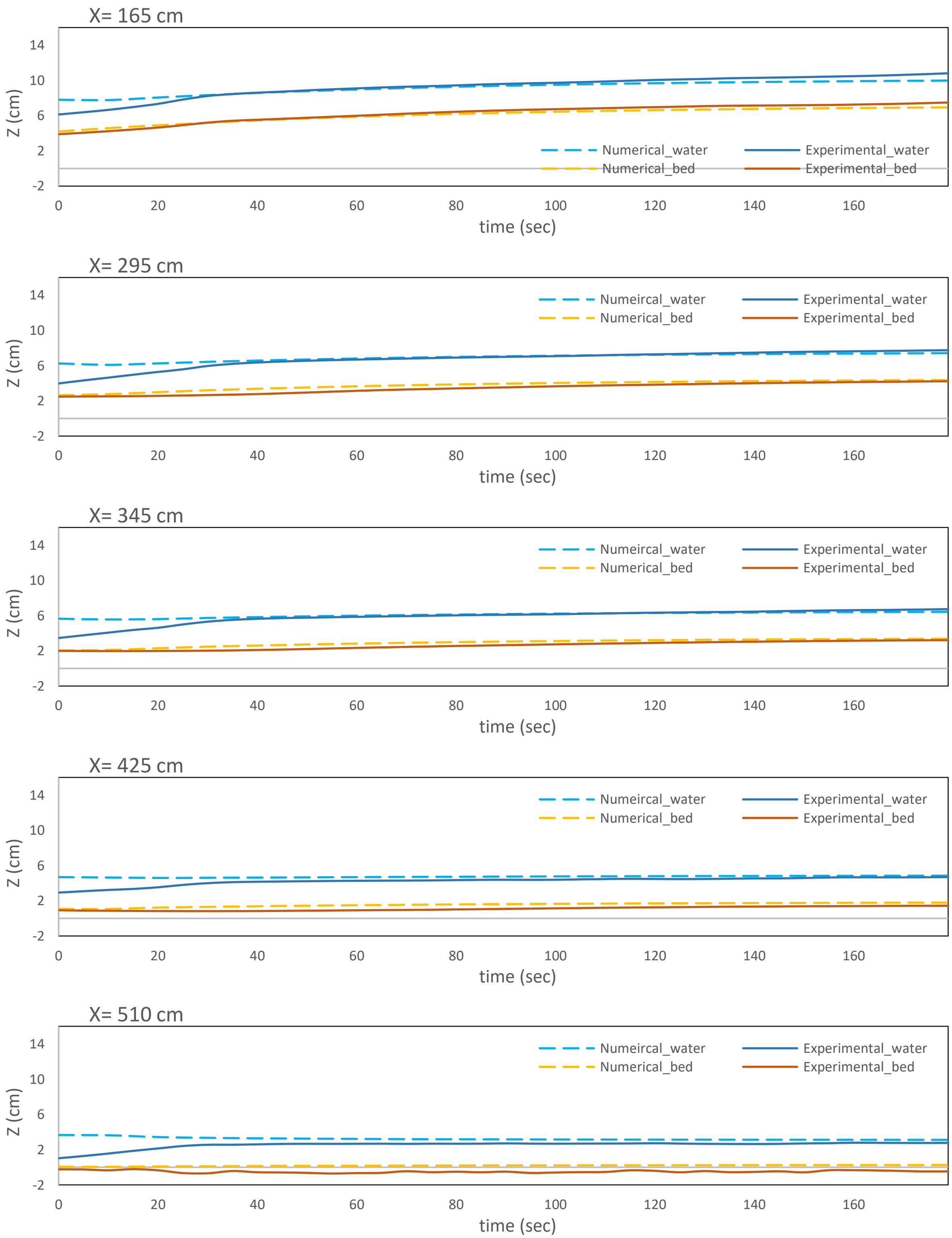

AE11 - 6 Temporal evolution of bed and water

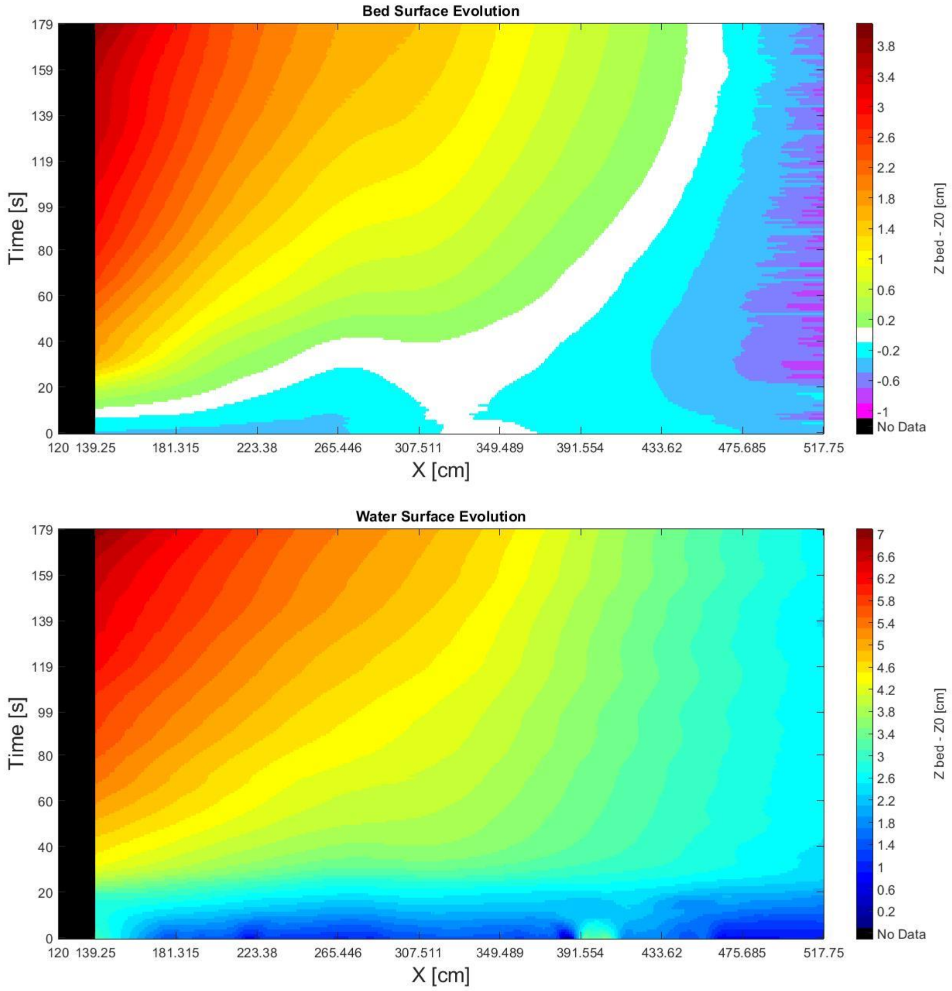

AE11 - 7 Color gradient maps for bed and water surface evolution in space and time

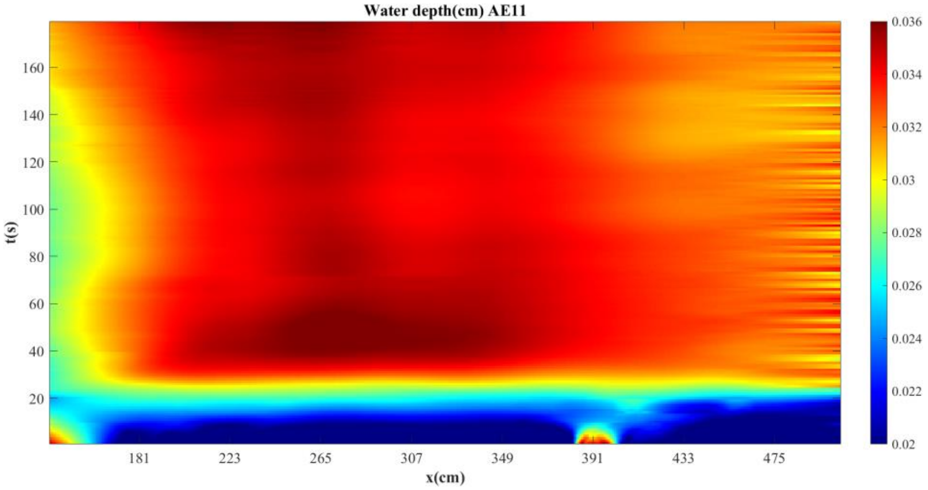

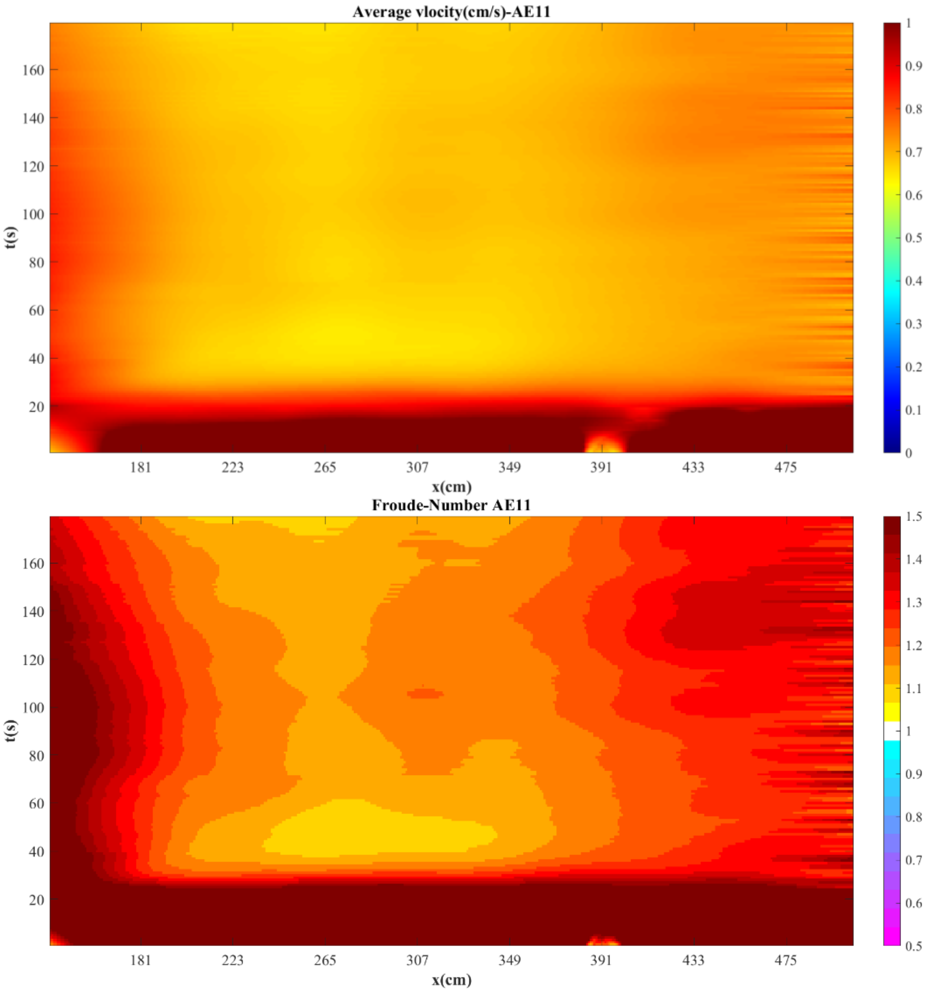

AE11 - 8 Color gradient maps for water depth, water average velocity, and Froude number Fr evolution in space and time

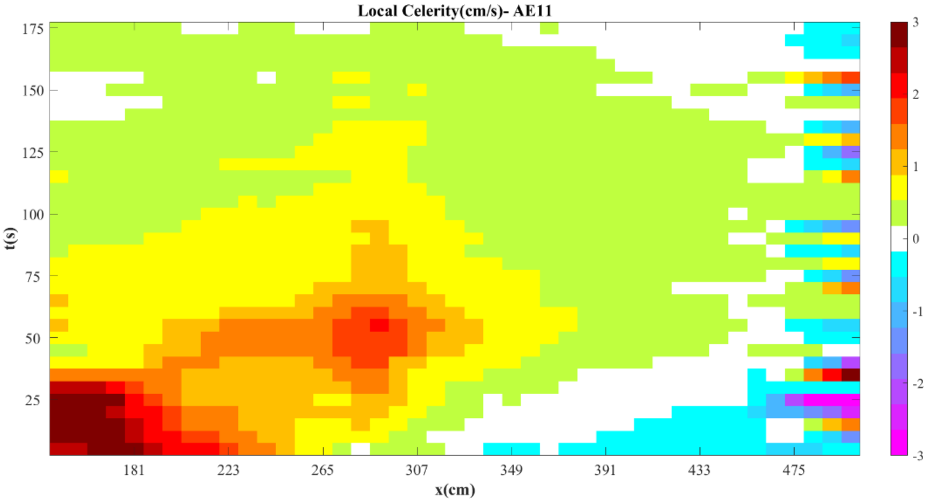

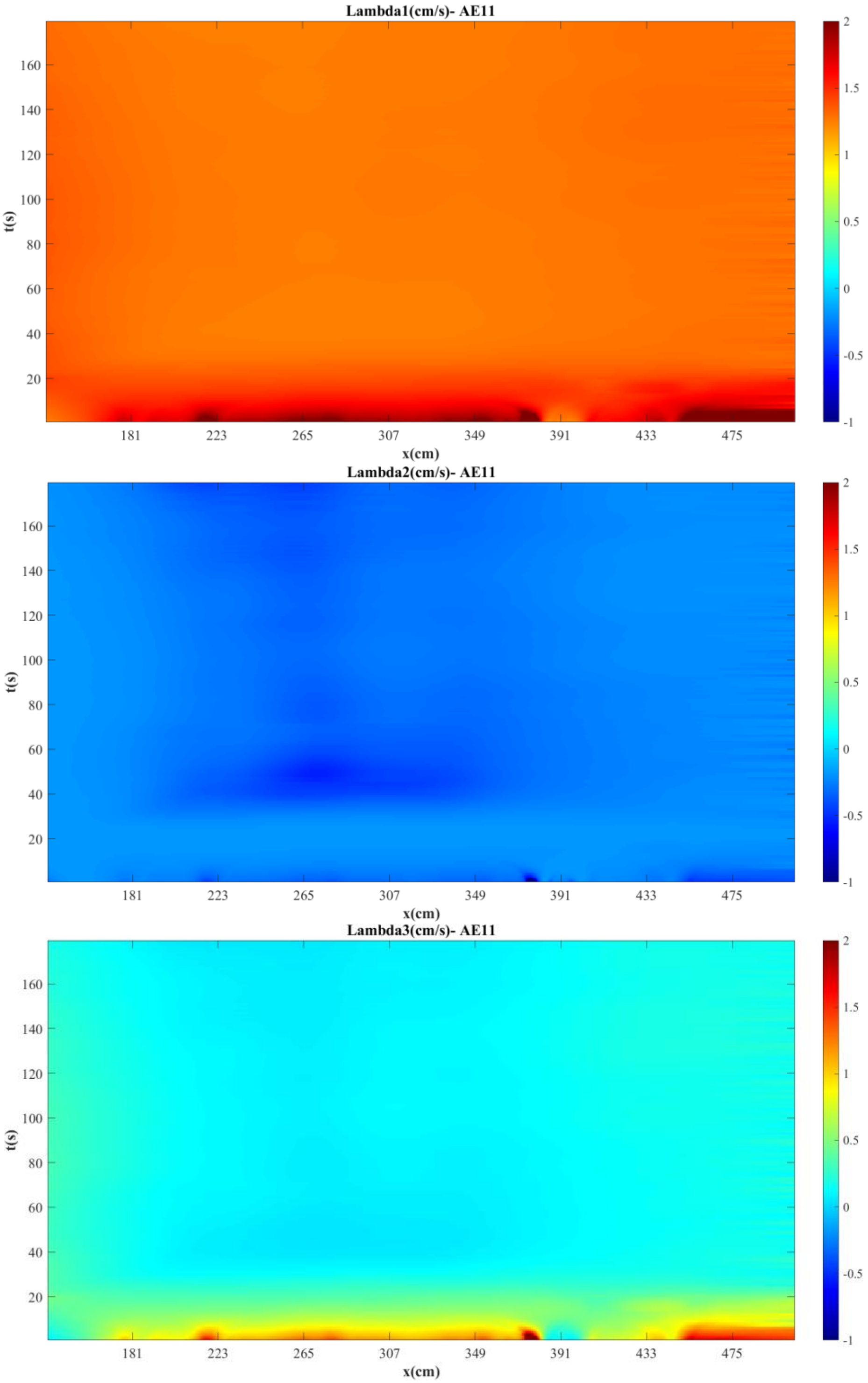

AE11 - 9 Color gradient maps for local celerity, Lambda 1, Lambda 2, and Lambda 3 evolution in space and time

Experiment AE13

Vibration level	Opening height (cm)	S_0 (%)	t (sec)	Q water (l/s)	Q_{sin} (m^3/s)	Q_{s0} (m^3/s)	Froude number Fr	Loading ratio Lr
8	2	1.2	376	7	1.49E-04	1.39E-04	1.02	1.07

AE13 - 1 Experimental parameters

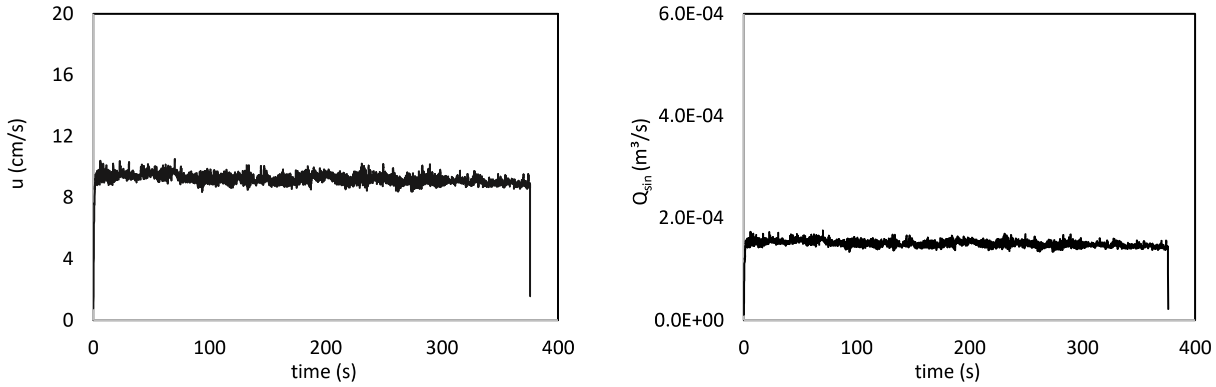

AE13 - 2 Temporal evolution of velocity and sediment discharge

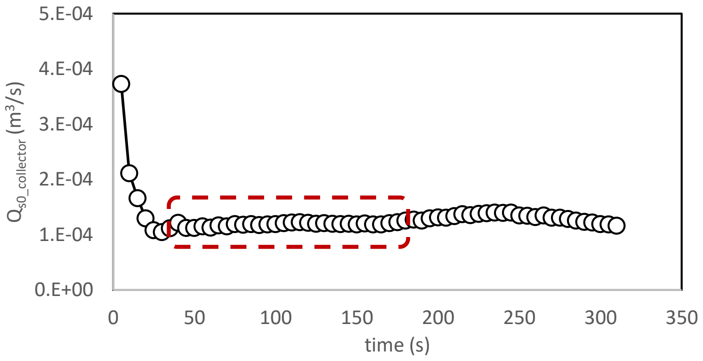

AE13 - 3 Temporal evolution of sediment transport capacity considering the collector method. The average of the constant values of Qs0 is considered as the Qs0, collector.

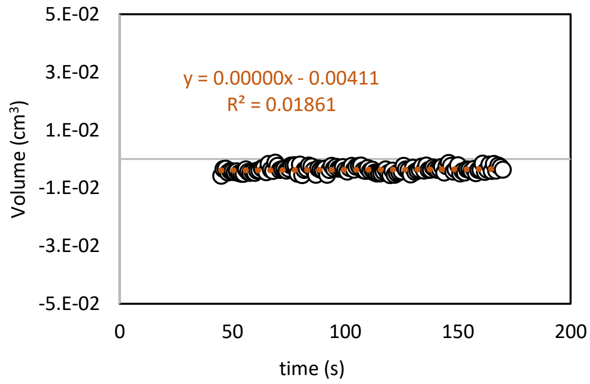

(a) CU2 Scenario

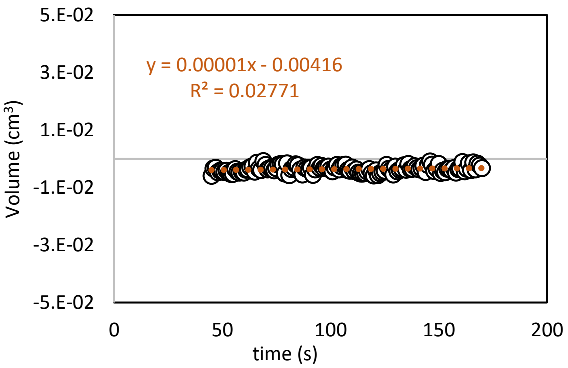

(b) IU2 Scenario

AE13 - 4 Temporal evolution of sediment transport capacity considering the continuity method and four scenarios. The average of the slope of the interpolating lines is used to calculate Qs0, monitored.

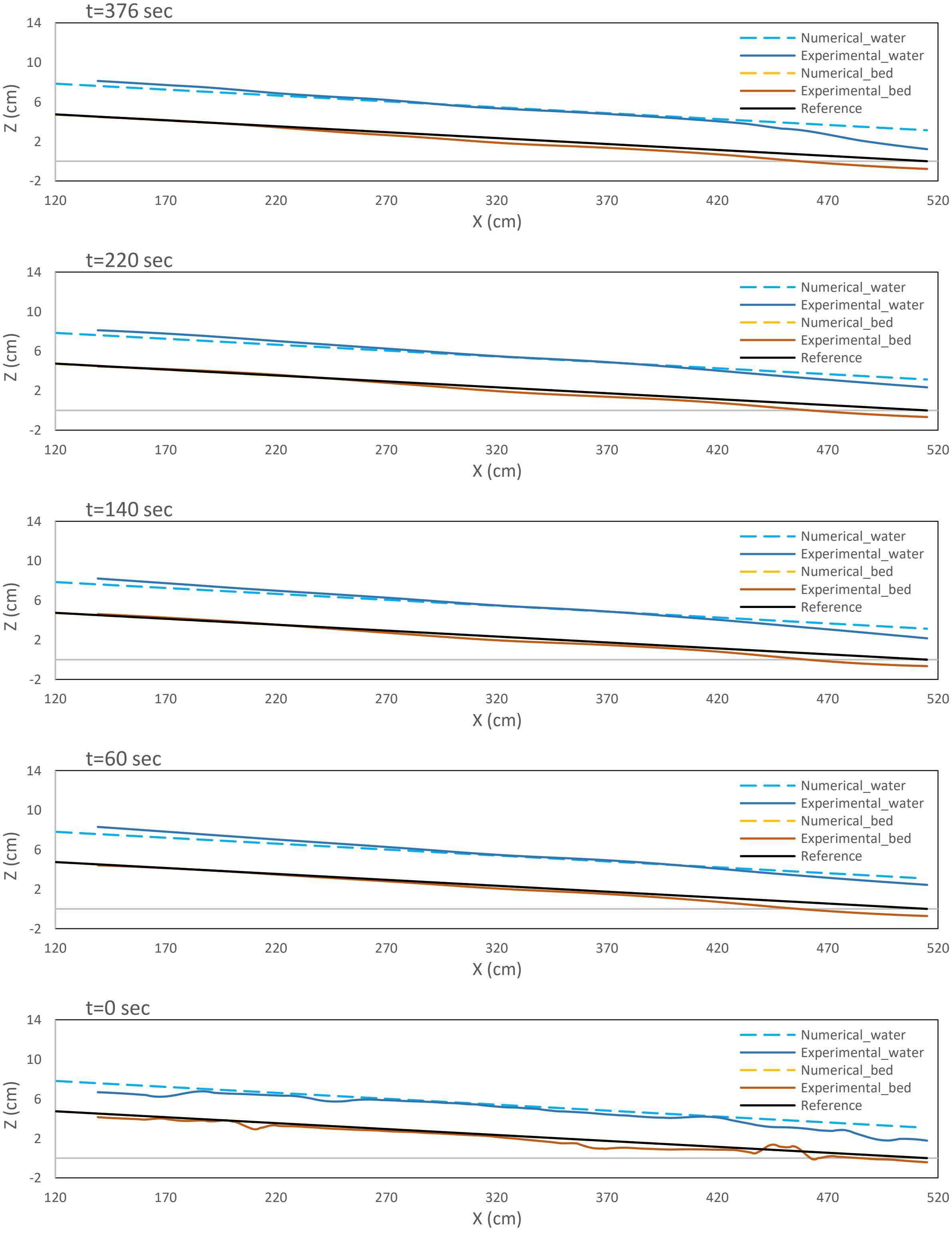

AE13 - 5 Spatial evolution of bed and water

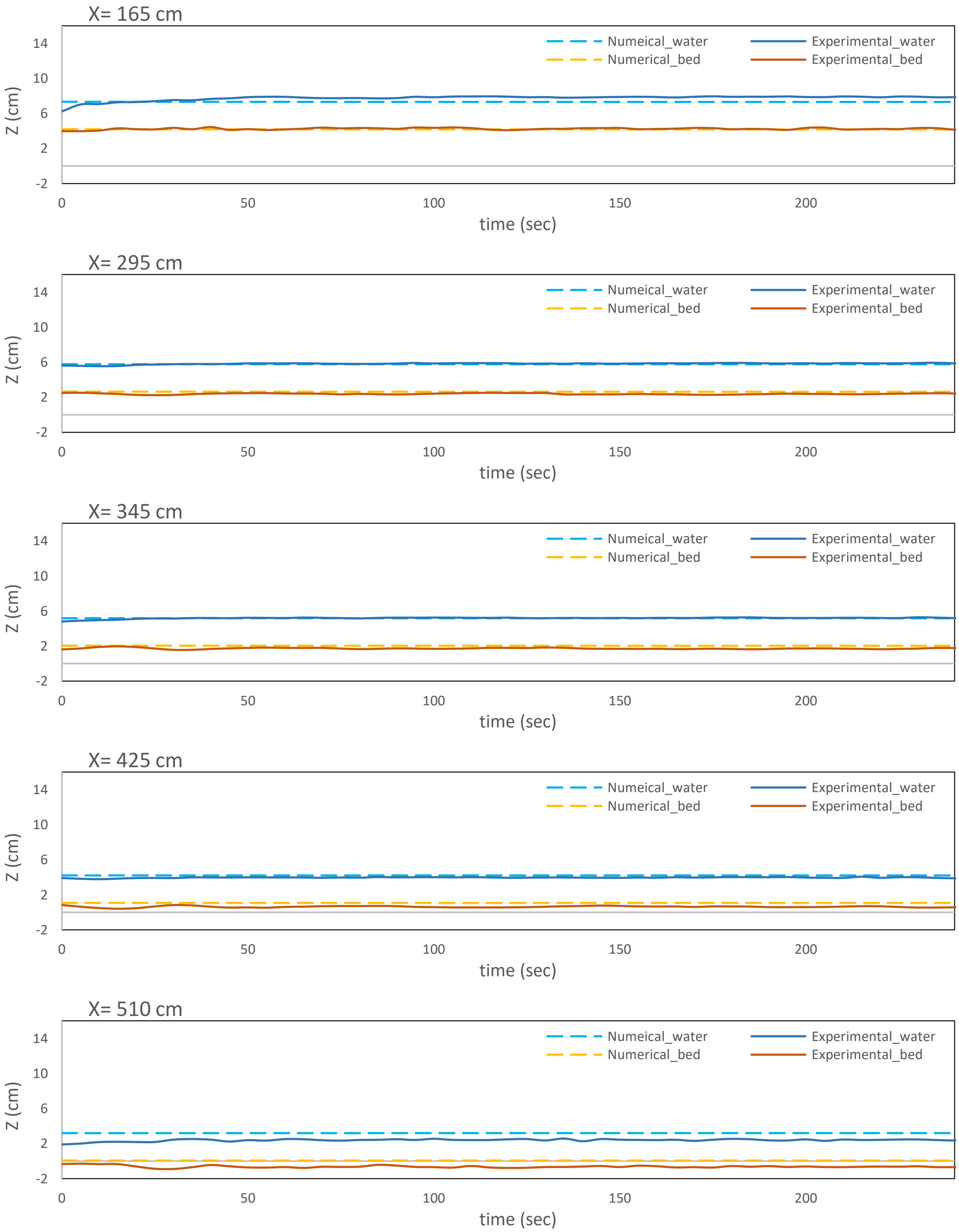

AE13 - 6 Temporal evolution of bed and water

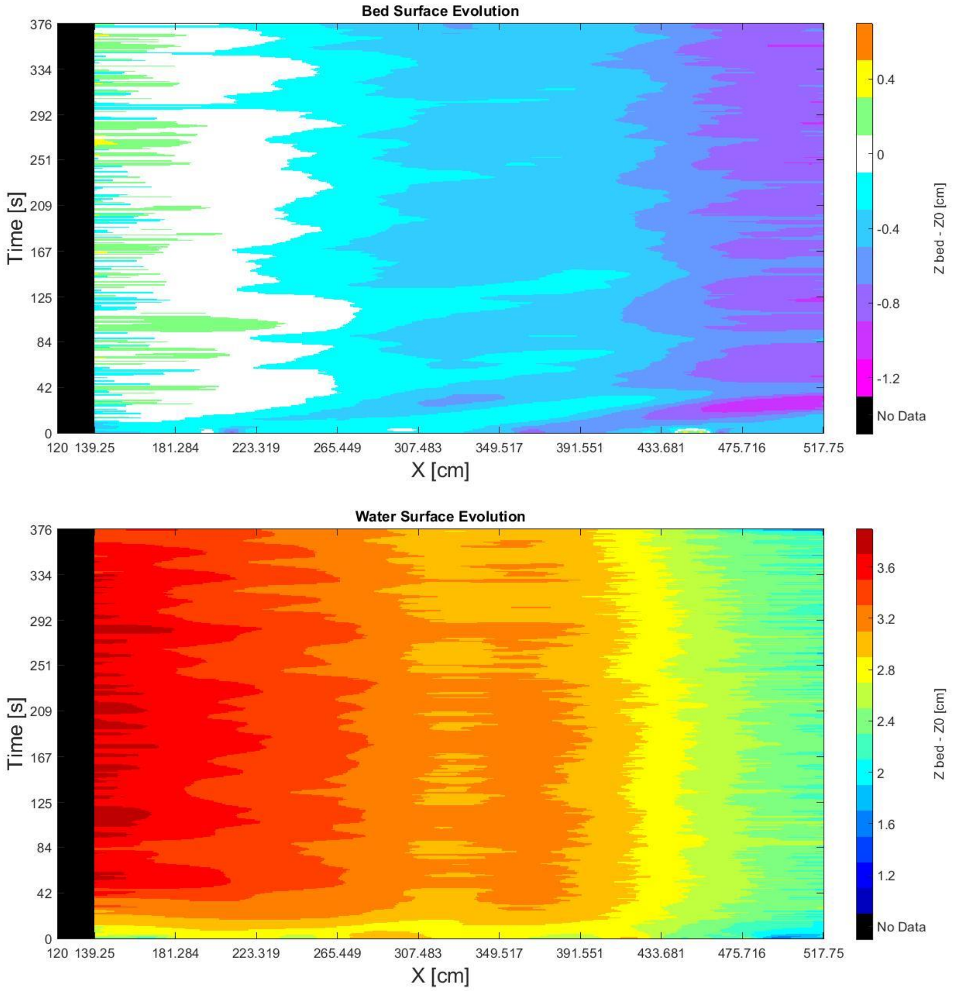

AE13 - 7 Color gradient maps for bed and water surface evolution in space and time

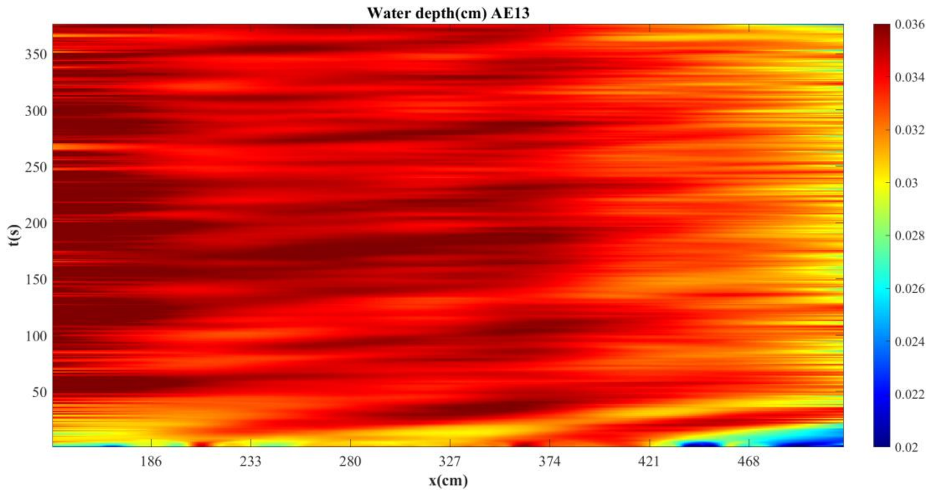

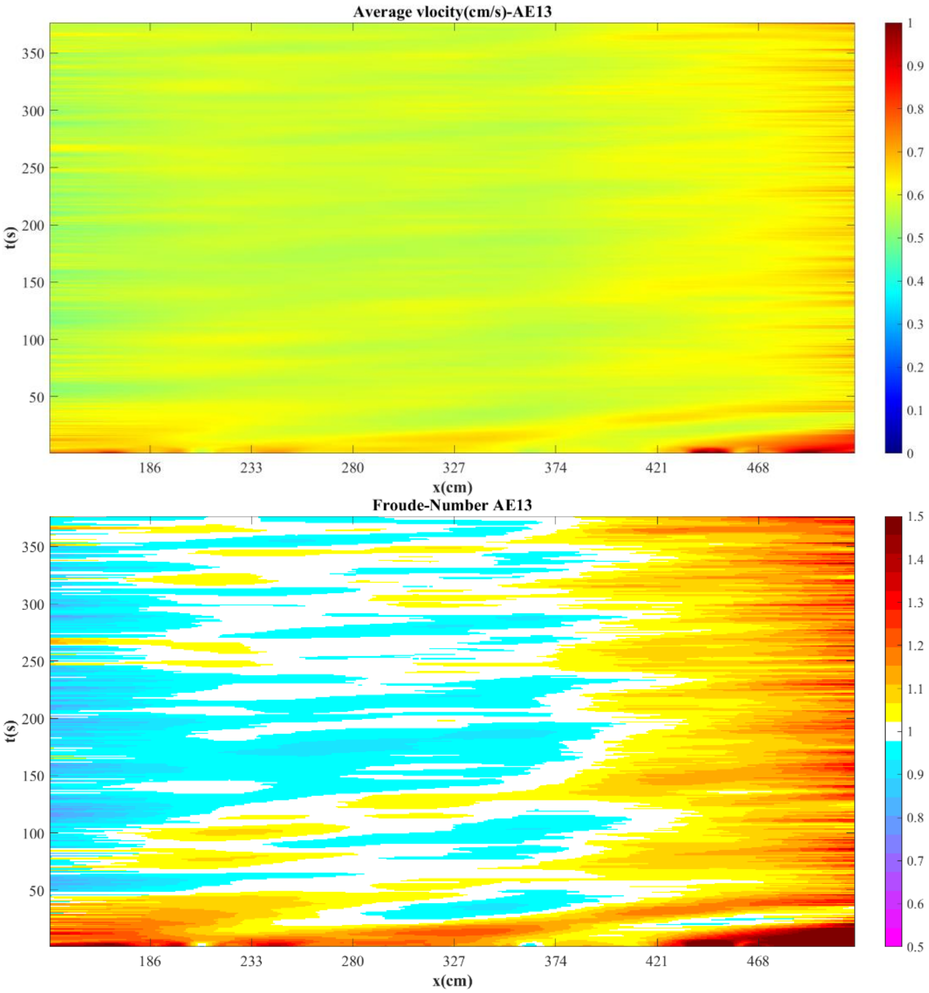

AE13 - 8 Color gradient maps for water depth, water average velocity, and Froude number Fr evolution in space and time

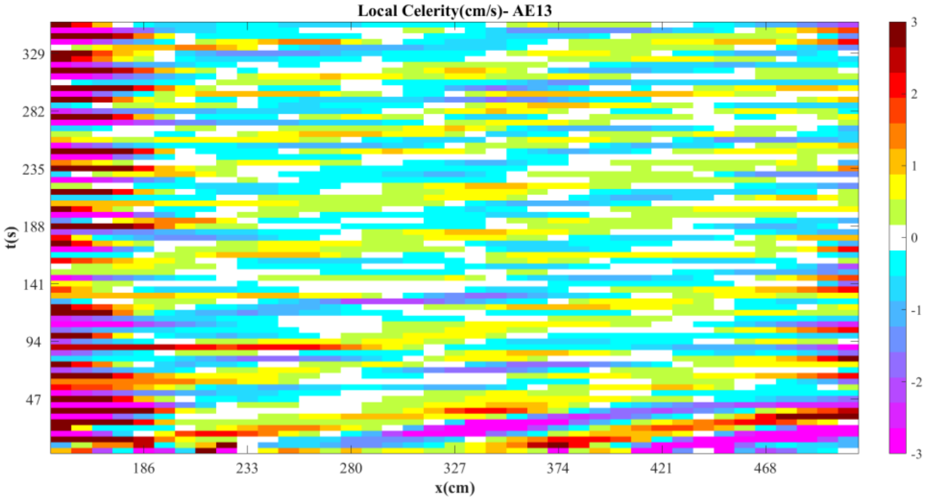

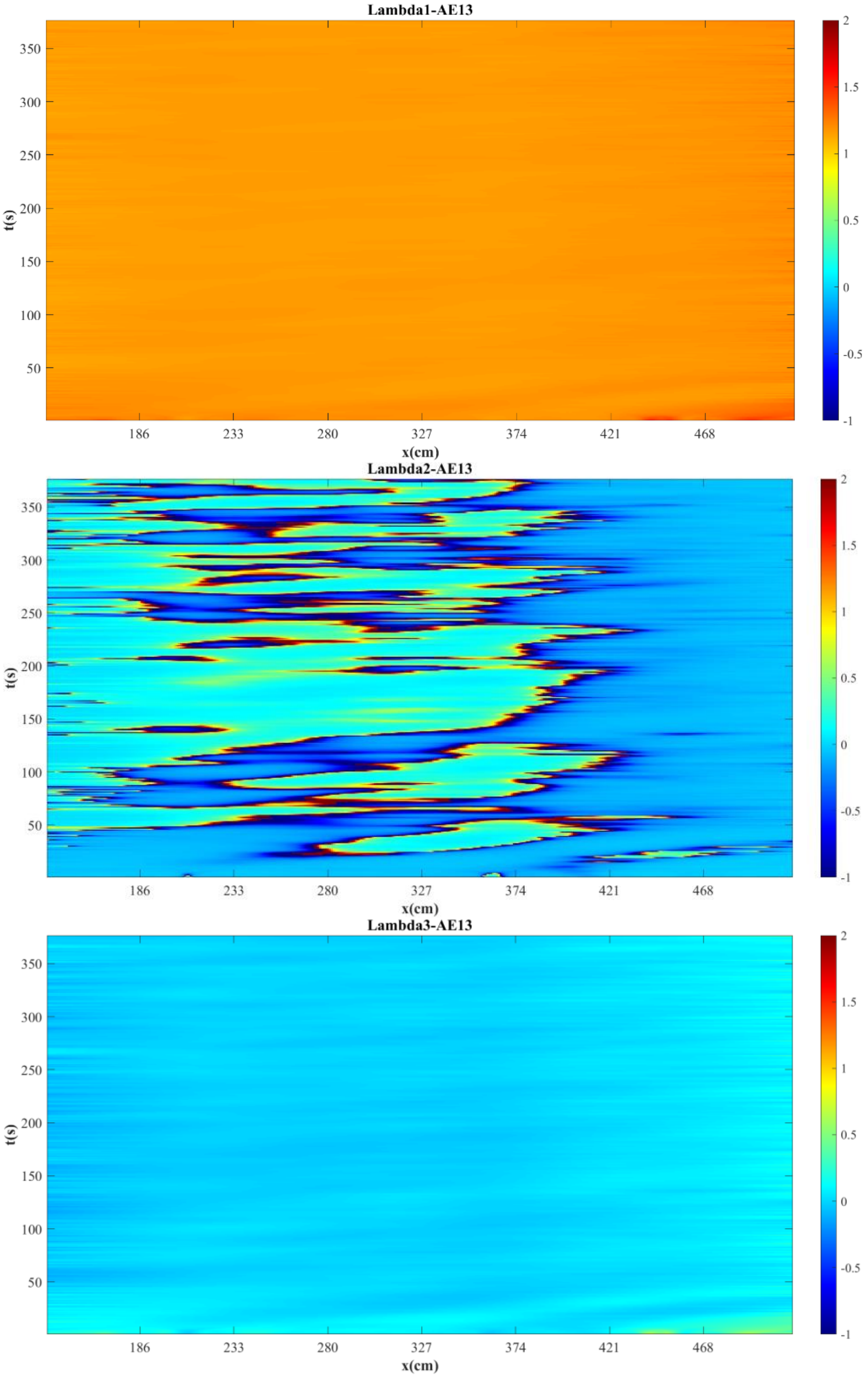

AE13 - 9 Color gradient maps for local celerity, Lambda 1, Lambda 2, and Lambda 3 evolution in space and time

Experiment AE14

Vibration level	Opening height (cm)	S_0 (%)	t (sec)	Q water (l/s)	Q_{sin} (m^3/s)	Q_{s0} (m^3/s)	Froude number Fr	Loading ratio Lr
8.75	2	1.2	240	7	2.58E-04	1.46E-04	1.01	1.76

AE14 - 1 Experimental parameters

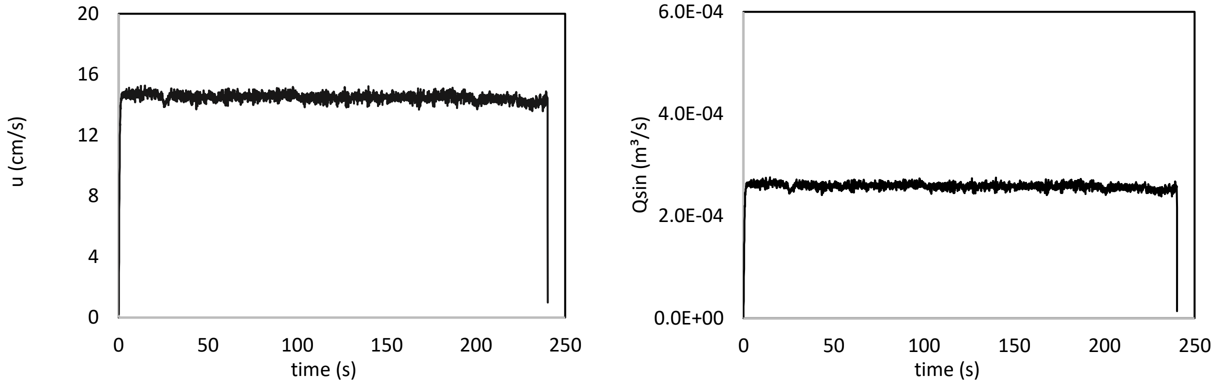

AE14 - 2 Temporal evolution of velocity and sediment discharge

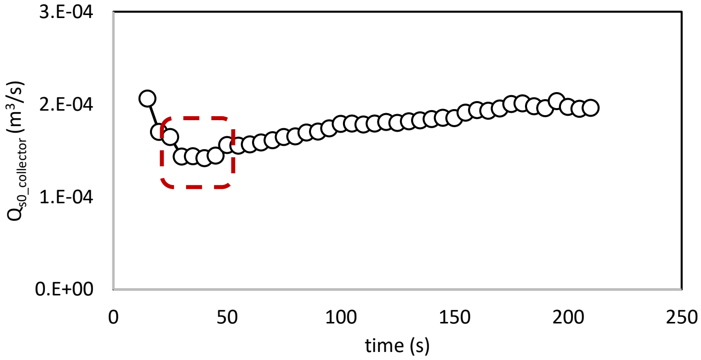

AE14 - 3 Temporal evolution of sediment transport capacity considering the collector method. The average of the constant values of Qs0 is considered as the Qs0, collector.

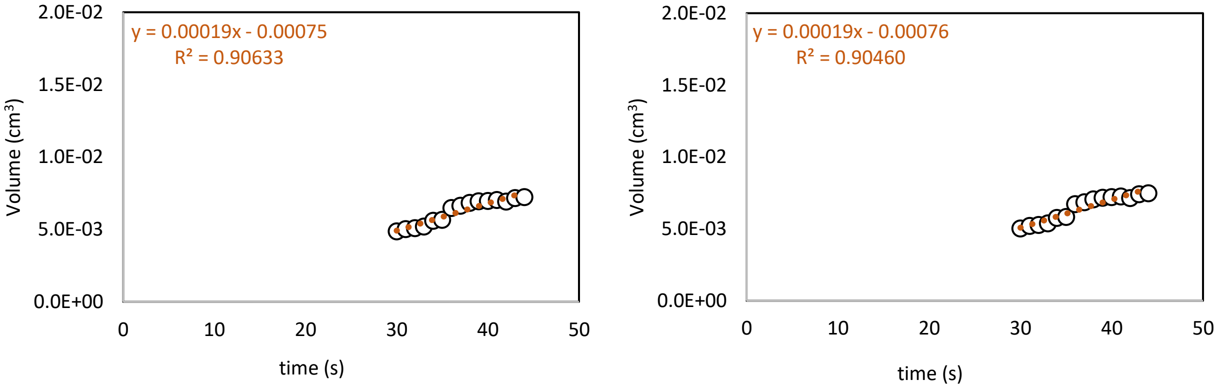

(a) CU2 Scenario *(b) IU2 Scenario*

AE14 - 4 Temporal evolution of sediment transport capacity considering the continuity method and four scenarios. The average of the slope of the interpolating lines is used to calculate Qs0, monitored.

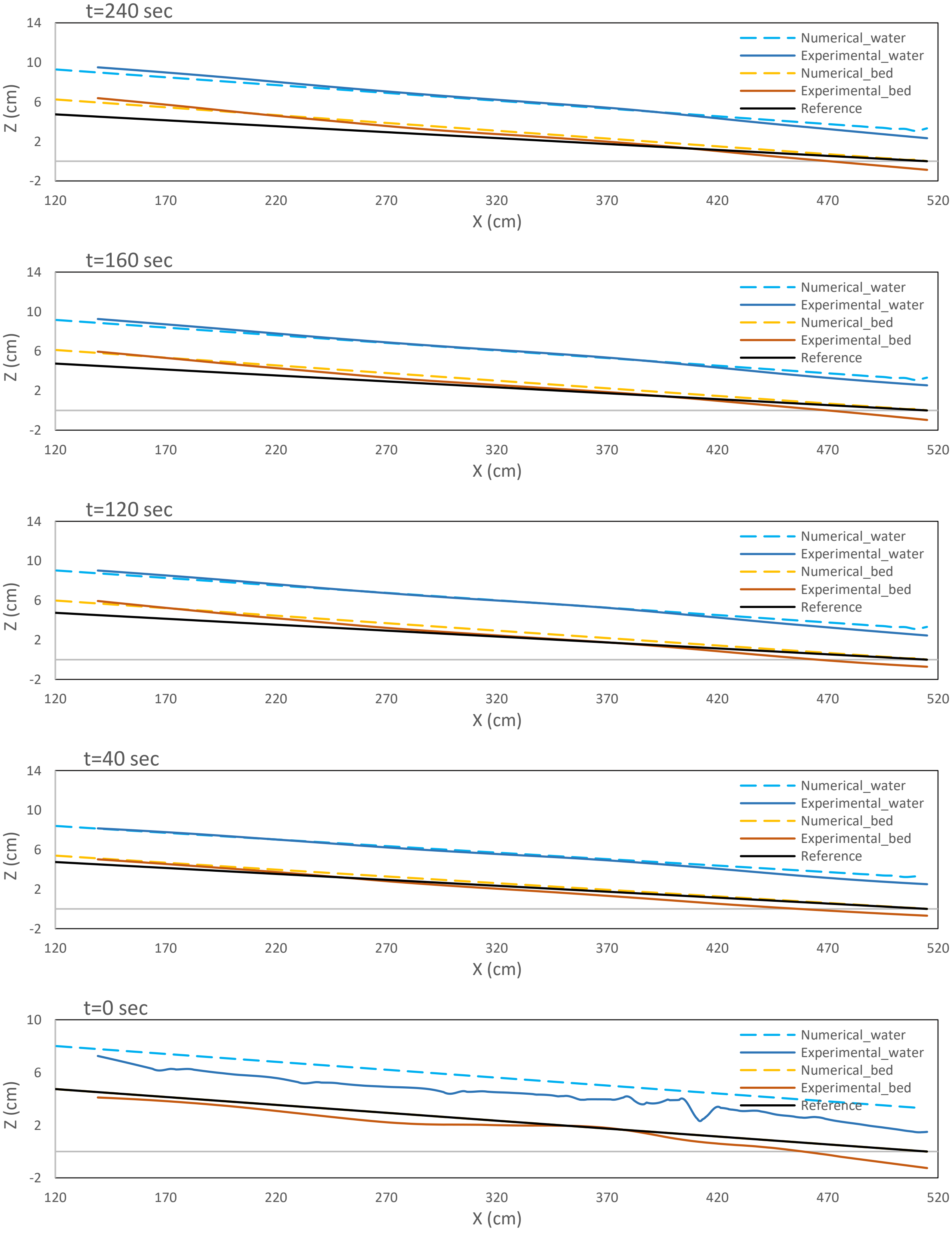

AE14 - 5 Spatial evolution of bed and water

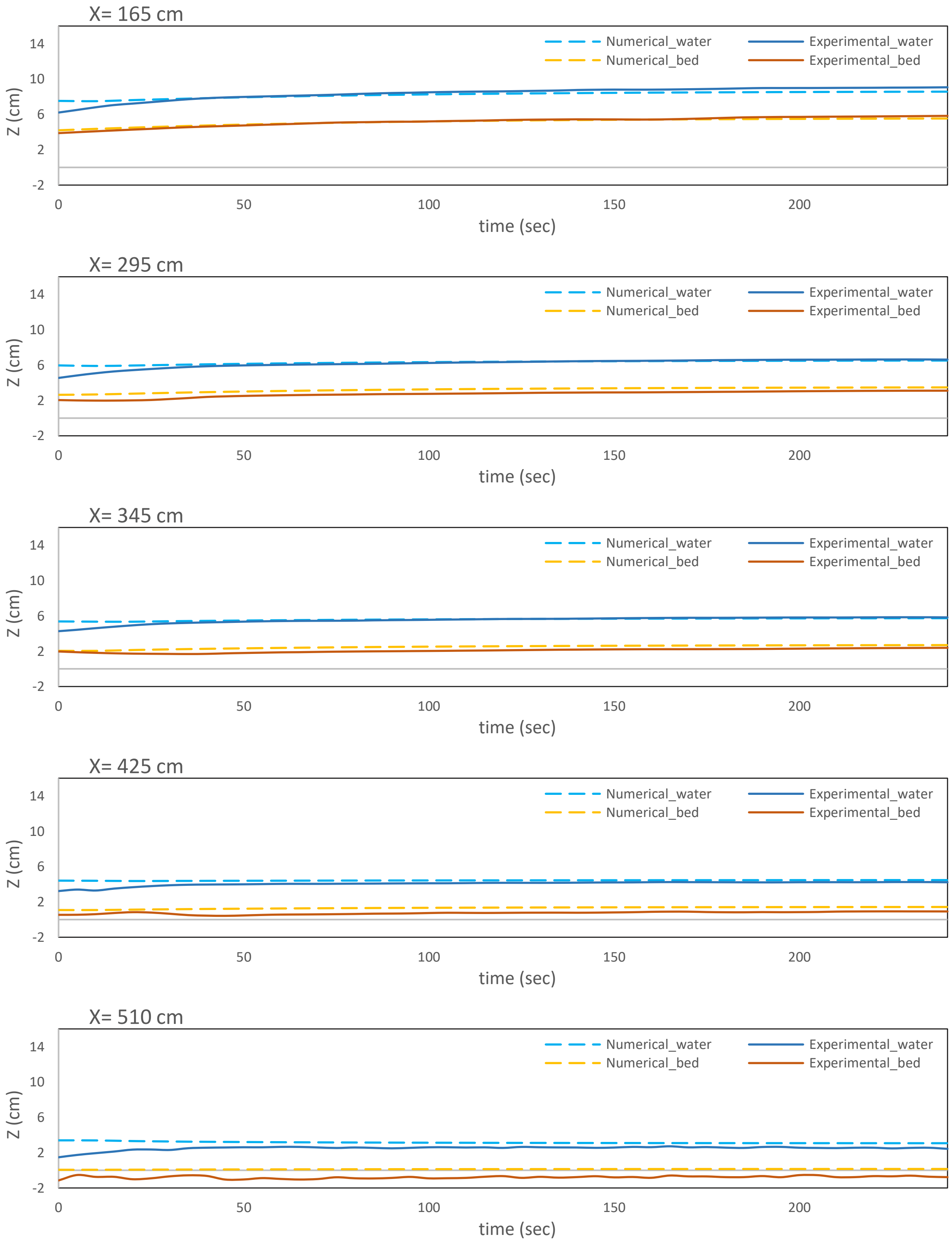

AE14 - 6 Temporal evolution of bed and water

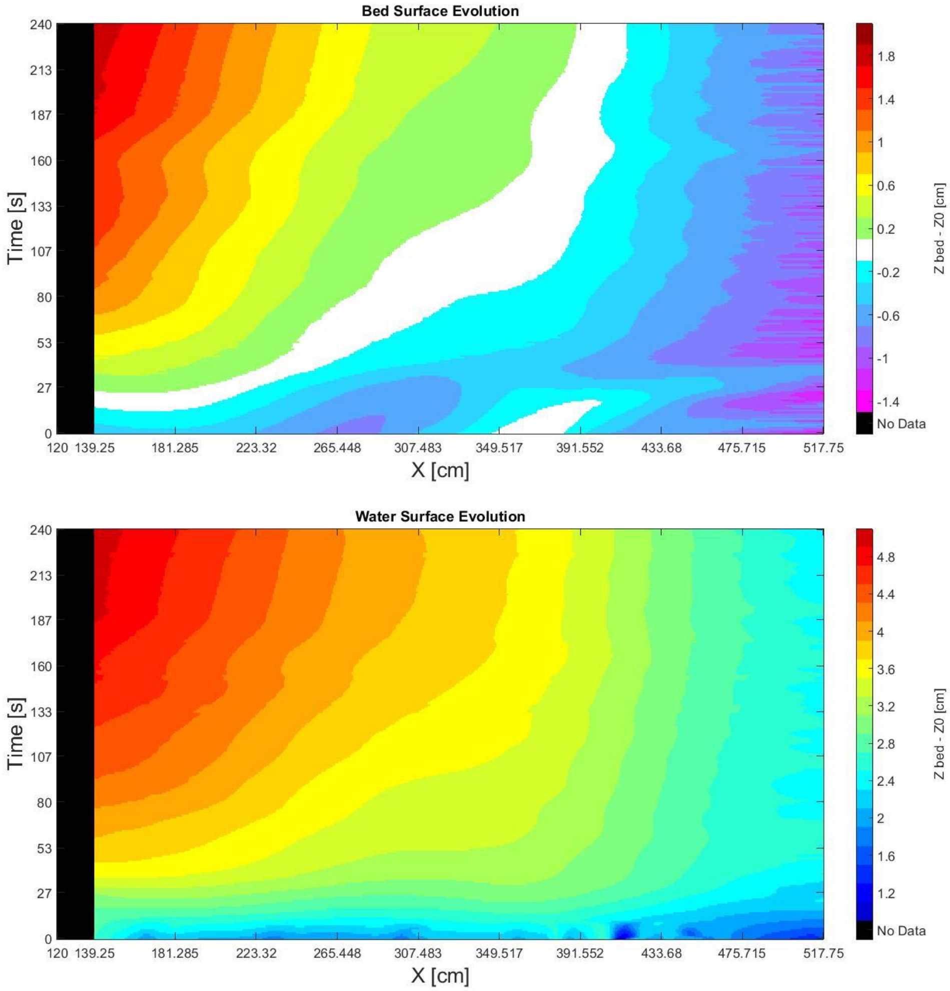

AE14 - 7 Color gradient maps for bed and water surface evolution in space and time

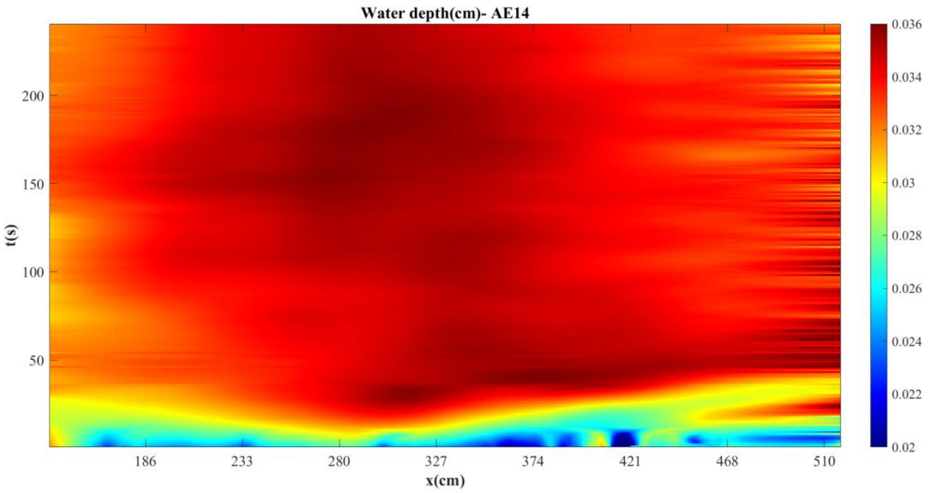

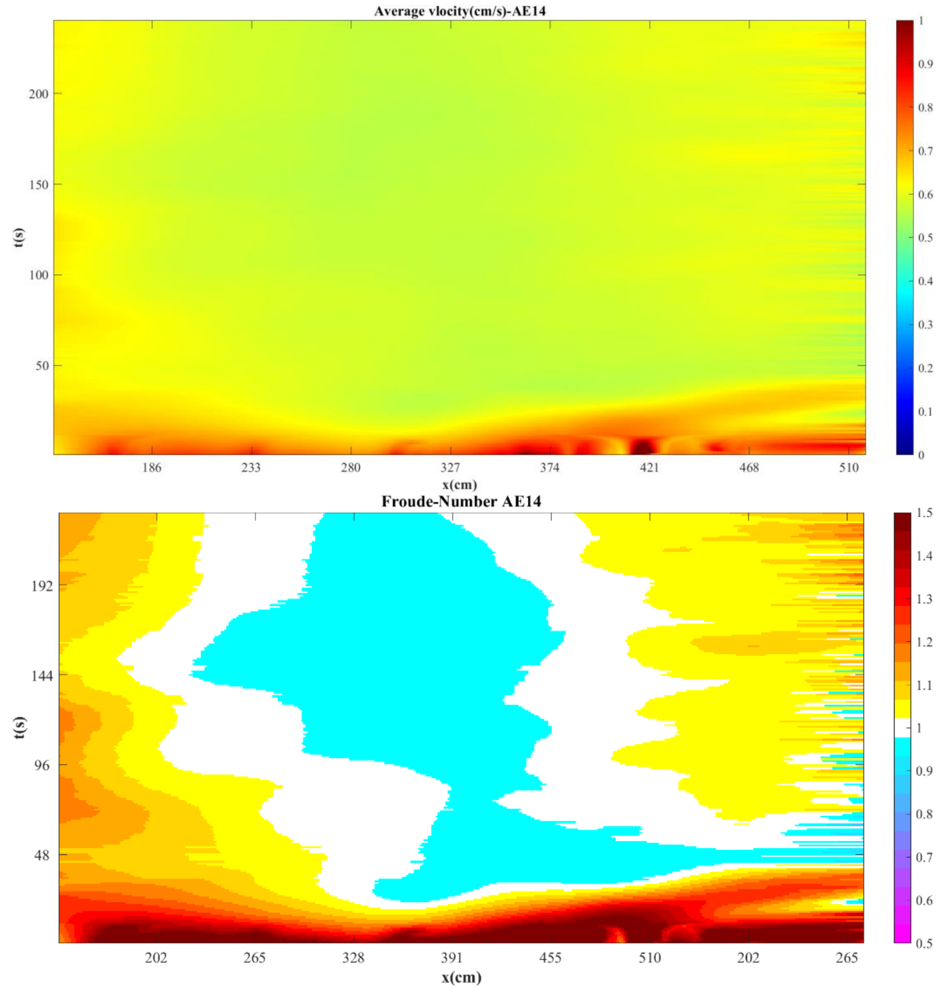

AE14 - 8 Color gradient maps for water depth, water average velocity, and Froude number Fr evolution in space and time

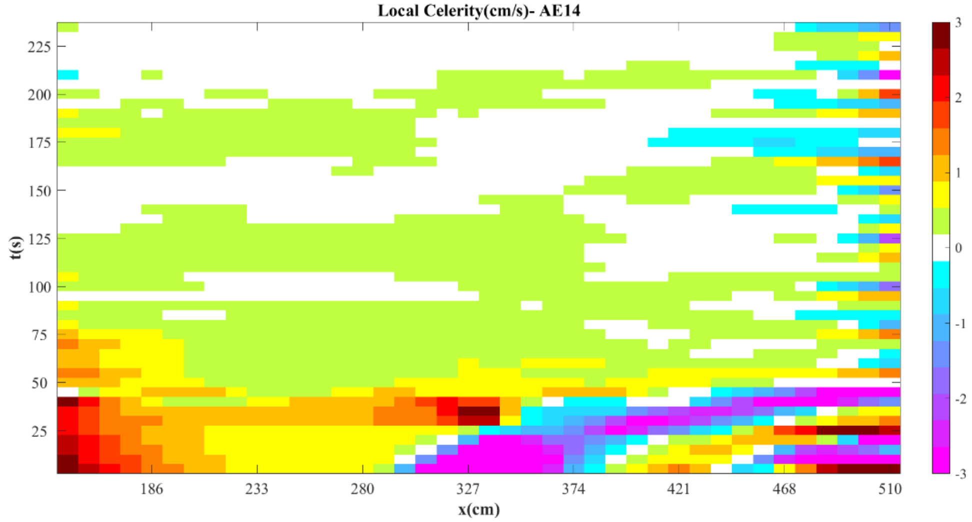

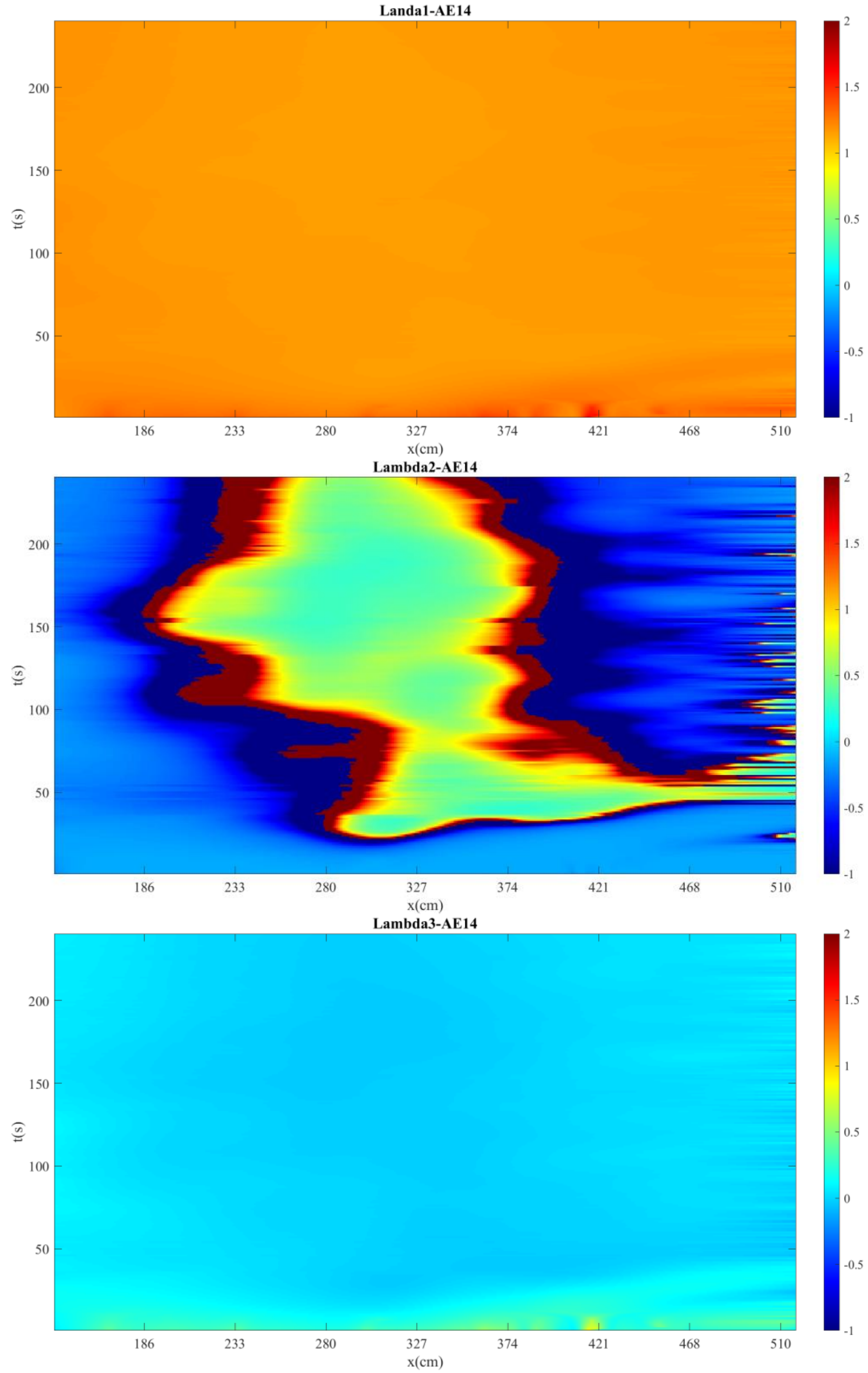

AE14 - 9 Color gradient maps for local celerity, Lambda 1, Lambda 2, and Lambda 3 evolution in space and time